Development of an enhanced finite element model for reinforced concrete menbers subjected to combined shear-bending-torsion actions

Tuan-Anh Nguyen

THESE DE DOCTORAT DE

L'INSTITUT NATIONAL DES SCIENCES APPLIQUEES RENNES
COMUE UNIVERSITE BRETAGNE LOIRE

ECOLE DOCTORALE N° 602
Sciences pour l'Ingénieur
Spécialité : Génie Civil

Par

Tuan-Anh NGUYEN

Développement d'un modèle d'élément fini 3D pour des poutres en béton arme soumis à des sollicitations complexes M-N-V-T.

Thèse présentée et soutenue à INSA de Rennes, le 28 Novembre 2019
Unité de recherche : LGCGM
Thèse N° : 19ISAR 25 / D19 - 25

Rapporteurs avant soutenance :

Enzo MARTINELLI	Ass. Professeur – Université de Salerno (Italie)
Frédéric RAGUENEAU	Professeur – ENS Cachan

Composition du Jury :

Président :	Panagiotis KOTRONIS	Professeur – Ecole Centrale Nantes
Examinateurs :	Phillippe LE GROGNEC	Professeur – ENSTA Bretagne
	Christelle COMBESCURE	MCF – Université de Paris-Est Marne-la-Vallée
Dir. de thèse :	Quang-Huy NGUYEN	MCF HDR – INSA Rennes

Invité(s)

Hugues SOMJA	Professeur – INSA Rennes

Intitulé de la thèse :

Développement d'un modèle d'élément fini 3D pour des poutres en béton armé soumis à des sollicitations complexes M-N-V-T

Tuan-Anh NGUYEN

En partenariat avec :

DEVELOPMENT OF AN ENHANCED FINITE ELEMENT MODEL FOR REINFORCED CONCRETE MEMBERS SUBJECTED TO COMBINED SHEAR-BENDING-TORSION ACTIONS

by

Tuan-Anh NGUYEN

A Thesis Submitted in Partial Fulfillment of
the Requirements for the Degree of

Doctor of Philosophy

in the Graduate Academic Unit of Civil Engineering

Supervisors:	Quang-Huy NGUYEN, A.Professor, INSA Rennes
Examining Board:	Enzo MARTINELLI, A.Professor, University of Salerno Frederic RAGUENEAU, Professor, ENS Cachan Panagiotis KOTRONIS, Professor, Ecole Centrale Nantes Philippe LE GROGNEC, Professor, ENSTA Bretagne Christelle COMBESCURE, PhD, University of Paris-Est Marne-la-Vallee
Invite:	Hugues SOMJA, Professor, INSA Rennes

Department of Civil Engineering and Urbanism

INSA RENNES
November, 2019

This thesis is dedicated...

to my beloved **Parents**

to my darling **Wife**

to my lovely **Kiwi**

to my home country **Vietnam**

Acknowledgments

First and foremost, I would like to express my most sincere gratitude to my supervisor A.Prof. NGUYEN Quang-Huy for the proposition of this research subject, for the continuous support and immense knowledge during my PhD study, and especially for being an excellent mentor from whom I have learned a lot. His guidance helped me in all the time of research and writing of this thesis. I could not have imagined having a better advisor and mentor for my PhD study. I would like to also thank Prof. Hugues SOMJA, the co-supervisor of my PhD, for his availability, his valuable advices and supports during my PhD study and also related research.

Sincere thank also goes to A. Prof. Enzo MARTINELLI and Prof. Fredric RAGUENEAU for their insightful comments and the interesting questions which allowed me to widen my research from various perspectives. I am also grateful to Prof. Panagiotis KOTRONIS, Prof. Phillippe LE GROGNEC and A. Prof. Christelle COMBESCURE who accepted to serve in my thesis committee.

Three years and a half in INSA Rennes have been a precious and unforgettable experience for me, I would like to express my gratitude to all the staff in the Department of Civil Engineering & Urbain, INSA Rennes and the members of GCGM Laboratory, it was great sharing experiences with all of you.

Finally, a last but not least gratitude from the bottom of my heart to my family: my parents, my sister, my little daughter and especially, my wife, for their endless support, encouragement and love during my PhD study.

This Ph.D thesis was carried with the financial support of Program 911 by Vietnamese government. Special thanks to the personnel in charge et the VIED and Campus France who gave me all the necessary helps in administration. I want also to express my gratitude to GCGM laboratory and Department of Civil Engineering, INSA Rennes that allowed me to carry out this doctoral thesis.

Abstract

Most civil engineering structures are subjected to multi-axial actions, including normal forces and tangential efforts. Even though the effects of shear and torsion have already been implemented in several theories and models of structural analysis, a rational theory is still lacking. In order to make some contributions to this field of research, the present PhD thesis deals with the development of a non-linear finite element model for reinforced concrete members under coupling of multi-axial actions and in particular under torsion.

Using the sectional-fiber approach and the displacement-based formulation, an enhanced multi-fiber 3D beam element is developed for predicting the behavior of reinforced concrete elements subjected to arbitrary loading conditions (shear, bending and/or torsion). The section kinematic is based on the enhancement of Timoshenko's beam kinematic assumptions with introducing of some additional degrees of freedom at each monitoring section in order to take into account the phenomena of warping and eventually, distortion. To do so, a system of fixed points is created and interpolated by Lagrange functions and polynomials. Otherwise, Saint-Venant theory for beam is also considered and used as a reference compared to the enhanced formulation. Focusing on reinforced concrete structures, in the multi-fiber approach, taking into account the contribution of transversal reinforcement is not straightforward. Thus, one of the objectives is to find the simple way to include the transversal reinforcement into the cross-section analysis of the multi-fiber FE model. In the present work, each monitoring cross-section is discretized into regions followed its material response and stress state. In each region, depending on its characteristics, an appropriate constitutive material model is applied and included with an iteration process satisfying internal equilibrium between concrete and transverse reinforcement. For this purpose, the proposed behavior models are based on the Modified of Compression Field Theory and its extension.

The assessment of the proposed FE model is performed with several numerical-analytical-experimental comparisons. Numerical analysis of concrete and RC members under elastic and inelastic material regimes are carried out for two cases of loading: pure torsion and combined shear-bending-torsion. In order to predict the pure torsional response of concrete and RC members, a constitutive law for concrete in tension is proposed within the framework of the Modified Compression Field Theory in which the material parameters are determined by the calibration process of several experimental tests. Regarding the case of combined actions, the shear-bending-torsion interaction is investigated by comparing with the analytical solutions of skew-bending theory and several experimental tests in literature. Finally, the study is completed with the investigation of the enhanced FE multi-fiber beam model under large displacement conditions, using a corotational framework. Several examples and comparison are performed for the illustration of nonlinear geometric effects to the coupling between the actions due to the torsional effect.

Contents

List of Figures

List of Tables

Chapter 1

Introduction

1.1 General

Most civil engineering structures are subjected to multi-axial actions, ranging from many kinds of structures (buildings, bridge decks, electric pylon, etc.) to many kinds of construction material (reinforced concrete, steel, wood or hybrid structure). Thus, in order to completely perform the modeling of the structures in real conditions, its model must be able to take into account the multi-axial actions, including normal forces (axial force and bending moments) and the tangential forces (shear forces and torsional moment). Between these states, axial force and bending moments are widely studied and simulated by an accepted rational theory based on the plane section hypothesis. Nevertheless, even though there are several theories of structural analysis under shear and torsion, a basic rational theory is still lacking. In addition, when determining the completed behaviors of structural element, especially reinforced concrete members, the coupling of actions still remains open to discussion although it has already been taken into account in various models. In particular, for the conception under hazardous conditions (typhoon or seismic risks), in which accurate analyzes at the local and structural scale are indispensable, it is increasingly necessary to develop theoretical and numerical models capable of representing the coupling of all external forces.

In professional structural engineering, finite element modeling is considered suitable for the analysis of all types of structures, from simple to complex, from one to three dimensions. In facts, although all real structures are in three dimension, many of them have one privileged direction over the other two and can be assimilated to 1D components, such as building's beams, columns, bridge decks or frame elements. Indeed, all

the mechanical characteristics of cross-section is condensed in the reference axis by imposing specifics static and kinematic hypotheses. Then, this one-dimensional structure, called beam-column or frame type elements, can be modeled and discretized in linear elements throughout a system of monitoring cross-section along the element axis (Figure 1-1). Frame elements can offer an optimal balance between accuracy and computational efficiency, therefore they are the most employed in structural analysis and simulations. In the case of structural elements with small span-to-depth ratio, such as shear wall or plate, two-dimensional or shell finite elements are employed for the modeling. Three-dimensional solid finite element models can provide the best response for the behavior of structures under complex load conditions. However, it requires a very high computational cost and complex material constitutive equations, so it is generally used for the analysis of special detailing problems.

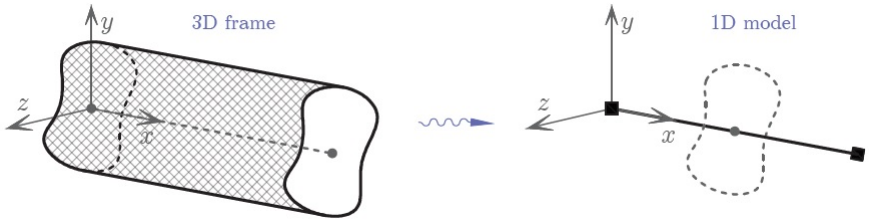

Figure 1-1 – Modeling of three-dimensional element as one-dimensional frame element

Nowadays, the design of structures is required in a safer and more economical way, so it is necessary to accurately simulate the structural performance in the inelastic range until failure. Handling the inelastic material response is therefore evident in the conception phase of conventional constructions. For structures designed against seismic or other extreme load conditions, non linear analysis becomes more evident and indispensable, not only for the material response but also for geometry conditions. Many finite element models and frame element approaches have been proposed to respond to this demand, numerous models between them can well describe the interaction of normal forces under non-linear geometry assumptions, such as fiber or multi-fiber beam elements. However, there are few beam-column models that are capable to account for the effect of shear, in which the stress state is enlarged to two dimensions with the contribution of the shear stress. In addition, the inclusion of torsion needs an extension to three dimensions and an increased complexity with the coupling of internal forces under nonlinear geometry conditions.

Indeed, the numerical modeling of civil engineering constructions under severe and

multi-axial coupling conditions is still a challenging problem, especially in the case of plain concrete and reinforced concrete structures due to the complex characteristics of its mechanical behavior. Although in the last thirty years fiber beam elements have been developed and applied successfully in the analysis of reinforced concrete members, the inclusion of shear and torsional effects in this model is not obvious and the effect of normal and shear stresses are usually treated separately. In this PhD thesis, the objective is to develop an enhanced multi-fiber beam finite element model in three dimensions, suitable for the simulation of reinforced concrete structures subjected to monotonic loads under consideration of multi-axial coupling of axial force, shear, bending and torsion. The developed model takes into account the material and geometrical nonlinearities. This PhD thesis is limited to the reinforced concrete members with rectangular cross-section. However, the element formulation and the constitutive equations is formulated general enough for being applied to any sectional model and any shape of cross-section.

1.2 Context and Motivation

Although considered as a major factor in the design code of reinforced concrete structures, torsion did not draw as much attention by design engineers and researches before the 1960. Prior to this period, knowing that the magnitudes of the stiffness and torsional resistance are in a lower order in comparisons with the one in bending, torsional effects were assumed minor and taken care by a safety factor used in flexural design. This assumption has been responsible for many cases of torsional distress and failure, such as the collapse of Tacoma Narrows Bridge in 1940 due to a torsional vibration mode (Figure 1-2).

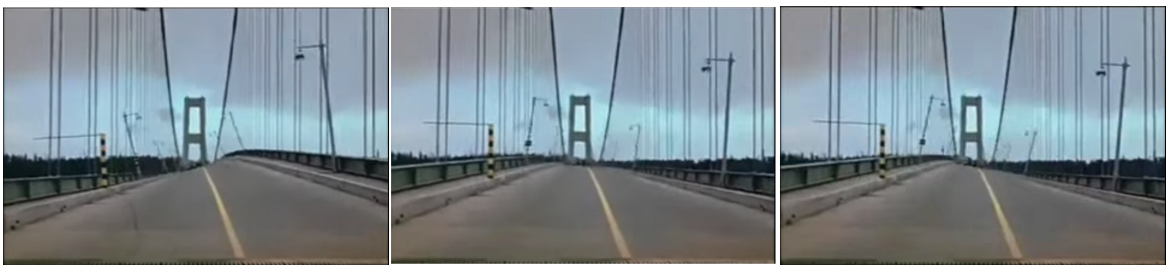

Figure 1-2 – Torsional motion of Tacoma Narrows bridge (screenshots taken from video)

In reality, torsional effects can play a determining role in the stability of structures, for example the electric pylon, skew bridge, railway curved viaduct or bridge desk under asymmetric loads, etc. (Figure 1-3). In the context of conventional reinforced concrete buildings, torsion can be found widely: beams that support cantilever slabs or balconies,

wall foundation beam, beams next to floor opening or spandrel beam. However, it is still usual to neglect the torsion in the simulation of frame elements such as beam and/or column.

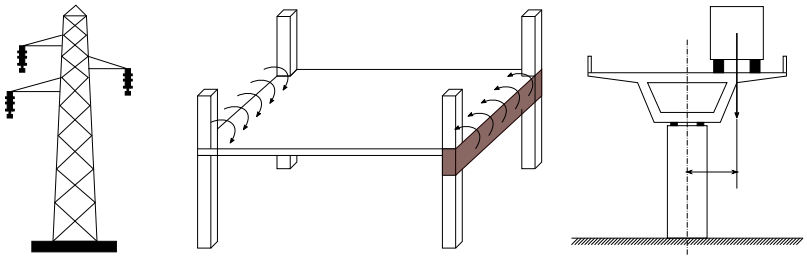

Figure 1-3 – Examples of usual structure where torsional effect is important.

In the case of RC buildings using thermal insulation from the inside, a thermal bridge is occurred at the floor-to-wall junction. This thermal bridge disturbs the continuity of the thermal insulation and must be treated by a thermal bridge breaker (Figure 1-4a), in accordance with the Thermal Regulation. In the case of holding the balcony, the floor slab extends through the building envelope, and in order to transfer the weight of the floor to the wall, it is necessary to provide the contribution of a structural element called *lintel* (Figure 1-4b), usually made of steel because of its lightness. However, the lintel is attached to the thermal bridge breaker, and steel is a low insulating material, its efficiency may be reduced accordingly. So, the lintel is designed as a horizontal beam of reinforced concrete of rectangular cross-section, subjected to a combined of bending, shear and torsion, for which the theoretical and numerical models are few in the literatures.

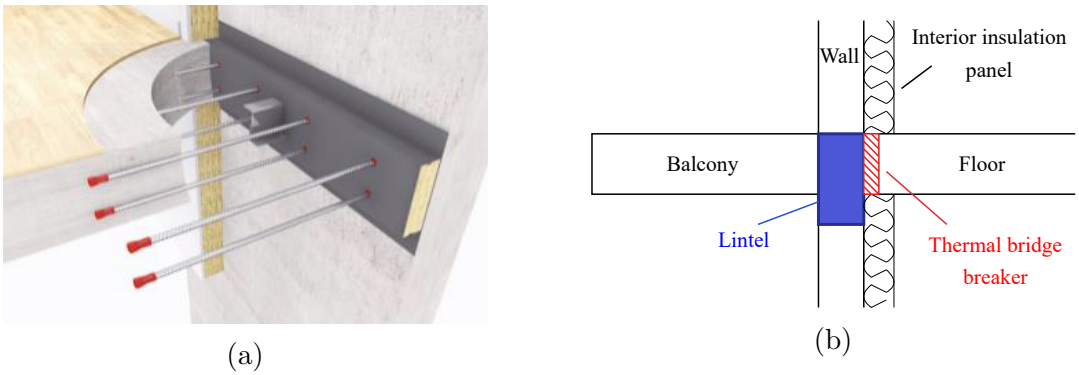

(a) (b)

Figure 1-4 – (a) Thermal bridge breaker. (b) Disposition of lintel beam in the case of holding the balcony for a building of thermal insulation from the inside.

In addition to the problem of coupling of multi-axial efforts and stresses, the inclusion of tangential effects in the modeling of reinforced concrete members is more complex as it requires a special treatment of the *warping phenomenon*. This phenomenon is described as a peculiar deformation of non circular cross-sections as they warp and come out of their

own plan under shear and torsional effect (Figure 1-5). This phenomenon is particularly important for torsional resistance because it reduces the sectional rigidity, generates the additional normal stresses which decrease the tangential stresses and so strongly influence the twist deformation.

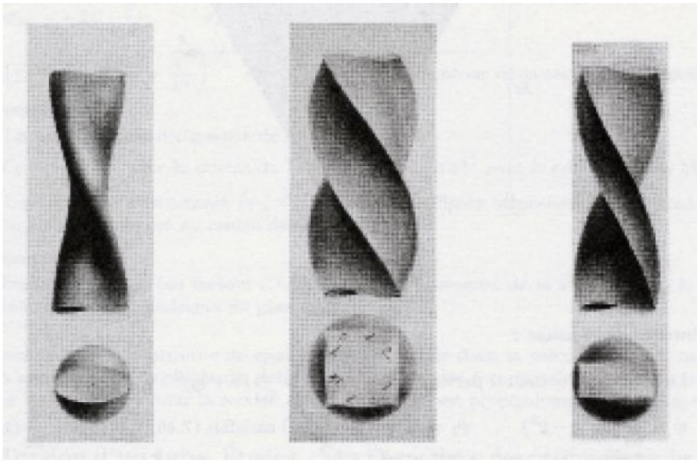

Figure 1-5 – Saint-Venant's original drawings of torsion bars for elliptical, square and rectangular section [97].

1.3 Beam theory and sectionally-based analysis

In the domain of linear elastic material behavior, the most models are based on the Euler-Bernoulli beam theory in which the plane cross-section is assumed to remain plane and orthogonal to the beam axis under deformation. The shear deformations are neglected, so it can only account for the axial and flexural behavior of the beam. It is well-known that the Euler-Bernoulli beam theory gives reasonable results for slender beams. However, in case of short beams, the shear flexibility needs to be accounted for. The simplest way to include the effect of the transversal shear is to use the Timoshenko beam theory [105], so called "first order shear beam theory". These two theories and the hypothesis of plane section are considered as the basic theory (or engineering beam theory) for the analysis of linear and nonlinear beam finite elements.

In the domain of nonlinear material behavior, the discrete finite element models give a very good compromise between accuracy and simplicity. In this approach, the structure is modeled as an assembly of interconnected elements and the constitutive nonlinearity is either introduced at the element level or sectional level. The *lumped-plasticity models* is widely regarded as the most basic type of discrete finite element models, in which the inelastic behavior is concentrated at the ends of elements, and the rest remains elastic. In

this end-fixed points, called plastic hinges, the nonlinear responses are given as generalized force-displacements characteristics such as axial force-elongation of moment-rotation relationships, based on the concepts of plasticity theory. The earliest models were introduced by Clough (Figure 1-6a), in which the element consists of two parallel elements, one elastic-perfectly plastic and the other perfectly elastic [21]; and by Giberson (Figure 1-6b) with a series model consist of a linear elastic element with one equivalent nonlinear rotational spring attached to each end [40].

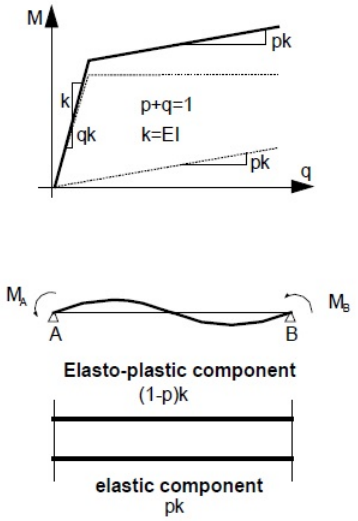

(a) Parallel model of Clough [21].

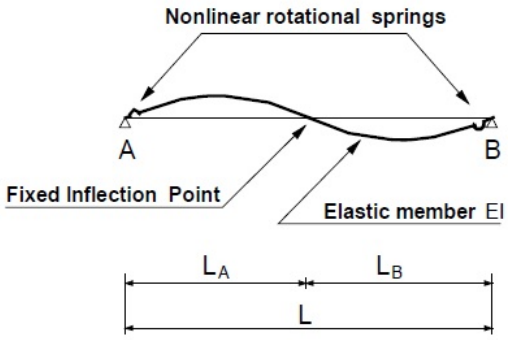

(b) Series model of Giberson [40].

Figure 1-6 – Lumped-plasticity models.

The second and more general approach of discrete finite element models is referred to as the *distributed nonlinearity models*. In contrast to lumped-plasticity models, the material inelastic behavior can take place at several selected points of the structure, then the element response is obtained by numerical integrations of the monitoring sections located at these selected points (or integration points) along the element. In each monitoring cross-section, the constitutive behavior can be formulated in accordance with plasticity theory for sectional stress and strain resultants, or explicitly derived by a discretization of the cross-section into a systems of integration points, called *fibers*. Between these two approaches, the second, also known as *sectional-fiber model*, does not require the definition of nonlinear constitutive relations in terms of cross-section resultants, instead the material behavior laws are defined at the fiber material level, so it leads to a simple way to account for the sectional response. For reinforced concrete members, the sectional fiber model has been widely developed and successfully applied with very high levels of accuracy when describing the coupling between axial force and bending moment in the models of Chan [20], Scordelis [101] or Taucer, Spacone & Filippou [104, 102]. In these models, the

constitutive equations require only one-dimensional material behavior for concrete and steel, thus they are very appropriate in the case where the effect of shear stress is not dominant. The proposed model in this study is constructed based on the development of this type of models, using a two-node finite element beam (Figure 1-7), but taking into account two and three dimensional material behaviors for concrete.

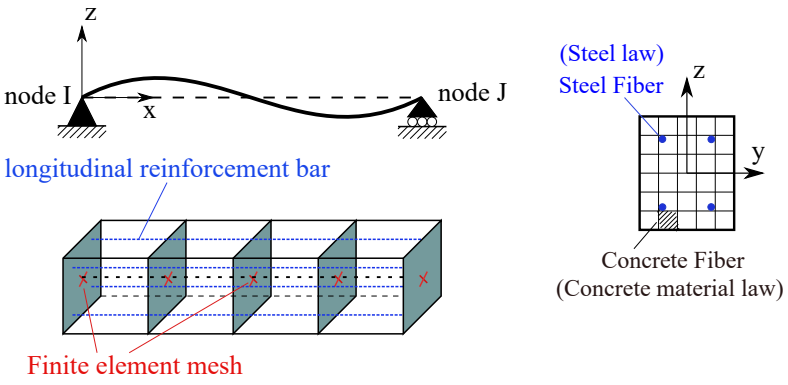

Figure 1-7 – Sectional-fiber approach for reinforced concrete member and local element frame coordinate using in this study.

The construction of distributed nonlinearity and sectional fiber models is based on the analysis of sectional response. In principle, two main factors are required in the sectional analysis:

- A suitable sectional kinematics to obtain the stress and strain distributions in the cross-section. In the classical sectional-fiber model, the plane section theory is used to relate the material strains to section deformations. However, as mentioned above, under shear and torsional effects, the warping phenomenon disturbs the validity of plane section assumption. In this study, the kinematic equations are based on Timoshenko beam theory and enhanced by an additional displacement field in order to take into account the warping deformation. This enhanced field is developed not only for warping displacement but also for the distortion of the cross-section's shape. The details of kinematics equations is expressed in Chapter 3.

- A consistent constitutive model of the materials to establish the stress-strain relationship. Under multi-axial loading, the modeling of the concrete behavior is quite complex, particularly because of the different of stress-strain relationships between compression and tension, which cause an anisotropic behavior under multi-axial stresses. In the last decades, many constitutive models have been proposed for the analysis of concrete structures, such as non linear elasticity, plasticity models,

damage mechanics or micro-plane models. Among them, the approach that is particularly suitable for sectional analysis under combined loading is *smeared crack approaches*, which can handle cracking of concrete as a distributed effect with directionality. A brief review of some smeared crack models will be described in Chapter 2. A consistent constitutive law of concrete will be proposed in Chapter 4 for the case of RC members under pure torsion.

Generally, in finite element analysis of beam-column element, the nodal variables are considered as global degrees of freedoms, from them the mechanical characteristics (displacements, strains, stresses) are derived and interpolated along the axis. Depending on the choice of the primary unknowns (displacement field, force field or both), the formulations of beam-column finite element are usually classified as:

- Displacement-based formulation: the relation between section and element response is based on kinematic equations with the use of appropriate shape functions. In this formulation the element variables are the nodal displacements while the primary unknowns are the element deformations.

- Force-based formulation: the element response are evaluated from the stress field that are interpolated along the element length by imposing the equilibrium with the nodal forces. The primary unknowns in this formulation are the internal element forces.

- Mixed-based formulation: this approach use the force interpolation functions like force-based formulation and a flexibility dependent shape functions for the deformation field of the element.

In this study, the displacement-based formulation was chosen because of its simplicity and the easily in the implementation of enhanced displacement fields. Although force or mixed-based formulation are capable of giving more adequate solutions, the numerical results performed by proposed model using displacement-based in this study is satisfactory and reasonable.

1.4 Objectives and Scope

The main objective of this doctoral thesis is to develop an enhanced finite element beam model for the material and geometrical analysis of reinforced concrete members subjected to combined loading: axial force, bending, shear and torsion. The specific objectives are as follows:

- The development of a 3D beam-column element for reinforced concrete members using multi-fiber discretization and sectional analysis approach. In this study the model is developed primarily for rectangular cross-section, but the formulation is expressed generally enough for arbitrary cross-sections.

- The implementation of an enhanced displacement field into kinematic equations in order to include the warping displacement of cross-section under the effect of shear and torsion. Then, numerical analysis is carried out to study the influence of the warping deformation on the stress state.

- The adaptation of the Modified Compression Field Theory (MCFT) to the concrete constitutive law.

- The adaptation of the cross-section discretization into different regions following the stress state (1D, 2D and 3D) in order to take into account the contribution of transversal reinforcements and the concrete confinement. A new parametric formulation for determining the rule of this discretization will be also proposed.

- The implementation and derivation of a general and consistent corotational framework into 3D beam-column formulation in order to take into account the nonlinear geometric condition.

This PhD thesis is organized into seven chapters. The first one is the current introduction chapter. Chapter 2 presents the state of the art including a bibliographical study. In this chapter a review of nonlinear analysis models for reinforced concrete element are briefly listed and discussed.

Chapter 3 deals with the development of the finite element model for RC members subjected to combined shear-bending-torsion. As mentioned above in Section 1.3, the proposed FE model is based on the fiber-sectional discretization and the displacement-based formulation. The enhancement of the kinematic equations is implemented and

expressed in two different approaches: using Saint-Venant warping function and using Lagrange interpolation polynomials. Then the chapter is followed by the derivation of the element response from the variational formulation based on the principal of virtual works, a solution scheme and concludes with the mechanical model for reinforced concrete members that was implemented in this sectional model. In order to take into account the contribution of transversal reinforcement, the cross-section is discretized into different regions following the stress state, based on the idea of Navarro-Gregori [76].

Chapter 4 is dedicated to investigate the behavior of the RC members under pure torsion using the proposed model. Because no specific rules are currently available for the determination of the thickness of the regions in the section discretization, a calibration study is performed for calculating this parameter is developed by the author. This calibration study was then used to propose a consistent behavior law for concrete under torsional effect, knowing that numerical cracking torsional moments are reduced about half of the experimental values when using the original MCFT. In this chapter, the numerical results performed by the proposed model are compared with numerous experimental date, others numerical results and design code prediction.

Chapter 5 deals with the numerical analysis of RC members under in shear-bending and shear-bending-torsion combination using the developed FE model presented in Chapter 3. The predictions of the proposed model are compared against the results of other numerical models and the experimental values. The aim of this model validation is to assess the capability of the proposed nonlinear technique to satisfactorily predict the structural behavior of RC members under combined loading of shear-bending-torsion.

Chapter 6 describes the model formulation under the hypothesis of large displacement conditions. The corotational framework is briefly presented and implemented in the beam element. Then, the interaction between axial and torsion effect at local level is considered and analyzed in the numerical examples.

Finally, the chapter 7 summarizes the study, offers conclusions and recommends some directions for further research study.

Chapter 2

State of the art

2.1 General

This chapter deals with a literature review of nonlinear analysis models for RC members subjected to bending, shear and/or torsion. The models can be classified according to their constitutive equations: theory of plasticity, micro-plane model, fracture or damage mechanics, etc.; or following the concept of modeling and discretization. To the best of the author's knowledge, the numerical models treating the behavior of RC members under combined shear-bending-torsion can be classified in three groups as follows:

- **Skew-bending theories**: an analytical approach in which the basic characteristic is the assumption of a skew failure surface.
- **Truss models**: derived from the concept of space truss analogy, this type of models can be subdivided into certain subgroups such as strut-and-tie models, equilibrium truss models and compatibility truss models.
- **Sectional-fiber models**: the most recent approach in which tangential and normal efforts are coupled directly. These models can be subdivided into certain subgroups following their strategy of discretization.

In the following, a brief presentation of each group is done.

2.2 Skew-Bending theories

The principal idea of Skew-Bending theories is that a helical crack is generated on three faces of a rectangular RC beam, and the ends of this helical crack are connected by

a compression zone near the fourth face. Both longitudinal reinforcement and closed stirrups are intersected in the failure surface and it is often assumed that they will both yield at the failure of the beam.

The first skew-bending theory was proposed by Lessig [66] in 1959, in which two modes of failure are introduced, concerning the position of the compression zone: near the top face of the beam (Mode 1 - Figure 2-1a) or along a side face (Mode 2 - Figure 2-1b). A set of three basic equations are produced for each mode of failure: one equilibrium of moments about the neutral axis, one equilibrium of forces along the normal to the compression zone and a third equation which minimizes the strength of the member. Lessig's theory was then simplified and incorporated into the Russian Code in 1962 [81] in order to recognize the shear failure mode and propose an empirical equation against its occurrence.

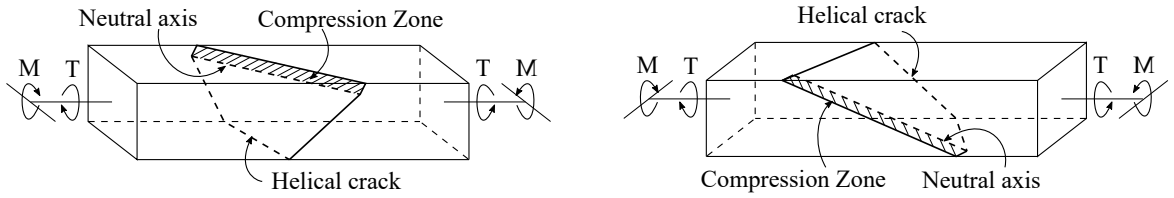

(a) Mode 1 - Flexural moment predominates

(b) Mode 2 - Torsional moment predominates

Figure 2-1 – Failure modes in Lessig's theory.

Collins et al. [23], [24] developed Lessig's theory by combining these three equations into a unique one for each failure mode and obtaining an interaction curve as a result: a torsion-bending interaction curve in Mode 1 and a torsion-shear interaction curve in Mode 2. A third mode failure accompanying by a third interaction curve was also discovered in this theory, in which a compression zone locates near to the bottom face of the beam (Figure 2-2). These three interaction curves formed an interaction surface between bending, shear and torsion (Figure 2-3), that was also modified by an empirical equation for shear failure, which may be considered as the fourth mode of failure. The Collins et al.'s theory served as a basis for the Australian Code (1973) [80]. In this design code, torsional moment is converted into an equivalent bending moment (and/or an equivalent shear force) that could be added to the actual bending moment (and/or flexural shear force) for the design of longitudinal steel according to the conventional flexural mechanics (and/or for the design of web reinforcement according to the conventional code method).

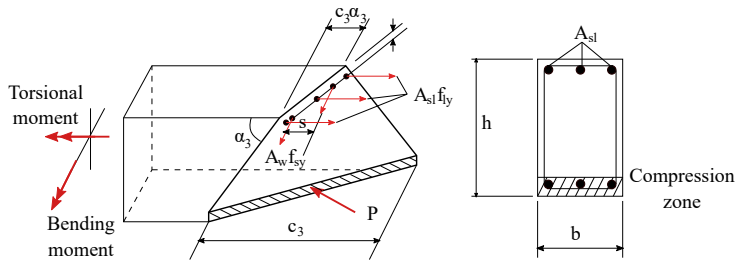

Figure 2-2 – Mode 3 failure in the theory of Collins et al. [23].

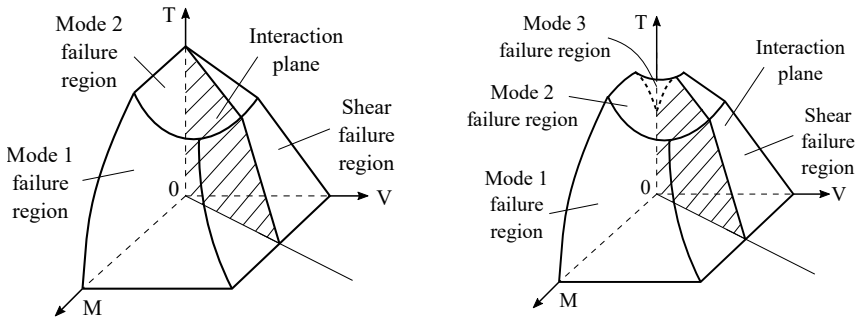

(a) Symmetrical members. (b) Unsymmetrical members.

Figure 2-3 – Interaction surface for combined bending, shear and torsion in the theory of Collins et al. [23].

Other skew-bending theories were also developed based on the Lessig's theory, such as the theory of Yudin [116] or Elfgren et al. [35]. Yudin's theory introduced two moment equilibrium equations instead of one, as a result it was able to derive two designs equations for the longitudinal and transversal reinforcements. In this theory the crack inclination was assumed constant and equal to 45 °. In a more general way, Elfgren et al. assumed a variable angle of crack inclination and it could also be different at the two side faces in Mode 1 and Mode 3 of failure. In this condition, internal vertical force must be balanced to the external shear, thus an additional equilibrium equation was introduced, that gave an explicit bending-shear interaction curve. As a result, this theory created a general and complete interaction surface for bending, shear and torsion (Figure 2-4).

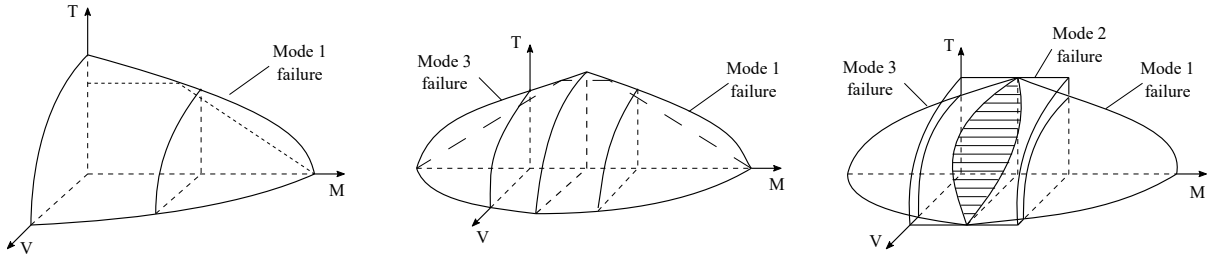

Figure 2-4 – Interaction surface in Elfgren et al.'s theory [35].

The above skew-bending theories may be related to the *kinematic approach* in terms of the plastic analysis of structures under uniaxial stress [54]. This approach seeks for

a deformation mechanism that satisfies the geometric boundary conditions. Another approach in the plastic analysis is the *static approach* that searches for a stress distribution in equilibrium internally and balanced with the external load. The concept of truss models in the following section relates to this static approach.

Analytical formulations for predicting the ultimate torsional and bending strengths of concrete and RC members according to skew-bending theories will be cited and used as a reference compared to the numerical results given by the proposed model in the numerical analysis in Chapter 4 and 5.

2.3 Truss models

All models in this section are inspired by the concept of truss model, firstly proposed by Ritter [95] and Mörsch [75] in the early of 20th century, whose purpose is to simulate a RC beam subjected to shear. In general, under shear effect, diagonal cracks occur and separate the beam into a series of concrete struts. An analogy of truss model was therefore assumed, where the longitudinal reinforcement steels act like the top and bottom chords of the truss, while the transversal stirrups and concrete struts hold the role of web members (Figure 2-5).

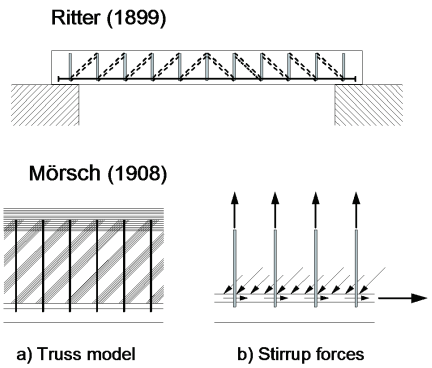

(a) Original concept of Truss model by Ritter [95] and Mörsch [75]

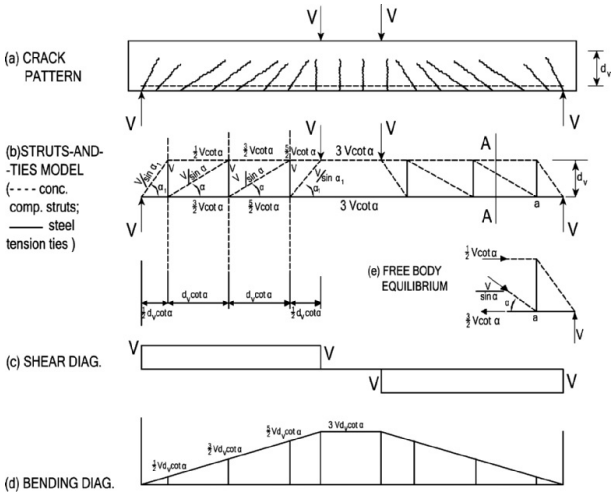

(b) Truss model of a RC beam with longitudinal and transversal reinforcements.

Figure 2-5 – Concept of Truss model for bending and shear.

In reality, the inclination of concrete struts may vary, but in the initial concept of truss model, it was assumed to be 45°. This 45° truss model, also called *fixed-angle truss model*, was then developed to carry out the modeling of the post-cracking behavior of RC members subjected to pure torsion by Rausch [93]. In this model, after cracking, the

whole member is assumed to act like a tube, in other words the solid section becomes a hollow section (Figure 2-6). As a consequence, the torsional moment is resisted only by shear stresses which flow around in the wall of the tube, which is called *shear flux*. This *space truss analogy* was reinforced when it was noticed in the experimental tests carried by Hsu [45] and Osongo [82] that the post-cracking stiffness of a hollow cross-section (with a reasonable wall thickness) has the same magnitude when comparing to a solid section.

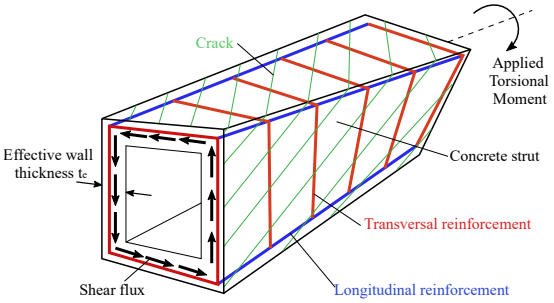

(a) Three-dimensional view.

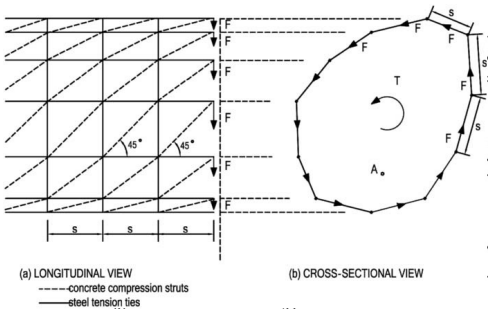

(b) Longitudinal and cross-sectional view.

Figure 2-6 – Space truss model for torsion resistance.

2.3.1 Strut and tie models

The common aspect of strut and tie models is the way in which the combined effects are taken into account: in this type of model the tangential efforts are usually uncoupled and superimposed into normal efforts. Guedes et al. [42, 43] developed a numerical model for RC beams and columns under dominated shear action, in which the model is subdivided into two sub-models: a two-node Timoshenko beam finite element model using sectional-fiber approach to take into account the axial components, while shear efforts are independently considered by a strut and tie model (Figure 2-7a). The direction of principal stresses and strains of concrete is represented by two diagonal concrete struts. The equilibrium conditions for reinforcement in longitudinal and transversal directions are represented in Figure 2-7b. Concerning the constitutive equations, uncoupled uniaxial behavior laws for concrete and steel are used. For concrete in compression, a parabolic behavior up to the peak stress point deformation followed by a straight line in the softening zone has been introduced, while a bilinear stress-strain law including the tension stiffening effect is adopted for concrete in tension. For steel, a hysteresis model based on the proposal of Menegotto & Pinto [73] is used.

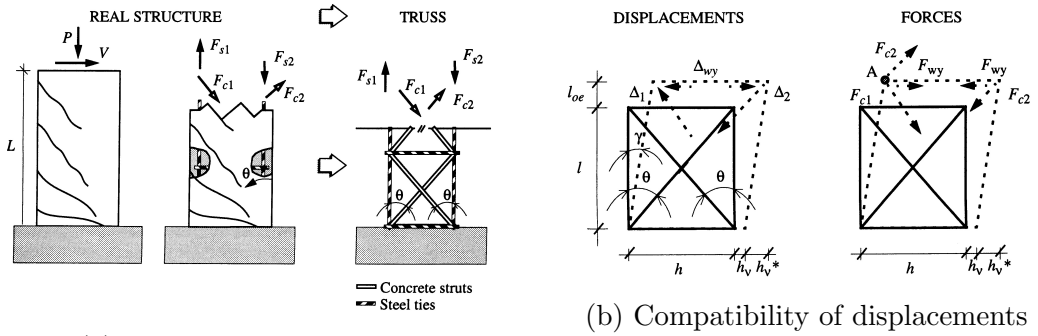

(a) Principe of truss model

(b) Compatibility of displacements and Equilibrium of forces

Figure 2-7 – Strut-and-tie Model of Guedes et al. [42, 43]

The idea of independently modeling shear forces using the concept of truss-and-tie model and then superimposing into axial and flexure efforts without direct coupling is shared by other models by Martinelli [68], Ranzo & Petrangeli [92] or Marini & Spacone [67]. In the Martinelli's model, shear resultant over the cross-section can be derived by different resisting mechanisms, including truss mechanism, in which a planar structural assemblage is composed by the transverse reinforcements and the concrete diagonals in compression and tension (Figure 2-8a). In the model by Ranzo & Petrangeli, the shear stiffness is derived from a shear-distortion curvature constitutive relationship that is defined by solving a truss mechanism as in Figure 2-8b. The shear curve is obtained by giving incremental values to the shear stress up to failure, then updating analytically the distortion curvature and thus leading to the determination of a continuous curve. The same idea of shear-distortion curve is also implemented in the model of Marini & Spacone but in a different procedure of obtaining the shear-curvature relationship. As in the model of Guedes et al., uniaxial constitutive laws for concrete and steel are implemented in all models above.

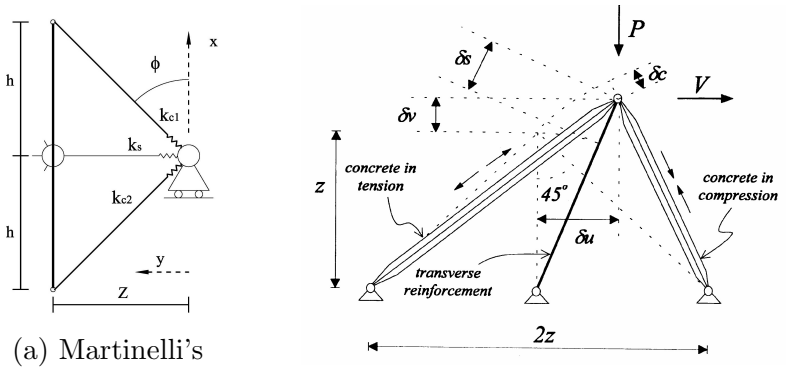

(a) Martinelli's model [68].

(b) Ranzo & Petrangeli's model [92]

Figure 2-8 – Truss mechanism and idealization

2.3.2 Equilibrium truss models

The equilibrium truss models can also be called plasticity truss model because they are all based on the theory of plasticity. This type of models were proposed by Nielsen [78] and Lampert & Thürlimann [61] by developing the concept of *fixed-angle truss model*, in which the fixed inclined angle of 45° was derived. The new concept was called the *variable-angle truss model* and was developed for elements subjected to torsion as well as to a combination of torsion and bending, with the application of the theory of plasticity for RC members. Elfgren [34] extended the use of *variable-angle truss model* to members subjected to bending-shear-torsion, with an assumption that the concrete struts take only compressive stress after cracking. The theory is therefore named the *Compressive Stress Field Theory*.

In these models, three equilibrium equations in bending and shear were derived for a two dimensional element and can be used to calculate the stresses in the steel bars and in concrete struts at the ultimate load stage (Figure 2-9). The stresses in concrete and steel in these three equations must satisfy the Mohr stress circle, and reinforcement steels are assumed to yield before failure. From these three equations and the yielding condition of reinforcement as well as the equilibrium in beam shear and in torsion, a set of 18 equations were established and formed the basic formulations of equilibrium truss models.

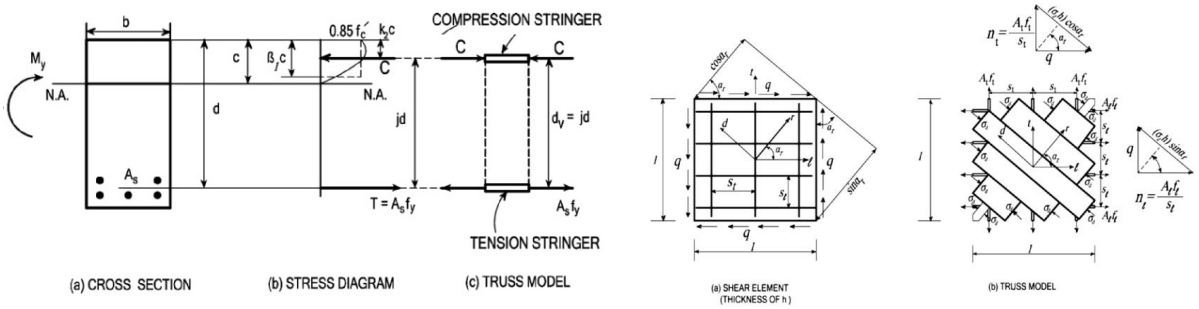

(a) in bending. (b) in element shear.

Figure 2-9 – Equilibrium of Truss model.

The interaction relationships of combined actions can be expressed between shear-bending, torsion-bending, shear-bending-torsion and axial-shear-bending, each relationship corresponds to a specific model. In the shear-bending model, the bending moment creates a tensile force in the bottom and a compressive force in the top stringer, while shear forces induce in longitudinal as well as transversal direction and are resisted by concrete struts, longitudinal steels and stirrups (Figure 2-10a). The failure may be occurred by two modes depending on the yielding of bottom or top stringer. In the torsion-bending model, the action of bending moment is similar to that of the shear-bending model, while

the torsional moment produces a tensile force in the longitudinal steels and a transverse force in the stirrups (Figure 2-10b). Two failure modes may be caused in this model, either by the yielding of the bottom stringer and the stirrups or by the yielding of the top stringer and the transverse steel.

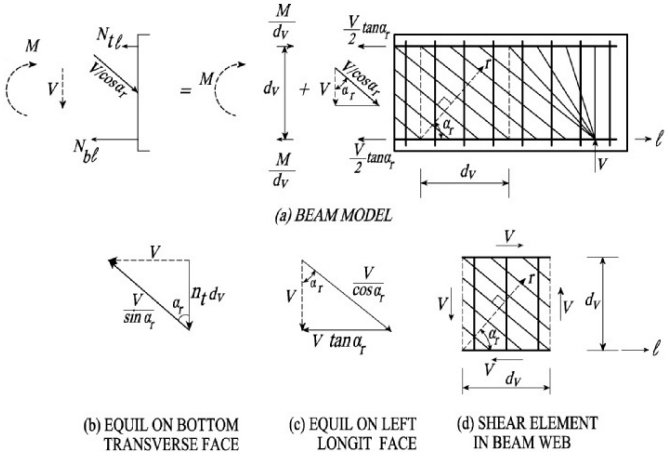

(a) Equilibrium between shear and bending.

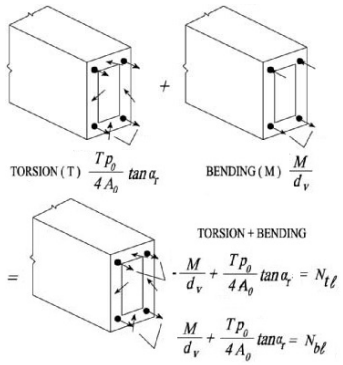

(b) Equilibrium between torsion and bending.

Figure 2-10 – Equilibrium truss models.

The interaction between shear, bending and torsion are more complex. A box section model is employed in which the shear flows on the four walls of the box section (Figure 2-11a). The shear flows due to shear and torsion are superimposed (Figure 2-11b), while the bending moment always induces tensile and compressive forces in bottom and top stringer. Three failure modes can be recorded in this model, causing by the yielding in the bottom stringer and in transverse steel, by the yielding in the top stringer and in transverse steel or by the yielding in both top and bottom longitudinal steel bars and in transverse steel. The interaction model for the combination of the axial force the shear force and the bending moment is quiet easily expressed, because the axial force is assumed to be resisted only by the longitudinal reinforcement bars, so it does not generate a new internal equilibrium condition of the shear-bending interaction model. It is required only a simple superposition of axial force on the equilibrium equation of shear and bending in the top and bottom stringer.

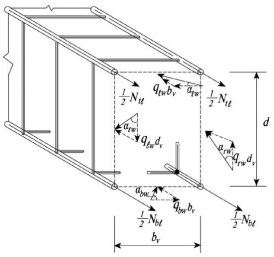

(a) Equilibrium of forces.

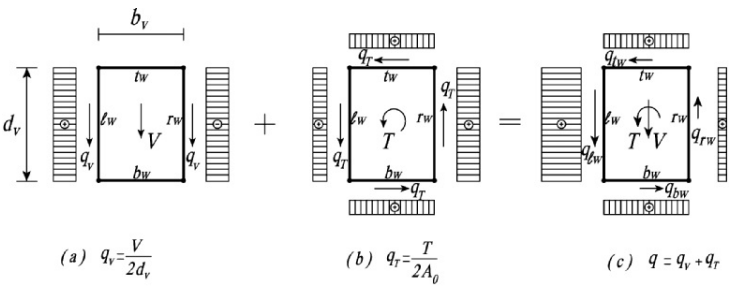

(b) Superposition of shear flow due to shear and torsion.

Figure 2-11 – Box section model for interaction of shear-bending-torsion.

The main advantage of equilibrium truss models is that, thanks to its completed set of basic equilibrium equations, it can be easily applied to all types of actions (axial force, bending, shear, torsion). As a result, the Compressive Stress Field Theory serves as a basic for the accurate method in the CEB-FIP Model Code of 1978 [17], while the shear and torsion provisions of the ACI Code 1995 (ACI 318-95) [1] were based on the equilibrium truss model. However, one important drawback of this type of models is that the load-deformation relationship of reinforced beam subjected to shear and torsion cannot be derived, because the compatibility equations and constitutive material laws are not used. Thus, more sophisticated theories that take care of all three principle mechanic equations must be developed.

2.3.3 Compatibility truss models

Instead of using the theory of plasticity and three equilibrium equations, the strain compatibility equations are derived and included in the truss model by Bauman [7], Collins [22] and Mitchell & Collins [74], in order to account for shear and torsional effect. In these models, a linear shear theory for two dimensional elements was developed combining the three principles of equilibrium: equilibrium equations, Mohr's compatibility equations and Hooke's law. The models could be used in the elastic behavior up to service load stage, to describe the element behavior up to ultimate load stage, a nonlinear shear theory is required.

2.3.3.1 Collins & Mitchell's Compression Field Theory

Collins & Mitchell [25] derived a theory predicting the nonlinear shear behavior of RC elements after cracking, called *Compression Field Theory*. In this theory, a RC element can be separated into a concrete element and a steel grid element (Figure 2-12a). The directions of the longitudinal and transverse steel bars form the $(x - y)$ global coordinate system, with x is the longitudinal direction and y the transverse direction. For a concrete membrane subjected to shear, the shear stress can be resolved into a principal tensile stress and a principal compressive stress, following the principal direction of crack (45° in this initial theory) (Figure 2-12b). The principal directions form a $(1 - 2)$ local coordinate system of crack direction. In this direction of compression and tension, the stresses and strains affect each other and this interaction causes some significant phenomenons, whose most important is the *softened* of principal compressive stress due to

principal tensile stress. Vecchio & Collins [109] then introduced a softening coefficient for the compressive stress-strain curve and discovered that this coefficient was a function of the principal tensile strain, rather than the principal tensile stress. After numerous experimented tests carried out in bi-dimensional RC panels under plane-stress loading (the Shell Element Tester) at the University of Toronto, Vecchio & Collins formulated the *Modified Compression Field Theory* (MCFT) for RC members subjected to shear force. Although originally developed for use in truss models, the MCFT is particularly suitable to the sectional analysis because it can handle cracking as a distributed effect. The theory has been employed as concrete constitutive model in many finite element sectional models as shown in the following section.

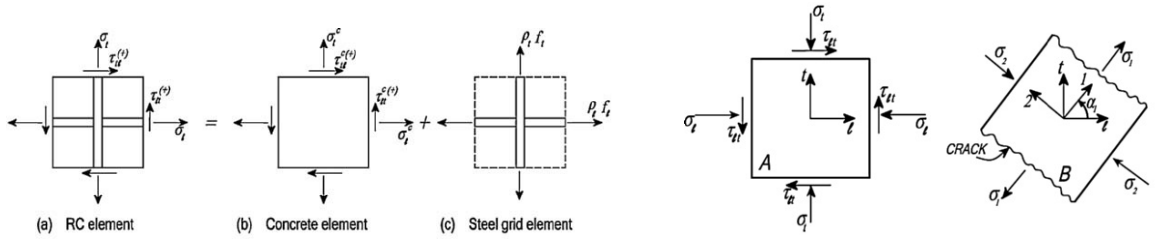

(a) Supposition of shear effect in RC element.

(b) Local and Principal direction of stress.

Figure 2-12 – Stress condition and crack pattern in RC element.

2.3.3.2 Model by Rahal [88]

The Compression Field Theory was also developed in the variable angle truss model by Rabbat & Collins [87] that is applied to rectangular sections of prestressed concrete subjected to combined efforts of bending, torsion and shear. In this model, the behavior of concrete and steel are regrouped in four corners of the cross-section and connected through the four concrete walls containing stirrups (Figure 2-13). The normal forces are resisted by four corners while tangential forces are resisted in four concrete walls.

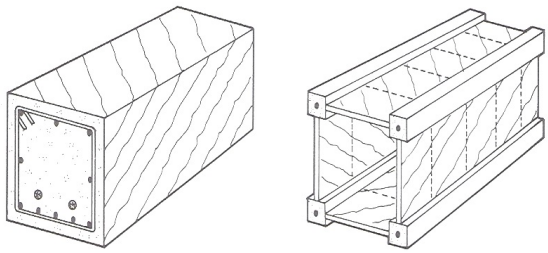

Figure 2-13 – Cross-section discretization in the model of Rabbat & Collins [87].

This idea of cross-section discretization is then developed by Rahal & Collins [88, 89] in a 3D model in which the 3D response is idealized into 1D and 2D sub-model (Figure

2-14). The 1D model captures only the normal stresses due to the axial force, bending moment as well as the diagonal cracks produced by shear and torsion. The shear stresses induced by shear force and torsional moment are taken into account by the 2D model, which consists of four transversely reinforced walls of variable thickness and cracking inclination. The interaction between normal and tangential forces is obtained by the equilibrium and compatibility equations at sectional level and at each wall. Over the section, the equilibrium between shear stresses (in 2D model) and normal stress (in 1D model) must be satisfied, as well as the compatibility of normal strain in 1D model. In each wall, an appropriate uniaxial stress-strain relationship for concrete and steel must be applied for 1D model, while the modified compression field theory (MCFT) is employed for the 2D model.

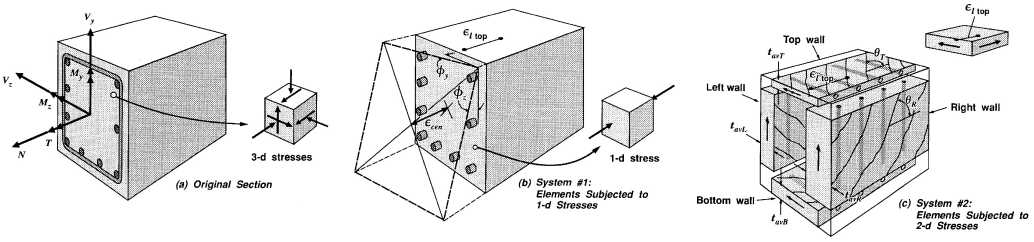

Figure 2-14 – Idealization of cross-section in the model of Rahal & Collins [88].

The constitutive equations are based on the MCFT with the kinematic hypothesis of Euler-Bernoulli and an assumption of perfect bond between the concrete and steel. An extension of this model is developed by Rahal & Collins [90] considering the variation of the longitudinal deformations of the walls. This sectional model is strong in predicting the element response and representing the interaction of combined loading, however it is limited only for rectangular cross-section.

2.3.3.3 Models by Hsu [52, 84, 50]

Based on the strain compatibility equations of the truss model, Hsu & Mo [52] indicated that in the variable-angle truss model, when using the stress-strain relationship obtained from the concrete compression cylinder test, the predicted torsional strength becomes very underestimated. Thus, they used a softened stress-strain curve to predict the torsional strength and strains throughout loading history. Hsu & Mo called this theory as *Rotating-Angle Softened-Truss Model* (RA-STM), in which many assumptions are shared with the MCFT, such as the same principal directions of stresses and strains, or the inclusion of a softening factor in compressive concrete after cracking.

In addition to the above theory, a *Fixed-Angle Softened-Truss Model* (FA-STM) was developed by Pang & Hsu [84], in which the concrete struts are assumed to remain parallel to the initial cracks inclination. For this, a third coordinate system $(1'-2')$ of the current principal stress directions is defined, rather than the global coordinate system $(x-y)$ and the local coordinate system at initial cracks $(1-2)$ (Figure 2-15). The FA-STM can give a more accurate prediction than RA-STM and is useful when interested in the ultimate shear strength and the behavior before it. However, the descending branch of the load-deformation curves cannot be represented correctly.

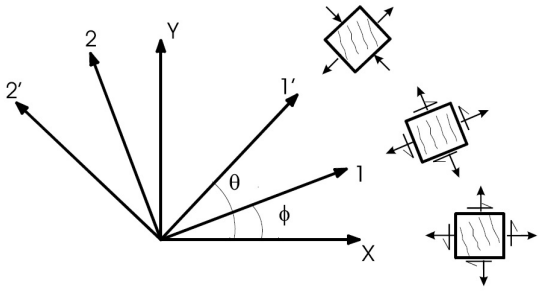

Figure 2-15 – Coordinate systems in the Fixed-Angle Softened-Truss Model.

Recently, Hsu & Zhu developed another model for treating RC membrane elements in shear called Softened Membrane Model (SMM) [50]. Based on the FA-STM, the SMM is able to satisfactorily predict the entire monotonic response of the load-deformation curves, including both the ascending and the descending branches, as well as the pre-cracking and post-cracking responses. The featured aspect of the SMM is that the Poisson effect is taken into account and is characterized by two ratios called Hsu/Zhu ratio [117]. As a result, the average strains in direction $(1-2)$ (Figure 2-15) when a panel is subjected to biaxial loading are expressed as:

$$\varepsilon_1 = \frac{\sigma_1^c}{\bar{E}_1^c} - \nu_{12}\frac{\sigma_2^c}{\bar{E}_2^c} = \bar{\varepsilon}_1 - \nu_{12}\bar{\varepsilon}_2; \qquad \varepsilon_2 = \frac{\sigma_2^c}{\bar{E}_2^c} - \nu_{21}\frac{\sigma_1^c}{\bar{E}_1^c} = \bar{\varepsilon}_2 - \nu_{21}\bar{\varepsilon}_1 \tag{2.1}$$

with ν_{12} and ν_{21} are the two Hsu/Zhu ratios; $\bar{E}_1^c$ and $\bar{E}_2^c$ are the moduli of concrete in the 1 and 2 direction when a panel is subjected to uniaxial loading; $\bar{\varepsilon}_1$ and $\bar{\varepsilon}_2$ are average strains in the direction 1 and 2 when a panel is subjected to uniaxial loading. The two Hsu/Zhu ratios are formulated based on a series of twelve tests using the Universal Panel Tester (UPT), realized by Hsu and his colleagues at the University of Houston from 1988 to 2009 [49]. The experimental tests obtained from the UPT allows also to establish the material behavior laws for RC members, as proposed by Belarbi & Hsu [8], [9] or Pang &

Hsu [83]. The softening of concrete in compression is taken into account by a softening coefficient ζ (Figure 2-16a), while the tension stiffening of concrete is also included in the tensile relationship (Figure 2-16b).

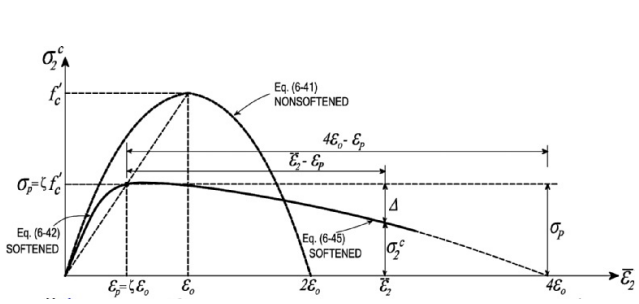

(a) Compressive curve.

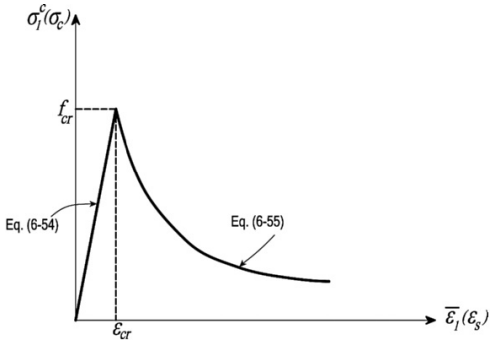

(b) Tensile curve.

Figure 2-16 – Stress-strain curve of concrete obtained from experimental tests using the UPT [48].

A Softened Membrane Model for Torsion (SMMT) is then developed from the SMM by Seng & Hsu [53] in order to account for the torsional response of RC members, which will be more discussed in Section 4.3.

2.4 Sectional-Fiber model

Sectional-fiber approach has been used widely by researches over the last thirty year to account for the responses of RC member under combined loading of normal and tangential forces. Many models have been developed and proposed in according to different criterions of classification. In this research work, the following principal strategy has been classified:

- Dual-sectional analysis: a non-local sectional model in which the element is discretized in various member of two section and the shear stress is determined by the finite difference of the normal stress on each side of this dual-section member.
- Longitudinal stiffness method: a local sectional model that satisfies the inter-fiber equilibrium between fiber/layer of element.
- Finite element beam-column formulation: an implementation of longitudinal stiffness method into two-node finite element frame model.
- Enhanced Finite element beam-column formulation: a specific strategy to account for distortion and warping phenomenon using the decomposition of cross-section characteristic into classical field following plane-section hypothesis and enhanced field of warping-distortion.

2.4.1 Constitutive Model

In the literature, many constitutive models have been developed to reproduce the behavior of concrete, following different approaches. Indeed, the mechanical response of concrete materials represents a brittle behavior and is influenced by complex phenomena, one of the most important is the propagation of cracks inside the elements. The adoption of finite element models with embedded (displacement or strains and stresses) discontinuities [10, 33] based on the fracture mechanics theory [44] is usually considered as one of the most accurate way for describing the evolution of cracking phenomena in concrete. However, this embedded discontinuity models are not suitable for large scale structure analysis. In practice, the following approaches have been widely used to simulate the concrete behavior of many numerical models:

- Smeared-crack approaches: cracking is handled as a distributed effect with directionality, of which the pioneering model is the MCFT.
- Damage mechanics approaches: the effect of damage of materials (initiation and propagation of crack or fracture of concrete) is represented by the state variables (crack density or coefficient of thermal expansion, etc.) and then lead to the constitutive equations. Model of Mazars [69] and Lemaitre [65] are usually considered as the most widely used damage models.

2.4.1.1 Modified compression field theory

In this theory, the principal idea is to replace the biaxial constitutive law of concrete by a uniaxial constitutive law, in which the stress-strain relationship is formulated in the principal direction of cracking. The primary assumptions of this theory is that crack is considered distributed in the concrete, and principal directions of strains and stresses are coincident. In addition, equilibrium and compatibility equations are evaluated with the average value of the stress and strain in the crack plane and in the concrete between cracks, because of the variation of the local stresses in both concrete and steel. According to Figure 2-17, the compatibility conditions of the MCFT are expressed as:

$$\begin{aligned} \varepsilon_x &= \frac{\varepsilon_1 \tan^2\theta + \varepsilon_2}{1+\tan^2\theta}; \qquad \varepsilon_y = \frac{\varepsilon_1 + \varepsilon_2 \tan^2\theta}{1+\tan^2\theta} \\ \gamma_{xy} &= \frac{2\left(\varepsilon_x - \varepsilon_2\right)}{\tan\theta}; \qquad \tan^2\theta = \frac{\varepsilon_x - \varepsilon_2}{\varepsilon_y - \varepsilon_2} \end{aligned} \tag{2.2}$$

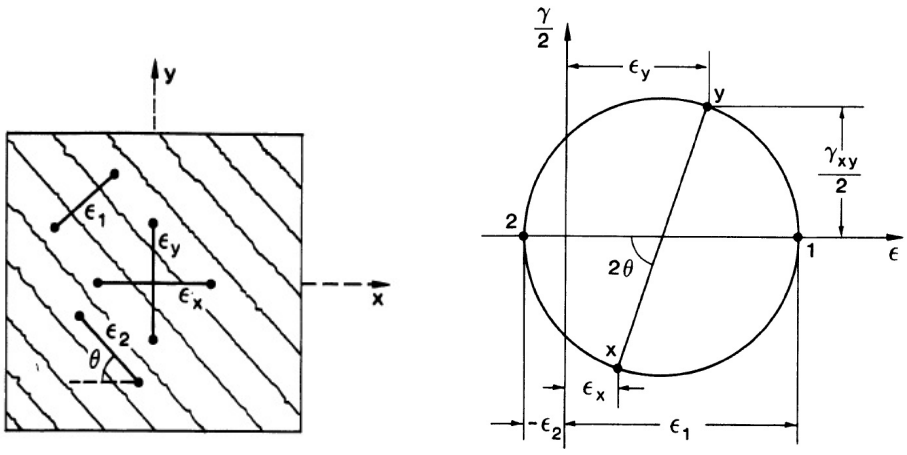

(a) Average strains.

(b) Mohr's Circle for average strains.

Figure 2-17 – Compatibility conditions for cracked RC element.

where ε_1 and ε_2 are the strain in principal directions; ε_x, ε_y and γ_{xy} are the element strain components; θ is the inclination of crack. The equilibrium conditions of averages stresses in an element are expressed as follows (Figure 2-18):

$$\begin{aligned} \sigma_x &= \sigma_1 - \tau_{cxy}\cot\theta + \rho_x\sigma_{sx} \\ \sigma_y &= \sigma_1 - \tau_{cxy}\tan\theta + \rho_y\sigma_{sy} \\ \sigma_2 &= \sigma_1 + \tau_{xy}\left(\tan\theta + \cot\theta\right) \end{aligned} \tag{2.3}$$

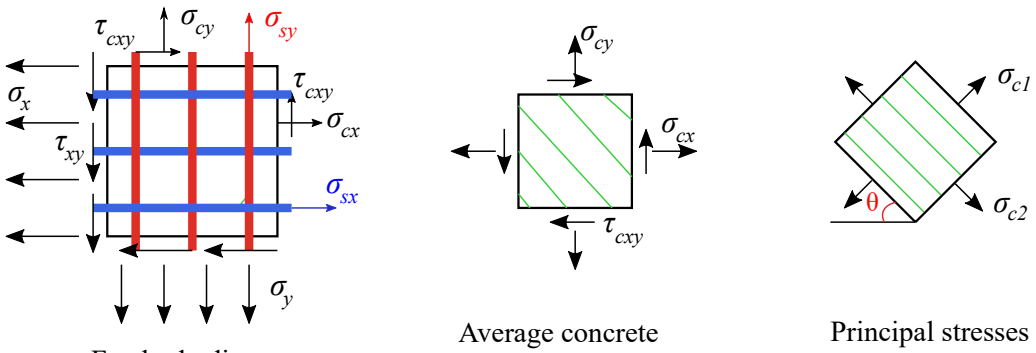

Figure 2-18 – Equilibrium conditions for cracked RC element.

where σ_1 and σ_2 are the stresses in principal directions; σ_x, σ_y and τ_{xy} are element stress components; σ_{sx} and ρ_x are stress and ratio of longitudinal reinforcement, respectively; σ_{sy} and ρ_y are stress and ratio of transversal reinforcement, respectively.

2.4.1.1.1 Constitutive modeling: For concrete in compression, the stress-strain relationship is computed following a parabolic equation (figure 2-19a):

$$\sigma_2 = f'_c \left[2\left(\frac{\varepsilon_2}{\varepsilon_0}\right) - \left(\frac{\varepsilon_2}{\varepsilon_0}\right)^2 \right] \tag{2.4}$$

where f'_c is the maximum stress resisted by crack concrete in the compression direction; ε_0 is the cylinder strain at peak strength. The softening of concrete is included in the stress-strain relationship by a softening parameter SF which depends on the tensile strain:

$$f'_c = \frac{f_c}{SF}; \qquad SF = 0.8 - 0.34\frac{\varepsilon_1}{\varepsilon_0} \tag{2.5}$$

where f_c is the concrete cylinder compressive strength.

For concrete in tension, the behavior is divided into two phase: before and after cracking (Figure 2-19b). Cracking of concrete appears when the tensile strain ε_1 is higher than the cracking strain ε_{cr}. An elastic linear relationship is suggested prior to cracking:

$$\begin{aligned} &\sigma_1 = E_c\varepsilon_1; \qquad 0 < \varepsilon_1 < \varepsilon_{cr} \\ &\varepsilon_{cr} = \frac{f_{cr}}{E_c} \\ &f_{cr} = 0.33\sqrt{f_c} \quad \text{in (MPa)} \end{aligned} \tag{2.6}$$

where E_c is the concrete modulus of elasticity; f_{cr} is the cracking stress. After cracking, tensile stresses in the uncracked concrete between the cracks continue to stiffen the concrete, thus increase the stiffness of concrete section. This effect leads to a decrease in average tensile stresses after cracking, and is named *tension stiffening* of concrete. In the original formulation of the MCFT [109], based on experimental results from shear tests on 70 mm thick panel elements, the tension relationship of concrete after cracking was proposed as follows:

$$\sigma_1 = \frac{f_{cr}}{1 + \sqrt{200\varepsilon_1}} \tag{2.7}$$

An adjustment of this previous expression suggested by Collins & Mitchell [26] based on shear tests conducted on larger panel of 285 mm thick:

$$\sigma_1 = \frac{f_{cr}}{1 + \sqrt{500\varepsilon_1}} \tag{2.8}$$

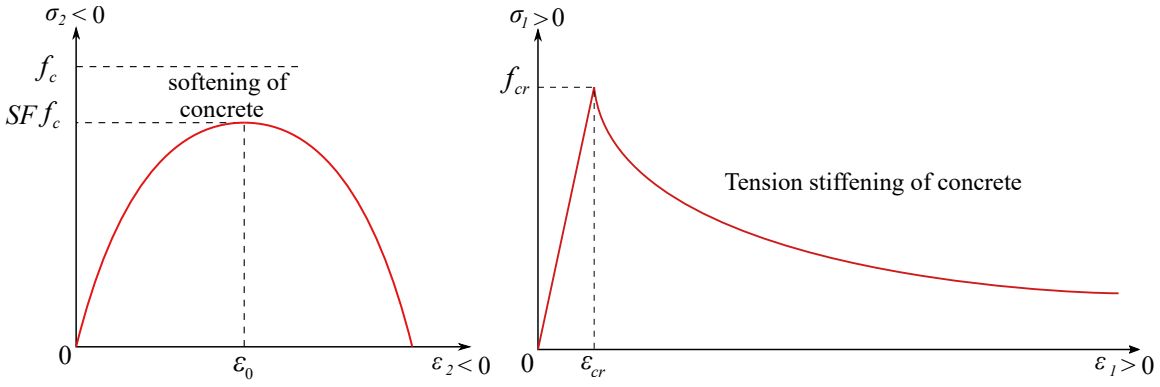

(a) Compression relationship [110] (b) Tension relationship

Figure 2-19 – Concrete constitutive relations in the MCFT.

For reinforcing steel, an uniaxial relationship is considered with a bilinear elasto-plastic stress-strain curve (Figure 2-20). In each direction, the steel characteristics must be accompanied with the reinforcement ratio ρ_x or ρ_y.

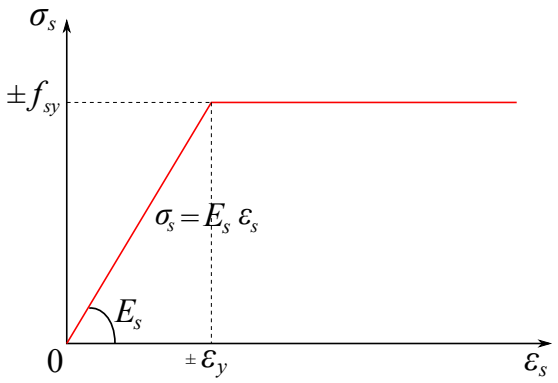

Figure 2-20 – Elasto-plastic model by Vecchio & Collins [110].

2.4.1.1.2 Crack-check: In order to ensure that the average stress can be resisted locally at a crack, a *crack-check* must be applied. In reality, applying the MCFT without including the crack-check can lead to very underestimated results [51]. Bentz [12] gave a clear example to demonstrate the need for crack-check by considering a concrete prism with longitudinal reinforcement steels subjected to axial tension (Figure 2-21a). The free body diagram of a member at crack is shown in Figure 2-21b: the left half drawn with average stresses (concrete tensile stress f_1 and steel stress f_{sx}) and the right half correspond to the local stresses at crack (only steel stress f_{sx} at crack). To ensure the equilibrium of local stresses at a crack, the concrete tensile stress f_{c1} must equal to zero.

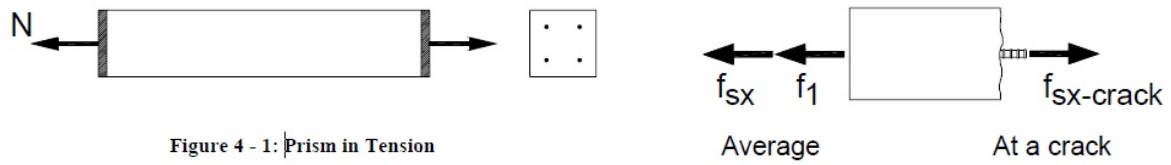

(a) Prism in Tension. (b) Free body diagram at a crack.

Figure 2-21 – Example of Bentz [12].

Next, the total stress-strain relationship of average concrete in tension and reinforcement steel are added together over the entire range of strain. Without crack-check, the total stress-strain relationship is shown in Figure 2-22a, and it is clear that the concrete tensile stress at crack f_{c1} is not equal to zero. Maintaining f_{c1} equal to zero, i.e ensuring that the local stresses at a crack do not exceed the yield stress, is the objective of the crack-check. The result of crack-check is shown in Figure 2-22b.

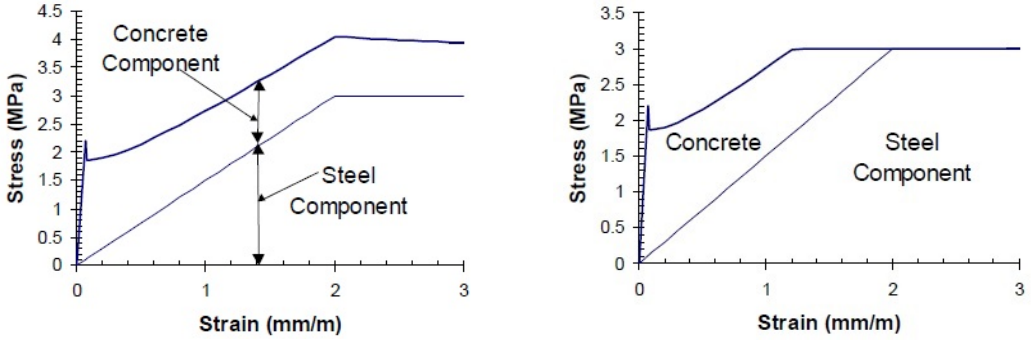

(a) Without crack-check. (b) With crack-check.

Figure 2-22 – Total stress of average tensile concrete and steel in the example of Bentz [12].

2.4.1.1.3 Material stiffness matrix for finite element formulation: In a finite element formulation, the stresses and strain vector are related by a material stiffness matrix **D**:

$$\begin{pmatrix} \sigma_x \\ \tau_{xy} \\ \tau_{xz} \end{pmatrix} = \mathbf{D} \begin{pmatrix} \varepsilon_x \\ \gamma_{xy} \\ \gamma_{xz} \end{pmatrix} \tag{2.9}$$

The contribution of concrete and steel are added separately:

$$\mathbf{D} = \mathbf{D}_c + \mathbf{D}_s \tag{2.10}$$

The concrete stiffness matrix is expressed in terms of the principal directions:

$$\mathbf{D}_c = \mathbf{T}_c^T \mathbf{D}_{prin} \mathbf{T}_c \tag{2.11}$$

The stiffness matrix in principal directions $\mathbf{D}_{prin}$ is evaluated in a simple secant-stiffness-based:

$$\mathbf{D}_{prin} = \begin{bmatrix} E_{c2} & 0 & 0 \\ 0 & E_{c1} & 0 \\ 0 & 0 & G_c \end{bmatrix} \qquad (2.12)$$
$$E_{c2} = \frac{\sigma_2}{\varepsilon_2}; \qquad E_{c1} = \frac{\sigma_1}{\varepsilon_1}; \qquad G_c = \frac{E_{c1}E_{c2}}{E_{c1} + E_{c2}}$$

$\mathbf{T}_c$ is the transformation matrix composed of the direction cosines, which define the direction of the principal concrete cracking:

$$\mathbf{T}_c^{2D} = \begin{bmatrix} \cos^2\theta & \sin^2\theta & \sin\theta\cos\theta \\ \sin^2\theta & \cos^2\theta & -\sin\theta\cos\theta \\ -\sin 2\theta & \sin 2\theta & \cos 2\theta \end{bmatrix} \qquad (2.13)$$

For the stiffness matrix of steel, while the longitudinal reinforcement can be taken into account in a straightforward way, it is not the same obvious work for the contribution of transverse reinforcement steel. Indeed, it requires an iteration process to handle the transverse equilibrium between concrete and steel at each material points, which will be expressed clearly in Chapter 3.

2.4.1.1.4 Model of Stevens et al. [103]: It should be noted that the MCFT can be developed by using different uniaxial strain-stress curve for concrete and steel, such as a Popovics curve [85] considering the size-effect phenomenon in the model of Benzt [13]. Stevens et al. [103] extended the MCFT to a new constitutive model that does not require the crack-check with a tangent-based stiffness matrix instead of secant-based. This model adopts the same hypothesis as the MCFT and requires more complex formulations, but the process of numerical convergence is improved consequently. One great advantage of this model is that the formulation can be used for the response of confined, unconfined and/or partially confined concrete, which depends on the determination of a coefficient factor K. In compression, when $\varepsilon > K\varepsilon_0$, the stress-strain curve follows the original parabolic relationship of the MCFT in equation (2.4), then the post-peak curve is modified using a cubic equation in function of ε_0 and the ultimate strain ε_{cu} (Figure 2-23a). The softening coefficient SF is always calculated as a function of the principal tensile strain with a slight change in the parabolic transition comparing to the original formulation in equation (2.5) (Figure 2-23b).

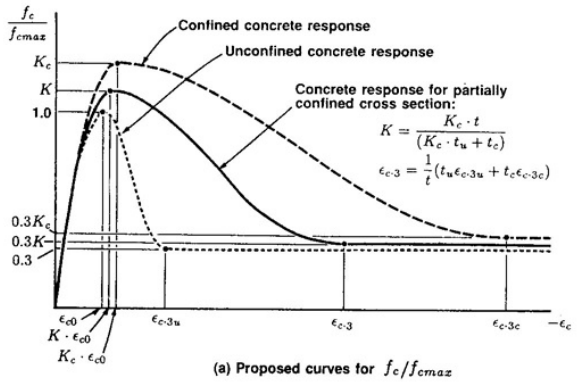

(a) Proposed stress-strain curve in compression

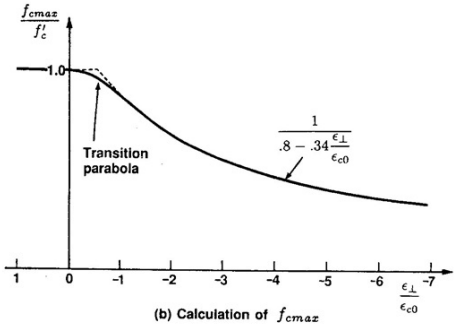

(b) Calculation of softening coefficient.

Figure 2-23 – Compression relationship of concrete proposed by Stevens et al. [103]

The tensile behavior of concrete is also based on the basic of the MCFT, with a linear elastic behavior until the cracking strength, followed by a descending curve describing the tension stiffening of concrete, which is formulated according to the longitudinal reinforcements disposition (Figure 2-24a). The steel behavior in this model is much more complex in order to avoid the crack-check imposed in the original MCFT, by accounting for the smeared reinforcement of crack concrete. Indeed, the reinforcement between the cracks does not reach its plastic limit since the surrounded concrete has already carried out a part of tensile stresses. The stress-strain curve of steel is therefore a function of concrete tensile strength f_{cr} (Figure 2-24b).

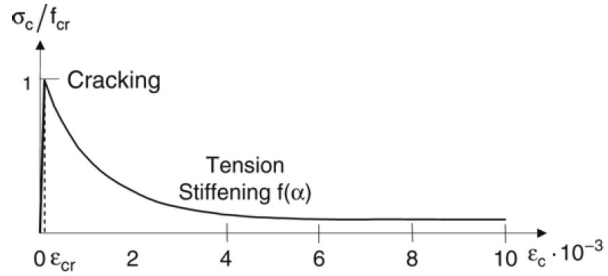

(a) Tension relationship of concrete.

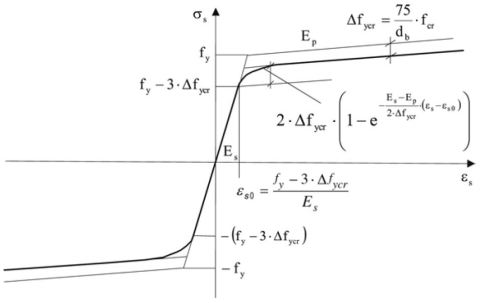

(b) Steel relationship.

Figure 2-24 – Concrete tensile and Steel relationship proposed by Stevens et al. [103].

The tangent-based material stiffness matrix of concrete in principal directions is expressed as follows:

$$\mathbf{D}_{prin} = \begin{bmatrix} \frac{\partial \sigma_1}{\partial \varepsilon_1} & \frac{\partial \sigma_1}{\partial \varepsilon_2} & \frac{\partial \sigma_1}{\partial \gamma_{12}} \\ \frac{\partial \sigma_2}{\partial \varepsilon_1} & \frac{\partial \sigma_2}{\partial \varepsilon_2} & \frac{\partial \sigma_2}{\partial \gamma_{12}} \\ 0 & 0 & \frac{\sigma_1 - \sigma_2}{2(\varepsilon_1 - \varepsilon_2)} \end{bmatrix} \tag{2.14}$$

2.4.1.2 Damage model of Mazars for concrete

One of the first damage models was introduced by Mazars [69], in which the influence of micro-cracking due to external load is introduced by a single scalar damage variable D, varying from 0 (undamaged material) to 1 (completely damage material). The expression of this variable is computed as follows:

$$D = \alpha_c D_c + \alpha_t D_t \tag{2.15}$$

where D_c and D_t are two damage variables independently describing the material degradation under compressive and tensile stresses; α_c and α_t are two weighting coefficients. The damage variable then lead to the definition of an effective stiffness matrix $\mathbf{C}$ relating the total stress and strain:

$$\boldsymbol{\sigma} = \mathbf{C}(\mathbf{C}_0, D)\boldsymbol{\varepsilon} \tag{2.16}$$

where $\mathbf{C}_0$ is the initial elastic stiffness matrix corresponding to undamaged state. Assuming that the strain state of the real damaged material is the same state considered in the constitutive law, the constitutive relation in equation (2.16) becomes:

$$\boldsymbol{\sigma} = (1 - D)\mathbf{C}\boldsymbol{\varepsilon} \tag{2.17}$$

The evolution of damage variable D depends on the mechanical state:

$$D_{c/t} = 1 - \frac{\varepsilon_0(1 - A_{c/t})}{\varepsilon_{eq}} - A_{c/t}\exp(-B_{c/t}(\varepsilon_{eq} - \varepsilon_0)) \tag{2.18}$$

with ε_{eq} is the equivalent strain representing the extension of strains in principal directions; ε_0 is the initial damage threshold; $A_{c/t}$ and $B_{c/t}$ are materials parameters. The details of formulation can be found in [69], [71]. This constitutive model is however only suitable for monotonic loading and has been refined after by Mazars [71] and Mazars et. al [70]. The latter model is called Mu model, considers two different equivalent strains $\varepsilon_{eq,c}$ (or $\varepsilon_{\mu,c}$) and $\varepsilon_{eq,t}$ ($\varepsilon_{\mu,c}$), associating to two thermodynamic variable $Y_{\mu c}$ and $Y_{\mu t}$. The combination of these two variables give a single internal variable Y_μ:

$$Y_\mu = rY_{\mu t} + (1 - r)Y_{\mu c} \tag{2.19}$$

where r is the tri-axial factor varying from 0 to 1. Then, the damage evolution law can be expressed as follows:

$$D = 1 - \frac{(1-A)Y_{\mu 0}}{Y_\mu} - A\exp(-B(Y_\mu - Y_{\mu 0})) \tag{2.20}$$

with $Y_{\mu 0}$ is the initial threshold; $A = f(r, A_c, A_t)$ and $B = f(r, B_c, B_t)$ are material parameters.

The uniaxial concrete behavior of Mu model can be found in Figure 2-25 with the following path: loading in tension from 0-A-B, then unloading in tension from B to 0, loading in compression from 0-C-D, then unloading in compression from C to 0, then re-loading and re-unloading in tension from 0-E-0 and finally re-loading in compression from 0-F-G. Other damage models can be found in the literature, such as model of Lemaitre [65], La Borderie [60], Faria et al. [37], etc., proposing different definitions of the equivalent strain and the damage evolution laws.

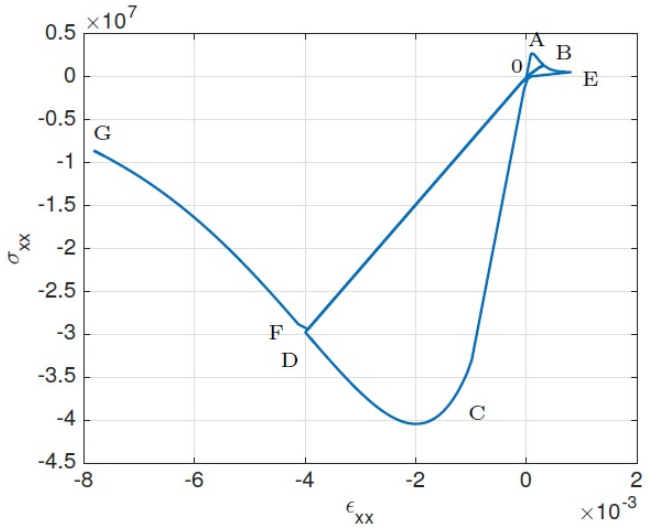

Figure 2-25 – Stress/strain relation for concrete in compression and tension.

2.4.2 Dual-section analysis

Vecchio & Collins [111] developed a beam model subjected to axial, bending and shear stresses, in which the entire cross-section is subdivide into a set of horizontal layers of concrete and steel (Figure 2-26). Each layer is analyzed separately with the corresponding constitutive behavior, based on the MCFT. The model was formulated as a sectional analysis model, however it was not introduced within a finite element formulation. The section kinematics follow Euler-Bernoulli assumption and the shear stresses are given by

the *dual-section analysis*, in which shear stress is equal to the finite difference of the normal stress value on each side of a finite-length layer (Figure 2-27a):

$$\tau_{xy}(x) = -\frac{1}{b(y)} \int_{-y_b}^{y} \frac{\partial \sigma_x}{\partial x} b(y) dy; \qquad \frac{\partial \sigma_x}{\partial x} \approx \frac{\sigma_x(x_2) - \sigma_x(x_1)}{S} \tag{2.21}$$

where b is the section's width, y_b is the coordinate of the bottom layer, $\sigma_x(x_2)$ and $\sigma_x(x_1)$ are the normal stresses of the layer in the two analyzed sections and S is the distance between the sections, which is recommended equal to $h/6$ with h is the section's height.

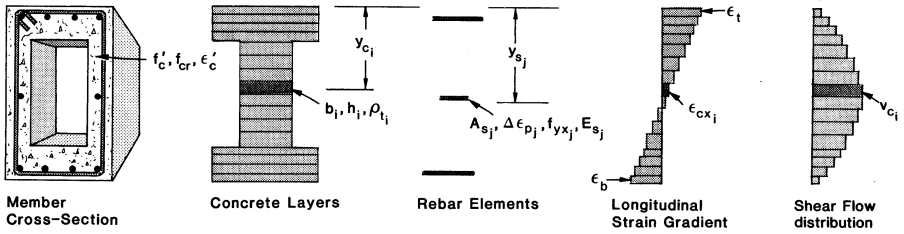

Figure 2-26 – Section's layers in the model of Vecchio & Collins [111].

An iterative procedure is then implemented to determine the shear strain distribution, by comparing the values of shear stress from the dual-section analysis and from the imposition of longitudinal equilibrium. In addition to this analytical solution which requires a considerable computational effort, Vecchio & Collins has also proposed two approximate solutions, one based on the constant shear flow, other based on a parabolic shear strain distribution. These two alternative solutions can give quite close results to those obtained with the iterative scheme, however the shear stresses may be poorly estimated.

This model is considered as a non-local sectional model, because the response of the cross-section depends on the information from outside of the geometric plane. This means that some specific conditions and formulations are required when implementing the proposed model into a frame analysis. For example, in the case of a 2D beam element, at least three integration points are required for flexure and two others for shear (Figure 2-27b). This aspect, along with the iterative procedure based on the summation of the trial-and-error small increments, makes the numerical implementation become complex and expensive. A similar dual-section analysis was also implemented in a beam element developed by Ranzo [91].

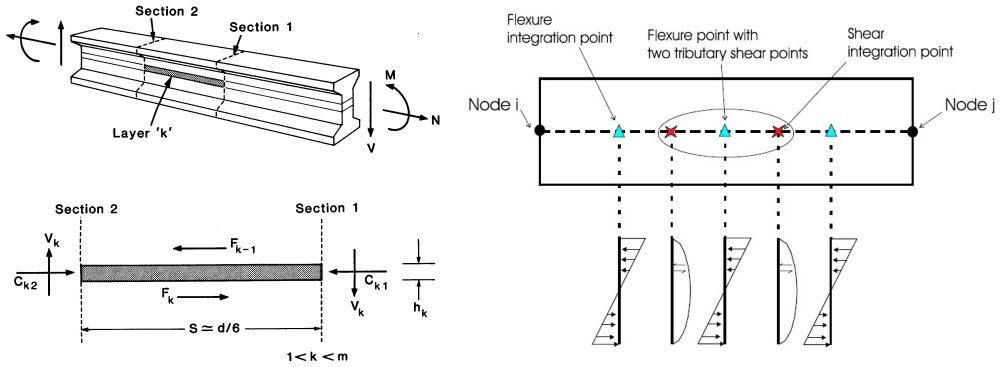

Figure 2-27 – (a) Dual section analysis scheme. (b) Implementation of dual-section analysis in a beam element.

2.4.3 Longitudinal stiffness method

In the dual-section analysis method, the choice of the finite distance between two sections S influences the results of shear stress determination. To overcome this, Bentz [12] presented a numerical model using the *longitudinal stiffness method*, in which the stresses and strains at each layer are related by a tangent stiffness matrix. For this, the plane-section Euler-Bernoulli hypothesis is employed to compute the axial strain from the section's elongation ε_0 and curvature κ_y, whereas the shear strain is defined initially as a function of the mean sectional shear deformation $\bar{\gamma}$: $\gamma_{xy} = f(y)\bar{\gamma}$. Thus, the strains vector at any layer can be computed from the vector of section *generalized* strains containing ε_0, κ_y and $\bar{\gamma}$:

$$\begin{pmatrix} \varepsilon_x \\ \gamma_{xy} \end{pmatrix} = \begin{bmatrix} 1 & y & 0 \\ 0 & 0 & f(y) \end{bmatrix} \begin{pmatrix} \varepsilon_0 \\ \kappa_y \\ \bar{\gamma} \end{pmatrix} \tag{2.22}$$

$$\boldsymbol{\varepsilon}(x,y) = \mathbf{B}(y)\mathbf{e}_s(x)$$

The constitutive relationship at each layer is computed as the differential increment of stress vector with respect to strain vector as follow:

$$\delta \begin{pmatrix} \sigma_x \\ \sigma_y \\ \tau_{xy} \end{pmatrix} = \frac{\partial \boldsymbol{\sigma}}{\partial \boldsymbol{\varepsilon}} \delta \begin{pmatrix} \varepsilon_x \\ \varepsilon_y \\ \gamma_{xy} \end{pmatrix} \tag{2.23}$$

$$\delta\boldsymbol{\sigma} = \mathbf{D}\delta\boldsymbol{\varepsilon}$$

where $\mathbf{D}$ is the layer tangent stiffness matrix. The transverse equilibrium is obtained by imposing independently that σ_y is null at each layer, this action results in a condensed

stiffness matrix at each layer:

$$\delta \begin{pmatrix} \sigma_x \\ \tau_{xy} \end{pmatrix} = \hat{\mathbf{D}} \delta \begin{pmatrix} \varepsilon_x \\ \gamma_{xy} \end{pmatrix} \tag{2.24}$$

Then, using the chain rule and equation (2.22), (2.24), the derivatives of normal and shear stresses with respect to cross-section coordinate x can be derived as follows:

$$\frac{\delta}{\delta x} \begin{pmatrix} \sigma_x \\ \tau_{xy} \end{pmatrix} = \hat{\mathbf{D}} \mathbf{B}(y) \frac{\delta \mathbf{e}_s(x)}{\delta x} \tag{2.25}$$

Then, the derivatives of the generalized stresses are computed by direct integration over the cross-section:

$$\begin{aligned} \frac{\delta}{\delta x} \begin{pmatrix} N_x \\ M_y \\ V \end{pmatrix} &= \iint_A \begin{bmatrix} 1 & 0 \\ y & 0 \\ 0 & 1 \end{bmatrix} \frac{\delta}{\delta x} \begin{pmatrix} \sigma_x \\ \tau_{xy} \end{pmatrix} \\ \frac{\delta \mathbf{D}_s}{\delta x} &= \iint_A \mathbf{A}(y) \hat{\mathbf{D}} \mathbf{B}(y) \frac{\delta \mathbf{e}_s(x)}{\delta x} = \mathbf{K}_s \frac{\delta \mathbf{e}_s(x)}{\delta x} \end{aligned} \tag{2.26}$$

where $\mathbf{D}_s$ is the generalized stresses or sectional forces, $\mathbf{K}_s$ is the sectional stiffness matrix, in which the first row includes the axial contributions, the second row features the bending moment contributions and the third row presents the shear stiffness coefficients. Because $\mathbf{A}^T \neq \mathbf{B}$, $\mathbf{K}_s$ is asymmetric.

Similar to the model of Vecchio & Collins, the MCFT is also employed for the constitutive model. This model of Bentz is a local sectional model that satisfies the inter-fiber equilibrium, thus it is suitable to be implemented within frame element.

2.4.4 Finite element beam-column model

An efficient modeling strategy for the sectional model of RC members subjected to combined actions is attempt to implement smeared crack approach within a beam element formulation, which usually formulated as a two-node FE beam. In this model, the nodal variables are considered as global degrees of freedoms, from them the mechanical characteristics of cross-section are derived and interpolated along the element axis. As mentioned in Chapter 1, the formulations of beam-column finite element can be classified as stiffness-based (displacement-based) or flexibility based (force-based or mixed-based) formulation.

2.4.4.1 Displacement-based formulation

A multifiber Timoshenko beam element was developed by Ceresa et al. [18], that dedicates to represent the shear responses of RC members under cyclic loading. A bi-axial fiber constitutive model for cracked RC member was implemented, based on the improved MCFT for cyclic loads proposed by Vecchio [107]. The model is formulated according to displacement-based approach, in which the vector of generalized displacements of cross-section $\mathbf{d}_s(x)$ is related to the nodal displacements vector $\mathbf{q}_{IJ}$ by linear interpolation shape functions (Figure 2-28). The shear locking phenomenon was avoided by adding a *bubble function* N_b to the linear shape functions for the transversal displacement field:

$$\begin{pmatrix} u(x) \\ v(x) \\ \theta_z(x) \end{pmatrix} = \begin{bmatrix} 1-\frac{x}{L} & 0 & 0 & \frac{x}{L} & 0 & 0 \\ 0 & 1-\frac{x}{L} & N_b L & 0 & \frac{x}{L} & -N_b L \\ 0 & 0 & 1-\frac{x}{L} & 0 & 0 & \frac{x}{L} \end{bmatrix} \begin{pmatrix} u_I \\ v_I \\ \theta_{zI} \\ u_J \\ v_J \\ \theta_{zJ} \end{pmatrix} \tag{2.27}$$

$$\mathbf{d}_s(x) = \mathbf{N}_s(x)\mathbf{q}_{IJ}$$

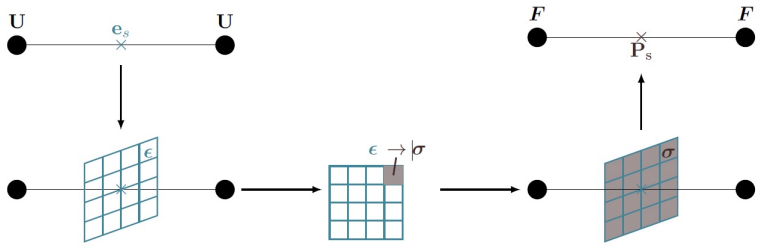

Figure 2-28 – Principle of multifiber beam element based on displacement-based formulation.

where the expression of bubble function is taken as $N_b = \frac{1}{2}(1-\frac{x}{L})\frac{x}{L}$ according to Auricchio [36]. The generalized normal and shear strain are derived from the vector of $\mathbf{d}_s(x)$ and then, for each fiber, according to the longitudinal stiffness method of Bentz, an iterative procedure for section state determination considering transverse equilibrium condition is applied to determine the strains and stresses in each fiber. The direct coupling between axial and shear strains (and stresses) at sectional level is established by a static condensation and a condensed material stiffness matrix is obtained as a result. At structural level, a linearization of the residual functions with respect to the nodal dis-

placement gives the element stiffness matrix, in which coupling between flexure and shear is included from the static condensation in the sectional state determination.

Navarro Gregori et al. [76] developed a 3D multifiber finite element displacement-based for RC member subjected to axial load, bending moment, shear and torsion. From the idea of section discretization proposed by Rahal & Collins [88], the cross-section in this model is discretized in three distinct regions following disposition of reinforcement steel: 1D regions composes only longitudinal steel, 2D regions locate in the zone in which the transverse steel crosses in one direction and 3D regions for the rest of cross-section. In each region, an appropriate constitutive model is defined, based on the MCFT (for 2D regions) and its extension by Vecchio & Selby [112] for 3D regions. Coupling between combined actions can be considered in the sectional analysis, and the model formulation can be applied for arbitrary cross-section. However warping phenomenon due to shear and torsion is not taken into account in this model.

Kotronis [58, 59] developed another 3D multifiber finite element for RC members where the transverse shear is taken into account by using Timoshenko's beam theory. The shear locking phenomenon is avoided by using cubic and quadratic shape functions for the interpolation of transverse and rotational displacements. The constitutive model is based on damage mechanism, in which uniaxial isotropic damage model of La Borderie is used for concrete [60], while a classical plasticity model is adopted for reinforcement steels. Another displacement-model for RC member subjected to shear and torsion was proposed by Mazars et al. [71], in which the warping kinematic for torsion is investigated initially in elasticity within the linear framework of Saint-Venant theory of torsion [97]:

$$u(x, y, z) = \alpha\varphi(y, z) \tag{2.28}$$

where $u(x, y, z)$ is the axial displacement of a fiber, α is the twist rate and $\varphi(y, z)$ is the warping function of the section. The equilibrium equation for warping function is expressed as:

$$\Delta\varphi(y, z) = 0 \tag{2.29}$$

The elastic linear warping problem for a section of various materials is solved using a warping-conduction analogy method, in which the warping function of cross-section is equivalent to the temperature function of a plate $T(y, z)$, the shear modulus G_i of the elastic material i is equivalent to the thermal conductivity λ_i of the isotropic material i.

While the equilibrium equation of warping in equation (2.29) correspond to $\Delta T(y,z) = 0$, the thermal boundary conditions can be expressed as:

$$\Phi_i \hat{n} = \begin{bmatrix} \lambda_i z \\ \lambda_i y \end{bmatrix} \begin{pmatrix} \hat{n}_y \\ \hat{n}_z \end{pmatrix} \tag{2.30}$$

where $\Phi_i = \lambda \, \mathrm{grad}(T(y,z))$ is the thermal density flux; $\hat{n}$ is the outward unit vector normal to the cross-section contour. Knowing the equilibrium equations and boundary conditions, the thermal conduction problem can be solved using finite element method, and so do the warping function. As a result, the shear strains due to pure torsion are obtained for each fiber:

$$\boldsymbol{\varepsilon} = \begin{bmatrix} 0 & \frac{1}{2}\alpha\left(\frac{\partial\varphi}{\partial y} - z\right) & \frac{1}{2}\alpha\left(\frac{\partial\varphi}{\partial z} + y\right) \\ \frac{1}{2}\alpha\left(\frac{\partial\varphi}{\partial y} - z\right) & 0 & 0 \\ \frac{1}{2}\alpha\left(\frac{\partial\varphi}{\partial z} + y\right) & 0 & 0 \end{bmatrix} \tag{2.31}$$

The calculated warping functions for plain concrete beams of rectangular and T-section subjected to pure torsion are shown in Figure 2-29.

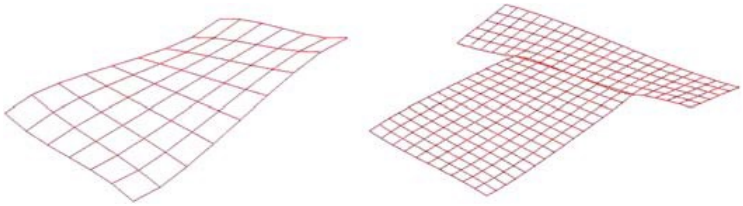

Figure 2-29 – Warping profile for rectangular and T-section under pure torsion obtained by Mazars et al. [71].

Capdevielle [15, 16] proposed a different way to include the warping phenomenon of torsion. The static equilibrium of beam element including warping in equation (2.29) can be expressed as follows:

$$\frac{\partial}{\partial y}\left(G\left(\frac{\partial\varphi}{\partial y} - z\right)\right) + \frac{\partial}{\partial z}\left(G\left(\frac{\partial\varphi}{\partial z} + y\right)\right) = 0 \tag{2.32}$$

Assuming that the lateral surface is free of load, the boundary condition of cross-section is expressed as:

$$G\left(\frac{\partial\varphi}{\partial y} - z\right)\hat{n}_y + G\left(\frac{\partial\varphi}{\partial z} + y\right)\hat{n}_z = 0 \tag{2.33}$$

From the strong form of the equilibrium equation in equation (2.32), the weak formulation of warping equilibrium can be derived as follows:

$$-\iint_A \left[\frac{\partial}{\partial y}\left(G\frac{\partial \varphi}{\partial y}\right)+\frac{\partial}{\partial z}\left(G\frac{\partial \varphi}{\partial z}\right)\right] w dS = \iint_A \left[\frac{\partial}{\partial y}(-Gz)+\frac{\partial}{\partial z}(-Gy)\right] w dS \quad (2.34)$$

where w is the weighting function. Integrating by part the first part of equation (2.34) and applying the boundary conditions in equation (2.33), the weak form of the cross-section equilibrium is obtained as follows:

$$\iint_A G\left(\frac{\partial \varphi}{\partial y}\frac{\partial w}{\partial y}+\frac{\partial \varphi}{\partial z}\frac{\partial w}{\partial z}\right) = \iint_A \left[\frac{\partial}{\partial y}(-Gz)+\frac{\partial}{\partial z}(Gy)\right] \quad (2.35)$$

A 2D finite element method with spatially discretized cross-section was used to solve equation 2.35 for the warping function φ. The section mesh discretization and warping profile obtained by Capdevielle for a concrete cross-section with longitudinal reinforcement are shown in Figure 2-30.

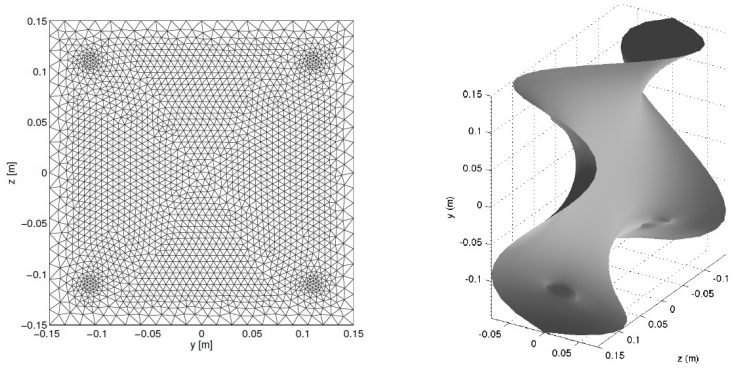

(a) Cross-section mesh.

(b) Warping profile.

Figure 2-30 – Warping obtained by Capdevielle [16].

More recently, Khoder [56] extended Capdevielle's model in order to take into account the lateral confinement of concrete due to stirrups. In her 3D multi-fiber model, the RC cross-section is discretized using three types of fiber: 2D triangular fibers of 6 nodes for concrete; 1D fibers for longitudinal and transversal reinforcements (Figure 2-31a). Each transversal steel is divided into several sub-element of composed of 2 nodes i and j each, which are interpolated by Lagrange linear polynomials (Figure 2-31b). The distortion field is therefore interpolated into one integration point P between two nodes, then the

distortion strain can be derived:

$$\begin{cases} u^w_{y,st}(P) = N_1 u^w_{y,i} + N_2 u^w_{y,j} \\ u^w_{z,st}(P) = N_1 u^w_{z,i} + N_2 u^w_{z,j} \end{cases} \Rightarrow \begin{cases} \varepsilon^w_{y,st}(P) = \dfrac{\partial u^w_{y,st}(P)}{\partial y} = -\dfrac{1}{l_{st}} u^w_{y,i} + \dfrac{1}{l_{st}} u^w_{y,j} \\ \varepsilon^w_{z,st}(P) = \dfrac{\partial u^w_{z,st}(P)}{\partial z} = -\dfrac{1}{l_{st}} u^w_{z,i} + \dfrac{1}{l_{st}} u^w_{z,j} \end{cases} \tag{2.36}$$

where $N_1 = \dfrac{1-\xi}{2}$ and $N_2 = \dfrac{1+\xi}{2}$ are the Lagrange linear polynomials; $u^w_{y,i}$,$u^w_{z,i}$, $u^w_{y,j}$ and $u^w_{z,j}$ are the transversal displacement of the distortion champ at node i and j; l_st is the length of stirrup sub-element. In this model, the concrete confinement is taken into account by considering different concrete regions where the constitutive relationship is selected in function of confinement degree.

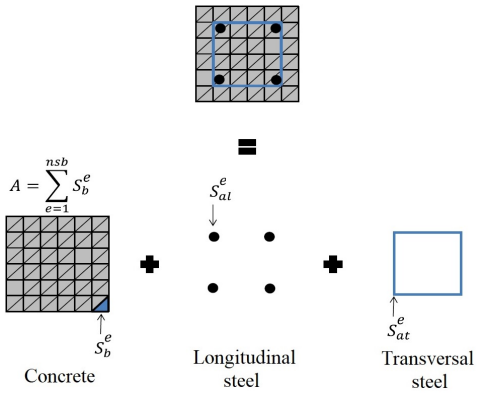

(a) Discretization of a RC cross-section into fiber of concrete, longitudinal and transversal steel.

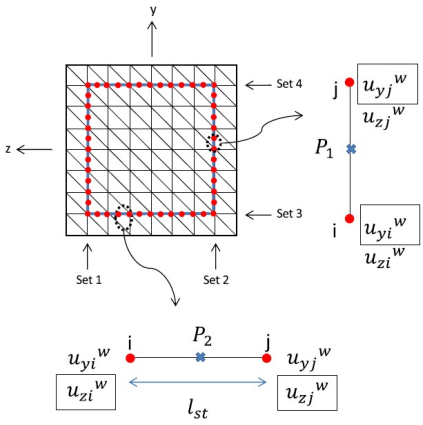

(b) Discretization of transversal steel.

Figure 2-31 – Model of Khoder [57].

2.4.4.2 Flexibility-based model

Spacone et al. [102] proposed a multifiber flexibility-based model for RC members subjected to axial force and bending. Then, Remino [94] developed this flexibility-based model for reinforced members subjected to shear force, using the kinematics of two-node Timoshenko beam (Figure 2-32). Starting form the nodal forces $\mathbf{P}_{IJ}$, the vector of sectional forces $\mathbf{D}_s(x)$ is computed as follows:

$$\begin{pmatrix} N \\ M \\ V \end{pmatrix} = \begin{bmatrix} 1 & 0 & 0 \\ 0 & \dfrac{x}{L} - 1 & \dfrac{x}{L} \\ 0 & \dfrac{x}{L} & \dfrac{1}{L} \end{bmatrix} \begin{pmatrix} N_J \\ M_I \\ M_J \end{pmatrix} + \begin{bmatrix} L(1-\dfrac{x}{L}) & 0 \\ 0 & \dfrac{1}{2}L^2\left[\left(\dfrac{x}{L}\right)^2 - \dfrac{x}{L}\right] \\ 0 & \dfrac{1}{2}L\left(1 - 2\dfrac{x}{L}\right) \end{bmatrix} \begin{pmatrix} p_x \\ p_y \end{pmatrix} \tag{2.37}$$

$$\mathbf{D}_s(x) = \mathbf{b}(x)\mathbf{P}_{IJ} + \mathbf{b}_p(x)\mathbf{p}$$

where x is the cross-section coordinate, L is the element length and $\mathbf{p}$ is the element load vector. The sectional stiffness matrix is evaluated numerically using the method of finite differences, in which the $mn-th$ component is determined as:

$$k_s^{mn} = \frac{D_s^m(\boldsymbol{\varepsilon}_s + \delta\varepsilon_s^n) - D_s^n(\boldsymbol{\varepsilon}_s)}{\delta\varepsilon_s^n}; \qquad \delta\varepsilon_s^n = \text{sign}(\Delta\varepsilon_s^n)\sqrt{\varepsilon_{tol}} \tag{2.38}$$

where D_s^m is the $m-th$ term of the vector $\mathbf{D}_s(x)$, $\boldsymbol{\varepsilon}_s$ is the vector of the section deformation; $\Delta\varepsilon_s^n$ is the variation of the $n-th$ section deformation with respect to the last converged step of the analysis and ε_{tol} is the numerical tolerance. In this model, the interaction between axial force, bending and shear are taken directly and the constitutive models are based on the MCFT with some slight modifications. However, this approach for constitutive model meets some numerical difficulties when trying to encounter the cyclic load conditions.

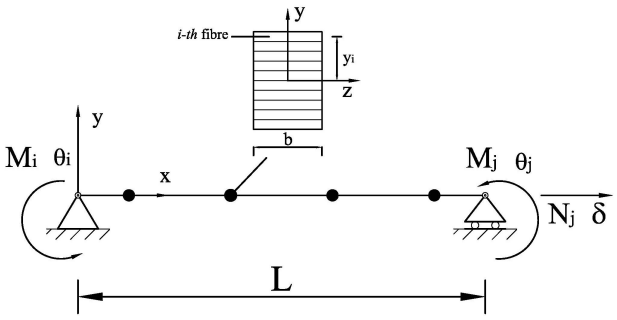

Figure 2-32 – Basic forces, elements and fiber discretization of multifiber beam element based on flexibility-based formulation.

Another flexibility-based model was developed by Saritas & Filippou [99]. In this model the relationship between the nodal forces and sectional forces is the same as in equation (2.37). The sectional state determination follows the longitudinal stiffness method proposed by Benzt [12] that is already described in Section 2.4.3, using Timoshenko's kinematic hypothesis and a parabolic correction form for the shear strain distribution function of rectangular cross-sections:

$$f(y) = \frac{5}{4}\left(1 - \frac{4y^2}{h^2}\right) \tag{2.39}$$

where h is the section's height. Static condensation is then performed in order to obtain the sectional stiffness matrix, which is symmetric rather than asymmetric in the model of Bentz, thanks to the correction form in equation 2.39. In each fiber/layer of the cross-section, a two-dimensional constitutive model based on the MCFT is applied. Based on

the formulation of this model, Saritas & Filippou [99], [100] then developed other models using damage mechanics for the constitutive model of concrete, in order to consider the cyclic load conditions for reinforced beam and wall element.

In order to account for torsional effect, Le Corvec [62] presented a mixed-formulation of 3D multi-fiber beam that is able to capture the local effects due to constrained warping of the section, so it can represent accurately the torsional response of beam under warping constraints conditions. For this, the additional warping degrees of freedom are introduced through a system of integration points and then interpolated by Lagrange polynomials to ensure equilibrium on the entire element (Figure 2-33). Assuming that the warping displacement profile over the cross-section $\psi(y,z)$ and the warping displacement distribution over the element length $\chi(x)$ are interpolated independently, the material warping displacement in each fiber can be expressed as the product of $\psi(y,z)$ and $\chi(x)$:

$$u^w(x,y,z) = \sum \chi_i(x)(\psi(y,z)\mathbf{u}_i^w) \tag{2.40}$$

where $\mathbf{u}_i^w$ is the vector of warping variables defined as additional degree of freedoms in the beam model. The material warping displacement in each fiber $u^w(x,y,z)$ is then superimposed into the axial displacement followings plane-section hypothesis, as suggested in the model of Bairan [4], which will be detailed clearly in section 2.4.5. The element equilibrium in equation 2.37 is extended to account for three-dimensional strain and stress state:

$$\begin{pmatrix} N \\ M_z \\ V_y \\ M_x \\ M_y \\ V_z \end{pmatrix} = \begin{bmatrix} 1 & 0 & 0 & 0 & 0 & 0 \\ 0 & \frac{x}{L}-1 & \frac{x}{L} & 0 & 0 & 0 \\ 0 & -\frac{1}{L} & -\frac{1}{L} & 0 & 0 & 0 \\ 0 & 0 & 0 & 1 & 0 & 0 \\ 0 & 0 & 0 & 0 & \frac{x}{L}-1 & \frac{x}{L} \\ 0 & 0 & 0 & 0 & \frac{1}{L} & \frac{1}{L} \end{bmatrix} \begin{pmatrix} N_J \\ M_{zI} \\ M_{zJ} \\ M_{xJ} \\ M_{yI} \\ M_{yJ} \end{pmatrix} + \mathbf{b}_p(x) \begin{pmatrix} p_x \\ p_y \\ p_z \\ m_x \\ m_y \\ m_z \end{pmatrix} \tag{2.41}$$

In this model, the effects of boundary conditions on the warping distribution under torsion can be represented for arbitrary cross-sections (Figure 2-33b), but the constitutive material model is limited only to steel. The warping profile of the rectangular cross-section of steel beam is shown in Figure 2-34a.

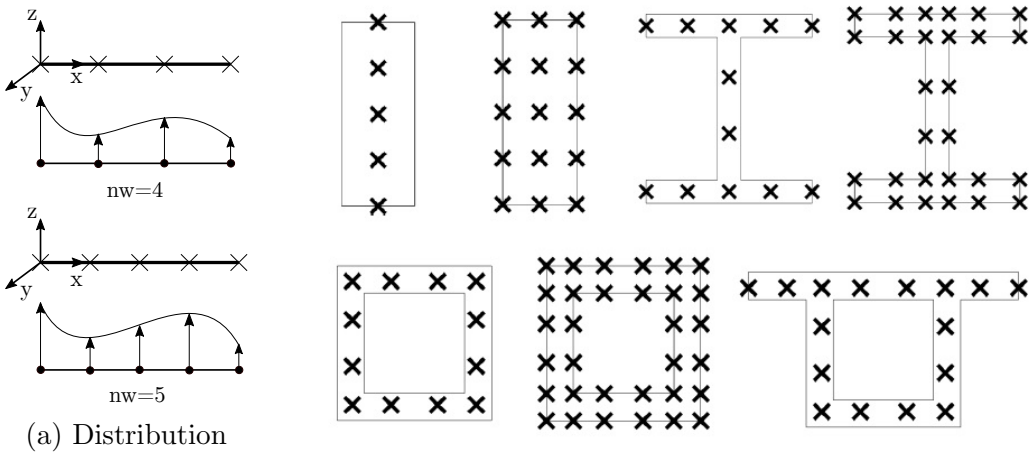

(a) Distribution over the element length.

(b) Distribution of interpolation points over the cross-section.

Figure 2-33 – System of interpolation points to account for warping in the model of Le Corvec [62].

Based on this idea of warping interpolation using additional degrees of freedom, Addessi & Di Re [2] extended Le Corvec's model to plain concrete member under torsion using an isotropic damage model for brittle-like materials. Then, Di Re [31] used Hermite polynomials instead of Lagrange polynomials for the interpolation functions in a flexibility-based model for RC beam. The warping profile of the rectangular cross-section of plain concrete beam is shown in Figure 2-34b.

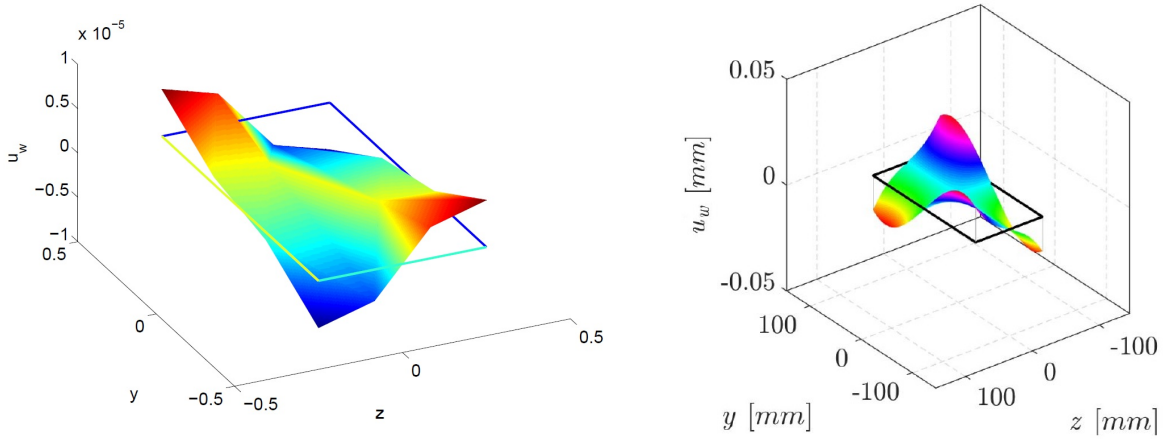

(a) Model of Le Corvec [62].

(b) Model of Di Re [30].

Figure 2-34 – Warping profile of rectangular cross-section under torsion.

2.4.5 Enhanced FE Model

Bairan [3] developed a general 3D nonlinear model for the analysis of RC sections under any combination of efforts. This local sectional-fiber model is formulated in a general way for arbitrary cross-section and independently of the beam element formulation.

The featured idea in this model is to reproduce the full 3D state of the cross-section characteristics by superimposing an enhanced distortion-warping displacement field with the classical plane-section displacement field (Figure 2-35a):

$$\mathbf{u} = \mathbf{u}^{ps} + \mathbf{u}^{w} \tag{2.42}$$

The classical displacement field $\mathbf{u}^{ps}$ is derived from the Euler-Bernoulli hypothesis, while the enhanced field $\mathbf{u}^{w}$ is constructed as a vector of three components, one for warping and two for the distortion with the cross-section, that must satisfy the condition of orthogonality with respect to the classical displacement field (Figure 2-35b). The same decomposition of displacement field is also applicable to strain and stress fields:

$$\begin{aligned} \boldsymbol{\varepsilon} &= \boldsymbol{\varepsilon}^{ps} + \boldsymbol{\varepsilon}^{w} \\ \boldsymbol{\sigma} &= \boldsymbol{\sigma}^{ps} + \boldsymbol{\sigma}^{w} \end{aligned} \tag{2.43}$$

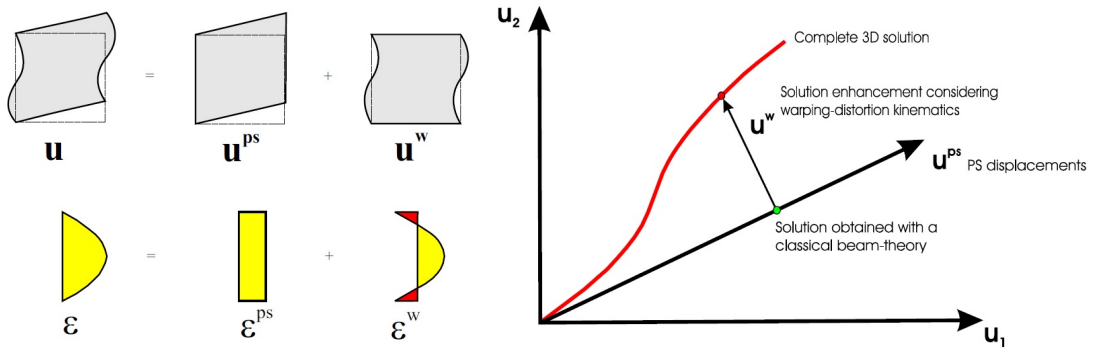

(a) Decomposition of displacement field.

(b) Orthogonality condition for the distortion field.

Figure 2-35 – Model of Bairan [3].

Due to the superposition, the equilibrium conditions are obtained at structural level and at sectional level. At structural level, equilibrium among sections of the beam is assured when the equilibrium residual on the plane-section displacement field is set to zero:

$$R^{ps}(x) = \delta\mathbf{u}_s^T \iint_A \mathbf{N}^{psT}\mathbf{L}_x^T(\boldsymbol{\sigma})dA - \delta\mathbf{u}_s^T \iint_A \mathbf{L}_{yz}(\mathbf{N}^{ps})^T\boldsymbol{\sigma}dA = 0 \tag{2.44}$$

with $\mathbf{u}_s$ is the generalized displacement vector of cross-section; $\mathbf{N}^{ps}$ is a compatibility matrix related $\mathbf{u}^ps$ and $\mathbf{u}_s$; $\mathbf{L}_x$ and $\mathbf{L}_{yz}$ are the linear operators containing the derivation following x and y, z respectively. At sectional level, the equilibrium among inner fibers is

assured when the equilibrium residual on the distortion displacement field is set to zero:

$$R^w(x) = \iint_A \delta \mathbf{u}^{wT} \mathbf{L}_x^T(\boldsymbol{\sigma}) dA - \iint_A \mathbf{L}_{yz}(\delta \mathbf{u}^w)^T \boldsymbol{\sigma} dA = 0 \tag{2.45}$$

The complete 3D equilibrium of beam is determined by solving the system of equation (2.44) and (2.45). For this, the strategic way is to obtain the $\boldsymbol{\sigma}^w$ field as a function of $\mathbf{u}^{ps}$ at each cross-section and then satisfy equation (2.45) at each integration point of the beam element. As a result, the 3D problem can be solved as the superposition of a 1D beam problem with standard frame elements in equation (2.44) and a 2D sectional model using bi-dimensional element locally at the beam's integration points equation (2.45). The finite elements in the section discretization for a RC beam element are summarized in Figure 2-36, where the concrete is simulated as 2D elements, the transversal reinforcements are reprensented by 1D elements and the longitudinal steels are simulated as point elements.

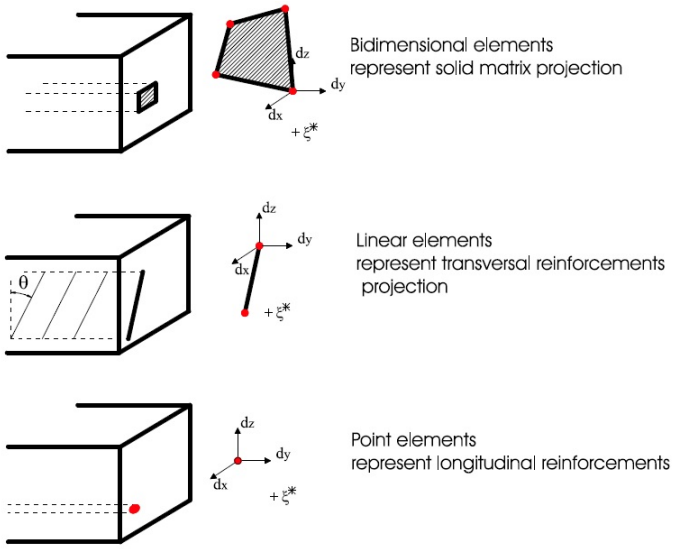

Figure 2-36 – Library of finite elements in a cross-section of Bairan's model [3].

The vector of distortion displacement field $\mathbf{u}^w$ is obtained from the additional nodal values $\mathbf{d}^w$ of the cross-section. Then, $\mathbf{d}^w$ is related to the vector of generalized strains $\mathbf{e}_s$ by several compatibility and interpolation matrices. Finally, through the virtual work principle, the sectional internal forces and sectional stiffness matrix can be derived in the form of a decomposition of the plane-section field and the distortion field, which includes coupling terms between plane-section and distortion deformations.

The constitutive model is based on a cyclic hypo-elastic model for concrete and an uni-axial elasto-plastic relationship for steel. Inelastic concrete is modeled as an orthotropic material whose behavior is described along the principal directions by an equivalent uni-

axial stress-strain relationship. The compression behavior follows a cyclic loading scheme suggested by Vecchio & Selby [112], whereas in tension, a linear elastic behavior is considered prior to cracking, then after cracking the stress-strain relationship follows a nonlinear softening curve with the damage variables proposed by Cervenka [19]. The triaxial characteristics are computed through a three-dimensional failure surface, in which the strains (and related stresses) are decomposed as a contribution of mechanical and non-mechanical part.

2.5 Overview and Discussion

Throughout this chapter, a literature review of the modeling strategy for RC members subjected to shear-bending and/or torsion has been carried out. The problematic of the RC members under bending and shear has been investigated and experienced by many researchers. Several numerical models with different degree of complexity have been developed. Among the existing models, the sectional-fiber finite element approach has been widely considered as one of the most adequate solutions, thanks to its excellent balance between accuracy of numerical results, calculation time and ergonomics. However, to the best of the author's knowledge, a rational sectional model accounting for tangential forces is still under study.

The longitudinal stiffness method has shown its advantage by considering the equilibrium as well as compatibility equations at local level, and more important, by giving a material stiffness matrix reflecting the coupling of normal and tangential forces when considering the transverse equilibrium conditions. For these reasons, although originally limited for mono-dimensional shear flow (i.e in-plane bending and shear), in this PhD we decided to apply this approach in the proposed formulation with an extension in bi-dimensional shear flow, thus three-dimensional loading. Considering the choice of finite element formulation, the flexibility-based method has shown its advantages over the stiffness-based method [102]: giving the exact solutions by satisfying strict conditions of equilibrium and compatibility; requiring fewer elements for the representation of the non-linear behavior of concrete by using exact force interpolation functions; avoiding the well known shear-locking phenomenon. On the other hand, over the flexibility method, the stiffness-based method accompanying by the displacement-based formulation has also significant advantages. First, once the analytical model has been defined, no further engineering decisions are required in this formulation to carry out the analysis, this method

is thus conducive to computer programing [114]. In addition, if the unknown quantities in the flexibility method are redundant actions that must be arbitrarily chosen, the unknowns in stiffness method are automatically specified as the nodal displacements of element, the number of unknowns to be determined is therefore the same as the degree of freedom of element. Otherwise, the obtained numerical results are also satisfied. To avoid the shear locking phenomenon, some solutions have been proposed such as a bubble function in the model of Ceresa [18] or Hermite and Lagrange shape functions for transverse and rotational displacements in the model of Kotronis [59].

In a 3D beam problem, when accounting for shear and especially torsion effect, it is indispensable to account for the warping phenomenon. For this, the Bairan's strategy [3] of decomposition cross-section characteristics into classical field following plane-section hypothesis and enhanced field of warping-distortion is adopted for the development of our FE model. One believes that this is the most suitable approach to representing the complete deformation state (warping and distortion) of cross-section. While the plane-section field can be represented by classical theory such as Euler-Bernoulli or Timoshenko, for the enhanced warping-distortion field, several solutions have been proposed, such as using warping-thermal analogy [71], using Saint-Venant theory and 2D finite element method [16] or using Lagrange polynomial and system of interpolation points defined as additional degree of freedoms [62], [30], etc. To the best of the author's knowledge, although successfully applied in the mixed-based formulation by Le Corvec [62], Addessi [2] and Di Re [31], the Lagrange polynomial approach accounting for warping displacement has not yet been implemented in any displacement-based model of RC. In this work, we would like to review and compare the use of Saint-Venant theory with that of Lagrange polynomials in the displacement-based formulation, then recommend the use of each method depending on requirements. These two approaches have been programmed and implemented in the proposed FE model.

Regarding the constitutive models, there are two favorable choices for sectional-fiber model, between smeared-crack approaches and damage mechanics. A constitutive model based on the MCFT [110] was chosen because of its simplicity and the fact that it can be enhanced by developing suitable uniaxial stress-strain relationship for concrete and steel, depending on the model's requirements. In this work, a parametric tensile relationship for concrete has been proposed by the authors for the responses of RC members subjected to pure torsion. In this formulation, only engineering parameters (e.g. material strengths, reinforcement geometrical ratios) are required as input, thus improving the ability to apply

the proposed model to practical simulations. Another important reason for the choice of the MCFT is that it is very suitable for the transverse equilibrium between the fibers, in particularly when taking into account the contribution of transverse reinforcements. Inspired by the idea of Navarro et al. [76], a specific section discretization following the reinforcement steel's disposition, accompanied by appropriate constitutive models based on the MCFT, was developed and implemented in the proposed model, which will be described in detail in the next Chapter.

Chapter 3

Enhanced multi-fiber 3D beam element for RC members

3.1 General

The present Chapter deals with the development of a finite element model for RC members subjected to arbitrary loading (Bending and/or shear and/or torsion). The developed model is able to take into account the material nonlinearity, the warping effect of cross-section, the contribution of transversal reinforcement, and the concrete confinement. As for the geometrical nonlinearity, it is treated separately in Chapter 6 by using the co-rotational framework. Therefore, this chapter is dedicated for the development of the local beam element. The two-node Timoshenko beam using multifiber discretization approach and displacement-based formulation are adopted. Based on the principle of distributed finite element method, the idea of multi-fiber finite element is to divide the structure into several longitudinal fibers and some control sections situated at the *Gauss-Lobatto points* along the element. At the intersection of longitudinal fibers and control sections, a system of integration points is obtained (Figure 3-1). Each point, called *fiber* and considered as a material point, has its own coordinates, surface and an appropriate material law in order to determine the strain and stress from the element's displacements. Therefore, the proposed model is described as a frame element with a set of cross-sections along its longitudinal axis.

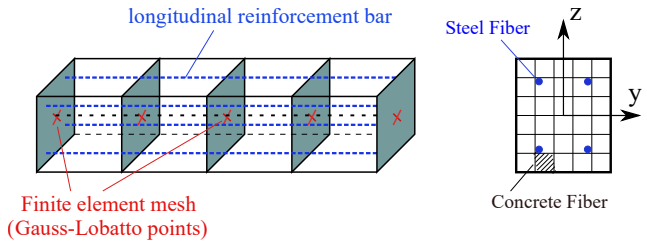

Figure 3-1 – Multifiber approach for a RC member and local element frame coordinate

As can be seen in Figure 3-1, while the concrete and the longitudinal rebar are distributed longitudinally in the element, the distribution of transversal reinforcement steels is discontinued in this direction by a spacing s. Taking into account the contribution of transversal reinforcement in a multi-fiber model is therefore not an obvious work. As mentioned in the Chapter 2, it can follow the strategy of using the MCFT and satisfying the internal equilibrium between concrete and stirrups in the constitutive model as proposed by Saritas & Filippou [99] or Navarro-Gregori et al. [76]; or considering the transversal steel as bar element and interpolating the distortion displacement by Lagrange linear polynomials, as suggested by Bairan [3] or Khoder et al. [57]. Between these proposals, the idea of Navarro Gregori is adopted in our model. The cross-section is discretized into several separated regions following the direction of transversal reinforcement and the contribution of stress state to the sectional response (Figure 3-2a). The following zones are considered:

- **1D-Zone**: This zone represents the longitudinal reinforcement position. In this zone only the normal stress in reinforcement steels is taken into account.

- **2D-Zone**: This zone corresponds to the regions where the transverse steel crosses in one direction and may also have the contribution of longitudinal steel bars. In this zone, under shear, bending or torsional effects, the direction of normal stress in transverse steels coincides to the direction of shear stresses in concrete (τ_{xz} in the vertical zone or τ_{xy} in the horizontal zone) (Figure 3-2b). Consequently, only normal stress (due to concrete) and one shear stress (due to concrete and stirrup) are taken into account in the sectional analysis, the other shear stress is set to zero.

- **3D-zone**: This zone corresponds to the regions of concrete in which transverse steels come across in two directions (the four corners of section) and the regions of concrete in the core of section without any reinforcement. In this zone, at each integration point the stress state contains 3 components: one normal and two transverse stresses.

For the numerical implementation, in 1D-zone, each longitudinal steel bar is considered as point fiber, characterized by the cross-section area A_{sl} of steel bar and its coordinate (y_{sl}, z_{sl}) in the local coordinate of cross-section. In 2D and 3D-zone, the regions are discretized into square fibers of centroid integration point P, characterized by the square fiber area A_f (numerical integration weight) and the coordinate of integration point P (y_f, z_f). The contribution of stirrup is taken into account by satisfying the internal equilibrium between concrete and stirrups in 2D-zone, which will be detailed in Section 3.5.2.

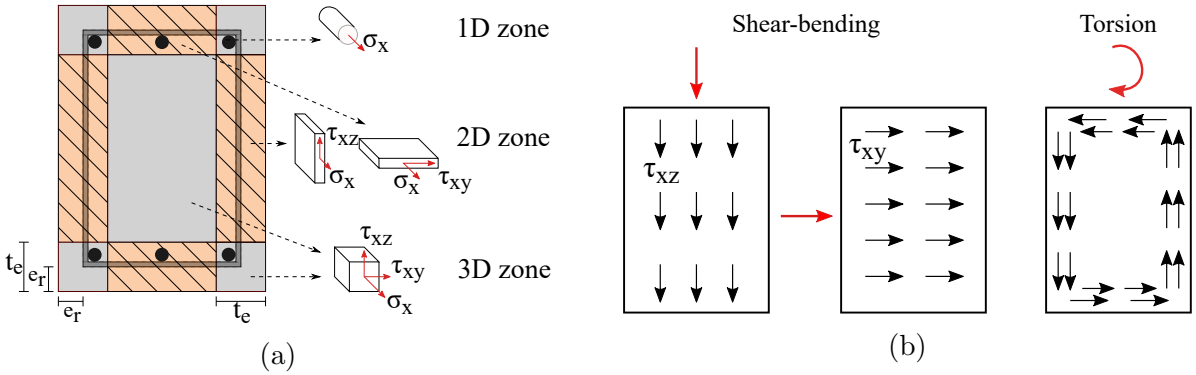

Figure 3-2 – (a) Discretization of cross-section following the material stress state in the model of Navarro-Gregori et al. [76]. (b) Shear stress direction under shear, bending or torsional effects.

The following presentation starts with the definition of element and section kinematics as well as the main assumptions of the model. In order to take into account the warping-distortion phenomenon, two approaches will be introduced and described in this chapter:

1. **Using Saint-Venant's warping function**: Based on two-node Timoshenko beam with 6 local displacements at each node, making a total of 12 degree of freedoms (DoFs) in each element. The formulation is then enhanced by Saint-Venant warping function when considering the kinematic conditions.

2. **Using Lagrange polynomials**: Introduction of an enhanced beam with a superposition of several additional warping DoFs into the two-node Timoshenko beam. The interpolation functions for warping/distortion over the cross-section and along the element are also described and implemented into the finite element discretization.

The element formulation is then derived following the principle of virtual work in order to obtain the consistent stiffness matrix and nodal forces vector of the element. Next, the solution schemes for two "warping" approaches are described. Finally, the mechanical model containing appropriate constitutive models for different discretized regions as described above is presented.

3.2 Element kinematics

Let's consider a two-node Timoshenko beam represented by a straight axis line delimited by end nodes I and J and the local frame system of coordinate (x, y, z) as shown in Figure 3-3. The displacement field contains three translations $u(x)$, $v(x)$, $w(x)$ and three rotations $\theta_x(x)$, $\theta_x(x)$, $\theta_x(x)$ about axes x, y, z, respectively. These components are collected in a single displacement vector called *generalized displacement* which depends on the section's position along the element axis:

$$\mathbf{d}_s(x) = \begin{pmatrix} u(x) & v(x) & w(x) & \theta_x(x) & \theta_y(x) & \theta_z(x) \end{pmatrix}^{\mathrm{T}} \tag{3.1}$$

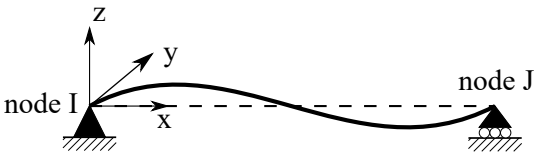

Figure 3-3 – Two-node Timoshenko beam and the local reference system.

In the displacement-based formulation, the *generalized displacement* is expressed in function of the principal variables which are the *nodal displacements* vector $\mathbf{q}_e$ by interpolation shape functions:

$$\mathbf{d}_s(x) = \mathbf{N}_s(x)\mathbf{q}_e \tag{3.2}$$

where:

$$\mathbf{q}_e = \begin{pmatrix} u^I & v^I & w^I & \theta_x^I & \theta_y^I & \theta_z^I & u^J & v^J & w^J & \theta_x^J & \theta_y^J & \theta_z^J \end{pmatrix}^{\mathrm{T}} \tag{3.3}$$

and $\mathbf{N}_s(x)$ is the matrix of shape function defined as [38]:

$$\mathbf{N}_s(x) = \begin{bmatrix} N_1 & 0 & 0 & 0 & 0 & 0 & N_2 & 0 & 0 & 0 & 0 & 0 \\ 0 & N_{3y} & 0 & 0 & 0 & N_{4y} & 0 & N_{5y} & 0 & 0 & 0 & N_{6y} \\ 0 & 0 & N_{3z} & 0 & -N_{4z} & 0 & 0 & 0 & N_{5z} & 0 & -N_{6z} & 0 \\ 0 & 0 & 0 & N_1 & 0 & 0 & 0 & 0 & 0 & N_2 & 0 & 0 \\ 0 & 0 & -N_{7z} & 0 & N_{8z} & 0 & 0 & 0 & -N_{9z} & 0 & N_{10z} & 0 \\ 0 & N_{7y} & 0 & 0 & 0 & N_{8y} & 0 & N_{9y} & 0 & 0 & 0 & N_{10y} \end{bmatrix} \tag{3.4}$$

As mentioned in Chapter 2, while the axial displacement and torsional rotation can be interpolated by linear shape function (N_1 and N_2), the transverse and rotational displacements must be interpolated by cubic or quadratic functions. The detailed expressions

of these shape functions can be found in the work of Friedman & Kosmatka [38] or in Appendix 7.2.

3.3 Section kinematics

At sectional level, in each material points (or fiber) the displacement has 3 components, one axial U and two transversal V, W gathered in a single vector $\mathbf{d}_f(x,y,z)$. As mentioned in Chapter 1, the plane-section theory is insufficient to reproduce the complete sectional deformation under shear and torsional effects (Figure 3-4a). According to the proposition of Bairan & Mari [4], the material displacement field is decomposed into two domains: a classical field describing the rigid body motion, consistent with the plan-section beam theory; and an *enhanced* field referring to warping-distortion phenomena (Figure 3-4b).

$$\mathbf{d}_f^m(x,y,z) = \mathbf{d}_f^p(x,y,z) + \mathbf{d}_f^e(x,y,z) = \begin{pmatrix} U^p(x,y,z) \\ V^p(x,y,z) \\ W^p(x,y,z) \end{pmatrix} + \begin{pmatrix} U^e(x,y,z) \\ V^e(x,y,z) \\ W^e(x,y,z) \end{pmatrix} = \begin{pmatrix} U^m(x,y,z) \\ V^m(x,y,z) \\ W^m(x,y,z) \end{pmatrix} \tag{3.5}$$

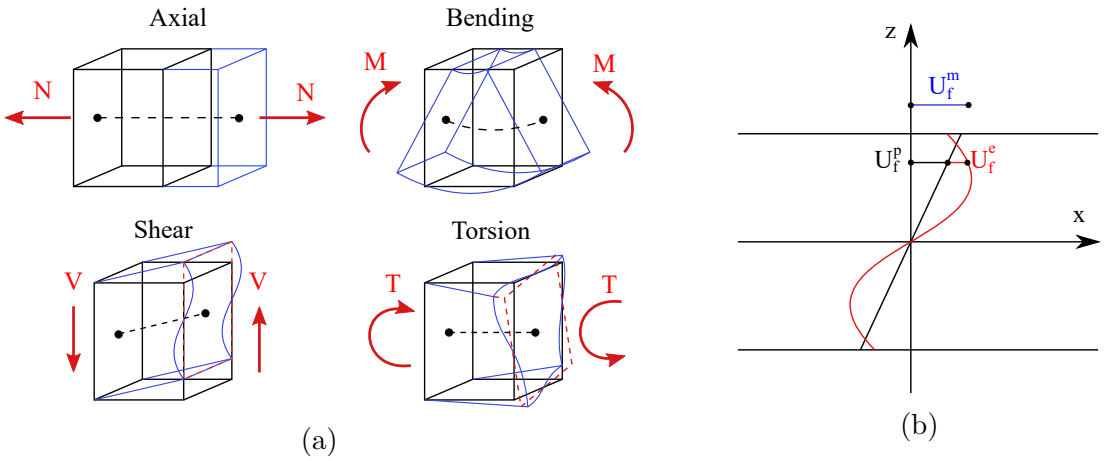

Figure 3-4 – (a) Section deformation under normal efforts (axial, bending) and tangential efforts (shear, torsion). (b) Decomposition of a material axial displacement.

Depending on the requirement, the enhanced material displacement vector $\mathbf{d}_f^e(x,y,z)$ may have one or three components : if only the warping phenomenon is taken into account, then only the axial displacement U^e is considered; otherwise, the two transversal displacements V^e and W^e in y and z direction are reserved for the distortion phenomenon. In the following the section kinematics will be described for the classical field, the enhanced field using Saint-Venant theory and the enhanced field using Lagrange polynomials.

3.3.1 Classical field

The material displacement of classical field is related to the generalized displacements vector according to the following relation kinematic:

$$\left.\begin{aligned} U^p(x,y,z) &= u(x) - y\theta_z(x) + z\theta_y(x) \\ V^p(x,y,z) &= v(x) - z\theta_x(x) \\ W^p(x,y,z) &= w(x) + y\theta_x(x) \end{aligned}\right\} \quad \Rightarrow \mathbf{d}_f^p(x,y,z) = \mathbf{a}_f^p(y,z)\mathbf{d}_s(x) \tag{3.6}$$

with the expression of the section compatibility matrix:

$$\mathbf{a}_f^p(y,z) = \begin{bmatrix} 1 & 0 & 0 & 0 & z & -y \\ 0 & 1 & 0 & -z & 0 & 0 \\ 0 & 0 & 1 & y & 0 & 0 \end{bmatrix} \tag{3.7}$$

The strains of any material point of the cross section are then evaluated with only three components considered in the sectional analysis as follows: one normal strain and two transverse strains collected in a single strain vector:

$$\mathbf{e}_f^p(x,y,z) = \begin{pmatrix} \varepsilon_{xx}^p & \gamma_{xy}^p & \gamma_{xz}^p \end{pmatrix}^T \tag{3.8}$$

with the assumption of small displacements, the material strains can be evaluated from first-order material displacement only:

$$\begin{aligned} \varepsilon_{xx}^p &= \frac{\partial U^p}{\partial x} = \frac{\partial u}{\partial x} - y\frac{\partial \theta_z}{\partial x} + z\frac{\partial \theta_y}{\partial x} \\ \gamma_{xy}^p &= \frac{\partial U^p}{\partial y} + \frac{\partial V^p}{\partial x} = \frac{\partial v}{\partial x} - \theta_z - z\frac{\partial \theta_x}{\partial x} \\ \gamma_{xz}^p &= \frac{\partial U^p}{\partial z} + \frac{\partial W^p}{\partial x} = \frac{\partial w}{\partial x} + \theta_y + y\frac{\partial \theta_x}{\partial x} \end{aligned} \tag{3.9}$$

It is important to note that without this assumption of small displacements, second and third-order of derivation must be taken into account and the section kinematics become a non-linear geometric problem, which will be investigated in Chapter 6. This chapter deals only with the linear geometric condition with the following definitions of sectional strains according to Timoshenko beam theory: $\varepsilon_x(x) = \dfrac{\partial u(x)}{\partial x}$ is the axial strain, $\gamma_y(x) = \dfrac{\partial v(x)}{\partial x} - \theta_z(x)$ and $\gamma_z(x) = \dfrac{\partial w(x)}{\partial x} + \theta_y(x)$ are the shear strains in the y and z direction, respectively; $\kappa_x(x) = \dfrac{\partial \theta_x(x)}{\partial x}$ is the torsional curvature and $\kappa_y(x) = \dfrac{\partial \theta_y(x)}{\partial x}$

and $\kappa_z(x) = \dfrac{\partial \theta_z(x)}{\partial x}$ are the flexural curvatures about the y and z axis respectively. From these definitions, the kinematic relation in Equation (3.9) can be expressed as a relation between the material strains and sectional strains as follows:

$$\mathbf{e}_f^p(x,y,z) = \mathbf{a}_f^p(y,z)\mathbf{e}_s(x) \tag{3.10}$$

with the expression of the compatibility matrix $\mathbf{a}_f^p(y,z)$ is the same as in Equation (3.7) and the vector $\mathbf{e}_s(x,y,z)$ is defined as the *generalized strains*:

$$\mathbf{e}_s(x) = \begin{pmatrix} \varepsilon_x(x) & \gamma_y(x) & \gamma_z(x) & \kappa_x(x) & \kappa_y(x) & \kappa_z(x) \end{pmatrix}^T \tag{3.11}$$

It is interesting to note that, in the Euler-Bernoulli beam theory, the generalized shear strains are equal to zero because this theory does not take into account the shear effect. In the longitudinal stiffness method proposed by Bentz [12] in Section 2.4.3, the shear strain is defined initially as a function of the mean sectional shear deformation $\bar{\gamma}$: $\gamma_{y/z} = f(y/z)\bar{\gamma}$. This proposition leads to a asymmetric sectional stiffness in the sectional state determination. The definition of generalized shear strain in Timoshenko beam theory can solve this problem of asymmetry, however it does not guarantee the longitudinal equilibrium at certain coordinates (y,z) of the section [98]. As a consequence, the correction parameters need to be introduced in order to describe the shear strain distribution over the cross-section. So, the expression of compatibility matrix $\mathbf{a}_f^p(y,z)$ in Equation (3.9) is rewritten as follows:

$$\mathbf{a}_f^p(y,z) = \begin{bmatrix} 1 & 0 & 0 & 0 & z & -y \\ 0 & k_y c_y(y,z) & 0 & -z & 0 & 0 \\ 0 & 0 & k_z c_z(y,z) & y & 0 & 0 \end{bmatrix} \tag{3.12}$$

where k_y and k_z are the shear correction factors; $c_y(y,z)$ and $c_z(y,z)$ are the shear correction functions. In this present work, for rectangular cross-section of width b and height h in a linear elastic material, a parabola correction function is proposed (Figure 3-5) and the following correction factors and functions are defined:

$$\begin{aligned} k_y &= \frac{5}{6}; \qquad c_y(y,z) = \frac{3}{2b^2}\left(b^2 - 4y^2\right) \\ k_z &= \frac{5}{6}; \qquad c_z(y,z) = \frac{3}{2h^2}\left(h^2 - 4z^2\right) \end{aligned} \tag{3.13}$$

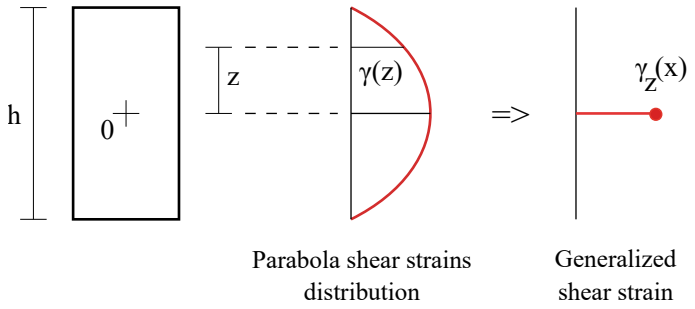

Figure 3-5 – Transformation of the shear strain distribution to a generalized shear strain in the case of rectangular cross-section.

From this definition of generalized strains and the relation between the generalized displacements and the nodal displacements in Equation (3.2), the generalized strains can be determined from the nodal displacements by another matrix of shape functions:

$$\mathbf{e}_s(x) = \mathbf{B}_s(x)\mathbf{q}_e \tag{3.14}$$

with the expression of $\mathbf{B}_s(x)$:

$$\mathbf{B}_s = \begin{bmatrix} B_1 & 0 & 0 & 0 & 0 & 0 & B_2 & 0 & 0 & 0 & 0 & 0 \\ 0 & B_{3y} & 0 & 0 & 0 & B_{4y} & 0 & B_{5y} & 0 & 0 & 0 & B_{6y} \\ 0 & 0 & B_{3z} & 0 & -B_{4z} & 0 & 0 & 0 & B_{5z} & 0 & -B_{6z} & 0 \\ 0 & 0 & 0 & B_1 & 0 & 0 & 0 & 0 & 0 & B_2 & 0 & 0 \\ 0 & 0 & -B_{7z} & 0 & B_{8z} & 0 & 0 & 0 & -B_{9z} & 0 & B_{10z} & 0 \\ 0 & B_{7y} & 0 & 0 & 0 & B_{8y} & 0 & B_{9y} & 0 & 0 & 0 & B_{10y} \end{bmatrix} \tag{3.15}$$

The expression of shape functions $B_i(x)$ can be found in Appendix 7.2.

3.3.2 Enhanced field using Saint-Venant theory

In a frame-fiber model, according to the Saint-Venant theory of torsion [97], the warping phenomenon is represented by a function $\psi(y, z)$ which describes the *warping displacement profile* over the cross-section and depends on the shape of cross-section [97]. It is also assumed by Saint-Venant that the warping profile is considered constant along the element, and the normalized warping displacement is proportional to this warping function $\psi(y, z)$. Then, Saint-Venant theory is extended when the distribution of warping over the element length becomes variant and is represented by a parameter $\alpha(x)$. As a consequence, the warping displacement is expressed proportional to the *warping profile*

(i.e warping function) and the *warping distribution*:

$$U^e(x,y,z) = \alpha(x)\psi(y,z) \tag{3.16}$$

In the case of solid cross-section, where the effect of warping is limited (but cannot be neglected), the warping is free and its distribution can be considered constant over the element length as mentioned in Saint-Venant theory. In this case, the warping distribution equals to the derivative of the twist angle: $\alpha(x) = \alpha = \partial\theta_x/\partial x = \kappa_x$, and $\partial\alpha/\partial x = 0$. In the case of thin-walled cross-section, as the role of warping becomes important, the warping distribution is not constant anymore and depends on the cross-section's position. Thus, Vlasov [113] proposed a new theory of torsion for thin-walled cross-sections with $\alpha(x) = \partial\theta_x/\partial x$ and $\partial\alpha/\partial x \neq 0$. Consequently, an additional DoF needs to be added to consider the contribution of the derivative of parameter $\alpha(x)$. Another torsional theory, proposed by Benscoter [11], defines that the warping distribution α is independent of the torsional angle: $\alpha(x) \neq \partial\theta_x/\partial x$. These two theories of torsion for thin-walled cross-sections, can be compared as the analogy of two classical bending theory Navier-Bernoulli and Timoshenko. Vlasov's assumption of neglecting the shear warping deformation is compatible with neglecting the shear bending strain in the Navier-Bernoulli's theory, while Benscoter's assumption of incorporating shear warping deformation can be regarded similar to the Timoshenko's assumption of taking into account the shear bending strain.

In this work, as the shape of cross-section is rectangular, Saint-Venant theory can be used for the sake of simplicity, from Equation (3.6) and Equation (3.16), the total displacement field in Equation (3.5) becomes:

$$\begin{aligned} U^m(x,y,z) &= u(x) - y\theta_z(x) + z\theta_y(x) + \kappa_x\psi(y,z) \\ V^m(x,y,z) &= v(x) - z\theta_x(x) \\ W^m(x,y,z) &= w(x) + y\theta_x(x) \end{aligned} \tag{3.17}$$

And the total material strains are expressed by:

$$\left.\begin{aligned} \varepsilon^m_{xx} &= \frac{\partial U^m}{\partial x} &&= \varepsilon_x - y\kappa_z + z\kappa_y \\ \gamma^m_{xy} &= \frac{\partial U^m}{\partial y} + \frac{\partial V^m}{\partial x} &&= \gamma_y - z\kappa_x + \frac{\partial\psi}{\partial y}\kappa_x \\ \gamma^m_{xz} &= \frac{\partial U^m}{\partial z} + \frac{\partial W^m}{\partial x} &&= \gamma_z + y\kappa_x + \frac{\partial\psi}{\partial z}\kappa_x \end{aligned}\right\} \quad \Rightarrow \mathbf{e}^m_f = \mathbf{a}^m_f(y,z)\mathbf{e}_s(x) \tag{3.18}$$

with the new compatibility matrix (taking into account the shear correction parameters):

$$\mathbf{a}_f^m(y,z) = \begin{bmatrix} 1 & 0 & 0 & 0 & z & -y \\ 0 & k_y c_y(y,z) & 0 & -z + \dfrac{\partial \psi}{\partial y} & 0 & 0 \\ 0 & 0 & k_z c_z(y,z) & y + \dfrac{\partial \psi}{\partial z} & 0 & 0 \end{bmatrix} \tag{3.19}$$

The expression of Saint-Venant warping function and its derivatives for the rectangular cross-section can be found in Section 4.1. It is important to note that in the case of a solid cross-section, this approach using Saint-Venant warping function maintains the element DoFs at 12, but can not take into account the distortion phenomenon.

3.3.3 Enhanced field using Lagrange polynomials

As mentioned above, according to Saint-Venant theory the warping displacement is proportional to two parameters: the warping function $\psi(y,z)$ representing the warping profile over the cross-section and the parameter $\alpha(x)$ representing the warping distribution along the element axis. In other words, the warping displacement is a multiplication of the warping profile and the warping distribution. In 2012, Le Corvec [62] proposed a new way to interpolate these two parameters, rather than using the Saint-Venant warping function and the parameter $\alpha(x)$: several fixed points are defined in the axis direction x, with index i (Figure 7-5a), and then, in each of cross-section with index i, a grid of fixed points is defined in the direction y, z with index j, k respectively (Figure (Figure 7-5b)). It is very important to remark that the position of longitudinal interpolation points is independent of the Gauss points along the element axis of the Timoshenko multifiber beam.

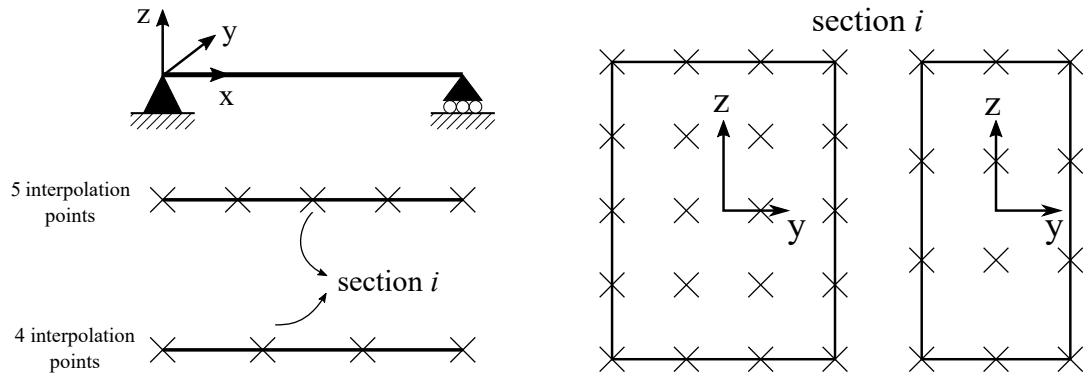

(a) Longitudinal interpolation points along the element axis.

(b) Sectional interpolation points over the rectangular cross-section.

Figure 3-6 – System of fixed interpolation points in the beam element.

Then, at any of these fixed interpolation points, with coordinate (x_i, y_j, z_k), *the en-*

hanced displacement values $\left(U^e_{ijk}, V^e_{ijk}, W^e_{ijk}\right)$ are defined as independent additional DoFs (Figure 3-7). These enhanced displacement values may have one to three components: U^e_{ijk} in the axial direction representing the warping field and the two V^e_{ijk}, W^e_{ijk} in transversal direction representing the distortion field.

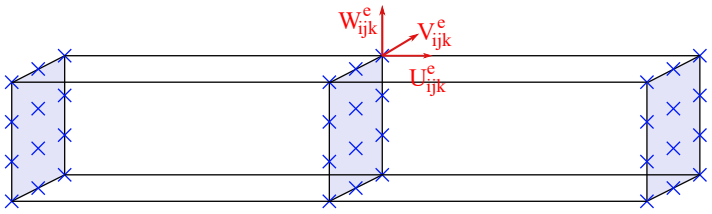

Figure 3-7 – Enhanced displacement values defined as independent additional DoFs.

In order to interpolate these enhanced displacement values to the enhanced displacement of any material point, the Lagrange polynomials are defined for the interpolation functions of the warping distribution and the warping profile. The reason for this choice is that the Lagrange polynomials are continuously differentiable, so they respond to the requirement to evaluate the material strain, as shown in Equation (3.18), similar to the Saint-Venant warping function. Moreover, Lagrange polynomials are applicable to any shape of section and any material response, thus they are general enough for further studies to be carried out.

The distribution of warping displacement is defined over a grid of n_w points along the element axis and is described with 1D interpolation function $L_i(x)$. The degree of interpolation function depends on the number of interpolation points n_w: quadratic if $n_w = 3$, cubic if $n_w = 4$ or even quartic if $n_w = 5$ (Figure 3-8).

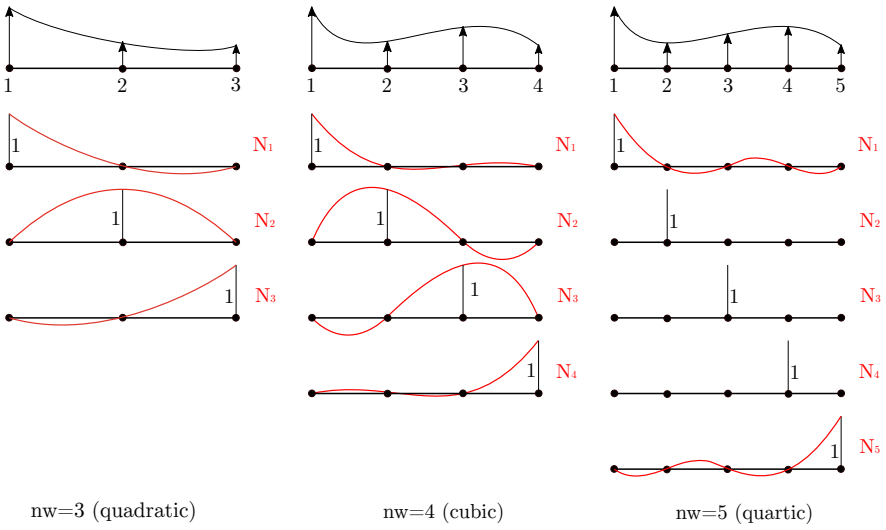

Figure 3-8 – Lagrange interpolation polynomials for one dimensional finite elements.

The warping profile is defined by a grid of s_w points distributed over the section i and is described using the 2D interpolation function $S_{jk}(y,z)$. This 2D interpolation function can be achieved by simple products of 1D Lagrange polynomials in the two coordinates (Figure 3-9). At section i, each interpolation point is accompanied by its 2D Lagrange polynomials $S_{jk}(y,z)$, this results in a total of s_w 2D polynomials over the cross-section.

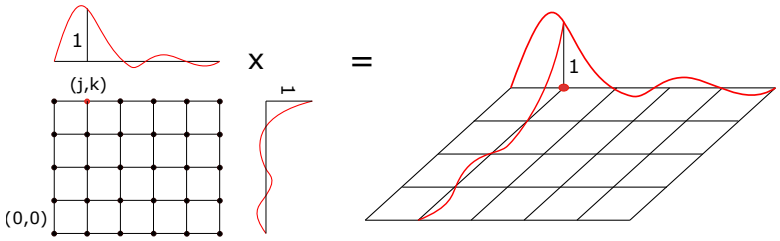

Figure 3-9 – Generation of Lagrange interpolation polynomials for 2D finite elements.

3.3.3.1 Interpolation of enhanced material displacement

Using the system above, at interpolated section x_i, the enhanced material displacement are defined as follows:

$$U^e(x_i,y,z) = \sum_{jk=1}^{s_w} S_{jk}(y,z)U^e_{ijk} = \bar{\mathbf{S}}(y,z)\mathbf{U}^e_i \tag{3.20a}$$

$$V^e(x_i,y,z) = \sum_{jk=1}^{s_w} S_{jk}(y,z)V^e_{ijk} = \bar{\mathbf{S}}(y,z)\mathbf{V}^e_i \tag{3.20b}$$

$$W^e(x_i,y,z) = \sum_{jk=1}^{s_w} S_{jk}(y,z)W^e_{ijk} = \bar{\mathbf{S}}(y,z)\mathbf{W}^e_i \tag{3.20c}$$

where $\bar{\mathbf{S}}(y,z) = \begin{pmatrix} S_1 & \dots & S_{jk} & \dots & S_{sw} \end{pmatrix}$ is a row vector of s_w columns $(1 \times s_w)$ containing the 2D interpolation functions of each interpolation point; $\mathbf{U}^e_i = \begin{pmatrix} U^e_{i1} & \dots & U^e_{ijk} & \dots & U^e_{isw} \end{pmatrix}^T$ is a column vector $(s_w \times 1)$ containing the axial enhanced displacement values at section i; similar definition can be applied for 2 vectors $\mathbf{V}^e_i$ and $\mathbf{W}^e_i$. Then, the enhanced material displacement at any points of element can be expressed as:

$$U^e(x,y,z) = \sum_{i=1}^{n_w} L_i(x)U^e(x_i,y,z) = \hat{\mathbf{L}}(x)\hat{\mathbf{S}}(y,z)\mathbf{U}^e \tag{3.21a}$$

$$V^e(x,y,z) = \sum_{i=1}^{n_w} L_i(x)V^e(x_i,y,z) = \hat{\mathbf{L}}(x)\hat{\mathbf{S}}(y,z)\mathbf{V}^e \tag{3.21b}$$

$$W^e(x,y,z) = \sum_{i=1}^{n_w} L_i(x)W^e(x_i,y,z) = \hat{\mathbf{L}}(x)\hat{\mathbf{S}}(y,z)\mathbf{W}^e \tag{3.21c}$$

where $\hat{\mathbf{L}}(x) = \begin{pmatrix} L_1 & \dots & L_i & \dots & L_{nw} \end{pmatrix}$ is a row vector $(1 \times n_w)$ containing the 1D interpolation functions of each interpolation point; $\mathbf{U}^e = \begin{pmatrix} U_1^{eT} & \dots & U_i^{eT} & \dots & U_{sw.nw}^{eT} \end{pmatrix}^T$ is a column vector $(n_w.s_w \times 1)$ containing the axial enhanced displacement values of element; similar definition can be applied for 2 vectors $\mathbf{V}^e$ and $\mathbf{W}^e$; $\hat{\mathbf{S}}(y,z)$ is a matrix $(n_w \times n_w.s_w)$ containing a number of n_w vector $\bar{\mathbf{S}}(y,z)$ and several zero row vectors $(1 \times s_w)$:

$$\hat{\mathbf{S}}(y,z) = \begin{bmatrix} \bar{\mathbf{S}}(y,z) & \mathbf{0}_{sw} & \dots & \mathbf{0}_{sw} \\ \mathbf{0}_{sw} & \bar{\mathbf{S}}(y,z) & \dots & \mathbf{0}_{sw} \\ \vdots & \vdots & \ddots & \vdots \\ \mathbf{0}_{sw} & \mathbf{0}_{sw} & \dots & \bar{\mathbf{S}}(y,z) \end{bmatrix} \tag{3.22}$$

3.3.3.2 Derivation of enhanced material strain

From the definition of enhanced displacements field, a complete strain state of 6 components for the enhanced material strains can be established as follows:

$$\varepsilon_{xx}^e = \frac{\partial U^e}{\partial x} = \frac{\partial \hat{\mathbf{L}}(x)}{\partial x}\hat{\mathbf{S}}(y,z)\mathbf{U}^e \tag{3.23a}$$

$$\varepsilon_{yy}^e = \frac{\partial V^e}{\partial y} = \hat{\mathbf{L}}(x)\frac{\partial \hat{\mathbf{S}}(y,z)}{\partial y}\mathbf{V}^e \tag{3.23b}$$

$$\varepsilon_{zz}^e = \frac{\partial W^e}{\partial z} = \hat{\mathbf{L}}(x)\frac{\partial \hat{\mathbf{S}}(y,z)}{\partial z}\mathbf{W}^e \tag{3.23c}$$

$$\gamma_{xy}^e = \frac{\partial U^e}{\partial y} + \frac{\partial V^e}{\partial x} = \hat{\mathbf{L}}(x)\frac{\partial \hat{\mathbf{S}}(y,z)}{\partial y}\mathbf{U}^e + \frac{\partial \hat{\mathbf{L}}(x)}{\partial x}\hat{\mathbf{S}}(y,z)\mathbf{V}^e \tag{3.23d}$$

$$\gamma_{xz}^e = \frac{\partial U^e}{\partial z} + \frac{\partial W^e}{\partial x} = \hat{\mathbf{L}}(x)\frac{\partial \hat{\mathbf{S}}(y,z)}{\partial z}\mathbf{U}^e + \frac{\partial \hat{\mathbf{L}}(x)}{\partial x}\hat{\mathbf{S}}(y,z)\mathbf{W}^e \tag{3.23e}$$

$$\gamma_{yz}^e = \frac{\partial V^e}{\partial z} + \frac{\partial W^e}{\partial y} = \hat{\mathbf{L}}(x)\frac{\partial \hat{\mathbf{S}}(y,z)}{\partial z}\mathbf{V}^e + \hat{\mathbf{L}}(x)\frac{\partial \hat{\mathbf{S}}(y,z)}{\partial y}\mathbf{W}^e \tag{3.23f}$$

Three column vectors $\mathbf{U}^e$, $\mathbf{V}^e$ and $\mathbf{W}^e$ can be grouped in only one column vectors $\mathbf{d}^e = \begin{pmatrix} \mathbf{U}^{eT} & \mathbf{V}^{eT} & \mathbf{W}^{eT} \end{pmatrix}^T$ of $(3.n_w.s_w \times 1)$, which represents the enhanced displacement values of element. The additional DoFs of the enhanced field is therefore equal to $3.n_w.s_w$. Equation (3.23) can be re-written as follows:

$$\mathbf{e}_f^{e*}(x,y,z) = \mathbf{a}_f^{e*}(x,y,z)\mathbf{d}^e \tag{3.24}$$

Where the expression of the enhanced compatibility matrix $\mathbf{a}_f^{e*}(x,y,z)$ is quite complex:

$$\mathbf{a}_f^{e*}(x,y,z) = \frac{\partial \mathbf{L}^*(x)}{\partial x}\mathbf{S}_x^*(y,z) + \mathbf{L}^*(x)\mathbf{S}_{yz}^*(y,z) \tag{3.25}$$

where $\mathbf{L}^*(x)$ is a longitudinal interpolation matrix of $(6 \times 6.3.n_w)$, containing the 1D Lagrange polynomial at section i:

$$\mathbf{L}^*(x) = \begin{bmatrix} \mathbf{L}_1^*(x) & \dots & \mathbf{L}_i^*(x) & \dots \mathbf{L}_{nw}^*(x) \end{bmatrix}$$

and

$$\mathbf{L}_i(x) = \begin{bmatrix} L_i(x) & 0 & \dots & 0 & L_i(x) & 0 & \dots & 0 & L_i(x) & 0 & \dots & 0 \\ 0 & L_i(x) & \dots & 0 & 0 & L_i(x) & \dots & 0 & 0 & L_i(x) & \dots & 0 \\ \vdots & \vdots & \ddots & \vdots & \vdots & \vdots & \ddots & \vdots & \vdots & \vdots & \ddots & \vdots \\ 0 & 0 & \dots & L_i(x) & 0 & 0 & \dots & L_i(x) & 0 & 0 & \dots & L_i(x) \end{bmatrix} \tag{3.26}$$

The sectional interpolation matrices $\mathbf{S}_x^*(y,z)$ has $6.3.n_w$ rows and $3.s_w.n_w$ columns:

$$\mathbf{S}_x^*(y,z) = \begin{bmatrix} \hat{\mathbf{S}}_x^*(y,z) & \mathbf{0}_w & \dots & \mathbf{0}_w \\ \mathbf{0}_w & \hat{\mathbf{S}}_x^*(y,z) & \dots & \mathbf{0}_w \\ \vdots & \vdots & \ddots & \vdots \\ \mathbf{0}_w & \mathbf{0}_w & \dots & \hat{\mathbf{S}}_x^*(y,z) \end{bmatrix} \quad \text{and} \quad \hat{\mathbf{S}}_x^*(y,z) = \begin{bmatrix} \mathbf{S}_x^{u*}(y,z) & \mathbf{0}_{6sw} & \mathbf{0}_{6sw} \\ \mathbf{0}_{6sw} & \mathbf{S}_x^{v*}(y,z) & \mathbf{0}_{6sw} \\ \mathbf{0}_{6sw} & \mathbf{0}_{6sw} & \mathbf{S}_x^{w*}(y,z) \end{bmatrix} \tag{3.27}$$

where $\mathbf{0}_w$ is a zero matrix of $(18 \times 3.s_w)$; $\mathbf{0}_{6sw}$ is a zero matrix of $(6 \times s_w)$; $\mathbf{S}_x^{u*}(y,z)$, $\mathbf{S}_x^{v*}(y,z)$ and $\mathbf{S}_x^{w*}(y,z)$ are three matrices of $(6 \times s_w)$ containing the row vector $\bar{\mathbf{S}}(y,z)$ in Equation (3.20) and the zero row vector of $(1 \times s_w)$:

$$\mathbf{S}_x^{u*}(y,z) = \begin{bmatrix} \bar{\mathbf{S}}(y,z) \\ \mathbf{0}_{sw} \\ \mathbf{0}_{sw} \\ \mathbf{0}_{sw} \\ \mathbf{0}_{sw} \\ \mathbf{0}_{sw} \end{bmatrix}; \quad \mathbf{S}_x^{v*}(y,z) = \begin{bmatrix} \mathbf{0}_{sw} \\ \mathbf{0}_{sw} \\ \mathbf{0}_{sw} \\ \bar{\mathbf{S}}(y,z) \\ \mathbf{0}_{sw} \\ \mathbf{0}_{sw} \end{bmatrix}; \quad \mathbf{S}_x^{w*}(y,z) = \begin{bmatrix} \mathbf{0}_{sw} \\ \mathbf{0}_{sw} \\ \mathbf{0}_{sw} \\ \mathbf{0}_{sw} \\ \bar{\mathbf{S}}(y,z) \\ \mathbf{0}_{sw} \end{bmatrix}; \tag{3.28}$$

Similar to the sectional interpolation matrices $\mathbf{S}_{yz}^*(y,z)$:

$$\mathbf{S}_{yz}^*(y,z) = \begin{bmatrix} \hat{\mathbf{S}}_{yz}^*(y,z) & \mathbf{0}_w & \dots & \mathbf{0}_w \\ \mathbf{0}_w & \hat{\mathbf{S}}_{yz}^*(y,z) & \dots & \mathbf{0}_w \\ \vdots & \vdots & \ddots & \vdots \\ \mathbf{0}_w & \mathbf{0}_w & \dots & \hat{\mathbf{S}}_{yz}^*(y,z) \end{bmatrix}; \quad \text{and} \quad \hat{\mathbf{S}}_{yz}^*(y,z) = \begin{bmatrix} \mathbf{S}_{yz}^{u*}(y,z) & \mathbf{0}_{6sw} & \mathbf{0}_{6sw} \\ \mathbf{0}_{6sw} & \mathbf{S}_{yz}^{v*}(y,z) & \mathbf{0}_{6sw} \\ \mathbf{0}_{6sw} & \mathbf{0}_{6sw} & \mathbf{S}_{yz}^{w*}(y,z) \end{bmatrix} \tag{3.29}$$

with $\mathbf{S}_{yz}^{u*}(y,z)$, $\mathbf{S}_{yz}^{v*}(y,z)$ and $\mathbf{S}_{yz}^{w*}(y,z)$ are three matrices of $(6 \times s_w)$ containing the derivation with respect to y and z of the row vector $\bar{\mathbf{S}}(y,z)$ in Equation (3.20) and the zero row

vector of s_w columns:

$$\mathbf{S}_{yz}^{u*}(y,z) = \begin{bmatrix} \mathbf{0}_{sw} \\ \mathbf{0}_{sw} \\ \mathbf{0}_{sw} \\ \dfrac{\partial \bar{\mathbf{S}}(y,z)}{\partial y} \\ \dfrac{\partial \bar{\mathbf{S}}(y,z)}{\partial z} \\ \mathbf{0}_{sw} \end{bmatrix} ; \quad \mathbf{S}_{yz}^{v*}(y,z) = \begin{bmatrix} \mathbf{0}_{sw} \\ \dfrac{\partial \bar{\mathbf{S}}(y,z)}{\partial y} \\ \mathbf{0}_{sw} \\ \mathbf{0}_{sw} \\ \mathbf{0}_{sw} \\ \dfrac{\partial \bar{\mathbf{S}}(y,z)}{\partial z} \end{bmatrix} ; \quad \mathbf{S}_{yz}^{w*}(y,z) = \begin{bmatrix} \mathbf{0}_{sw} \\ \mathbf{0}_{sw} \\ \dfrac{\partial \bar{\mathbf{S}}(y,z)}{\partial z} \\ \mathbf{0}_{sw} \\ \mathbf{0}_{sw} \\ \dfrac{\partial \bar{\mathbf{S}}(y,z)}{\partial y} \end{bmatrix} \tag{3.30}$$

The superposition of enhanced material strain in Equation (3.23) into classical material strain gives the following kinematic relation:

$$\mathbf{e}_f^{m*}(x,y,z) = \mathbf{a}_f^{p*}(y,z)\mathbf{e}_s(x) + \mathbf{a}_f^{e*}(x,y,z)\mathbf{d}^e \tag{3.31}$$

where $\mathbf{e}_f^{m*}(x,y,z)$ is the total material strain of six components, $\mathbf{a}_f^{p*}(y,z)$ is the classical compatibility matrix modified from the compatibility matrix in Equation (3.12):

$$\mathbf{a}_f^{p*}(y,z) = \begin{bmatrix} 1 & 0 & 0 & 0 & z & -y \\ 0 & 0 & 0 & 0 & 0 & 0 \\ 0 & 0 & 0 & 0 & 0 & 0 \\ 0 & k_y c_y(y,z) & 0 & -z & 0 & 0 \\ 0 & 0 & k_z c_z(y,z) & y & 0 & 0 \\ 0 & 0 & 0 & 0 & 0 & 0 \end{bmatrix} \tag{3.32}$$

Equation (3.31) relates the total material strain to the classical generalized strains and the enhanced displacement values. This kinematic relation is general and can be used to take into account the distortion and warping phenomenon. However, in this work, only the warping phenomenon is considered while the distortion is neglected. As a result, the enhanced displacement values in the transversal directions V_{ijk}^e and W_{ijk}^e become zero, and the enhanced strain state has only 3 components similar to the classical one. The kinematic relation in Equation (3.31) can be re-written as follows:

$$\mathbf{e}_f^{m}(x,y,z) = \mathbf{a}_f^{p}(y,z)\mathbf{e}_s(x) + \mathbf{a}_f^{e}(x,y,z)\mathbf{U}^e \tag{3.33}$$

where the classical compatibility matrix $\mathbf{a}_f^{p}(y,z)$ is the same as in Equation (3.12); the

total material strain $\mathbf{e}_f^m(x,y,z)$ is reduced from 6 to 3 components:

$$\varepsilon_{xx}^m = \varepsilon_{xx}^p + \varepsilon_{xx}^e = \varepsilon_x - y\kappa_z + z\kappa_y + \frac{\partial \hat{\mathbf{L}}(x)}{\partial x}\hat{\mathbf{S}}(y,z)\mathbf{U}^e \tag{3.34a}$$

$$\gamma_{xy}^m = \gamma_{xy}^p + \gamma_{xy}^e = \gamma_y - z\kappa_x + \hat{\mathbf{L}}(x)\frac{\partial \hat{\mathbf{S}}(y,z)}{\partial y}\mathbf{U}^e \tag{3.34b}$$

$$\gamma_{xz}^m = \gamma_{xz}^p + \gamma_{xz}^e = \gamma_z + y\kappa_x + \hat{\mathbf{L}}(x)\frac{\partial \hat{\mathbf{S}}(y,z)}{\partial z}\mathbf{U}^e \tag{3.34c}$$

the enhanced compatibility matrix $\mathbf{a}_f^e(x,y,z)$ is modified from the matrix $\mathbf{a}_f^{e*}(x,y,z)$ in Equation (3.25):

$$\mathbf{a}_f^e(x,y,z) = \frac{\partial \mathbf{L}(x)}{\partial x}\mathbf{S}_x(y,z) + \mathbf{L}(x)\mathbf{S}_{yz}(y,z) \tag{3.35}$$

the sub-compatibility matrix $\mathbf{L}(x)$, containing 1D polynomials $L_i(x)$, is a longitudinal interpolation matrix of $(3 \times 3.3.n_w)$ modified from matrix $\mathbf{L}^*(x)$ in Equation (3.26); the sub-compatibility matrix $\mathbf{S}_x(x)$, containing 2D polynomials $S_i(x)$, is a sectional interpolation matrix of $(3.3.n_w \times s_w.n_w)$ modified from matrix $\mathbf{S}_x^*(x)$ in Equation (3.27); and the sub-compatibility matrix $\mathbf{S}_{yz}(x)$, containing the derivations with respect to y and z of 2D polynomials $S_i(x)$, is a sectional interpolation matrix of $(3.3.n_w \times s_w.n_w)$ modified from matrix $\mathbf{S}_{yz}^*(x)$ in Equation (3.29). The detailed expression of theses sub-compatibility matrix can be found in Appendix 7.2.

It is worth to note that, comparing to the total material strains built up using Saint-Venant warping function in Section 3.3.2, in this approach the enhanced terms $\frac{\partial \psi}{\partial y}\kappa_x$ and $\frac{\partial \psi}{\partial z}\kappa_x$ in shear strains are replaced by $\hat{\mathbf{L}}(x)\frac{\partial \hat{\mathbf{S}}(y,z)}{\partial y}\mathbf{U}^e$ and $\hat{\mathbf{L}}(x)\frac{\partial \hat{\mathbf{S}}(y,z)}{\partial z}\mathbf{U}^e$, respectively. Moreover, in the axial strain, an additional enhanced term $\frac{\partial \hat{\mathbf{L}}(x)}{\partial x}\hat{\mathbf{S}}(y,z)\mathbf{U}^e$ is added, which allows to calculate and represent the warping displacement profile and the additional normal stress due to warping in the case of shear effect.

Another important remark is that the number of DoFs in this approach is increased considerably. While Saint-Venant warping function approach maintains the element DoFs at 12, this method requires a total number of DoFs equal to $12 + n_w.s_w$, where $n_w.s_w$ is the total number of fixed interpolation points. If distortion phenomenon is included, the number of additional DoFs increases to $3.n_w.s_w$, making a total of $12 + 3.n_w.s_w$ DoFs in each element. The computational cost is therefore much more expensive.

3.4 Variational formulation

Once the material strain vector $\mathbf{e}_f^m$ is obtained at each material point, an appropriate behavior constitutive model is applied in order to determine the material stresses, which are collected in a single stress vector $\mathbf{s}_f^m = \begin{pmatrix} \sigma_{xx}^m & \tau_{xy}^m & \tau_{xz}^m \end{pmatrix}^T$. This constitutive relation is expressed as follows:

$$\delta \mathbf{s}_f^m = \mathbf{k}_f \delta \mathbf{e}_f^m \tag{3.36}$$

where $\mathbf{k}_f$ is the material stiffness matrix, which is determined in Section 3.5.

Next, the element equilibrium is considered between internal and external potential energy. Let the element be subjected by a virtual displacement δd, then the principle of virtual work gives an equation between internal and external energy:

$$\delta \mathbf{W}_i = \delta \mathbf{W}_e \Rightarrow \iiint_V \delta \mathbf{e}_f^{mT} \mathbf{s}_f^m dV = \delta \mathbf{q}_e^{mT} \mathbf{Q}_e^m + \int_L \delta \mathbf{d}_s^m \mathbf{P}_u^m dx \tag{3.37}$$

where the internal virtual work is represented by the left-hand side, while the external virtual work is expressed by the right-hand; $\mathbf{Q}_e^m$ is the external nodal forces and $\mathbf{P}_u^m$ is the external uniform loading. Depending on the approach of enhanced field, two different cases are investigated as follows:

3.4.1 Enhanced field using Saint-Venant warping function

The left-hand side of Equation (3.37) represents the equilibrium conditions at sectional level. Using Equation (3.18), the variation of internal work can be expressed as follows:

$$\delta \mathbf{W}_i = \iiint_V \delta \mathbf{e}_f^{mT} \mathbf{s}_f^m dV = \iiint_V \delta \mathbf{e}_s^T(x) \mathbf{a}_f^{mT}(y,z) \mathbf{s}_f^m dV \tag{3.38}$$

As the term $\delta \mathbf{e}_s(x)$ is a function of the cross-section coordinate x and $\mathbf{a}_f^m(y,z)^T \mathbf{s}_f^m$ is a function of the fiber coordinates y and z, the variation of virtual internal work can be decomposed into an integral over the element length and another over the cross-section area:

$$\delta \mathbf{W}_i = \int_L \delta \mathbf{e}_s^T(x) \left(\iint_A \mathbf{a}_f^{mT}(y,z) \mathbf{s}_f^m dA \right) dx \tag{3.39}$$

At sectional level, the *generalized stresses* (or *sectional forces*) can be defined as an integral over the cross-section area of the stress field:

$$\mathbf{D}_s(x) = \iint_A \mathbf{a}_f^m(y,z)^T \mathbf{s}_f^m dA \tag{3.40}$$

By exploiting the expression of $\mathbf{a}_f^m(y,z)$ in Equation (3.19) and $\mathbf{s}_f^m$, we obtain, in an explicit manner, a vector of sectional forces containing 6 components:

$$\mathbf{D}_s(x) = \begin{pmatrix} N_x \\ V_y \\ V_z \\ M_x \\ M_y \\ M_z \end{pmatrix} = \begin{pmatrix} \iint_A \sigma_{xx} dA \\ \iint_A k_y c_y(y,z) \tau_{xy} dA \\ \iint_A k_z c_z(y,z) \tau_{xz} dA \\ \iint_A \left[\left(y + \dfrac{\partial \psi}{\partial z} \right) \tau_{xz} - \left(z - \dfrac{\partial \psi}{\partial y} \right) \tau_{xy} \right] dA \\ \iint_A z \sigma_{xx} dA \\ - \iint_A y \sigma_{xx} dA \end{pmatrix} \tag{3.41}$$

As we see, all the internal actions can be determined from the stress resultants. We can observe that the expression of the internal torsional moment M_x has been enhanced by the introduction of the warping function ψ, which will affect the values of the twist κ_x and the twist angle θ_x, consequently. Equation (3.40) can be re-written with the aid of the constitutive relation in Equation (3.36):

$$\mathbf{D}_s(x) = \iint_A \mathbf{a}_f^{mT}(y,z) \mathbf{k}_f \mathbf{e}_f^m dA = \left(\iint_A \mathbf{a}_f^{mT}(y,z) \mathbf{k}_f \mathbf{a}_f^m(y,z) dA \right) \mathbf{e}_s(x) \tag{3.42}$$

the sectional stiffness matrix can thus be defined as follows:

$$\mathbf{K}_s = \iint_A \mathbf{a}_f^{mT}(y,z) \mathbf{k}_f \mathbf{a}_f^m(y,z) dA \tag{3.43}$$

Therefore, the equilibrium at sectional level between the generalized stresses and the generalized strain can be expressed as follows:

$$\delta \mathbf{D}_s(x) = \mathbf{K}_s \delta \mathbf{e}_s(x) \tag{3.44}$$

3.4.1.1 Element state determination

The right-hand side of Equation (3.37) can be exploited with the aid of Equation (3.2) as follows:

$$\delta \mathbf{W}_e = \delta \mathbf{q}_e^T \mathbf{Q}_e + \int_L \delta \mathbf{d}_s^T \mathbf{P}_u dx = \delta \mathbf{q}_e^T \mathbf{Q}_e + \int_L \delta \mathbf{q}_e^T \mathbf{N}_s^T \mathbf{P}_u^d x = \delta \mathbf{q}_e^T \left(\mathbf{Q}_e + \int_L \mathbf{N}_s^T \mathbf{P}_u dx \right) \tag{3.45}$$

Hence, the virtual work equilibrium from Equation (3.37) has now become:

$$\int_L \delta \mathbf{e}_s^T \mathbf{D}_s dx = \delta \mathbf{q}_e^T \left(\mathbf{Q}_e + \int_L \mathbf{N}_s^T \mathbf{P}_u dx \right) \tag{3.46}$$

Using the relation from Equation (3.14) and (3.44), we obtain:

$$\begin{aligned} \delta \mathbf{q}_e^T \left(\int_L \mathbf{B}_s^T \mathbf{K}_s \mathbf{B}_s dx \right) \mathbf{q}_e &= \delta \mathbf{q}_e^T \left(\mathbf{Q}_e + \int_L \mathbf{N}_s^T \mathbf{P}_u dx \right) \\ \Rightarrow \left(\int_L \mathbf{B}_s^T \mathbf{K}_s \mathbf{B}_s dx \right) \mathbf{q}_e &= \mathbf{Q}_e + \int_L \mathbf{N}_s^T \mathbf{P}_u dx \end{aligned} \tag{3.47}$$

The *element stiffness matrix* can be defined as:

$$\mathbf{K}_e = \int_L \mathbf{B}_s^T \mathbf{K}_s \mathbf{B}_s dx \tag{3.48}$$

And the element equilibrium becomes:

$$\mathbf{K}_e \mathbf{q}_e = \mathbf{Q}_e + \int_L \mathbf{N}_s^T \mathbf{P}_u dx \tag{3.49}$$

The element stiffness matrix $\mathbf{K}_e$ and the nodal forces $\mathbf{Q}_e$ are then assembled into the structure stiffness matrix and nodal forces vector using standard procedures of structural analysis. All the necessary equations for the element state determination are completed.

3.4.2 Enhanced field using Lagrange polynomials

While the number of DoFs in the latter approach is maintained at 12 for each element, in this approach, the number of DoFs increases considerably to $n_w.s_w$ (or $3.n_w.s_w$ if distortion is considered), as mentioned in Section 3.3.3. With the present of additional DoFs, all the variables are now separated into two sets: the *basic set* of 12 DoFs and the *additional set* of $n_w.s_w$ (or $3.n_w.s_w$) DoFs. It is worth to note that the basic set is also a combined of classical and enhanced displacement/strain fields.

3.4.2.1 Sectional state determination

Considering the sectional equilibrium in the left-hand side of Equation (3.37) in the case that the distortion phenomenon is neglected, the following expression of the variation of virtual internal work is obtained using Equation (3.34):

$$\delta \mathbf{W}_i = \iiint_V \delta \mathbf{e}_f^{mT} \mathbf{s}_f^m dV = \iiint_V \delta \left(\mathbf{e}_s^T(x) \mathbf{a}_f^{pT}(y,z) + \mathbf{U}^{eT} \mathbf{a}_f^{eT}(x,y,z) \right) \mathbf{s}_f^m dV \tag{3.50}$$

Using the expression of $\mathbf{a}_f^e(x,y,z)$ in Equation (3.35), Equation (3.50) becomes:

$$\begin{aligned} \delta \mathbf{W}_i &= \int_L \delta \mathbf{e}_s^T(x) \left(\iint_A \mathbf{a}_f^{pT}(y,z) \mathbf{s}_f^m dA \right) dx \\ &+ \delta \mathbf{U}^{eT} \left[\int_L \frac{\partial \mathbf{L}^T(x)}{\partial x} \left(\iint_A \mathbf{S}_x^T(y,z) \mathbf{s}_f^m dA \right) dx + \int_L \mathbf{L}^T(x) \left(\iint_A \mathbf{S}_{yz}^T(y,z) \mathbf{s}_f^m dA \right) dx \right] \end{aligned} \tag{3.51}$$

Corresponding to the sectional forces in Equation (3.40), the "basic" sectional forces in this approach can be defined as follows:

$$\mathbf{D}_s^b(x) = \iint_A \mathbf{a}_f^p(y,z)^T \mathbf{s}_f^m dA \tag{3.52}$$

This basic sectional forces can be expressed as a combination of the classical field and the enhanced one with the aid of the constitutive relation in Equation (3.36):

$$\begin{aligned} \mathbf{D}_s^b(x) &= \left(\iint_A \mathbf{a}_f^{pT}(y,z) \mathbf{k}_f \mathbf{a}_f^p(y,z) dA \right) \mathbf{e}_s(x) \\ &+ \left[\left(\iint_A \mathbf{a}_f^{pT}(y,z) \mathbf{k}_f \mathbf{S}_x(y,z) dA \right) \frac{\partial \mathbf{L}(x)}{\partial x} + \left(\iint_A \mathbf{a}_f^{pT}(y,z) \mathbf{k}_f \mathbf{S}_{yz}(y,z) dA \right) \mathbf{L}(x) \right] \mathbf{U}^e \end{aligned} \tag{3.53}$$

Due to the present of additional DoFs, the following additional sectional forces are also defined:

$$\mathbf{D}_s^{ax}(x) = \iint_A \mathbf{S}_x^T(y,z) \mathbf{s}_f^m dA \tag{3.54a}$$

$$\mathbf{D}_s^{ayz}(x) = \iint_A \mathbf{S}_{yz}^T(y,z) \mathbf{s}_f^m dA \tag{3.54b}$$

which can also be exploited as follows:

$$\mathbf{D}_s^{ax}(x) = \left(\iint_A \mathbf{S}_x^T(y,z)\mathbf{k}_f\mathbf{a}_f^p dA\right)\mathbf{e}_s(x) + \left[\left(\iint_A \mathbf{S}_x^T(y,z)\mathbf{k}_f\mathbf{S}_x(y,z)dA\right)\frac{\partial\mathbf{L}(x)}{\partial x} + \left(\iint_A \mathbf{S}_x^T(y,z)\mathbf{k}_f\mathbf{S}_{yz}(y,z)dA\right)\mathbf{L}(x)\right]\mathbf{U}^e \tag{3.55a}$$

$$\mathbf{D}_s^{ayz}(x) = \left(\iint_A \mathbf{S}_{yz}^T(y,z)\mathbf{k}_f\mathbf{a}_f^p dA\right)\mathbf{e}_s(x) + \left[\left(\iint_A \mathbf{S}_{yz}^T(y,z)\mathbf{k}_f\mathbf{S}_x(y,z)dA\right)\frac{\partial\mathbf{L}(x)}{\partial x} + \left(\iint_A \mathbf{S}_{yz}^T(y,z)\mathbf{k}_f\mathbf{S}_{yz}(y,z)dA\right)\mathbf{L}(x)\right]\mathbf{U}^e \tag{3.55b}$$

From these expressions of sectional forces, a system of 9 sectional stiffness matrices can be defined as follows:

$$\mathbf{K}_s^{bb} = \iint_A \mathbf{a}_f^{pT}\mathbf{k}_f\mathbf{a}_f^p dA \tag{3.56a}$$

$$\mathbf{K}_s^{bax} = \iint_A \mathbf{a}_f^{pT}\mathbf{k}_f\mathbf{S}_x dA \tag{3.56b}$$

$$\mathbf{K}_s^{bayz} = \iint_A \mathbf{a}_f^{pT}\mathbf{k}_f\mathbf{S}_{yz} dA \tag{3.56c}$$

$$\mathbf{K}_s^{axb} = \iint_A \mathbf{S}_x^T\mathbf{k}_f\mathbf{a}_f^p dA \tag{3.56d}$$

$$\mathbf{K}_s^{ax} = \iint_A \mathbf{S}_x^T\mathbf{k}_f\mathbf{S}_x dA \tag{3.56e}$$

$$\mathbf{K}_s^{axyz} = \iint_A \mathbf{S}_x^T\mathbf{k}_f\mathbf{S}_{yz} dA \tag{3.56f}$$

$$\mathbf{K}_s^{ayzb} = \iint_A \mathbf{S}_{yz}^T\mathbf{k}_f\mathbf{a}_f^p dA \tag{3.56g}$$

$$\mathbf{K}_s^{ayzx} = \iint_A \mathbf{S}_{yz}^T\mathbf{k}_f\mathbf{S}_x dA \tag{3.56h}$$

$$\mathbf{K}_s^{ayz} = \iint_A \mathbf{S}_{yz}^T\mathbf{k}_f\mathbf{S}_{yz} dA \tag{3.56i}$$

The expression of the variation of internal virtual work in Equation (3.50) can be re-written as follows:

$$\delta\mathbf{W}_i = \int_L \delta\mathbf{e}_s^T(x)\mathbf{D}_s^b(x)dx + \left(\int_L \frac{\partial\mathbf{L}^T(x)}{\partial x}\mathbf{D}_s^{ax}(x)dx + \int_L \mathbf{L}^T(x)\mathbf{D}_s^{ayz}(x)dx\right)\delta\mathbf{d}^{eT} \tag{3.57}$$

3.4.2.2 Element state determination

The right-hand side of Equation (3.37) is expressed as:

$$\delta \mathbf{W}_e = \delta \mathbf{q}_e^{mT} \mathbf{Q}_e^m + \int_L \delta \mathbf{d}_s^{mT}(x) \mathbf{P}_u^m dx \tag{3.58}$$

where the nodal displacements $\mathbf{q}_e^m$ is expressed as: $\mathbf{q}_e^m = \begin{pmatrix} \mathbf{q}_e \\ \mathbf{U}^e \end{pmatrix}$, containing the classical nodal displacements $\mathbf{q}_e$ of 12 DoFs and the enhanced displacement values $\mathbf{U}^e$ of $n_w.s_w$ DoFs. Similarly, the generalized displacements $\mathbf{d}_s^m(x)$, the external nodal forces $\mathbf{Q}_e^m$ and the external uniform loading $\mathbf{P}_u^m$ must also be decomposed into two parts: $\mathbf{d}_s^m(x) = \begin{pmatrix} \mathbf{d}_s(x) \\ \mathbf{d}_s^e(x) \end{pmatrix}$, $\mathbf{Q}_e^m = \begin{pmatrix} \mathbf{Q}_e \\ \mathbf{Q}_e^e \end{pmatrix}$, $\mathbf{P}_u^m = \begin{pmatrix} \mathbf{P}_u \\ \mathbf{P}_u^e \end{pmatrix}$. Since all the sections are assumed *free to warp*, the additional forces (or warping forces in the case that only warping is taken into account) $\mathbf{Q}_e^e$ and $\mathbf{P}_u^e$ are zero to ensure the condition of element equilibrium.

Using Equation (3.57) and (3.58), the basic part of the element equilibrium can be expressed as follows:

$$\int_L \delta \mathbf{e}_s^T(x) \mathbf{D}_s^b(x) dx = \delta \mathbf{q}_e^T \mathbf{Q}_e + \int_L \delta \mathbf{d}_s^T(x) \mathbf{P}_u dx \tag{3.59}$$

from Equation (3.2) and (3.14):

$$\begin{aligned} \int_L \delta \mathbf{q}_e^T \mathbf{B}_s^T \mathbf{D}_s^b dx &= \delta \mathbf{q}_e^T \mathbf{Q}_e + \delta \mathbf{q}_e^T \int_L \delta \mathbf{N}_s^T \mathbf{P}_u \\ \Rightarrow \int_L \mathbf{B}_s^T \mathbf{D}_s^b dx &= \mathbf{Q}_e + \int_L \mathbf{N}_s^T \mathbf{P} dx \end{aligned} \tag{3.60}$$

Similarly for the additional part, from Equation (3.57) and (3.58):

$$\begin{aligned} \left(\int_L \frac{\partial \mathbf{L}^T(x)}{\partial x} \mathbf{D}_s^{ax}(x) dx + \int_L \mathbf{L}^T(x) \mathbf{D}_s^{ayz}(x) dx \right) \delta \mathbf{U}^{eT} &= 0 \\ \Rightarrow \int_L \frac{\partial \mathbf{L}(x)}{\partial x} \mathbf{D}_s^{ax}(x) dx + \int_L \mathbf{L}(x) \mathbf{D}_s^{ayz}(x) dx &= 0 \end{aligned} \tag{3.61}$$

Finally, from 2 equations (3.60) and (3.61), the right-hand side of Equation (3.37) can

be expressed as follows:

$$\begin{bmatrix} \mathbf{K}_e^{bb} & \mathbf{K}_e^{ba} \\ \mathbf{K}_e^{ab} & \mathbf{K}_e^{aa} \end{bmatrix} \begin{pmatrix} \mathbf{q}_e \\ \mathbf{U}^e \end{pmatrix} = \begin{pmatrix} \mathbf{Q}_e + \int_L \mathbf{N}_s^T \mathbf{P}_u dx \\ 0 \end{pmatrix} \tag{3.62}$$

where the matrix components are constructed from the interpolation functions and the sectional stiffness matrix in Equation (3.56):

$$\begin{aligned} \mathbf{K}_e^{bb} &= \int_L \mathbf{B}_s^T \mathbf{K}_s^{bb} \mathbf{B}_s dx \\ \mathbf{K}_e^{ba} &= \int_L \mathbf{B}_s^T \left(\mathbf{K}_s^{bax} \frac{\partial \mathbf{L}(x)}{\partial x} + \mathbf{K}_s^{bayz} \mathbf{L}(x) \right) dx \\ \mathbf{K}_e^{ab} &= \int_L \left(\frac{\partial \mathbf{L}(x)^T}{\partial x} \mathbf{K}_s^{bax} + \mathbf{L}(x)^T \mathbf{K}_s^{bayz} \right) \mathbf{B}_s dx \\ \mathbf{K}_e^{aa} &= \int_L \frac{\partial \mathbf{L}(x)^T}{\partial x} \left(\mathbf{K}_s^{ax} \frac{\partial \mathbf{L}(x)}{\partial x} + \mathbf{K}_s^{abyz} \mathbf{L}(x) \right) dx \\ &+ \int_L \mathbf{L}(x)^T \left(\mathbf{K}_s^{ayzx} \frac{\partial \mathbf{L}(x)}{\partial x} + \mathbf{K}_s^{ayz} \mathbf{L}(x) \right) dx \end{aligned} \tag{3.63}$$

A static condensation is applied in order to obtain the final expression of equilibrium conditions at element level, from Equation (3.62) the enhanced displacement values can be evaluated as follows:

$$\begin{aligned} \mathbf{K}_e^{ab} \mathbf{q}_e + \mathbf{K}_e^{aa} \mathbf{U}^e = 0 \\ \Rightarrow \mathbf{U}^e = - \left(\mathbf{K}_e^{aa} \right)^{-1} \mathbf{K}_e^{ab} \mathbf{q}_e \end{aligned} \tag{3.64}$$

As a result:

$$\begin{aligned} \mathbf{K}_e^{bb} \mathbf{q}_e + \mathbf{K}_e^{ba} \mathbf{U}^e &= \mathbf{Q}_e + \int_L \mathbf{N}_s^T \mathbf{P}_u dx \\ \mathbf{K}_e^{bb} \mathbf{q}_e - \mathbf{K}_e^{ba} \left(\mathbf{K}_e^{aa} \right)^{-1} \mathbf{K}_e^{ab} \mathbf{q}_e &= \mathbf{Q}_e + \int_L \mathbf{N}_s^T \mathbf{P}_u dx \\ \Rightarrow \mathbf{K}_e \mathbf{q}_e &= \mathbf{Q}_e + \int_L \mathbf{N}_s^T \mathbf{P}_u dx \end{aligned} \tag{3.65}$$

with the expression of the element stiffness matrix as follows:

$$\mathbf{K}_e = \mathbf{K}_e^{bb} - \mathbf{K}_e^{ba} \left(\mathbf{K}_e^{aa} \right)^{-1} \mathbf{K}_e^{ab} \tag{3.66}$$

3.4.2.3 Orthogonality condition

The rigid body movements are described by the displacement vector $\mathbf{d}_f^p(x,y,z)$, consisted to the generalized displacements $\mathbf{d}_s(x)$. When the displacement field is enhanced with $\mathbf{d}_f^e(x,y,z)$, this vector can reproduce a new generalized field that coincides with the previous one. In other words, the generalized displacements field can be reproduced by both the classical plane-section field and the enhanced warping-distortion field, and consequently create a field of redundancy on the total displacement, which does not guarantee a unique displacement solution [3]. In order to avoid this possible redundancy, the enhanced displacement field $\mathbf{d}_f^e(x,y,z)$ must be free of rigid body mode, or orthogonal to the classical displacement vector $\mathbf{d}_f^p(x,y,z)$ in other words (Figure 3-10).

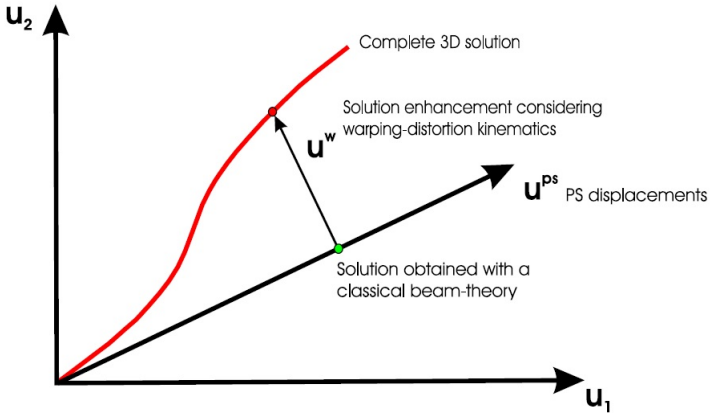

Figure 3-10 – Orthogonality condition of displacement field [3].

Le Corvec [62] used a projection matrix $\mathbf{P}_r$ to enforce the orthogonality of the sectional interpolation functions $S_{jk}(y,z)$ to the classical field $\mathbf{d}_f^p(x,y,z)$. This matrix is constructed from two other matrices: a matrix $\mathbf{R}$ consists of three vectors describing each rigid body mode of the section plane, and a matrix $\mathbf{V}$ which is defined as the product of the classical displacements $\mathbf{d}_f^p(x,y,z)$ with the vector of sectional interpolation functions $\hat{\mathbf{S}}(y,z)$. The new expressions have been obtained for $\hat{\mathbf{S}}(y,z)$ and the sectional forces in equation 3.54:

$$\tilde{\mathbf{S}}(y,z) = \mathbf{P}_r\hat{\mathbf{S}}(y,z) \tag{3.67a}$$

$$\tilde{\mathbf{D}}_s^{ax}(x) = \mathbf{P}_r\mathbf{D}_s^{ax}(x) \tag{3.67b}$$

$$\tilde{\mathbf{D}}_s^{ayz}(x) = \mathbf{P}_r\mathbf{D}_s^{ayz}(x) \tag{3.67c}$$

In our model, we use the method proposed by Capdevielle [15] which is based on the suggestion of Le Corvec, but allows to modify directly the expression of sectional

interpolation functions $S_{jk}(y,z)$ without using the projection matrix $\mathbf{P}_r$, thus reduce the complexity and the calculation cost. This method is originally developed only for the warping field and then extended to the distortion field by the authors. For the warping, only the axial component U^e of enhanced field is considered. Knowing that the axial component U^p of classical field is generated by a basic set $(1, y, z)$, the projection of sectional interpolation functions $S_{jk}(y,z)$ on the orthogonal space to U^p gives the following new expression of $S_{jk}(y,z)$:

$$\tilde{S}^U_{jk}(y,z) = S_{jk}(y,z) - \iint_A S_{jk}(y,z) \begin{pmatrix} \frac{1}{a_1} & \frac{y}{a_2} & \frac{z}{a_3} \end{pmatrix} dA \begin{pmatrix} 1 \\ y \\ z \end{pmatrix} \tag{3.68}$$

with the following definition of the constants a_i:

$$a_1 = \iint_A dA; \qquad a_2 = \iint_A y^2 dA; \qquad a_3 = \iint_A z^2 dA; \tag{3.69}$$

The derivations of these new interpolation functions with respect to y and z are expressed as follows:

$$\begin{aligned} \frac{\partial \tilde{S}^U_{jk}(y,z)}{\partial y} &= \frac{\partial S_{jk}(y,z)}{\partial y} - \iint_A S_{jk}(y,z) \frac{y}{a_2} dA; \\ \frac{\partial \tilde{S}^U_{jk}(y,z)}{\partial z} &= \frac{\partial S_{jk}(y,z)}{\partial z} - \iint_A S_{jk}(y,z) \frac{z}{a_3} dA \end{aligned} \tag{3.70}$$

For the distortion field, knowing that the transversal component V^p and W^p of classical field is generated by two basic sets $(1, y)$ and $(1, z)$, respectively, the projection of sectional interpolation functions $S_{jk}(y,z)$ on the orthogonal space to V^p and W^p gives the following new expression of $S_{jk}(y,z)$:

$$\tilde{S}^V_{jk}(y,z) = S_{jk}(y,z) - \iint_A S_{jk}(y,z) \begin{pmatrix} \frac{1}{a_1} & \frac{z}{a_3} \end{pmatrix} dA \begin{pmatrix} 1 \\ z \end{pmatrix} \tag{3.71a}$$

$$\tilde{S}^W_{jk}(y,z) = S_{jk}(y,z) - \iint_A S_{jk}(y,z) \begin{pmatrix} \frac{1}{a_1} & \frac{y}{a_2} \end{pmatrix} dA \begin{pmatrix} 1 \\ y \end{pmatrix} \tag{3.71b}$$

and the expression of their derivation with respect to y and z:

$$\begin{aligned}
\frac{\partial \tilde{S}^V_{jk}(y,z)}{\partial y} &= \frac{\partial S_{jk}(y,z)}{\partial y} \\
\frac{\partial \tilde{S}^V_{jk}(y,z)}{\partial z} &= \frac{\partial S_{jk}(y,z)}{\partial z} - \iint_A S_{jk}(y,z)\frac{z}{a_3}dA \\
\frac{\partial \tilde{S}^W_{jk}(y,z)}{\partial y} &= \frac{\partial S_{jk}(y,z)}{\partial y} - \iint_A S_{jk}(y,z)\frac{y}{a_2}dA \\
\frac{\partial \tilde{S}^W_{jk}(y,z)}{\partial z} &= \frac{\partial S_{jk}(y,z)}{\partial z}
\end{aligned} \tag{3.72}$$

It is worth to mention that the sub-index U, V and W in the new expression of interpolation functions indicate that the corresponding interpolation functions are only used for the components U^e, V^e and W^e respectively.

3.4.3 Solution scheme

The present FE formulation is programmed using Matlab according to the solution schemes illustrated in Figure 3-11.

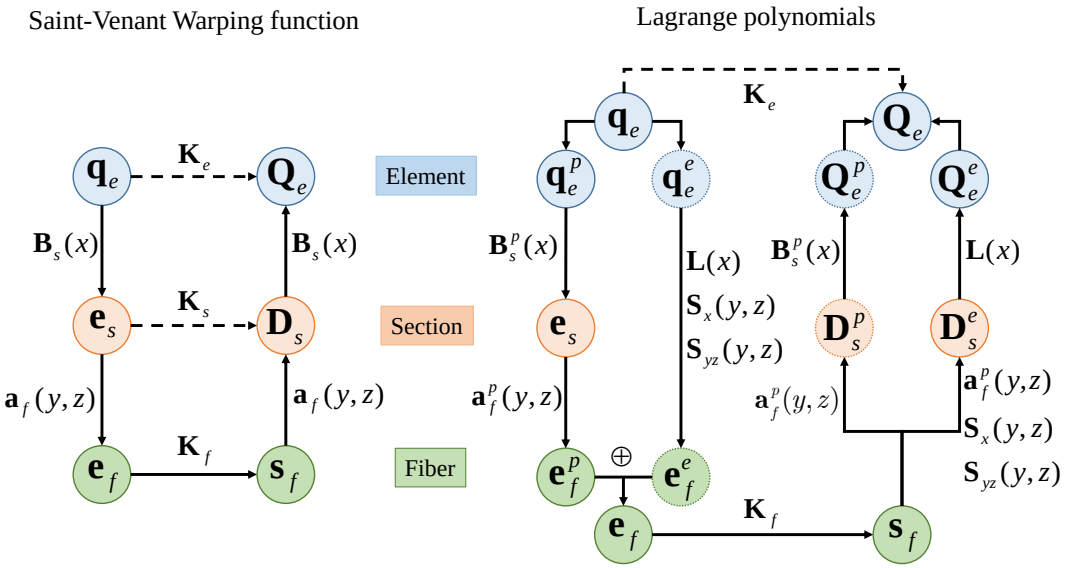

Figure 3-11 – Resume chart for the multi-fiber FE beam in displacement-based formulation.

3.5 Regional constitutive model for RC members

In the model formulation described above, the determination of the constitutive relationship between the stress and the strain in Equation (3.36) requires to define an adequate constitutive equation and material law. The consistent constitutive model must be able to represent the typical effects of RC members such as the cracking, the stress-stiffening effect or the compression softening effect due to transverse tensile strains. According to the section discretization as described in Section 3.1, in this Section the constitutive equations and the material laws for each discretized region will be described in detail. The material stiffness matrix as well as the *regional* stiffness matrix $\mathbf{K}_s^{1D}$, $\mathbf{K}_s^{2D}$ or $\mathbf{K}_s^{3D}$ are obtained as a result. Then, for the entire section, the sectional stiffness matrix in equation is obtained by summarizing all these *regional* stiffness matrices:

$$\mathbf{K}_s = \mathbf{K}_s^{1D} + \mathbf{K}_s^{2D} + \mathbf{K}_s^{3D} \tag{3.73}$$

The element stiffness matrix in Equation (3.48) can then be determined and assembled into the structural stiffness matrix.

3.5.1 1D-Zone

This region takes into account only the contribution of the longitudinal reinforcing steel (rebar), and the only stress accounted for is the axial component σ_{xx}, which can be easily computed from the axial strain using an uniaxial behavior law of steel. In this work, a bilinear elasto-plastic steel model is used in both compression and tension (Figure 3-12).

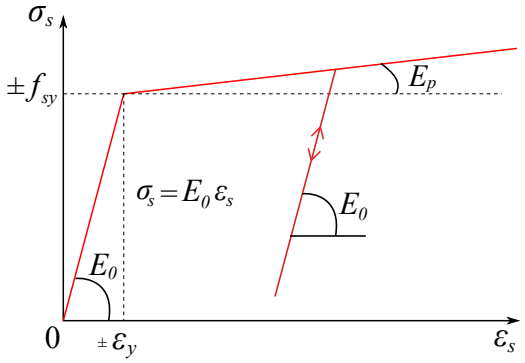

Figure 3-12 – Stress-strain relationship for steel.

where

ε_s: steel's strain;

σ_s: steel's stress.

f_{sy}: steel's yield strength.

E_o: elastic modulus of steel.

E_p: plastic modulus of steel.

ε_{sy}: steel's strain at yield.

The stress vector can be expressed by:

$$\mathbf{s}_f^{1D} = \begin{pmatrix} \sigma_{xx}^{1D} \\ 0 \\ 0 \end{pmatrix} = \begin{pmatrix} E_s \varepsilon_{xx}^m \\ 0 \\ 0 \end{pmatrix} = \begin{bmatrix} E_s & 0 & 0 \\ 0 & 0 & 0 \\ 0 & 0 & 0 \end{bmatrix} \begin{pmatrix} \varepsilon_{xx}^{1D} \\ \gamma_{xy} \\ \gamma_{xz} \end{pmatrix} = \mathbf{k}_f^{1D} \mathbf{e}_f^{1D} \tag{3.74}$$

Where E_s is the secant or tangent modulus of steel. From the material stiffness matrix $\mathbf{k}_f^{1D}$, the *1D-regional* stiffness matrix $\mathbf{K}_s^{1D}$ can then be determined using the kinematic condition in Equation (3.43).

3.5.2 2D-Zone

This region corresponds to the portion in which the transverse steel crosses in one direction and may also have the contribution of longitudinal reinforcement bars. In this 2D-zone, the constitutive behavior of materials is based on the original MCFT [112] as described in Section 2.4.1.

Corresponding to the sectional analysis of a frame element, in which only warping phenomenon is taken into account and distortion of cross-section is neglected, the stress state of this zone has only two non-zero components instead of three: one axial and one transversal which correspond to the direction of stirrups. This results in a stress vector $\mathbf{s}_{f-h}^{2D} = \begin{pmatrix} \sigma_{xx} & \tau_{xy} & 0 \end{pmatrix}^T$ (in the zone of stirrups disposed in horizontal direction or *horizontal stirrups* - called 2D-horizontal zone) or $\mathbf{s}_{f-v}^{2D} = \begin{pmatrix} \sigma_{xx} & 0 & \tau_{xz} \end{pmatrix}^T$ (in the zone of stirrups disposed in vertical direction or *vertical stirrups* - called 2D-vertical zone) (Figure 3-2a). It's worth to note that, for a RC element, the contribution of transversal reinforcement is taken into account by considering a third stress component: σ_{yy} or σ_{zz}, depending on the direction of stirrups. This component must be considered firstly, and then will be imposed to zero in order to satisfy the internal transversal equilibrium of RC members without distortion. The stress vector to be considered in the element state therefore

becomes $\mathbf{s}_{f-h}^{*2D} = \begin{pmatrix} \sigma_{xx} & \tau_{xy} & 0 & \sigma_{yy} & 0 & 0 \end{pmatrix}^T$ or $\mathbf{s}_{f-v}^{*2D} = \begin{pmatrix} \sigma_{xx} & 0 & \tau_{xz} & 0 & \sigma_{zz} & 0 \end{pmatrix}^T$. For the sake of generality, the full stress vector for the following will take the expression of $\mathbf{s}_f^{*2D} = \begin{pmatrix} \sigma_{xx} & \tau_{xy} & \tau_{xz} & \sigma_{yy} & \sigma_{zz} & \tau_{yz} \end{pmatrix}^T$, where some components are zero depending on the stirrup's direction. Corresponding to this 2D-general stress state, the 2D-strain vector must also have 6 components $\mathbf{e}_f^{*2D} = \begin{pmatrix} \varepsilon_{xx} & \gamma_{xy} & \gamma_{xz} & \varepsilon_{yy} & \varepsilon_{zz} & \gamma_{yz} \end{pmatrix}^T$, but unlike in the stress state, ε_{yy} (2D-horizontal zone) and ε_{zz} (2D-vertical zone) are not imposed to zero, and must be determined in the process of satisfying the transversal equilibrium. However, they will not be taken into account in the sectional analysis thereafter, except for the distortion phenomenon.

3.5.2.1 In-plane frame system

Knowing that the original MCFT is designed for membrane members, it is practical to explore the constitutive formulation of this theory in an *in-plane frame system* of coordinate axes (l, t) following the longitudinal and transversal direction (Figure 3-13). For this, a change of reference is applied to transform the strain vector from the local frame system (x, y, z) to the in-plane system (l, t):

$$\mathbf{e}_{ip}^{*2D} = \mathbf{T}_{ip}\mathbf{e}_f^{*2D} \tag{3.75}$$

where $_{ip}$ is the index of parameters expressed in the in-plane system, $\mathbf{T}_{ip}$ is the transformation matrix:

$$\mathbf{T}_{ip} = \begin{bmatrix} 1 & 0 & 0 & 0 & 0 & 0 \\ 0 & 0 & 0 & \cos^2\alpha & \sin^2\alpha & \sin\alpha\cos\alpha \\ 0 & \cos\alpha & \sin\alpha & 0 & 0 & 0 \\ 0 & 0 & 0 & \sin^2\alpha & \cos^2\alpha & -\sin\alpha\cos\alpha \\ 0 & -\sin\alpha & \cos\alpha & 0 & 0 & 0 \\ 0 & 0 & 0 & -\sin 2\alpha & \sin 2\alpha & \cos 2\alpha \end{bmatrix} \tag{3.76}$$

α is the rotation angle between the two frames whose value is either 0 for the 2D-horizontal zone or $\frac{\pi}{2}$ for the 2D-vertical one.

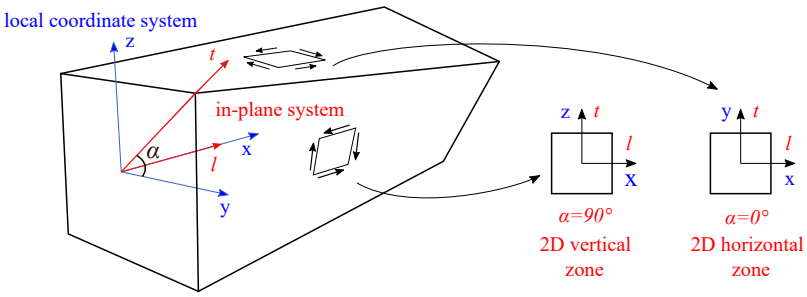

Figure 3-13 – In-plane frame system

As a consequence, the in-plane strain vector becomes:

$$\mathbf{e}_{ip-h}^{*2D} = \begin{pmatrix} \varepsilon_{xx} & \varepsilon_{yy} & \gamma_{xy} & \varepsilon_{zz} & \gamma_{xz} & \gamma_{yz} \end{pmatrix}^T \quad \text{2D-horizontal} \tag{3.77a}$$

$$\mathbf{e}_{ip-v}^{*2D} = \begin{pmatrix} \varepsilon_{xx} & \varepsilon_{zz} & \gamma_{xz} & \varepsilon_{yy} & -\gamma_{xy} & -\gamma_{yz} \end{pmatrix}^T \quad \text{2D-vertical} \tag{3.77b}$$

Only the first three components are considered in the in-plane coordinate system, the others are given a null value, so:

$$\mathbf{e}_{ip}^{2D} = \begin{pmatrix} \varepsilon_l \\ \varepsilon_t \\ \gamma_{lt} \end{pmatrix} = \begin{pmatrix} \varepsilon_{xx} \\ \varepsilon_{yy} \\ \gamma_{xy} \end{pmatrix} \text{(2D-horizontal)} \quad \text{or} \quad \begin{pmatrix} \varepsilon_{xx} \\ \varepsilon_{zz} \\ \gamma_{xz} \end{pmatrix} \text{(2D-vertical)} \tag{3.78}$$

Among these 3 in-plane strain components, ε_l and γ_{lt} can be obtained from the kinematic condition in Equation (3.18), while ε_t must be handled separately by satisfying the transversal equilibrium conditions. The determination of ε_t as well as the transversal equilibrium follow an iterative process and will be described later. Corresponding to this strain vector, the in-plane stress vector has 3 components: $\mathbf{s}_{ip}^{2D} = \begin{pmatrix} \sigma_l & \sigma_t & \tau_{lt} \end{pmatrix}^T$. The stress and strain vectors are related by an in-plane material stiffness matrix $\mathbf{D}_{ip}^{2D}$:

$$\mathbf{s}_{ip}^{2D} = \mathbf{D}_{ip}^{2D} \mathbf{e}_{ip}^{2D} \tag{3.79}$$

The contribution of concrete and reinforcement are added separately to the material stiffness matrix and the stress vector of the in-plane frame (Figure 3-14):

$$\mathbf{s}_{ip}^{2D} = \mathbf{s}_{ip,c}^{2D} + \mathbf{s}_{ip,s}^{2D} \tag{3.80a}$$

$$\mathbf{D}_{ip}^{2D} = \mathbf{D}_{ip,c}^{2D} + \mathbf{D}_{ip,s}^{2D} \tag{3.80b}$$

where $\mathbf{D}_{ip,c}^{2D}$ is the concrete stiffness matrix and $\mathbf{D}_{ip,s}^{2D}$ is the stiffness matrix of reinforce-

ment. While $\mathbf{D}_{ip,s}^{2D}$ can be set up easily in the in-plane system, it's more convenient to express the concrete relation in principal directions of crack, as described in the original MCFT (Figure 3-14).

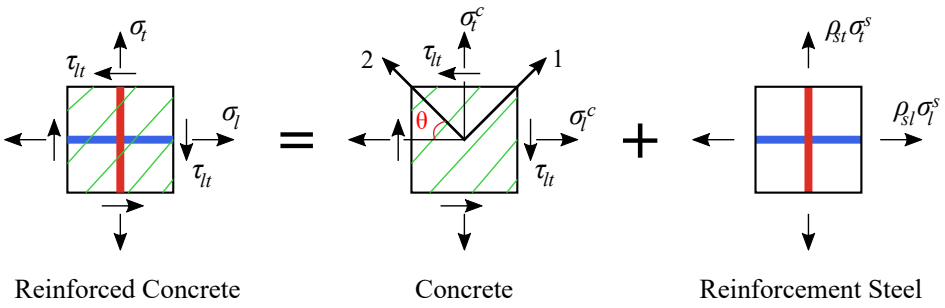

Figure 3-14 – Stress composition for RC members in the MCFT [110].

A change of reference from principal direction to in-plane axes systems is therefore required as described in Equation (2.11), and Equation (3.80b) becomes:

$$\mathbf{D}_{ip}^{2D} = \mathbf{T}_c^{2DT}\mathbf{D}_{prin,c}^{2D}\mathbf{T}_c^{2D} + \mathbf{D}_{ip,s}^{2D} \tag{3.81}$$

Where $\mathbf{T}_c^{2D}$ is the transformation matrix described in Equation (2.13). The direction of principal strains θ can be determined from the in-plane strain vector using Mohr's circle:

$$\theta = \frac{1}{2}\arctan\left(\frac{\gamma_{lt}}{\varepsilon_l - \varepsilon_t}\right) \tag{3.82}$$

The concrete stiffness matrix in principal direction $\mathbf{D}_{prin,c}^{2D}$ can be evaluated in secant-stiffness based as described in Equation (2.12), or in tangent-based as described in Equation (2.14). The expression of $\mathbf{D}_{prin,c}^{2D}$ depends on the stresses and strains of concrete in principal directions. The concrete strains ε_1 and ε_2 can be obtained from the in-plane concrete strain vector $\mathbf{e}_{ip}^{2D}$ and the transformation matrix $\mathbf{T}_c^{2D}$:

$$\mathbf{e}_{prin,c}^{2D} = \begin{pmatrix}\varepsilon_1 & \varepsilon_2 & \gamma_{12}\end{pmatrix}^T = \mathbf{T}_c^{2D}\mathbf{e}_{ip}^{2D} \tag{3.83}$$

From theses principal strains, the concrete principal stresses σ_1 and σ_2 can be determined from the uniaxial stress-strain relation as described in Section 2.4.1. The principal stiffness matrix $\mathbf{D}_{prin,c}^{2D}$ in Equation (3.81) and the vector of principal stresses $\mathbf{s}_{prin,c}^{2D} = \begin{pmatrix}\sigma_1 & \sigma_2 & 0\end{pmatrix}^T$ are all obtained, as well as the concrete constitutive relation in principal directions as follows:

$$\mathbf{s}_{prin,c}^{2D} = \mathbf{D}_{prin,c}^{2D}\mathbf{e}_{prin,c}^{2D} \tag{3.84}$$

The in-plane stress vector of concrete in Equation (3.80a) can be obtained thanks to the hypothesis of same principal directions between strains and stresses:

$$\mathbf{s}_{ip,c}^{2D} = \mathbf{T}_{c}^{2DT}\mathbf{s}_{prin,c}^{2D} \tag{3.85}$$

Considering the reinforcement's contribution, the steel stiffness matrix is expressed in the in-plane coordinate system:

$$\mathbf{D}_{ip,s}^{2D} = \begin{bmatrix} \rho_{sl}E_{sl} & 0 & 0 \\ 0 & \rho_{st}E_{st} & 0 \\ 0 & 0 & 0 \end{bmatrix} \tag{3.86}$$

where the modulus of longitudinal (transversal) reinforcement E_{sl} (E_{st}) can be expressed in secant or tangent-based, using the in-plane strain components ε_l (ε_t) in Equation (3.78) and the steel behavior law in Figure 3-12; ρ_{sl} and ρ_{st} are the reinforcement ratio in the in-plane directions l, t respectively, which have been determined as follows:

$$\rho_{sl} = \frac{A_{sl}}{A_c^{2D}} \tag{3.87a}$$

$$\rho_{st} = \frac{A_{st}P_{st}}{A_c^{2D}s} \tag{3.87b}$$

where A_{sl} is the total area of longitudinal reinforcing steel situated in 2D-zone, A_c^{2D} is the area of 2D-zone, A_{st} is the area of one leg of a transverse steel bar, P_{st} is the perimeter of the stirrup centerline in 2D-zone and s denotes the average spacing of stirrups. It should be noted that the reinforcement percentages are evaluated with respect to the discretized cross-section area.

3.5.2.2 Transverse equilibrium

All the expression of constitutive equations above can not be determined without the in-plane transverse strains ε_t, which can be calculated by satisfying the condition of transverse equilibrium between concrete and stirrup at each material point. This condition is expressed by the following relation:

$$\rho_{st}\sigma_{st} + \left(\sigma_1 \sin^2\theta + \sigma_2 \cos^2\theta\right) = 0 \tag{3.88}$$

In other words, the transverse stress σ_t of the in-plane stress vector $\mathbf{s}_{ip}^{2D}$ must be zero (regarding Equation (3.80a) and (3.85)). In order to satisfy this condition from unknown value of ε_t, a numerical iterative process using Newton-Raphson method is carried out (Figure 3-15). The kinematic conditions in Section 3.2 and 3.3 give the components ε_l and γ_{lt} of the in-plane strain vector $\mathbf{e}_{ip}^{2D}$, while an initial value is given to the unknown transverse strain equal to that of previous iteration: $\varepsilon_t = \varepsilon_t^{i-1}$. Then the constitutive equations above can be expressed to determine the in-plane stiffness matrix $\mathbf{D}_{ip}^{2D}$ and stresses $\mathbf{s}_{ip}^{2D}$. Equation (3.79) gives:

$$\mathbf{s}_{ip}^{2D} = \mathbf{D}_{ip}^{2D}\mathbf{e}_{ip}^{2D} \Leftrightarrow \begin{pmatrix} \sigma_l \\ \sigma_t \\ \tau_{lt} \end{pmatrix} = \begin{bmatrix} D_{ip,11}^{2D} & D_{ip,12}^{2D} & D_{ip,13}^{2D} \\ D_{ip,21}^{2D} & D_{ip,22}^{2D} & D_{ip,23}^{2D} \\ D_{ip,31}^{2D} & D_{ip,32}^{2D} & D_{ip,33}^{2D} \end{bmatrix} \begin{pmatrix} \varepsilon_l \\ \varepsilon_t \\ \gamma_{lt} \end{pmatrix} \tag{3.89}$$

By imposing $\sigma_t = 0$, one obtains the following expression of ε_t:

$$\varepsilon_t = -\frac{D_{ip,21}^{2D}\varepsilon_l + D_{ip,23}^{2D}\gamma_{lt}}{D_{ip,22}^{2D}} \tag{3.90}$$

the difference between the value of ε_t in Equation (3.90) will be compared to the initial value ε_t^{i-1} and the convergence is achieved when the control parameter $\left\| \frac{\varepsilon_t - \varepsilon_t^{i-1}}{\varepsilon_t^{i-1}} \right\|$ is smaller than a specified tolerance.

3.5.2.3 Transformation to local frame system

After determining the transverse strains and stresses in the in-plane system following the equations above, another change of reference needs to be applied to transform the stress, strain vector and the stiffness matrix to the local frame system:

$$\mathbf{D}_f^{2D} = \mathbf{T}_{ip}^T \begin{bmatrix} \mathbf{D}_{ip}^{2D} & \mathbf{0}_3 \\ \mathbf{0}_3 & \mathbf{0}_3 \end{bmatrix} \mathbf{T}_{ip} \tag{3.91a}$$

$$\mathbf{s}_f^{*2D} = \mathbf{T}_{ip}^T \mathbf{s}_{ip}^{*2D} \tag{3.91b}$$

$$\mathbf{s}_f^{*2D} = \mathbf{D}_f^{2D}\mathbf{e}_f^{*2D} \tag{3.91c}$$

Where $\mathbf{0}_3$ is a (3×3) zero matrix, resulting from the exclusion of unnecessary strain components in Equation (3.77); $\mathbf{s}_{ip}^{*2D} = \begin{pmatrix} \mathbf{s}_{ip}^{2DT} & 0 & 0 & 0 \end{pmatrix}^T$ is the full in-plane stress vector.

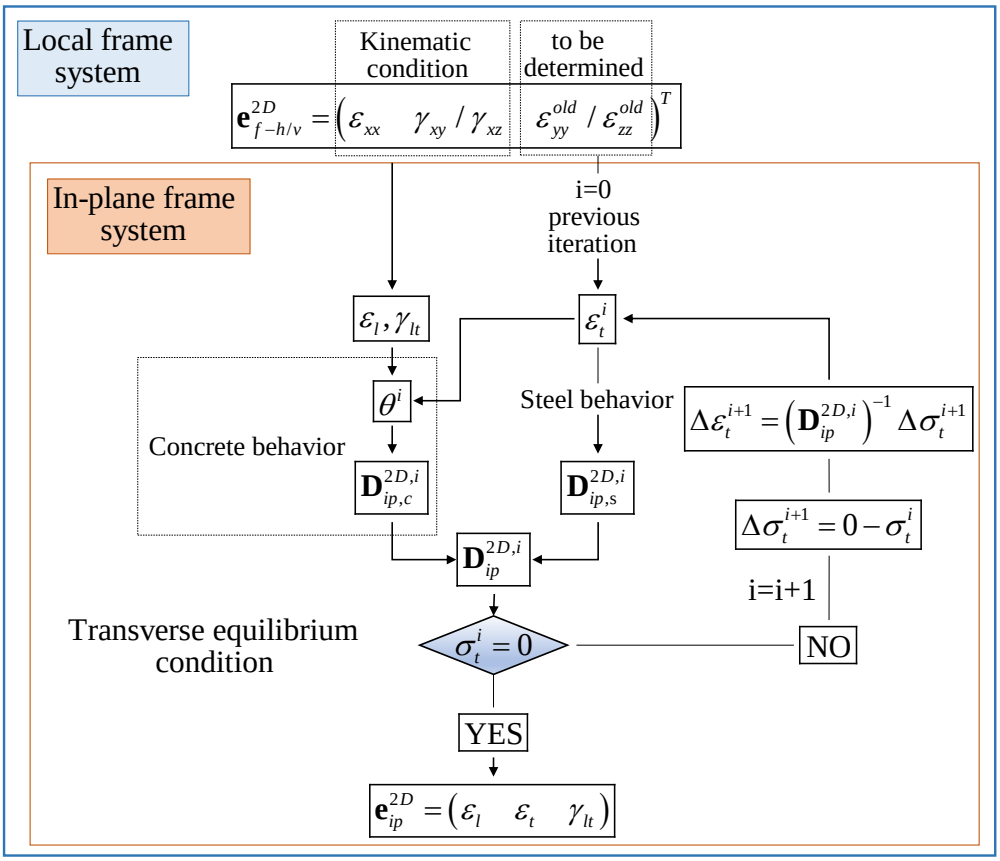

Figure 3-15 – Iteration process satisfying internal equilibrium between concrete and transverse reinforcement

The 2D material stiffness matrix in Equation (3.91a) can be expressed as follows:

$$\mathbf{D}_{f-h}^{2D} = \begin{bmatrix} D_{ip,11}^{2D} & D_{ip,13}^{2D} & 0 & D_{ip,12}^{2D} & 0 & 0 \\ D_{ip,31}^{2D} & D_{ip,33}^{2D} & 0 & D_{ip,32}^{2D} & 0 & 0 \\ 0 & 0 & 0 & 0 & 0 & 0 \\ D_{ip,21}^{2D} & D_{ip,23}^{2D} & 0 & D_{ip,22}^{2D} & 0 & 0 \\ 0 & 0 & 0 & 0 & 0 & 0 \\ 0 & 0 & 0 & 0 & 0 & 0 \end{bmatrix} \quad \text{or} \quad \mathbf{D}_{f-v}^{2D} = \begin{bmatrix} D_{ip,11}^{2D} & 0 & D_{ip,13}^{2D} & 0 & D_{ip,12}^{2D} & 0 \\ 0 & 0 & 0 & 0 & 0 & 0 \\ D_{ip,31}^{2D} & 0 & D_{ip,33}^{2D} & 0 & D_{ip,32}^{2D} & 0 \\ 0 & 0 & 0 & 0 & 0 & 0 \\ D_{ip,21}^{2D} & 0 & D_{ip,23}^{2D} & 0 & D_{ip,22}^{2D} & 0 \\ 0 & 0 & 0 & 0 & 0 & 0 \end{bmatrix} \tag{3.92}$$

and the full stress vector:

$$\begin{aligned} \mathbf{s}_{f-h}^{*2D} &= \begin{pmatrix} \sigma_{xx} & \tau_{xy} & 0 & \sigma_{yy} & 0 & 0 \end{pmatrix}^T = \begin{pmatrix} \sigma_l & \tau_{lt} & 0 & \sigma_t & 0 & 0 \end{pmatrix}^T \\ \mathbf{s}_{f-v}^{*2D} &= \begin{pmatrix} \sigma_{xx} & 0 & \tau_{xz} & 0 & \sigma_{zz} & 0 \end{pmatrix}^T = \begin{pmatrix} \sigma_l & 0 & \tau_{lt} & 0 & \sigma_t & 0 \end{pmatrix}^T \end{aligned} \tag{3.93}$$

Knowing that $\sigma_t = 0$ to satisfy the internal equilibrium above, the following static condensation can be established with the aid of Equation (3.91c), for the 2D-horizontal zone

first:

$$\begin{aligned}
\begin{pmatrix} \sigma_{yy} \\ 0 \\ 0 \end{pmatrix}_{f-h}^{2D} &= \begin{pmatrix} 0 \\ 0 \\ 0 \end{pmatrix} = \begin{pmatrix} D_{ip,21}^{2D}\varepsilon_{xx} + D_{ip,23}^{2D}\gamma_{xy} + D_{ip,22}^{2D}\varepsilon_{yy} \\ 0 \\ 0 \end{pmatrix} \\
\Rightarrow \begin{pmatrix} \varepsilon_{yy} \\ 0 \\ 0 \end{pmatrix}_{f-h}^{2D} &= -\frac{1}{D_{ip,22}^{2D}} \begin{bmatrix} D_{ip,21}^{2D} & D_{ip,23}^{2D} & 0 \\ 0 & 0 & 0 \\ 0 & 0 & 0 \end{bmatrix} \begin{pmatrix} \varepsilon_{xx} \\ \gamma_{xy} \\ 0 \end{pmatrix}
\end{aligned} \tag{3.94}$$

and for the 2D-vertical zone:

$$\begin{aligned}
\begin{pmatrix} 0 \\ \sigma_{zz} \\ 0 \end{pmatrix}_{f-v}^{2D} &= \begin{pmatrix} 0 \\ 0 \\ 0 \end{pmatrix} = \begin{pmatrix} 0 \\ D_{ip,21}^{2D}\varepsilon_{xx} + D_{ip,23}^{2D}\gamma_{xz} + D_{ip,22}^{2D}\varepsilon_{zz} \\ 0 \end{pmatrix} \\
\Rightarrow \begin{pmatrix} 0 \\ \varepsilon_{zz} \\ 0 \end{pmatrix}_{f-v}^{2D} &= -\frac{1}{D_{ip,22}^{2D}} \begin{bmatrix} 0 & 0 & 0 \\ D_{ip,21}^{2D} & 0 & D_{ip,23}^{2D} \\ 0 & 0 & 0 \end{bmatrix} \begin{pmatrix} \varepsilon_{xx} \\ 0 \\ \gamma_{xz} \end{pmatrix}
\end{aligned} \tag{3.95}$$

Then, the stress vector $\mathbf{s}_f^{2D}$ used in the sectional analysis can now be expressed as follows:

$$\mathbf{s}_{f-h}^{2D} = \begin{pmatrix} \sigma_{xx} \\ \tau_{xy} \\ 0 \end{pmatrix} = \begin{bmatrix} D_{ip,11}^{2D} & D_{ip,13}^{2D} & 0 \\ D_{ip,31}^{2D} & D_{ip,33}^{2D} & 0 \\ 0 & 0 & 0 \end{bmatrix} \begin{pmatrix} \varepsilon_{xx} \\ \gamma_{xy} \\ 0 \end{pmatrix} + \begin{bmatrix} D_{ip,12}^{2D} & 0 & 0 \\ D_{ip,32}^{2D} & 0 & 0 \\ 0 & 0 & 0 \end{bmatrix} \begin{pmatrix} \varepsilon_{yy} \\ 0 \\ 0 \end{pmatrix} \tag{3.96a}$$

$$\mathbf{s}_{f-v}^{2D} = \begin{pmatrix} \sigma_{xx} \\ 0 \\ \tau_{xz} \end{pmatrix} = \begin{bmatrix} D_{ip,11}^{2D} & 0 & D_{ip,13}^{2D} \\ 0 & 0 & 0 \\ D_{ip,31}^{2D} & 0 & D_{ip,33}^{2D} \end{bmatrix} \begin{pmatrix} \varepsilon_{xx} \\ 0 \\ \gamma_{xz} \end{pmatrix} + \begin{bmatrix} 0 & D_{ip,12}^{2D} & 0 \\ 0 & 0 & 0 \\ 0 & D_{ip,32}^{2D} & 0 \end{bmatrix} \begin{pmatrix} 0 \\ \varepsilon_{zz} \\ 0 \end{pmatrix} \tag{3.96b}$$

From Equation (3.94), (3.95) and (3.96), the following material constitutive relation can be obtained in 2D-zone:

$$\mathbf{s}_f^{2D} = \mathbf{k}_f^{2D}\mathbf{e}_f^{2D} \tag{3.97}$$

with the expression of the material stiffness matrix:

$$\mathbf{k}_{f-h}^{2D} = \begin{bmatrix} D_{ip,11}^{2D} & D_{ip,13}^{2D} & 0 \\ D_{ip,31}^{2D} & D_{ip,33}^{2D} & 0 \\ 0 & 0 & 0 \end{bmatrix} - \frac{1}{D_{ip,22}^{2D}} \begin{bmatrix} D_{ip,12}^{2D} D_{ip,21}^{2D} & D_{ip,12}^{2D} D_{ip,23}^{2D} & 0 \\ D_{ip,21}^{2D} D_{ip,32}^{2D} & D_{ip,23}^{2D} D_{ip,32}^{2D} & 0 \\ 0 & 0 & 0 \end{bmatrix} \tag{3.98a}$$

$$\mathbf{k}_{f-v}^{2D} = \begin{bmatrix} D_{ip,11}^{2D} & 0 & D_{ip,13}^{2D} \\ 0 & 0 & 0 \\ D_{ip,31}^{2D} & 0 & D_{ip,33}^{2D} \end{bmatrix} - \frac{1}{D_{ip,22}^{2D}} \begin{bmatrix} D_{ip,12}^{2D} D_{ip,21}^{2D} & 0 & D_{ip,12}^{2D} D_{ip,23}^{2D} \\ 0 & 0 & 0 \\ D_{ip,21}^{2D} D_{ip,32}^{2D} & 0 & D_{ip,23}^{2D} D_{ip,32}^{2D} \end{bmatrix} \tag{3.98b}$$

Using Equation (3.43), the 2D-*regional* stiffness matrix $\mathbf{K}_s^{2D}$ can then be determined from the material stiffness matrix $\mathbf{k}_f^{2D}$. An algorithm for determining the material stiffness matrix of 2D-zone $\mathbf{k}_f^{2D}$ is shown in Figure 3-16.

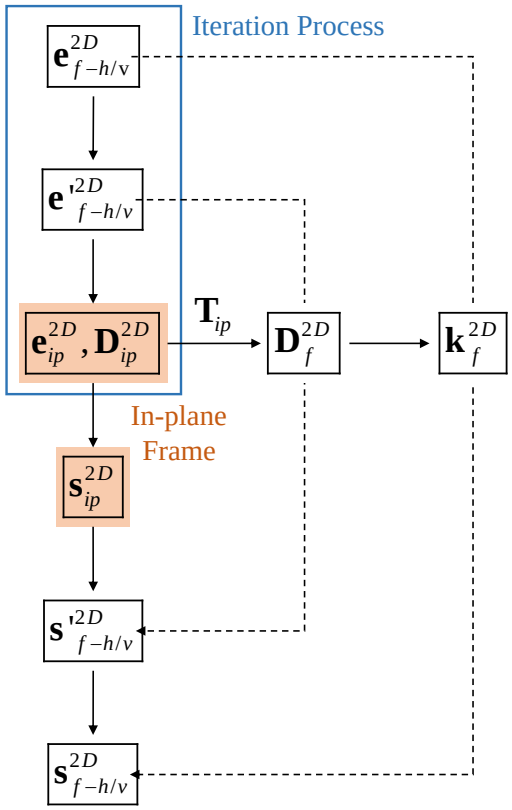

Figure 3-16 – Process determining the material stiffness matrix of 2D-zone

3.5.3 3D-Zone

This zone corresponds to the regions of concrete in which transverse steels come across in two directions (the four corners of section) and the regions of concrete in the core of section without any reinforcement (Figure 3-2a). In this 3D-zone, the constitutive behavior of

materials is based on the extension of the original MCFT, proposed by Vecchio & Selby [112], which will be detailed in the following.

Similar to the 2D-zone, in the case where only warping is taken into account and distortion is neglected, the stress state of this zone has three components: one normal σ_{xx} and two transverses τ_{xy} and τ_{xz}, included in a stress vector $\mathbf{s}_f^{3D} = \begin{pmatrix} \sigma_{xx} & \tau_{xy} & \tau_{xz} \end{pmatrix}^T$. Same as in the 2D-zone, in the 3D-zone even though only 3 stress components are considered in the sectional analysis, the full stress vector has a total of 6 components $\mathbf{s}_f^{*3D} = \begin{pmatrix} \sigma_{xx} & \tau_{xy} & \tau_{xz} & \sigma_{yy} & \sigma_{zz} & \tau_{yz} \end{pmatrix}^T$. The three components σ_{yy}, σ_{zz} and τ_{yz} will then be set to zero in order to satisfy the internal equilibrium without distortion. The corresponding strain vector has therefore six components: $\mathbf{e}_f^{*3D} = \begin{pmatrix} \varepsilon_{xx} & \gamma_{xy} & \gamma_{xz} & \varepsilon_{yy} & \varepsilon_{zz} & \gamma_{yz} \end{pmatrix}^T$. Unlike the stress vector, three strains ε_{yy}, ε_{zz} and γ_{yz} are not zero, but they are not taken into account in the sectional analysis, as the distortion phenomenon is not considered in this work.

The full stresses $\mathbf{s}_f^{*3D}$ and strains $\mathbf{e}_f^{*3D}$ are related by a material stiffness matrix $\mathbf{D}_f^{3D}$ in the following constitutive relation:

$$\mathbf{s}_f^{*3D} = \mathbf{D}_f^{3D} \mathbf{e}_f^{*3D} \tag{3.99}$$

Similar to the two dimensional case, in 3D-zone the material stiffness matrix $\mathbf{D}_f^{3D}$ can be determined as a superposition of concrete and reinforcement:

$$\mathbf{D}_f^{3D} = \mathbf{D}_{f,c}^{3D} + \mathbf{D}_{f,s}^{3D} \tag{3.100}$$

The steel stiffness $\mathbf{D}_{f,s}^{3D}$ can be set up easily in the local frame system, while the determination of concrete stiffness matrix $\mathbf{D}_{f,c}^{3D}$ required a change of reference from principal directions to local axes. Equation (3.100) becomes:

$$\mathbf{D}_f^{3D} = \mathbf{T}_c^T \mathbf{D}_{prin,c}^{3D} \mathbf{T}_c + \mathbf{D}_{f,s}^{3D} \tag{3.101}$$

The concrete stiffness matrix $\mathbf{D}_{prin,c}^{3D}$ in the principal direction can be evaluated in a

secant-based as proposed by Vecchio & Selby [112]:

$$\mathbf{D}^{3D}_{prin,c} = \begin{bmatrix} E_1 & 0 & 0 & 0 & 0 & 0 \\ 0 & E_2 & 0 & 0 & 0 & 0 \\ 0 & 0 & E_3 & 0 & 0 & 0 \\ 0 & 0 & 0 & \dfrac{E_1 E_2}{E_1 + E_2} & 0 & 0 \\ 0 & 0 & 0 & 0 & \dfrac{E_2 E_3}{E_2 + E_3} & 0 \\ 0 & 0 & 0 & 0 & 0 & \dfrac{E_1 E_3}{E_1 + E_3} \end{bmatrix} \tag{3.102}$$

with E_1, E_2 and E_3 are the secant moduli, defined as follows:

$$E_1 = \frac{\sigma_1}{\varepsilon_1}; \quad E_2 = \frac{\sigma_2}{\varepsilon_2}; \quad E_3 = \frac{\sigma_3}{\varepsilon_3}; \tag{3.103}$$

or in a tangent-based approach:

$$\mathbf{D}^{3D}_{prin,c} = \begin{bmatrix} \dfrac{\partial \sigma_1}{\partial \varepsilon_1} & 0 & 0 & 0 & 0 & 0 \\ \dfrac{\partial \sigma_2}{\partial \varepsilon_1} & \dfrac{\partial \sigma_2}{\partial \varepsilon_2} & 0 & 0 & 0 & 0 \\ \dfrac{\partial \sigma_3}{\partial \varepsilon_1} & 0 & \dfrac{\partial \sigma_3}{\partial \varepsilon_3} & 0 & 0 & 0 \\ 0 & 0 & 0 & \dfrac{\sigma_1 - \sigma_2}{2(\varepsilon_1 - \varepsilon_2)} & 0 & 0 \\ 0 & 0 & 0 & 0 & \dfrac{\sigma_1 - \sigma_3}{2(\varepsilon_1 - \varepsilon_3)} & 0 \\ 0 & 0 & 0 & 0 & 0 & \dfrac{\sigma_2 - \sigma_3}{2(\varepsilon_2 - \varepsilon_3)} \end{bmatrix} \tag{3.104}$$

$\mathbf{T}_c$ is the transformation matrix composed of the direction cosines which define the direction of the principal concrete strains:

$$\mathbf{T}_c = \begin{bmatrix} l_1^2 & l_1 m_1 & m_1 n_1 & m_1^2 & n_1^2 & n_1 l_1 \\ l_2^2 & l_2 m_2 & m_2 n_2 & m_2^2 & n_2^2 & n_2 l_2 \\ l_3^2 & l_3 m_2 & m_3 n_2 & m_3^2 & n_3^2 & n_3 l_3 \\ 2 l_1 l_2 & l_1 m_2 + l_2 m1 & m_1 n_2 + m_2 n_1 & 2 m_1 m_2 & 2 n_1 n_2 & n_1 l_2 + n_2 l_1 \\ 2 l_2 l_3 & l_2 m_3 + l_3 m2 & m_2 n_3 + m_3 n_2 & 2 m_2 m_3 & 2 n_2 n_3 & n_2 l_3 + n_3 l_2 \\ 2 l_3 l_1 & l_3 m_1 + l_1 m3 & m_3 n_1 + m_1 n_3 & 2 m_3 m_1 & 2 n_3 n_1 & n_3 l_1 + n_1 l_3 \end{bmatrix} \tag{3.105}$$

The concrete strains in principal direction ε_1, ε_2, ε_3 ($\varepsilon_1 > \varepsilon_2 > \varepsilon_3$) and the direction cosines are calculated from the eigenvalues and eigenvector of the strain tensor, obtained

from the kinematic condition in Equation (3.18). The concrete stresses in principal directions σ_1, σ_2, σ_3 are then deduced from the uniaxial stress-strain relations in Figure 2-19. According to Vecchio & Selby [112], in direction 3 (the direction of principal compressive strain), the compressive stress σ_3 depends on the strain compressive strain ε_3 and the tensile strain ε_1: $\sigma_3 = f(\varepsilon_3, \varepsilon_1)$. In direction 1 (the direction of principal tensile strain), the tensile stress σ_1 depends only on the tensile strain ε_1: $\sigma_1 = f(\varepsilon_1)$. Finally, in the intermediate direction 2 (that can be compressive or tensile), the stress σ_2 depends on ε_2 and ε_1: $\sigma_2 = f(\varepsilon_2, \varepsilon_1)$.

Then, for the reinforcement's contribution, the steel stiffness matrix is expressed in the local coordinate system as:

$$\mathbf{D}_{f,s}^{3D} = \begin{bmatrix} \rho_{sx}E_{sl} & 0 & 0 & 0 & 0 & 0 \\ 0 & \rho_{sy}E_{st} & 0 & 0 & 0 & 0 \\ 0 & 0 & \rho_{sy}E_{st} & 0 & 0 & 0 \\ 0 & 0 & 0 & 0 & 0 & 0 \\ 0 & 0 & 0 & 0 & 0 & 0 \\ 0 & 0 & 0 & 0 & 0 & 0 \end{bmatrix} \tag{3.106}$$

Similar to the 2D-zone, the modulus of longitudinal (transversal) reinforcement E_{sl} (E_{st}) can be expressed in secant or tangent-based, using the strain components ε_{xx} (γ_{xy} and/or γ_{xz}) and the steel behavior law in Section 3.5.1 and Figure 3-12; ρ_{sx}, ρ_{sy} and ρ_{sz} are the reinforcement ratio in the directions of x, y and z, respectively, which have been determined as follows:

$$\rho_{sx} = \frac{A_{sl}}{A_c^{3D}} \tag{3.107a}$$

$$\rho_{sy} = \frac{A_{st}P_{st}^{y}}{A_c^{3D}s} \tag{3.107b}$$

$$\rho_{sy} = \frac{A_{st}P_{st}^{z}}{A_c^{3D}s} \tag{3.107c}$$

where A_{sl} is the total area of longitudinal reinforcing steel situated in 3D-zone, A_c^{3D} is the area of 3D-zone, A_{st} is the area of one leg of a transverse steel bar, P_{st}^{y} is the perimeter of the stirrup centerline disposed in horizontal direction and P_{st}^{z} is the perimeter of the stirrup centerline disposed in vertical direction in 3D-zone; s denotes the average spacing of stirrups. It should be noted that the reinforcement percentages are evaluated with respect to the discretized cross-section area.

As mentioned above, the internal equilibrium is satisfied by imposing the stresses components σ_{yy}, σ_{zz} and τ_{yz} equal to zero. Regrouping these three stresses into one single vector $\mathbf{s}_{of}^{3D} = \begin{pmatrix} \sigma_{yy} & \sigma_{zz} & \tau_{yz} \end{pmatrix}$, with the corresponding strain vector $\mathbf{e}_{of}^{3D} = \begin{pmatrix} \varepsilon_{yy} & \varepsilon_{zz} & \gamma_{yz} \end{pmatrix}$, the constitutive relation in Equation (3.99) becomes:

$$\mathbf{s}_f^{*3D} = \mathbf{D}_f^{3D}\mathbf{e}_f^{*3D} \Leftrightarrow \begin{pmatrix} \mathbf{s}_f^{3D} \\ \mathbf{s}_{of}^{3D} \end{pmatrix} = \begin{bmatrix} \mathbf{D}_{f,11}^{3D} & \mathbf{D}_{f,12}^{3D} \\ \mathbf{D}_{f,21}^{3D} & \mathbf{D}_{f,22}^{3D} \end{bmatrix} \begin{pmatrix} \mathbf{e}_f^{3D} \\ \mathbf{e}_{of}^{3D} \end{pmatrix} \tag{3.108}$$

A static condensation is realized to obtain the strain vector $\mathbf{e}_{of}^{3D}$:

$$\mathbf{s}_{of}^{3D} = \begin{bmatrix} \mathbf{D}_{f,21}^{3D} & \mathbf{D}_{f,22}^{3D} \end{bmatrix} \begin{pmatrix} \mathbf{e}_f^{3D} \\ \mathbf{e}_{of}^{3D} \end{pmatrix} = \mathbf{0}_3 \Rightarrow \mathbf{e}_{of}^{3D} = -\left(\mathbf{D}_{f,22}^{3D}\right)^{-1}\mathbf{D}_{f,21}^{3D}\mathbf{e}_f^{3D} \tag{3.109}$$

The non-zero terms $\mathbf{e}_{of}^{3D}$ in the strain vector $\mathbf{e}_f^{*3D}$, which can not be determined from the kinematic condition, are calculated from the equation 3.109. The stress vector $\mathbf{s}_f^{3D}$ used in the sectional analysis is therefore expressed by:

$$\begin{aligned} \mathbf{s}_f^{3D} = \mathbf{D}_{f,11}^{3D}\mathbf{e}_f^{3D} + \mathbf{D}_{f,12}^{3D}\mathbf{e}_{of}^{3D} = \mathbf{D}_{f,11}^{3D}\mathbf{e}_f^{3D} - \mathbf{D}_{f,12}^{3D}\left(\mathbf{D}_{f,22}^{3D}\right)^{-1}\mathbf{D}_{f,21}^{3D}\mathbf{e}_f^{3D} \\ \Rightarrow \mathbf{s}_f^{3D} = \mathbf{k}_f^{3D}\mathbf{e}_f^{3D} \end{aligned} \tag{3.110}$$

with the expression of the material stiffness matrix in 3D-zone:

$$\mathbf{k}_f^{3D} = \mathbf{D}_{f,11}^{3D} - \mathbf{D}_{f,12}^{3D}\left(\mathbf{D}_{f,22}^{3D}\right)^{-1}\mathbf{D}_{f,21}^{3D} \tag{3.111}$$

The process of determining the material stiffness matrix $\mathbf{k}_f^{3D}$ of 3D-zone is generally similar to that of 2D-zone in Figure 3-16, except that the transformation to in-plane frame system is not necessary. The *regional* stiffness matrix $\mathbf{K}_s^{3D}$ can be calculated from $\mathbf{k}_f^{3D}$ using Equation (3.43).

In this mechanical model for RC member, the constitutive model is formulated general enough for being used for any shape of cross-section and any type of formulation (forces or mixed based) in further studies.

3.6 Effective wall thickness

An important parameter to consider carefully in this discretization is the width of the 2D-zone. However it is not validated by a specific rule, but only suggested equal to the double

of concrete cover over the transverse reinforcement [76]. Taking care of this indication, during the construction of the model, two remarks have been concluded by the authors:

1. Under shear-bending: the choice of 2D-width does not have much influence on the numerical results, as observed by the authors during the numerical modelings.

2. Under pure torsion: a lack of definition for the 2D-width can pose some critical problems to the numerical result, in other words, such a simple formulation (as suggested by Navarro Gregori) can not represent accurately enough the torsional response.

These remarks can be explained by the fact that as mentioned above, under torsional effects, the behavior of RC member after cracking is assumed to be carried out by a tube of hollow section. That is to say that the behavior of 3D-zone of the concrete in the section core is set to zero and the sectional behavior depends only on 2D-zone and 3D-zone at the four corners of section. The width of 2D-zone is defined as the *effective wall thickness* of the tube, and determining this parameter becomes an obvious question to investigate the post-cracking behavior of RC members under torsional effect. In shear-bending, a lack of definition for the 2D-width can only pose some small problems in the calculation of steel percentage for each region, but it does not have as much influence to the numerical results as in the case of torsional effect.

In the literature, several formulations were proposed: Rahal & Collins proposed an average value of the effective thickness of concrete in resisting the torsional moment which depends on the section dimensions [88]; the formulation used in the model of Valipour & Foster is a function of stirrup's spacing, reinforcement bar disposition and concrete section dimension [106]; while Hsu proposed another formulation for design based on the torsional strength [47]. After consulting the proposed formulations cited above and a formulation calibrated by Hsu [46], the authors noted that the effective wall thickness should be a function of the section width and of the reinforcement ratio. A parametric study was investigated from the 45 specimens below and gave the following formulation:

- For usual repartition of reinforcement bars at corner:

$$t_e = b\left(0.0130\frac{h}{b}m\rho_s + 0.1\right) \tag{3.112}$$

- For repartition with additional of reinforcement bars along the perimeter:

$$t_e = b\left(0.0088\frac{h}{b}m\rho_s + 0.1\right) \tag{3.113}$$

where ρ_s is the reinforcement percentage; b, h the section dimension; m is the ratio between longitudinal and transversal reinforcement and $m \leq 1.5$. The details of parametric study as well as the explication of two proposed formulation following the repartition of reinforcement bars over the cross-section are described clearly in Section 4.3.

3.7 Conclusions

In this chapter, an enhanced multi-fiber 3D beam element for RC members subjected to combined loadings has been developed. The proposed model is able to take into account the material nonlinearity, the warping effect of cross-section, the contribution of transversal reinforcement, and eventually the concrete confinement.

Between two enhanced approaches, the Saint-Venant warping function's formulation is simpler and requires less calculation time. However, the use of the formulation developed in Section 3.3.2 is limited to solid cross-section. For a thin-walled cross-section, additional DoFs need to be added and as a consequence, change considerably the variational formulation in Section 3.4.1. In the other hand, the development of Lagrange polynomials approach is quite complex and requires more coding functions as well as calculation time, however its application is general and can be used to study the distortion phenomenon, as described in Section 3.3.3.2. The variational formulation developed in Section 3.4.2 is also general and independent to the type of cross-section.

Regarding the constitutive model, the contribution of transversal reinforcement is taken into account by the iteration process satisfying internal equilibrium between concrete and stirrup, while the static condensation in 2D and 3D zone ensure the coupling between multi-axial efforts. The concrete behavior is based on the original MCFT [110], as described in Section 2.4.1.1, however other suitable uniaxial stress-strain relationships in compression and tension can also be applied in the constitutive model of the proposed formulation, such as Stevens et al.'s model [103].

The model formulation was written in Matlab, thanks to its powerful for handling matrix expressions. The model code can be further translated to more efficient languages such as FORTRAN, C++ or Python.

Chapter 4

Numerical analysis of Concrete and RC members under Pure Torsion

The present chapter is dedicated to the numerical analysis of concrete and RC members subjected to pure torsion. An enhanced multi-fiber 3D beam model is proposed. This model takes into account all the aspects of torsional effects, including the warping phenomenon, the behavior before and after cracking as well as the contribution of stirrups. It is worth to note that this proposed model is the improved version of the multi-fiber frame model proposed by Navarro Gregori [76], taking advantage of its sectional discretization which is very suitable for the specific behavior of RC elements under pure torsion. For the constitutive model of concrete, the MCFT is employed, due to its suitability for multi-fiber section discretization, as well as its simplicity and its wide use in engineering applications. A new constitutive model for concrete under torsional effect will be proposed based on the fact that numerical cracking torsional moments are reduced about half of the experimental values when using the original MCFT as concrete constitutive model [53]. The numerical examples are then compared to the analytical and experimental results for the validation of the proposed model.

The Chapter is organized as follow. A brief summary of torsion theory and the expression of warping function is presented firstly in Section 4.1. Next, the element formulation and the proposed constitutive model of concrete, which are specifically developed for RC members under pure torsion, are respectively described in Section 4.2 and Section 4.3. The following sections (4.4 and 4.5) deal with the numerical examples in elastic and inelastic material regime. Finally, Section 4.6 summarizes the Chapter and offers some conclusions.

4.1 Theory of Torsion

The problem of torsion in a straight member was first investigated in 1784 by Coulomb [27], during his study of the property of electric charges. When carrying out the torsional oscillation of a weight suspended on a wire, Coulomb found that torsional moment is proportional to the angle of twist. This discovery was then introduced in a theoretical equation for torsion by Navier [77] in 1826, in which the proportionality between torque T and twist angle θ is represented by a constant called the torsional rigidity. This constant is equal to the multiplication of the modulus of rigidity (shear modulus) G and the polar moment of inertia I_p:

$$T = GI_p\theta \tag{4.1}$$

However, this theory was limited to members with a circular section: torsional tests made by Duleau [32] in 1820 noted a 20% difference between the moduli of rigidity for a circular and a square section. This difference was then explained by a change of sectional rigidity, caused by a particular phenomenon called *warping*, meaning that the cross sections, under torsional effect, are deformed and come out of their original plan. In Figure 4-1, the signal + means that the cross-section come out following the positive direction of x axis, while the signal − indicates that the warping follows the negative direction of x axis. The iso-curves in solid represent the points having the same warping magnitude in the positive direction, while the iso-curves in dashed line represent the points having the same warping magnitude in the negative direction.

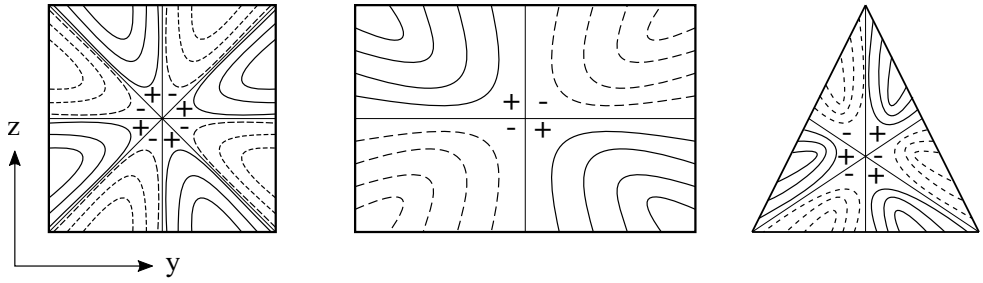

Figure 4-1 – Warping for several non circular section [97].

This warping phenomenon was first solved by Saint-Venant in 1855 using mathematical tools included the Fourier series and the theory of elasticity. For the problem of torsion of a straight element with an arbitrary cross section, Saint-Venant proposed to substitute the polar moment I_p in Equation (4.1) by a new constant J called *Saint-Venant's torsional constant*, whose expression is explicit and can be widely found in the literature. The

product of the shear modulus G and Saint-Venant torsional constant J is defined as the *torsional rigidity*. For a beam of length L, the quotient of the torsional rigidity and the beam length L is defined as the *torsional stiffness*.

To represent the warping phenomenon, although the use of torsional constant is explicit and can be easily formulated, its use is limited to sections of regular shape. Moreover, since this parameter is computed for the whole section, it is impossible to apply this constant into a finite element sectional fiber approach. In this case, Saint-Venant also proposed another approach to represent the warping phenomenon, using a function called *Saint-Venant warping function* which depends on the coordinates of material points in the cross-section. This function is formulated by a semi-inverse method, and is restricted to linear behavior with two assumptions:

1. Cross-section shape remains unchanged after twisting. In other words the distortion phenomenon is neglected;

2. Warping of the cross-section is identical throughout the length of the member. This assumption recalls to the problem of uniform torsion.

According to Saint-Venant, the warping function is described as a solution of the Neumann problem:

$$\frac{\partial^2\psi}{\partial y^2} + \frac{\partial^2\psi}{\partial z^2} = 0 \text{ in } \Omega \text{ (Laplace equation)} \tag{4.2a}$$

$$\frac{\partial\psi}{\partial y}n_y + \frac{\partial\psi}{\partial z}n_z = zn_y - yn_z \text{ on } \partial\Omega \text{ (Neumann boundary conditions)} \tag{4.2b}$$

where Ω represent the domain of cross section and $\partial\Omega$ its boundary, n_y and n_z are the vector normal to the boundary. Exact solution can be expressed for any arbitrary kind of solid cross-section, for example the rectangular cross-section [39]:

$$\psi(y,z) = \frac{4}{\pi^3}\sum_{n=1}^{\infty}\frac{(-1)^{n-1}}{(2n-1)^3}\left[b^2\frac{\sinh\left(\frac{2n-1}{b}\pi y\right)}{\cos\left(\frac{2n-1}{b}\pi\frac{h}{2}\right)}\sin\left(\frac{2n-1}{b}\pi z\right) - h^2\frac{\sinh\left(\frac{2n-1}{h}\pi z\right)}{\cos\left(\frac{2n-1}{h}\pi\frac{b}{2}\right)}\sin\left(\frac{2n-1}{h}\pi y\right)\right] \tag{4.3}$$

where b is the section width and h is the section height, with $b \leq h$. A simplified exponential expression was proposed by Xu et al. [115]:

$$\psi(y,z) = A_n\exp\left[\beta_{1n}\left(y-\frac{b}{2}\right)\right] + B_n\exp\left[-\beta_{2n}\left(y+\frac{b}{2}\right)\right] - \frac{\lambda C_n}{b\alpha^2\xi_n^2} - yz \tag{4.4}$$

where h is the section height; α is the shear modulus ratio; λ is the gradient factor; and

β_{1n}, β_{2n}, C_n and ξ_n are defined as follows:

$$\beta_{1n} = \sqrt{\frac{\lambda^2}{4h^2} + \alpha^2\xi_n^2} - \frac{\lambda}{2h}; \quad \beta_{2n} = \sqrt{\frac{\lambda^2}{4h^2} + \alpha^2\xi_n^2} + \frac{\lambda}{2h}; \quad \xi_n = \frac{n\pi}{b}; \quad C_n = \frac{8b}{\pi^2}\frac{(-1)^{\frac{n-1}{2}}}{n^2}$$

with b is the section width and $b \leq h$. If the material is isotropic, $\lambda = 0$, in this case:

$$A_n = \frac{[1 - \exp(-h\beta_{2n})]\, C_n}{\beta_{1n}\{1 - \exp[-h(\beta_{1n} + \beta_{2n})]\}}; \quad B_n = \frac{[1 - \exp(-h\beta_{1n})]\, C_n}{\beta_{2n}\{\exp[-h(\beta_{1n} + \beta_{2n})] - 1\}};$$

In this exponential expression, the index n is impair ($n = 1, 3, 5, ...$).

Instead of warping function $\psi(y, z)$, Prandtl [86] also introduced a stress function $\Phi(y, z)$ to represent the warping, with simpler equations for the boundary condition and for the torsional moment. Otherwise, there are other approaches to interpolate the warping function to solid or composite cross-section, as described in Chapter 2. Solving the warping problem is indispensable to figure out the torsional response of a straight element with an arbitrary cross section in the elastic behavior range.

4.2 Beam FE formulation for Pure Torsion

Under pure torsion, the torsional rotation θ_x is the only generalized displacement to be considered at sectional level, and the vector of nodal displacements reduces from 12 elements to only 2 values of nodal twist angle: $\mathbf{q}_{e,t} = \begin{pmatrix} \theta_x^I & \theta_x^J \end{pmatrix}^T$. Here as sequel, the sub-index t is used to denoted the parameters under pure torsion. Using the kinematic relation in Equation (3.2), the twist angle θ_x and the twist rate κ_x are then equal to:

$$\theta_x(x) = \frac{1-x}{L}\theta_x^I + \frac{x}{L}\theta_x^J = \begin{pmatrix} \frac{1-x}{L} & \frac{x}{L} \end{pmatrix} \begin{pmatrix} \theta_x^I \\ \theta_x^J \end{pmatrix} = \mathbf{N}_{s,t}(x)\mathbf{q}_{e,t} \tag{4.5a}$$

$$\kappa_x = \frac{\partial\theta_x(x)}{\partial x} = \begin{pmatrix} -1 & 1 \end{pmatrix} \begin{pmatrix} \theta_x^I \\ \theta_x^J \end{pmatrix} = \mathbf{B}_{s,t}\mathbf{q}_{e,t} \tag{4.5b}$$

$\mathbf{N}_{s,t}(x)$ and $\mathbf{B}_{s,t}(x)$ are two interpolation matrices in pure torsion formulation. Hereafter, the sectional and element state determinations are described following two approaches for enhanced displacement field: using Saint-Venant warping function and using Lagrange polynomials.

4.2.1 Using Saint-Venant warping function

Under the hypothesis of small displacements, from Equation (3.17) the following kinematic relation is established for the material displacement field under pure torsion according to Saint-Venant torsional theory:

$$\begin{aligned} U_t(x,y,z) &= \kappa_x \psi(y,z) \\ V_t(x,y,z) &= -z\theta_x(x) \\ W_t(x,y,z) &= y\theta_x(x) \end{aligned} \tag{4.6}$$

The material strains, grouped in a single strain vector $\mathbf{e}_{f,t}(y,z)$, are evaluated as follows:

$$\left.\begin{aligned} \varepsilon_{xx,t} &= 0 \\ \gamma_{xy,t} &= \left(-z + \frac{\partial \psi}{\partial y}\right)\kappa_x \\ \gamma_{xz,t} &= \left(y + \frac{\partial \psi}{\partial z}\right)\kappa_x \end{aligned}\right\} \quad \Rightarrow \mathbf{e}_{f,t}(y,z) = \mathbf{a}_{f,t}(y,z)\kappa_x \tag{4.7}$$

with the definition of the compatibility matrix as follows:

$$\mathbf{a}_{f,t}(y,z) = \begin{pmatrix} 0 & -z + \dfrac{\partial \psi}{\partial y} & y + \dfrac{\partial \psi}{\partial z} \end{pmatrix}^T \tag{4.8}$$

Once the strain vector $\mathbf{e}_{f,t}$ is obtained at each material point, an appropriate material law is applied to determine the material stresses, which are collected in a single stress vector $\mathbf{s}_{f,t} = \begin{pmatrix} \sigma_{xx} & \tau_{xy} & \tau_{xz} \end{pmatrix}^T$. The constitutive relation can be established with the aid of the material constitutive matrix $\mathbf{k}_f$ as in Equation (3.36):

$$\delta \mathbf{s}_{f,t} = \mathbf{k}_{f,t} \delta \mathbf{e}_{f,t} \tag{4.9}$$

Under pure torsion, the mechanical and constitutive model is based on the one described in Section 3.5 and will be specifically developed for RC members in Chapter 4.

Then, the element equilibrium is imposed by means of the principle of virtual work as in Equation (3.37):

$$\delta \mathbf{W}_i = \delta \mathbf{W}_e \Rightarrow \iiint_V \delta \mathbf{e}_{f,t}^T \mathbf{s}_{f,t} dV = \delta \mathbf{q}_{e,t}^T \mathbf{Q}_{e,t} + \int_L \delta\theta_x(x) \mathbf{T}_u dx \tag{4.10}$$

By exploiting the left hand of Equation (4.10), the following expression is obtained for

the torsional moment:

$$M_{x,s}(x) = \iint_A \mathbf{a}_{f,t}^T \mathbf{s}_{f,t} dA = \iint_A \mathbf{a}_{f,t}^T \mathbf{k}_{f,t} \mathbf{a}_{f,t} dA \kappa_x = \mathbf{K}_{s,t} \kappa_x \tag{4.11}$$

with $\mathbf{K}_{s,t}$ defined as sectional stiffness matrix. Then, with the aid of equations (4.5a) and (4.5b), the Saint-Venant warping function approach gives the following expression for the element equilibrium in Equation (4.10):

$$\mathbf{K}_{e,t} \mathbf{q}_{e,t} = \mathbf{M}_{x,e} + \int_L \mathbf{N}_{s,t}^T \mathbf{T}_u dx \tag{4.12}$$

with $\mathbf{M}_{x,e}$ the nodal torsional moments and $\mathbf{K}_{e,t}$ is defined as the element stiffness matrix:

$$\mathbf{K}_{e,t} = \int_L \mathbf{B}_{s,t}^T \mathbf{K}_{s,t} \mathbf{B}_{s,t} dx \tag{4.13}$$

Similar to the proposed formulation for combined loading in Chapter 3, the element state determination is completed with the calculation of the stiffness matrix $\mathbf{K}_{e,t}$ and the nodal torsional moment $\mathbf{M}_{x,e}$. In this approach, the element DoFs is only 2 instead of 12 in the case of RC members subjected to combined loading.

4.2.2 Using Lagrange polynomials

In this approach, from Equation (3.6) and (3.21), we obtain:

$$\begin{aligned} U_t(x,y,z) &= \hat{\mathbf{L}}(x) \hat{\mathbf{S}}(y,z) \mathbf{U}^e \\ V_t(x,y,z) &= -z\theta_x(x) \\ W_t(x,y,z) &= y\theta_x(x) \end{aligned} \tag{4.14}$$

with $\hat{\mathbf{L}}(x)$ and $\hat{\mathbf{S}}(y,z)$ the interpolation matrices as in Equation (3.21). The material strains can be evaluated as follows:

$$\left.\begin{aligned} \varepsilon_{xx,t} &= \frac{\partial \hat{\mathbf{L}}(x)}{\partial x} \hat{\mathbf{S}}(y,z) \mathbf{U}^e \\ \gamma_{xy,t} &= -z\kappa_x + \hat{\mathbf{L}}(x) \frac{\partial \hat{\mathbf{S}}(y,z)}{\partial y} \mathbf{U}^e \\ \gamma_{xz,t} &= y\kappa_x + \hat{\mathbf{L}}(x) \frac{\partial \hat{\mathbf{S}}(y,z)}{\partial z} \mathbf{U}^e \end{aligned}\right\} \quad \Rightarrow \mathbf{e}_{f,t}(x,y,z) = \mathbf{a}_{f,t}^p(y,z)\kappa_x + \mathbf{a}_{f,t}^e(x,y,z)\mathbf{U}^e \tag{4.15}$$

with the definition of the enhanced compatibility matrices:

$$\mathbf{a}^{p}_{f,t}(y,z) = \begin{pmatrix} 0 & -z & y \end{pmatrix}^{T}; \qquad \mathbf{a}^{e}_{f,t}(x,y,z) = \frac{\partial \mathbf{L}(x)}{\partial x}\mathbf{S}_{x}(y,z) + \mathbf{L}(x)\mathbf{S}_{yz}(y,z) \tag{4.16}$$

where $\mathbf{a}^{e}_{f,t}(x,y,z)$ is a matrix of $(3 \times n_w.s_w)$ which has the same expression with the compatibility matrix $\mathbf{a}^{e}_{f}(x,y,z)$ in Equation (3.35). Similar to Section 3.4.2, in this approach all the variables are separated into the basic and additional set, due to the introduction of additional DoFs. The following expression is obtained for the torsional moment:

$$\begin{aligned} M_{x,s}(x) &= \iint_A \mathbf{a}^{pT}_{f,t}\mathbf{s}_{f,t}dA = \iint_A \mathbf{a}^{pT}_{f,t}\mathbf{k}_{f,t}\left(\mathbf{a}^{p}_{f,t}\kappa_x + \left(\mathbf{a}^{e}_{f,t}\right)\mathbf{U}^{e}\right)dA \\ &= \iint_A \mathbf{a}^{pT}_{f,t}\mathbf{k}_{f,t}\mathbf{a}^{p}_{f,t}dA\kappa_x + \iint_A \mathbf{a}^{pT}_{f,t}\mathbf{k}_{f,t}\mathbf{a}^{e}_{f,t}dA\mathbf{U}^{e} \\ &= \mathbf{K}^{bb}_{s,t}\kappa_x + \left(\mathbf{K}^{bax}_{s,t}\frac{\partial \mathbf{L}(x)}{\partial x} + \mathbf{K}^{bayz}_{s,t}\mathbf{L}(x)\right)\mathbf{U}^{e} \end{aligned} \tag{4.17}$$

and the additional sectional forces can be also expressed as follows:

$$\begin{aligned} \mathbf{D}^{ax}_{s,t}(x) &= \iint_A \mathbf{S}^{T}_{x}(y,z)\mathbf{s}_{f,t}dA = \mathbf{K}^{axb}_{s,t}\kappa_x + \left(\mathbf{K}^{ax}_{s,t}\frac{\partial \mathbf{L}(x)}{\partial x} + \mathbf{K}^{axyz}_{s,t}\mathbf{L}(x)\right)\mathbf{U}^{e} \\ \mathbf{D}^{ayz}_{s,t}(x) &= \iint_A \mathbf{S}^{T}_{yz}(y,z)\mathbf{s}_{f,t}dA = \mathbf{K}^{ayzb}_{s,t}\kappa_x + \left(\mathbf{K}^{ayzx}_{s,t}\frac{\partial \mathbf{L}(x)}{\partial x} + \mathbf{K}^{ayz}_{s,t}\mathbf{L}(x)\right)\mathbf{U}^{e} \end{aligned} \tag{4.18}$$

The expressions of the 9 sectional stiffness matrices in Equation (4.17) and (4.18) are similar to Equation (3.56), unless the replacement of the compatibility matrix $\mathbf{a}^{p}_{f,t}$ in the matrix $\mathbf{a}^{p}_{f}$. Then, the element equilibrium in Equation (4.10) can be expressed as follows:

$$\begin{bmatrix} \mathbf{K}^{bb}_{e,t} & \mathbf{K}^{ba}_{e,t} \\ \mathbf{K}^{ab}_{e,t} & \mathbf{K}^{aa}_{e,t} \end{bmatrix} \begin{pmatrix} \mathbf{q}_{e,t} \\ \mathbf{U}^{e} \end{pmatrix} = \begin{pmatrix} \mathbf{M}_{x,e} + \int_L \mathbf{N}^{T}_{s,t}\mathbf{T}_{u}dx \\ 0 \end{pmatrix} \tag{4.19}$$

with the expression of sub-element stiffness matrix similar to Equation (3.63), and a static condensation to determine the values of the enhanced displacements $\mathbf{U}^{e}$ and the expression of the element stiffness matrix:

$$\begin{aligned} \mathbf{U}^{e} &= -\mathbf{K}^{aaT}_{e,t}\mathbf{K}^{ab}_{e,t}\mathbf{q}_{e,t} \\ \mathbf{K}_{e,t} &= \mathbf{K}^{bb}_{e,t} - \mathbf{K}^{ba}_{e,t}\mathbf{K}^{aaT}_{e,t}\mathbf{K}^{ab}_{e,t} \end{aligned} \tag{4.20}$$

And the element equilibrium in Equation (4.10) can be rewritten as follows:

$$\mathbf{K}_{e,t}\mathbf{q}_{e,t} = \mathbf{Q}_{e,t} + \int_L \mathbf{N}^{T}_{s,t}\mathbf{T}_{u}dx \tag{4.21}$$

In this approach, the element DoFs is $2 + s_w.n_w$ instead of $12 + n_w.s_w$.

4.3 Proposed constitutive model of concrete under Pure Torsion

4.3.1 RC members under Pure Torsion

The mechanical model for RC members under pure torsion is based on the one proposed in Chapter 3, using the same section discretization and the regional constitutive model as described in Section 3.5, with some major modifications.

The first modification comes from the special behavior of RC members under pure torsion. For a RC members, the torsional response can be divided into 2 different phases: before and after cracking of concrete.

- Before cracking, the response of the section is considered elastic and the behavior is very similar to that of a plain concrete member, which can be predicted by the Saint-Venant torsional theory.

- After cracking, the material is not continuous anymore, the theory of elasticity becomes useless and a new mechanism is required to interpret the torsional response in this phase, as described in Chapter 2.

From the concept of truss model as described in Section 2.3 and the experimental test results from Hsu [45] and Onsongo [82], the behavior of RC member after cracking can be assumed to be carried out by a tube of hollow section. This special behavior leads to the first modification of the mechanical model for RC members under pure torsion: the behavior of 3D-zone of the concrete in the section core is set to zero after cracking. The non-linear torsional response after cracking therefore depends only on the behavior of the 2D-zone and the 3D-zone at the four corners of section, and the width of 2D-zone, called the *effective wall thickness*, plays a significant role. The formulation of the effective wall thickness has already been realized in Section 3.6, while the process of determination will be described in the following section.

The second modification needs to be carried out concerning the behavior law of concrete under pure torsion. In compression, the same relationship as the original MCFT (or other formulations) may be retained, however, in tension, the concrete stress-strain relationship must be reconsidered. This is because, as mentioned above in Chapter 1 and

Section 2.3.3, in the original MCFT and/or in the constitutive model for RC members of Belarbi & Hsu [9], the tensile relationship is based on experimental tests of shear panels (the Shell Element Tester at the University of Toronto and/or the Universal Panel Tester at the University of Houston), so not really suitable for the torsional behavior. Indeed, Jeng & Hsu [53] recorded that the cracking torsional moment, calculated by an analytical model based on the constitutive model of Belarbi & Hsu, is much smaller than the experimental values. By conducting a systematic parametric study with several experimental tests, another tensile constitutive law was proposed by Jeng & Hsu (Figure 4-2):

$$E_{cr} = 5620\sqrt{f_c} \quad (f_c \text{ in MPa}) \tag{4.22a}$$

$$\varepsilon_{cr} = 0.000116 \tag{4.22b}$$

$$f_{cr} = E_{cr}\varepsilon_{cr} \tag{4.22c}$$

where E_{cr} is the proposed elastic modulus; f_{cr} is the tensile concrete cracking strength; ε_{cr} is the cracking strain. Before cracking, the tensile stress-strain relationship is assumed elastic linear:

$$\text{For } \varepsilon_1 \leq \varepsilon_{cr} : \sigma_1 = E_c\varepsilon_1 \tag{4.23}$$

while after cracking, the tension-stiffening effect is taken into account by:

$$\text{For } \varepsilon_1 > \varepsilon_{cr} : \sigma_1 = f_{cr}\left(\frac{\varepsilon_{cr}}{\varepsilon_1}\right)^{0.4} \tag{4.24}$$

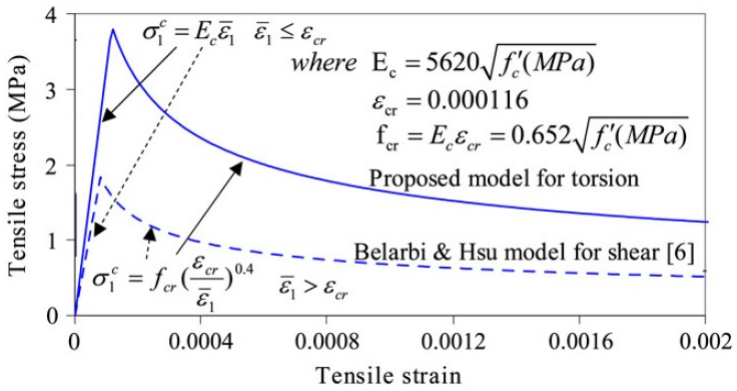

Figure 4-2 – Tensile stress-strain relationship of concrete proposed by Jeng & Hsu [53] .

This new tensile relationship is developed from the constitutive laws of softened concrete in biaxial tension-compression proposed by Belarbi & Hsu [9], and were then used in the Softened Membrane Model for Torsion (SMMT) by Jeng & Hsu [53], as described in

Section 2.3.3. As can be seen in Figure 4-2, the main difference from the original tensile law of Belarbi & Hsu is a stronger cracking strength of concrete: the pre-cracking stiffness is 45% higher, the concrete cracking strength f_{cr} is 110% stronger. The cracking strain ε_{cr} comes from observations of tests for concrete members in uniaxial tension, in which the failure of concrete occur at a strain of approximately 0.0001.

4.3.1.1 Author's observations

The proposed tensile relationship for concrete is modified with respect to the tensile relationship used in the proposed constitutive model in Section 3.5, which is based on the MCFT as described in Section 2.4.1.1. During the calibration process, the proposed formulation is expressed based on the following observations:

1. According to the series of torsional tests carried out by Hsu [45], the cracking torque of a RC beam T_{cr} is a mild function of reinforcement steel percentage ρ_s and the cracking torque of a corresponding plain concrete beam (with the same cross-section dimension) T_{cr}^{PC}.

2. The cracking torque of a plain concrete beam T_{cr}^{PC} can be determined by several theories in the literatures, such as elastic theory [97], plastic theory [79] or skew-bending theory [45]. In theses formulations, T_{cr}^{PC} depend on the tensile strength of concrete f_t and the dimension of cross-section.

   From these two observations, we can conclude that, similar to the proposition in the model of Jeng & Hsu, the concrete cracking strength f_{cr} must be increased and this parameter should be a function of the concrete strength, the reinforcement ratio and the cross-section dimension. Moreover, from the first observation, it is reasonable to express f_{cr} as a function of the cracking strength of the corresponding plain concrete members under pure torsion f_{cr}^{PC}, which has already been proposed by Hsu in an empirical equation [45]:

$$f_{cr}^{PC} = 0.76\left(1+\frac{6452}{b^2}\right) f_c^{1/3} \text{ (MPa)} \quad \text{for} \quad b > 100 \text{ (mm)} \tag{4.25a}$$

$$f_{cr}^{PC} = 6.13\left(\frac{f_c}{b}\right)^{1/3} \text{ (MPa)} \quad \text{for} \quad b \leq 100 \text{ (mm)} \tag{4.25b}$$

   where f_c is the cylinder compressive strength; h, b are the section height and width.

3. According to experimental tests, the impact of longitudinal reinforcement steel bars

to torsional strength is small, but can not be neglected [45].

In the proposed model, the longitudinal reinforcement bars only have an impact on the normal stress state, so do not have any contribution to the torsional response. Indeed, experimental tests by Hsu [45] show that, for concrete members with longitudinal steel only, the effect of the longitudinal reinforcements is small, and the cracking torque is very similar to that of a plain concrete member. This ineffectiveness can be explained by the location of longitudinal steels bar, which are always placed at the corners of section beam where the shear stress is zero according to Saint-Venant's stress distribution (Figure 4-3a).

However, for RC members with longitudinal steel and stirrups, the cracking torque might be a function of the total steel percentage (Figure 4-3b). Hsu also remarked that a better repartition (or distribution) of longitudinal reinforcement over the cross-section will increase the cracking torque somewhat: it is the case of beam G6, G7 and G8 in which the longitudinal bars also located at the center of the section.

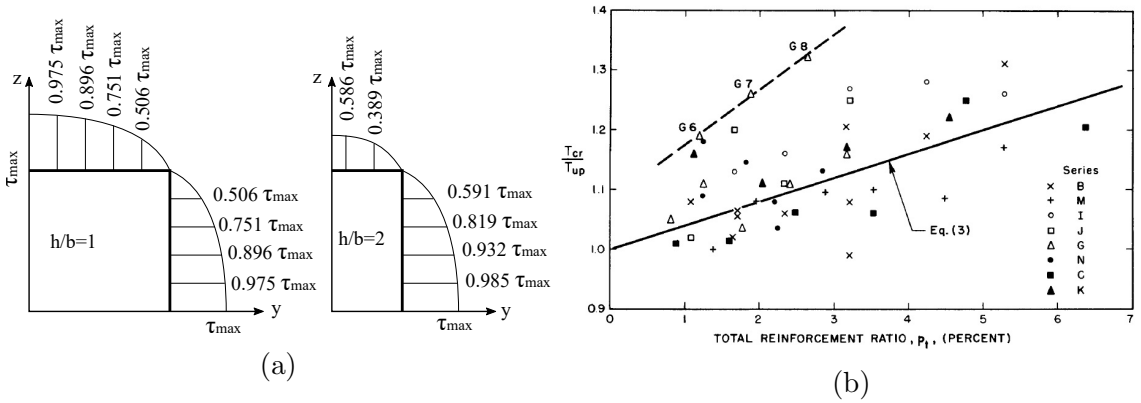

Figure 4-3 – (a) Distribution of Saint-Venant stresses along edges, the shear stress at each point is calculated by $\sqrt{\tau_{xy}^2 + \tau_{xz}^2}$ [46]. (b) Cracking torque as a function of reinforcement ratio in Hsu tests (1968) [45].

Moreover, during the calibration process, the authors also noted that the contribution of reinforcement bars to torsional strength comes not only from their percentage, but also from their repartition over the cross-section. Indeed, an usual repartition of longitudinal steel at four corners of the section (Figure 4-4a) can result in a different cracking torque than a repartition with additional longitudinal steel bars along the perimeter (Figure 4-4b). Therefore, the reinforcement percentage ρ_s must become an indispensable parameter for the formulation of cracking strength f_{cr}, and the latter should be distinguished for different cases of longitudinal steel repartitions.

(a) Usual repartition of longitudinal reinforcement at corners.

(b) Repartition with additional longitudinal reinforcement along the perimeter.

Figure 4-4 – Two case of distribution of longitudinal reinforcement steel bars.

4.3.1.2 Proposed formulation

From the three observations above, the following formulations are proposed for the concrete cracking strength of RC members under pure torsion:

- For an usual repartition of reinforcement bars concentrated at four corners:

$$f_{cr} = f_{cr}^{PC}\left(0.38\frac{b}{h}\rho_s + 1\right) \tag{4.26}$$

- For a repartition with additional reinforcement bars along the perimeter:

$$f_{cr} = f_{cr}^{PC}\left(0.22\frac{b}{h}\rho_s + 1.3\right) \tag{4.27}$$

The authors decided to keep the same formulation of the elastic modulus of concrete under torsion: $E_c = 5620\sqrt{f_c}$ (f_c in MPa), and the cracking strain is determined in function of f_{cr} and E_c as a result: $\varepsilon_{cr} = \dfrac{f_{cr}}{E_c}$. Comparing to the original tensile relationship of the MCFT in Figure 2-19b, Chapter 2, the proposed formulation gives a higher cracking strain and strength, while the expression of the tensile-stiffening phenomenon after cracking has been changed to the formulation proposed by Jeng in Equation (4.24) (Figure 4-5). It is worth to note that this proposed constitutive model is the improved version of the constitutive model proposed by Jeng [53]. A comparison between two versions will be presented below to validate the pertinence of the new model.

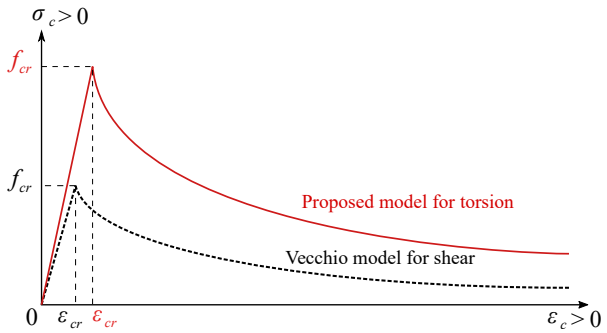

Figure 4-5 – Proposed tensile relation for torsion compared to the tensile relation for shear model in the original MCFT [110].

4.3.1.3 Calibration study

Although this new model for torsion has been showed some satisfactory responses in the simulation compared to experimental tests, the choice of cracking strain is a bit unnatural to the authors. This is why, the authors decided to proposed another tensile constitutive law for RC members of rectangular cross-section under pure torsion. The proposed tensile relationship is formulated using a parametric calibration which was studied by the authors in 60 specimens of experimental tests, with various concrete strengths, section dimensions and reinforcement ratios:

- *Test by Hsu in 1963 at the Structural Laboratory of the Portland Cement Association* [45]: 40 specimens from 8 beam series: 9 of Series B (B2-B10), 6 of Series C (C1-C6), 8 of Series G (G1-G8), 6 of series M (M1-M6), 6 of Series N (N1-N4, N1a, N2a) 5 of Series I (I2-I6). The cross-dimensions and reinforcement distributions are showed in Figure 4-6, all the specimens have a concrete cover thickness of 20 mm, while the material properties of concrete and steel can be found in Appendix 7.2.

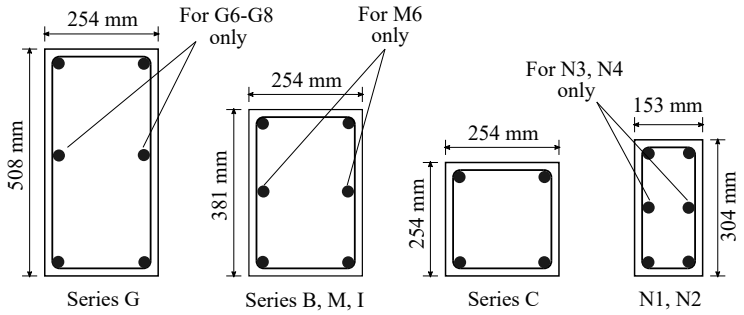

Figure 4-6 – Cross-section dimensions in the test of Hsu. [45].

- *Test by Csikos & Hegedus in 1998 at the Technical University of Budapest* [29]: 12 specimens from 4 beam series B, C, D and E, each consist of three specimens. All the beams had the same outer dimensions ($h \times b \times L = 130 \times 130 \times 2000$) (mm), while the reinforcement ratios varied both in the longitudinal and the transversal directions. The loads are applied by steel arms which were attached to both ends of the beam (Figure 4-7a), while the twist at mid-span section was measured by the shift of attached arms. The details of material properties and the reinforcement distributions of each series can be found in Appendix 7.2.

- *Test by Lee et al. in 2008 at the Sungkyunkwan University* [63]: 8 specimens from 2 beam series: T1-1 to T1-4 and T2-1 to T2-4, with the same outer dimensions ($h \times$

$b \times L = 350 \times 300 \times 3000$) (mm) and the concrete cover thickness of 20 mm. Similar to the test at the Technical University of Budapest, the reinforcement percentage and disposition varied both in the longitudinal and the transversal directions, whose details can be found in Appendix 7.2. The angle of twist is measure by the LVDT (Linear Variable Differential Transformer) sensor, whose location and the loading condition of test can be found in Figure 4-7b. During the test, specimens were loaded monotonically by displacement control method.

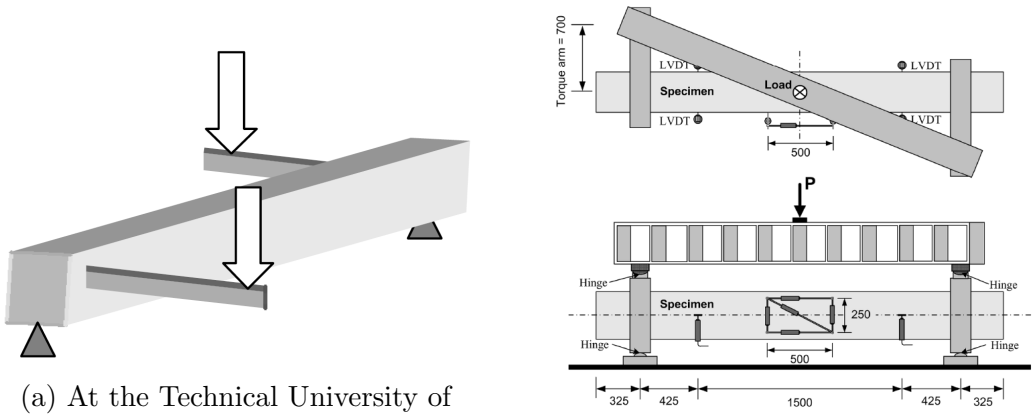

(a) At the Technical University of Budapest [29].

(b) At the Sungkyunkwan University [63].

Figure 4-7 – Layout of the torsion tests.

The calibration process begins by collecting all the experimental data, including the beam dimensions, disposition and dimension of reinforcement steel, material properties of concrete and steel, experimental values of cracking and ultimate torque. Then, according to the author's observation above, the following variables have been chosen for the parametric formulation of determining the concrete tensile strength under torsion f_{cr} and the effective wall thickness t_e:

- Cracking strength of plain concrete members under torsion f_{cr}^{PC}.
- Reinforcement percentage (including longitudinal, transversal steels and the total ratio): ρ_{sl}, ρ_{st} and ρ_s.
- The ratio between ρ_{sl} and ρ_{st}: $m = \dfrac{\rho_{sl}}{\rho_{st}}$.
- The ratio between section height and width: $\dfrac{h}{b}$.

4.3.1.3.1 Calibration of the concrete tensile strength f_{cr} This parameter was determined in the phase before cracking of concrete, knowing that in this phase the torsional behavior of RC member is similar to that of a corresponding plain concrete

member. The cross-section discretization contains therefore only the 3D-zone of concrete fiber.

In the first time, for each specimen of test, an initial and arbitrary value of f_{cr} (f_{cr}^{o}) is chosen to evaluate the initial numerical value of cracking torque T_{cr} obtained by the proposed model. Then, considering the experimental values, this initial value f_{cr}^{o} is modified/calibrated in order to obtain the new values of T_{cr}. This step must be performed until the values of T_{cr} are close to the experimental ones, in other word the relative difference between experimental and numerical values are as small as possible:

$$R_{cr} = \frac{T_{cr} - T_{cr}^{exp}}{T_{cr}^{exp}} 100\%$$

The value of f_{cr} at this moment is called as *calibrated value* f_{cr}^{c}.

Next, all the values of f_{cr}^{c} and the variables mentioned above are plotted in a diagram in order to determine a reasonable relationship between them. The proportion of f_{cr}^{c} and f_{cr}^{PC} (in Equation 4.25) is put in the vertical axis, while in the horizontal axis, several possibilities have been tested, such as $\frac{h}{b}\rho_s$, $\frac{h}{b}\rho_{st}$ or $\frac{b}{h}m\rho_s$, etc., in order to select the best trend fitting for two set of data. For the sake of simplicity, a linear fitting is applied for the data set, and the best result has been selected between various possibilities in the horizontal axis (Figure 4-8, 4-9 and 4-10). The best result can be found for the set of $\frac{b}{h}\rho_s$ as in Equation (4.26) and (4.27), and the final expression could be therefore deduced.

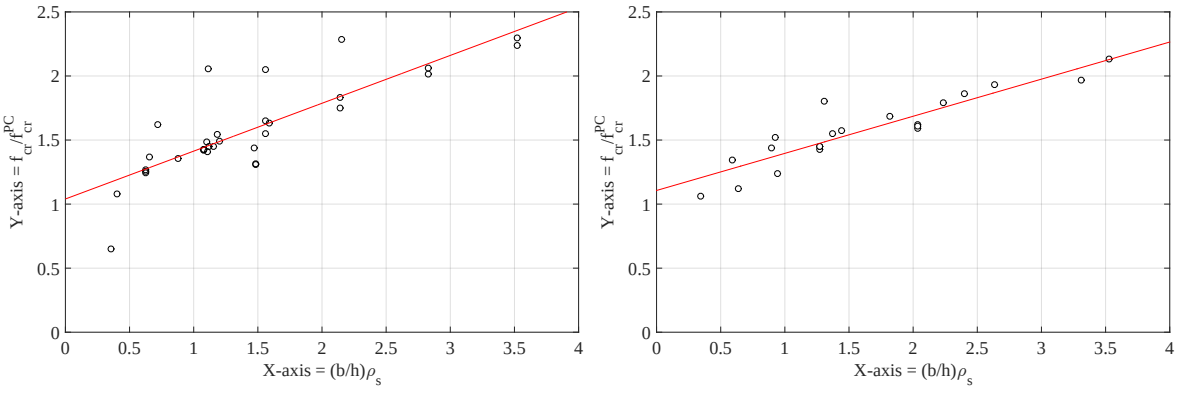

(a) Usual repartition of longitudinal reinforcement at corners.

(b) Repartition with additional longitudinal reinforcement along the perimeter.

Figure 4-8 – Linear fitting in the calibration process of determining f_{cr}, with $\frac{b}{h}\rho_s$ in the horizontal axis.

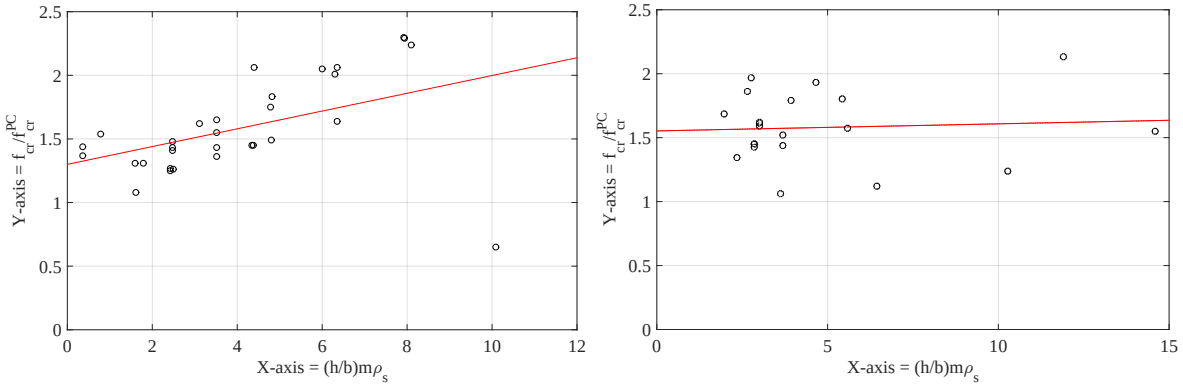

(a) Usual repartition of longitudinal reinforcement at corners.

(b) Repartition with additional longitudinal reinforcement along the perimeter.

Figure 4-9 – Linear fitting in the calibration process of determining f_{cr}, with $\frac{h}{b}m\rho_s$ in the horizontal axis.

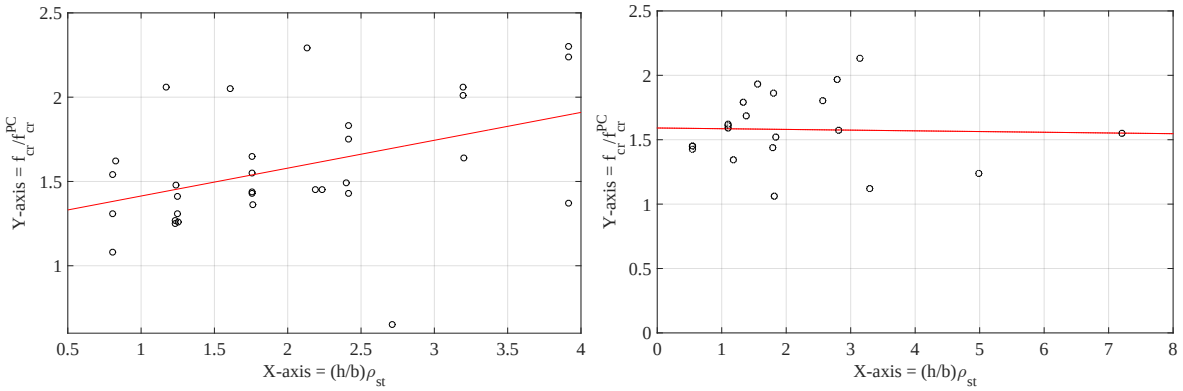

(a) Usual repartition of longitudinal reinforcement at corners.

(b) Repartition with additional longitudinal reinforcement along the perimeter.

Figure 4-10 – Linear fitting in the calibration process of determining f_{cr}, with $\frac{h}{b}\rho_{st}$ in the horizontal axis.

4.3.1.3.2 Calibration of the effective wall thickness t_e The determination of this parameter was carried out in the phase after cracking of concrete, knowing that the torsional behavior of RC member in this phase depends strongly on this parameter. In this phase, the discretization of cross-section contains 3 zones as described in Section 3.5. The same process has been applied to the determination of the effective wall thickness t_e, but this time the value of ultimate cracking torque T_u is used to evaluate the *calibrated* value of t_e, the relative difference between experimental and numerical values is therefore:

$$R_u = \frac{T_u - T_u^{exp}}{T_u^{exp}} 100\%$$

A linear fitting is also applied for the data set, with the proportion of t_e and the section width b in the vertical axis and the best fitting set values ($\frac{h}{b}m\rho_s$ as in Equation (3.112)

and (3.113) in the horizontal axis (Figure 4-11), and the final expression could be deduced.

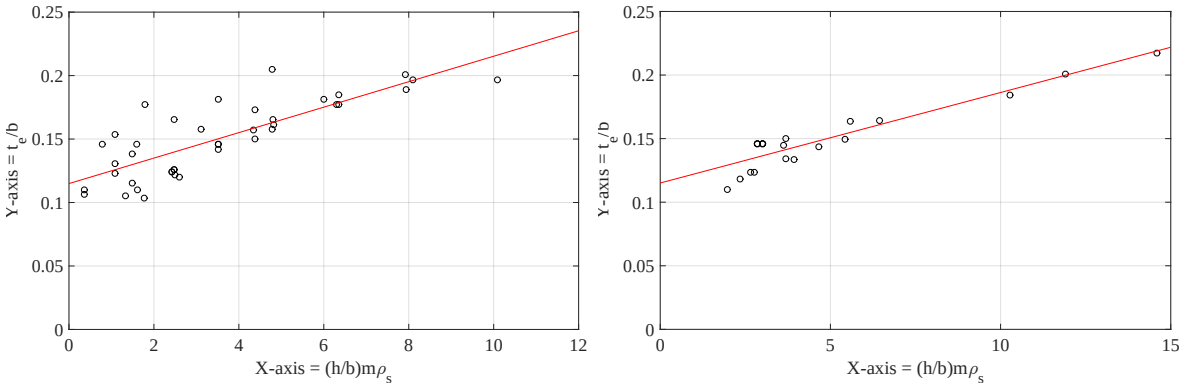

(a) Usual repartition of longitudinal reinforcement at corners.

(b) Repartition with additional longitudinal reinforcement along the perimeter.

Figure 4-11 – Linear fitting in the calibration process of determining t_e.

4.3.2 Plain concrete members under Pure Torsion

Not as complex as the behavior of RC members, the torsional behavior of plain concrete members can be represented by a typical torque-twist curve as shown in Figure 4-12: at low torque, the behavior is linear elastic, then becomes curved at high torque until a brittle failure just after the first crack.

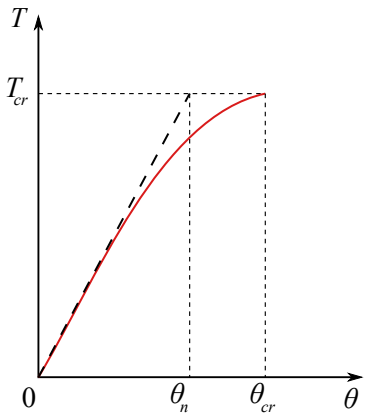

Figure 4-12 – Typical torque-twist curve of plain concrete beam [46].

In this case, the torsional rigidity can be related to the stress-strain relation in uniaxial compression and tension of concrete members (Figure 4-13). Generally in the literature, the compressive stress-strain curve is approximately linear up to about one half of the ultimate compressive strength, while a tensile stress-strain curve is approximately straight up to failure at a strain of approximately 0.0001.

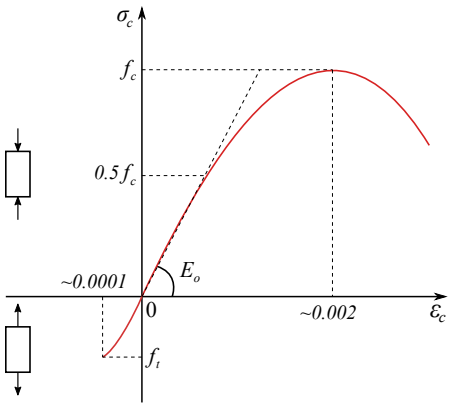

Figure 4-13 – Typical stress-strain curve of concrete in uniaxial compression and tension.

Knowing that the ultimate tensile strength is much smaller than the ultimate compressive strength (about one-tenth to one-seventh), we can notice that under torsional effect, the compressive stress-strain curve is perfectly elastic linear. In order to obtain the shape of torque-twist curve in Figure 4-12, some improvements have been made to the tensile relationship. Indeed, a bi-linear stress-strain curve has been proposed by the authors (Figure 4-14), in which the coefficient 0.7 in the tensile strength and 1.5 in the strain were carefully calibrated according to several experimental tests listed below. The choice of bi-linear curve and these coefficient allow a simple but effective model to predict the torsional behavior of a plain concrete member. For rectangular cross-sections, the cracking stress f_{cr}^{PC} is calculated from Equation (4.25), while the first slope is taken from Equation (4.22a).

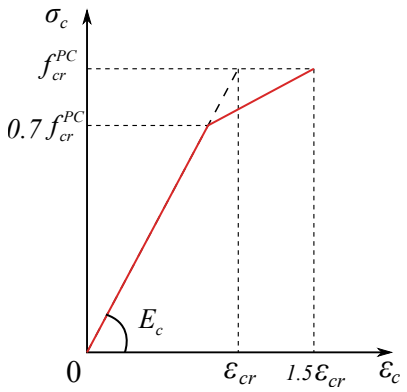

Figure 4-14 – Proposed relationship for tension stress-strain curve of plain concrete members under pure torsion.

4.4 Numerical examples for Elastic Torsion

In this section, the numerical results obtained by the proposed model in Section 4.2 will be compared to the theoretical formulations, and other model's results. The first example concerns a cantilever beam subjected to pure torsion at the free end under small displacement hypothesis (Figure 4-15), which was also simulated by Le Corvec in her PhD thesis [62]. The FE proposed model are constructed from 4 elements, with 5 Gauss points in each element and a system of square mesh of 100×50 fibers for each section. The interpolation points system using Lagrange polynomial, marked by the red cross, are constructed from 5 interpolation points along the element and a grid of 4×4 points over the section. The numerical results for twist angle at the free end of the beam computed by the model of Le Corvec and the proposed model (in two approaches) are collected in Table 4.1.

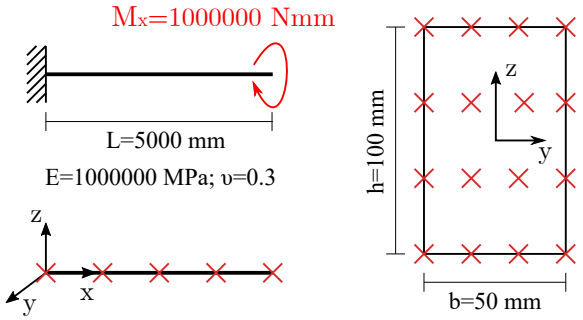

Figure 4-15 – Cantilever beam subjected to pure torsion at free end and system of interpolation points .

Table 4.1 – End twist angle for cantilever beam under mid span torque

	Theory	Model of Le Corvec	Proposed Model		
			No warping	Saint-Venant warping function	Lagrange polynomials
Twist angle (10^{-3} rad)	4.548	4.554	2.496	4.550	4.566
Relative error (%)		0.13	45.11	0.04	0.39
Execution time (second)			9	9	18

The relative errors are calculated with respect to the theoretical value, which can be obtained from the following expression, according to Saint-Venant's theory [97]:

$$\theta_x = \frac{M_x L}{GJ}; \qquad G = \frac{E}{2(1+\nu)}; \qquad J \approx b^3 h \left[\frac{1}{3} - 0.21\frac{b}{h}\left(1 - \frac{b^4}{12h^4}\right)\right] \tag{4.28}$$

where M_x is the torsional moment at mid-span; L is the beam length; J is the torsional constant as cited in Section 4.1 and its expression in Eq. (4.28) is only applied for rectangular cross-section. From Table 4.1, we concludes that the numerical results, given by the proposed model in both enhanced approaches, correlate very well with the one given by the theoretical formulation. Then, it confirms that neglecting the effect of warping will strongly influence on the twist angle. Moreover, it is worth to note that the theoretical formulation in Eq. (4.28) is only validated for the case of Saint-Venant torsion with *free warping*, in the case of torsion with constrained warping, the following expression must be used:

$$\theta_x = \frac{M_x L}{GJ} - \frac{M_x}{GJ}\sqrt{\frac{EI_w}{GJ}}\tanh\left(\sqrt{\frac{GJ}{EI_w}}L\right); \tag{4.29}$$

where $I_w = \alpha h b^3$ is the warping constant of rectangular cross-section, α is the Saint-Venant's coefficient which depends on the ratio of section width and height. In this example, Eq. (4.29) gives a value of 4.542×10^{-3} for the end twist angle, that means a relative difference of 0.13 % with respect to the value given by Eq. (4.28). The effect of constrained warping can be therefore neglected in the case of solid cross-section.

The warping profile of the cross-section is represented in Figure 4-16a. It gives a good illustration of the phenomenon: under torsional effect, the section warps and comes out of their own plane. As a consequence, the sectional rigidity is changed and the twist deformation is strongly influenced. As mentioned in the expression of warping functions, we do not need an infinite (or great) number of items to obtain a satisfying result: in Figure 4-16b, from a number $n \geq 5$, the relative difference is less than 0.01%.

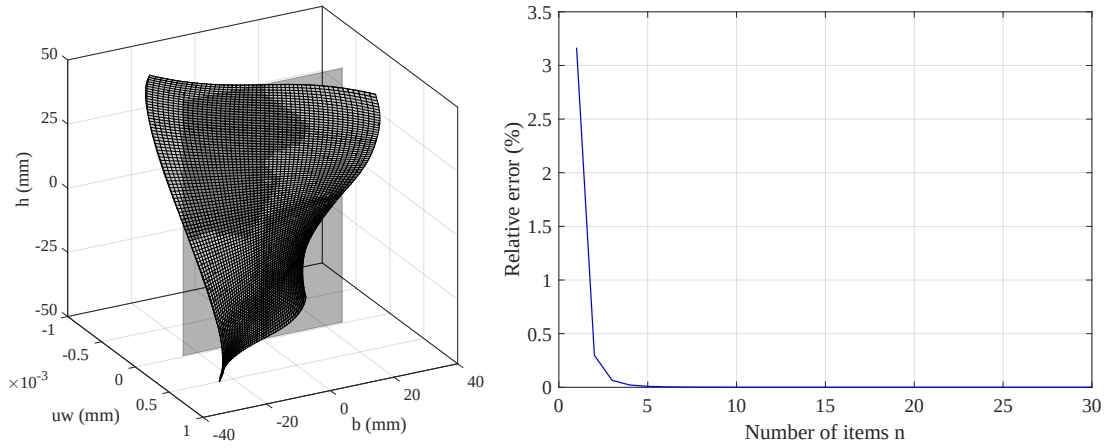

(a) Warping of end cross-section under torsional effect.

(b) Necessary numbers of items in warping function

Figure 4-16 – Representation of warping phenomenon by the proposed model.

In order to analyze the section deformation under the effect of warping phenomenon,

the shear stress profiles at free-end cross section are plotted in Figure 4-17. In Figure 4-17a and 4-17b, we can see two different distribution of shear stresses:

- Shear stress profile of classical field (no warping): plane distribution of τ_{xy}^{p} and τ_{xz}^{p} over the cross-section, according to plane section beam theory.
- Shear stress profile of enhanced field: the shear distributions are no more plane and tend to reduce the value of the total shear stresses. Thus, the section rigidity becomes less and the twist angle increases consequently, as represented in Table 4.1.

The superposition of this two shear stress profiles gives the total shear stress distribution at free-end section, which are represented in Figure 4-17c and 4-17d. These total shear stress profiles are strongly different from the case of no warping, which follows plane section theory.

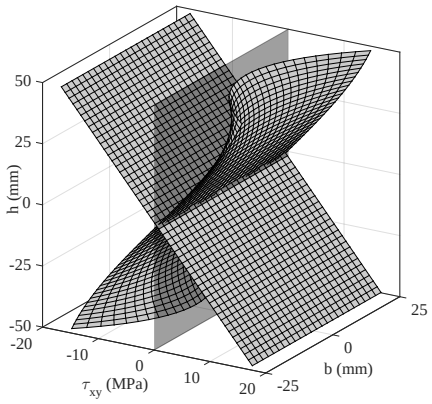

(a) Distribution of τ_{xy}^{p} in classical and enhanced field.

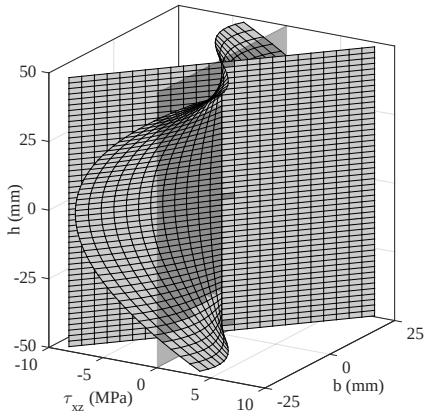

(b) Distribution of τ_{xz}^{p} in classical and enhanced field.

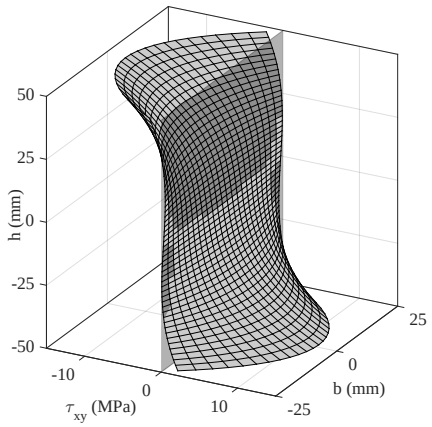

(c) Distribution of τ_{xy}^{p} in final field.

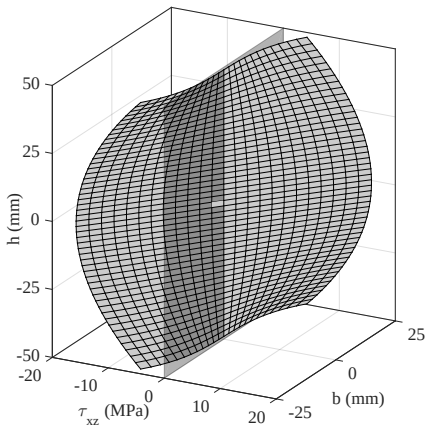

(d) Distribution of τ_{xz}^{p} in final field.

Figure 4-17 – Shear stress's profile at free-end cross-section under pure torsional effect.

The execution times, as cited in the Table 4.1, are about 9 seconds using Saint-Venant warping function approach and 18 seconds using Lagrange polynomials. In a multi-fiber

model, it is obvious that the more number of fibers, better the results obtained, however calculation time becomes higher. In a simple elastic model, the difference is not very important, but in order to apply the model in more complex problems, an adequate size of fiber needs to be fixed. From Figure 4-18, a number more than 30 fibers through the section depth is enough to ensure a good balance between accuracy and calculation time.

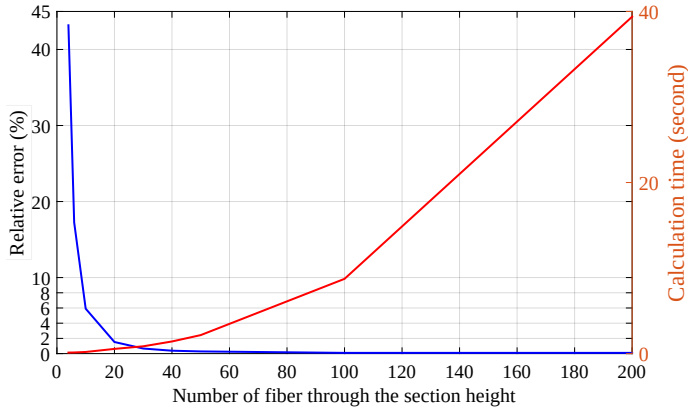

Figure 4-18 – Mesh's refinement investigation.

It is worth to notice that in this multi-fiber finite element model subjected to pure torsion, it is impossible to get an exact result compared to the theoretical formulation, because of two reasons:

1. The warping function is calculated with limited items, instead of infinity.

2. Sectional integration points situate in the center of fiber, not on the border.

Despite this fact, the use of multi-fiber approach is very effective and highly recommended by the authors, considering its good balance between the result obtained (relative error less than 0.5%) and the calculation time. From this example, the following statement can be obtained:

- The numerical results given by the two proposed approaches correlates very well with the one given by the theoretical formulation.

- Under torsional effect, the twist angle is strongly reduced without taking into account the warping of cross-section.

- For solid cross-section, free warping can be applied instead of restrained warping, as mentioned in Section 3.3.2.

4.5 Numerical examples for Inelastic Torsion

4.5.1 Plain concrete members

In this section, the behavior of plain concrete member under pure torsion will be represented and compared to a series of test carried out by Hsu [45], Csikos & Hegedus [29] and Lee et al. [63]. The details of beam sections and material properties can be found in Table 4.2. For a plain concrete member, without contribution of reinforcement, it's obvious that the whole section is considered as a 3D-zone (Section 3.5.3), but with a constitutive model as proposed in Section 4.3.2.

Table 4.2 – Details of specimens of tests in pure torsion for plain concrete members.

Test	Specimen	Dimension (mm)	h/b ratio	f'_c (MPa)
Hsu [45]	A2	381 × 254	1.5	31.2
	A4	254 × 254	1	32.49
	A8	280 × 152	1.84	31.2
Csikos & Hegedus [29]	A-1	130 × 130	1	23.7
	A-2	130 × 130	1	30
Lee et al. [63]	T0	350 × 300	1.17	42.6

In the literature, there are three basic methods to determine the cracking load of rectangular plain concrete members under pure torsion:

- The elastic theory presented by Saint-Venant [97]:

$$T_{cr,e}^{PC} = \alpha b^2 h f_t \tag{4.30}$$

  where α is the Saint-Venant's coefficient which depends on the ratio of section width and height; b is the section width, h is the section height and f_t is the tensile strength of concrete obtained from an uniaxial tension test.

- The plastic theory developed by Nylander [79]:

$$T_{cr,p}^{PC} = \alpha_p b^2 h f_t \tag{4.31}$$

  where $\alpha_p = 0.5 - b/6h$ is the plastic coefficient which is about 50% greater than the Saint-Venant's coefficient; b is the section width, h is the section height and f_t is the tensile strength of concrete obtained from an uniaxial tension test.

- The skew-bending theory based on observations of torsion tests by Hsu [46]:

$$T_{cr,sb}^{PC} = 0.217(b^2 + 6451.6)h\sqrt[3]{f_c} \quad \text{(N.m)} \tag{4.32}$$

where f_c is the compressive strength of concrete in MPa.

When consulting all the results calculated by these three theoretical formulations and the numerical results, then comparing to the experimental tests (Table 4.3), we can see that the cracking strength obtained by the elastic theory is always conservative, the plastic theory gives unconservative results, while the results given by skew-bending theory are more reasonable, but generally the proposed numerical model can give the best results: in most cases the relative difference with respect to experimental test is less than 5%.

Table 4.3 – Cracking torsional model for Plain concrete member: Comparison between experimental, numerical result and theoretical formulations

Test	Beam	Exp Value	Proposed Model	Elastic Theory	Plastic Theory	Skew-bending Theory
Hsu [45]	A2	19.1	19.7 / 3.1%	13.8 / -27.8%	23.2 / 22.1%	18.50 / -3.1%
	A4	11.3	10.2 / -9.7%	8.62 / -23.7%	13.8 / 22.3%	12.50 / 10.6%
	A8	6.38	6.70 / 5.0%	3.82 / -40.1%	6.46 / 1.3%	5.66 / -11.3 %
Csikos & Hegedus [29]	A-1	1.61	1.60 / -0.6%	1.13 / -29.7 %	1.81 / 12.6 %	1.54 / -17.7 %
	A-2	1.69	1.71 / 1.2 %	1.32 / -21.7 %	2.12 / 25.5 %	1.79 / 5.9 %
Lee et al. [63]	T0	23.2	22.9 / -1.3%	25.3 / -9.0 %	35.8 /54.2 %	29.4 / 26.6 %

The torque-twist curves obtained by the proposed model shows a good agreement with the experimental results (Figure 4-19). The slope of at high torque until failure is well represented with the aid of the proposed constitutive model in Section 4.3.2.

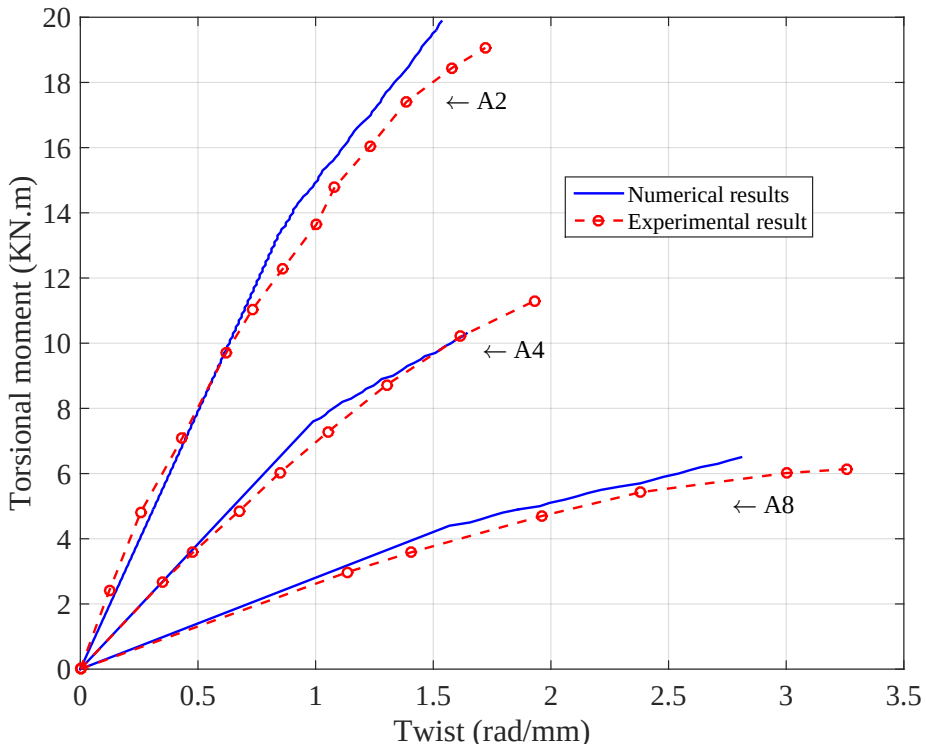

Figure 4-19 – Torque-twist curve for series A of Hsu's test.

4.5.2 Reinforced concrete members

In this section, the behavior of RC members under pure torsion will be represented and compared to the series of test mentioned in the calibration section, which were carried out by Hsu [45], Csikos & Hegedus [29], Lee et al. [63] and Lee et al. [64]. The specimens can be divided into two categories, according to its repartition of longitudinal reinforcements on the cross-section:

1. Usual repartition of reinforcement bars at corner: Series B (B2-B10), Series C (C1-C6), Series G (G1-G5), Series I (I2-I6), Series M (M1-M5), Series N (N1, N1a, N2, N2a) of Hsu's test; Series B (B1-B3), Series C (C1-C3) of Csikos & Hegedus's test; Series T (T1-1, T2-1, T2-2) of Lee et al. test.

2. Repartition with additional reinforcement bars along the perimeter: Beam M6, N3, N4, G6, G7, G8 of Hsu's test; Series T (T1-2, T1-3, T1-4 ,T2-3, T2-4) of Lee et al. test; Series D (D1-D3), E (E1-E3) of Csikos & Hegedus's test.

The cracking and ultimate torsional moment calculated for 61 specimens of tests cited above are compared to theoretical formulations, numerical results of Jeng's model and 2 international standards for torsional design of RC members (Eurocode 2 and ACI).

4.5.2.1 Cracking Torque

As mentioned in Section 4.5.1, there are three analytical methods to calculate the cracking torque of rectangular plain concrete members T_{cr}^{PC}: the elastic theory presented by Saint-Venant [97], the plastic theory developed by Nylander [79] and the skew-bending theory based on experimental tests by Hsu [45]. For RC members with a rectangular cross-section, based on T_{cr}^{PC}, Hsu proposed a new formulation for the cracking load:

$$T_{cr} = (1 + 4\rho_s)T_{cr}^{PC} \tag{4.33}$$

where ρ_s is the total percentage of reinforcement with respect to the whole section. The cracking torque T_{cr} calculated by theses three analytical methods are then compared to the numerical results obtained by the proposed model and Jeng's model [53].

4.5.2.1.1 Usual repartition of longitudinal reinforcement at four corners In Table 4.4, for each series of tests, the average relative differences (calculated with respect to the experimental tests) are indicated, and the smallest average relative error is shown in bold and highlighted in red.

Table 4.4 – Cracking torsional moment: average relative error with respect to experimental test calculated.

Test	Beams	Proposed Model	Jeng's Model	Elastic Theory	Plastic Theory	Skew-bending Theory
Hsu [45]	Series B	**4.4%**	7.1%	33.1%	13.2%	8.0%
	Series C	**5.3%**	10.8%	33.9%	5.9%	6.0%
	Series G	**3.0%**	6.2%	38.6%	11.7%	14.3%
	Series I	**4.5%**	4.7%	20.2%	34.9%	12.3%
	Series M	4.7%	**3.7%**	31.5%	15.8%	3.9%
	Series N	4.5%	12.3%	46.4%	**4.1%**	12.7%
Lee et al. [63]	Series T1	**4.5 %**	-	25.8 %	26.2 %	10.8 %
	Series T2	4.9 %	-	18.7 %	38.3 %	**2.9 %**
Csikos & Hegedus [29]	Series D	**0.6%**	-	26.1 %	18.4 %	12.9 %
	Series E	**3.8%**	-	28.5 %	14.6 %	8.6 %

We can see that the proposed modifications are very relevant as the smallest average relative error can be found in most cases, and in all series the relative error is always less then 5 %, except in series C (5.3 %). The numerical results given by Jeng's model

are also satisfactory, although some large average relative errors (more than 10%) were found in series C and N of Hsu's test. When considering the analytical formulations, while the elastic theory always gives the unsatisfactory results, reasonable cracking loads can be sometimes obtained by the plastic theory (series C and N of Hsu's test). The skew-bending theory shows the best ability of predicting the cracking torsional moment between the three formulations, but its results are still far from satisfactory when comparing to the experimental results.

Go further in detail, the numerical results of series B in Hsu's test can be found in Table 4.5, with the best numerical cracking torque (compared to experimental values) always highlighted in red. The proposed model gives the best prediction in 6 specimens, and 6 of 9 specimens give a relative error less than 5%. Other numerical results and comparisons for each series of torsional test can be found in Appendix.

Table 4.5 – Cracking torsional moment - Series B of Hsu Test: experimental and numerical values and relative error with respect to experimental values.

Beams	Exp values	Proposed Model	Jeng's Model	Elastic Theory	Plastic Theory	Skew-bending Theory
B2	20.00	19.1 / -4.5 %	-	13.58 / -32.1 %	22.96 / 14.8 %	18.99 / -5.0 %
B3	20.11	20.0 / -0.6 %	20.61 / 2.5 %	13.69 / -31.9 %	23.15 / 15.1 %	19.37 / -3.7 %
B4	21.92	22.4 / 2.2 %	21.69 / -1.0 %	15.26 / -30.4 %	25.80 / 17.7 %	20.55 / -6.3 %
B5	22.60	23.2 / 2.7 %	21.44 / -5.1 %	15.09 / -33.2 %	25.51 / 12.9 %	20.92 / -7.4 %
B6	24.97	24.2 / -3.1 %	21.62 / -13.4 %	15.52 / -37.8 %	26.25 / 5.1 %	21.61 / -13.4 %
B7	20.22	19.7 / -2.6 %	18.7 / -7.5 %	12.43 / -38.6 %	21.01 / 3.9 %	18.43 / -8.9 %
B8	21.81	25.2 / 15.6 %	20.28 / -7.0 %	13.45 / -38.3 %	22.74 / 4.3 %	19.58 / -10.2
B9	19.66	18.1 / -7.9 %	20.67 / 5.1 %	13.72 / -30.2 %	23.20 / 18.0 %	19.10 / -2.8 %
B10	17.63	18.7 / 6.1 %	20.25 / 14.9 %	13.38 / -24.1 %	22.62 / 28.3 %	19.61 / 11.2 %

4.5.2.1.2 Repartition with additional longitudinal reinforcement along the perimeter Another strong aspect of the proposed model is the ability of calculating for the case of additional distribution of longitudinal reinforcement bars along the perimeter. In Table 4.6, the numerical and analytical cracking torque for this case of reinforcement distribution are all indicated, with a highlight in bold and red for the model with the smallest relative difference compared to the experimental result. Unconservative results can be found in many cases, except the plastic theory, but the best agreements are usually obtained with the proposed model. Although giving the smallest differences in two specimens (G8 and N3), the predictions of the plastic theory are too conservative, which

is not really suitable for the design process. We can also see that, while the model of Jeng does not consider the impact of reinforcement distribution, the relative errors in this case of distribution with additional longitudinal reinforcement along the perimeter are higher than the average ones obtained by this model (Table 4.4).

Table 4.6 – Distribution with additional longitudinal reinforcement bars: Cracking torsional moment (KNm) and Relative error with respect to experimental test.

Test	Beam	EXP Values	Proposed Model	Jeng's Model	Elastic Theory	Plastic Theory	Skew-bending Theory
Hsu [45]	G6	30.96	**33.2 / 7.2%**	-	18.47 / -40.3%	33.61 / 8.6%	25.27 / -18.4%
	G7	33.67	**34.2 / 1.6%**	31.24 / -7.2%	19.53 / -42.0%	35.53 / 5.5%	26.21 / -22.2%
	G8	33.67	32.6 / -3.2%	30.32 / -9.9%	18.53 / -45.0%	**33.72 / 0.1%**	26.18 / -22.3%
	M6	22.71	**21.9 / -3.9%**	21.81 / -4.0 %	15.83 / -30.3%	26.76 / 17.8%	21.79 / -4.0 %
	N3	7.41	6.80 / -8.3%	6.37 / -14.1%	3.80 / -48.7%	**6.91 / -6.7%**	6.36 / -14.1%
	N4	7.60	**7.50 / -1.4%**	6.45 / -15.1%	3.94 / -48.1%	7.18 / -5.6%	6.61 / -13.1%
Lee et al. [63]	T1-2	31.4	**30.1 / -4.1%**	-	22.95 / -26.9%	39.03 / 24.3%	27.59 / -12.1%
	T1-3	31.8	**31.5 / -0.9%**	-	23.52 / -26.0%	40. 1/ 25.8%	28.28 / -11.1%
	T1-4	33.7	**34.6 / 2.7%**	-	24.42 / -27.5%	41.53 / 23.2%	29.35 / -12.9%
	T2-3	29.8	**29.0 / -2.7%**	-	23.36 / -21.6%	39.73 / 33.3%	28.08 / -5.8%
	T2-4	29.9	**29.5 / -1.3%**	-	23.75 / -20.6%	40.40 / 35.1%	28.55 / -4.5%
Csikos & Hegedus [29]	D2	1.69	**1.70 / 0.6%**	-	1.49 / -11.6%	2.40/ 41.7%	2.31 / 36.6%
	D3	1.69	**1.68 / -0.6%**	-	1.47 / -13.0%	2.36 / 39.4%	2.29 / 35.6%
	E1	2.25	**2.09 / -7.1%**	-	1.55 / -30.9%	2.49 / 10.8%	2.35 / 4.2%
	E3	2.06	**2.05 / -0.5%**	-	1.52 / -26.1%	2.44 / 18.4%	2.33 / 12.9%

4.5.2.2 Ultimate Torque

In this section, the ultimate torque calculated by the proposed model is compared to the numerical results of Jeng's model, the analytical formulations proposed by Rausch, Cowan and Hsu and two standards for torsional design: Eurocode 2 and ACI.

The first formulation to calculate the ultimate torsional moment was proposed by Rausch in his space truss theory [93]. The main hypotheses are that both longitudinal and transversal steels are yielding at the ultimate torque and the inclination of concrete cracks is fixed at 45°. This formulation is an ingenious concept which gives torsional strength as a function of reinforcements and concrete:

$$T_{uR} = \min\left(\frac{2A_cA_{sl}f_{sly}}{u}; \frac{2A_cA_{st}f_{sty}}{s}\right) \tag{4.34}$$

where A_c is the area enclosed by the centerline of stirrups; A_{sl} and f_{sly} are the total area and the yield strength of longitudinal bars; A_{st} is the cross-section area of one hoop bar and f_{slt} are the yield strength of stirrups; u is the perimeter of the area bounded by the

centerline of a completed hoop bar; s is the stirrup's spacing. Several years later, Cowan modified Rausch's equation and proposed a new formulation based on Saint-Venant's stress and strain distribution for rectangular cross-section [28]:

$$T_{uC} = T_e + 1.6\frac{A_c A_{st} f_{sty}}{s} \tag{4.35}$$

where T_e is the torsional cracking strength calculated by the elastic theory (Equation (4.30)). In this formulation, the torsional failure mode depends on the yielding of stirrups. Another formulation based on experimental tests' observations was proposed by Hsu [46]:

$$T_{uH} = \frac{b^2 h}{3} 2.4\sqrt{f'_c} + \sqrt{m}\frac{f_{sly}}{f_{sty}}\left(1 + 0.2\frac{b_1}{h_1}\right)\frac{b_1 h_1 A_{st} f_{sty}}{s} \tag{4.36}$$

where f'_c is the compressive strength of concrete; b_1 and h_1 is the width and the height of the area enclosed by the centerline of stirrups; m is the ratio between longitudinal and transversal steel percentage.

In the ACI standard, torsional strength of RC members is calculated as [1]:

$$T_{uS} = \frac{2A_o A_{sl} f_{sly}}{s}\cot\theta \tag{4.37}$$

where A_o is the gross area enclosed by the shear flow path, which can be taken equal to $0.85A_c$, with A_c the area enclosed by the centerline of stirrups; θ is the cracks angle which can be taken as 45° for non-prestressed or low-prestressed members. In the European standard Eurocode 2, three different values are calculated depending on the torsional failure modes and the minimum one has to be chosen [96]. The first value is related to the stirrups' yielding, the second one corresponds to the longitudinal bars capacity and the third one is related to the torsional capacity of concrete struts:

$$T_{uE} = \min\left(\frac{2A_k A_{sl} f_{sly}}{s}\cot\theta; \frac{2A_c A_{sl} f_{sly}}{u_k}\tan\theta; 2\nu f'_c A_k t_{ef}\sin\theta\cos\theta\right) \tag{4.38}$$

A_k is the area enclosed by the centre-lines of the effective wall thickness; t_{ef} is the effective wall thickness and can be calculated as A/u with A the total area and u the perimeter of cross-section. The cracks angle is variable but can be taken as 45°.

In Table 4.7, the relative differences (calculated with respect to the experimental tests) are indicated. In each series of tests, the smallest average relative error is shown in bold and highlighted in red. Similar to the cracking torque, in most cases the smallest

average relative error was obtained by the proposed model. The numerical results given by Jeng's model are also satisfactory with the best average relative error in series M and N of Hsu's test. Although the average level of predictive performance is not better than Jeng's model (5.4% in comparison with 5.1%) in the test of Hsu, we can state that this lower performance of the proposed model is submitted by a big influence from the series C (12.5%). Without this series C, 5/6 series has a relative error less than 5/6, and the average value decreases to only 4%. When considering the analytical formulations, Rausch's and Cowan's formulations often give too high average relative error in all cases, while Hsu's formulation performs better, with one best result in series C of Hsu's test. Finally, the torsional strength given by the design standards are far from satisfactory.

Table 4.7 – Ultimate torsional moment: average relative error calculated with respect to experimental test values.

Test	Beams	Proposed Model	Jeng's Model	Rausch's Formulation	Cowan's Formulation	Hsu's Formulation	Eurocode 2	ACI
Hsu [45]	Series B	**4.9%**	7.9%	56.0%	54.8%	16.1%	23.2%	41.4%
	Series C	12.5%	5.6%	81.3%	69.9%	**5.1%**	14.4%	52.2%
	Series G	**3.8%**	4.8%	11.1%	21.0%	20.5%	29.5%	10.5%
	Series I	**2.8%**	6.1%	18.0%	29.9%	24.1%	14.8 %	9.6 %
	Series M	5.9%	**3.2%**	22.6%	18.7%	17.1%	20.7%	19.2%
	Series N	2.9%	**2.5%**	12.0%	24.1%	22.1%	22.2%	10.8%
Lee et al. [63]	Series T1	**4.4%**	-	59.6%	74.4%	9.7%	19.8%	35.8%
	Series T2	6.5%	-	18.1%	46.1%	**0.9%**	15.7%	10.6 %
Csikos & Hegedus [29]	Series B	**1.3%**	-	40.3%	21.7%	31.4%	50.4%	49.2%
	Series C	**5.3%**	-	6.7%	44.6%	30.4%	43.1%	12.6%
	Series D	**7.6%**	-	39.4%	9.7%	33.6%	56.2%	48.5 %
	Series E	**5.3%**	-	26.0%	6.3%	38.0%	59.1%	37.1%
Average		5.4%	5.1%	32.9%	35.9%	19.5%	27.3%	26.6%

A more detailed comparison will be examined for the case of repartition with additional longitudinal reinforcement bars along the perimeter. Similar to Section 4.5.2.1, in Table 4.8, the numerical and analytical ultimate torque for this case of reinforcement distribution are all indicated, with a highlight in bold and red for the cases with the smallest relative difference compared to the experimental results. In Hsu's test, the two numerical models show their advantage by their ability to predict the torsional strength with a very reasonable error in most cases (except specimen G8), while in the test of Lee et al., Hsu's formulation also gives very good results. In the test of Csikos & Hegedus, the proposed model is still giving the best predictions.

Table 4.8 – Repartition with additional longitudinal reinforcement bars: Ultimate torsional moment (KNm) and Relative error with respect to experimental test.

Test	Beams	EXP	Proposed Model	Jeng's Model	Hsu's Formulation	Eurocode 2	ACI
Hsu [45]	G6	39.09	**40.30 / 3.1%**	-	30.52 / -21.9%	27.98 / -28.4%	33.68 / -13.8%
	G7	52.65	**50.3 / -4.5%**	55.87 / 6.1%	41.07 / -22.0%	40.14 / -23.8%	48.32 / -8.2%
	G8	73.44	61.4 / -16.4%	**70.49 / -4.0%**	54.26 / -26.1%	57.02 / -22.4%	68.64 / -6.5%
	M6	60.11	**60.10 / 0.1%**	55.29 / -3.2%	60.85 / 1.2%	64.22 / 6.8%	77.82 / 29.5%
	N3	12.20	**12.05 / -1.2%**	12.49 / 2.4%	9.37 /-23.2%	9.27 / -24.0%	11.14 / -8.7%
	N4	15.70	**15.75 / 0.3%**	15.08 / -4.0%	12.99 / -17.3%	14.76 / -6.0%	17.75 / 13.0%
Lee et al. [63]	T1-2	42.9	44.5 / 3.7%	-	**41.86 / -2.4%**	47.52 / 10.8%	55.16 / 28.6%
	T1-3	54.1	**52.5 / -3.0%**	-	51.84 / -4.2%	62.15 / 14.9%	72.14 / 33.3%
	T1-4	62.4	**63.4 / 1.6%**	-	79.51 / 27.42%	92.29 / 47.91%	107.13 / 71.68%
	T2-3	50.2	49.4 / -1.6%	-	**49.95 / -0.5%**	45.90 / -8.6%	53.28 / 6.1%
	T2-4	56.4	55.2 / -2.1%	-	**56.75 / 0.6%**	53.86 / -4.5%	62.52 / 10.9%
Csikos & Hegedus [29]	D2	2.25	**2.38 / 6.7%**	-	1.51 / -33.1%	0.99 / -55.9%	1.02 / -54.8%
	D3	2.06	**2.20 / 6.8%**	-	1.50 / -27.3%	0.99 / -51.8%	1.02 / -50.7%
	E1	3.38	**3.10 / -9.5%**	-	2.01 / -4.0%	1.32 / -60.9%	2.03 / -39.9%
	E3	3.23	**3.06 / -5.3%**	-	2.00 / -38.0%	1.32 / -59.1%	2.03 / -37.1%

4.5.2.3 Torque-twsit curve

The torque-twist curve obtained by the proposed model is compared to the experimental results of specimen M2 and M3 in the test of Hsu (Figure 4-20), with and without the proposed modification of the tensile behavior. A very good agreement was achieved between experimental and numerical results: the cracking and the ultimate torsional moment have the same magnitude, the slopes in the post-cracking phase are identical, and the featured horizontal plateau manifested by the transition between the two phases before and after the cracking is well represented. Moreover, we can conclude that without the proposed modification of tensile behavior, the cracking moment achieved is about half of the one of the experimental test, and therefore the torque twist curve can not be similar to the experimental one.

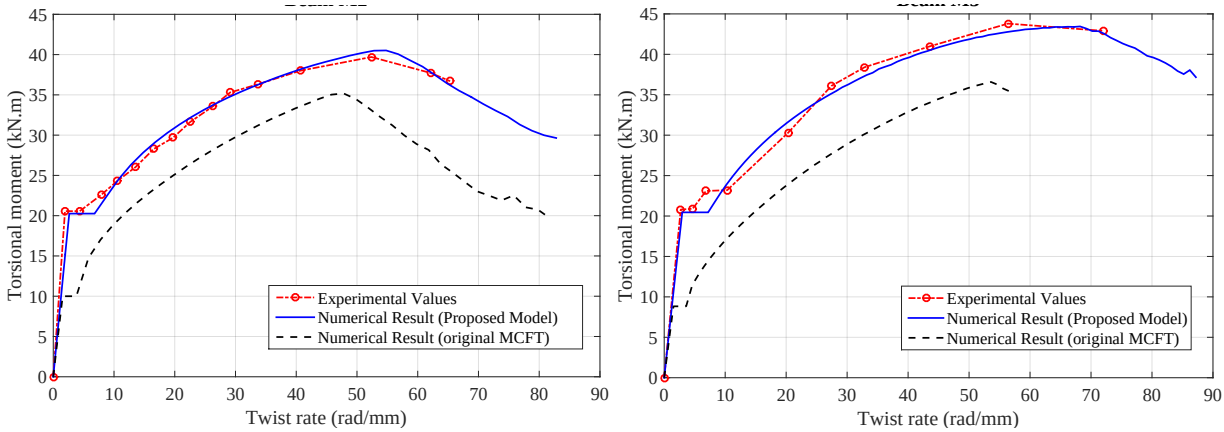

(a) Beam M2 (b) Beam M3

Figure 4-20 – Torsional moment versus Twist rate diagram for two specimens M2 and M3 in the torsional test of Hsu [45].

Another comparison of the torque-twist curves was made for series B of Hsu's test and series T1, T2 of Lee et al.'s test: once again the proposed model gave a good agreement with the experimental results (Figure 4-21, 4-22). In the series B of Hsu's test (Figure 4-21), the cracking and ultimate torsional moments were strongly a function of the reinforcement ratio, while the post cracking torsional stiffness were also well represented.

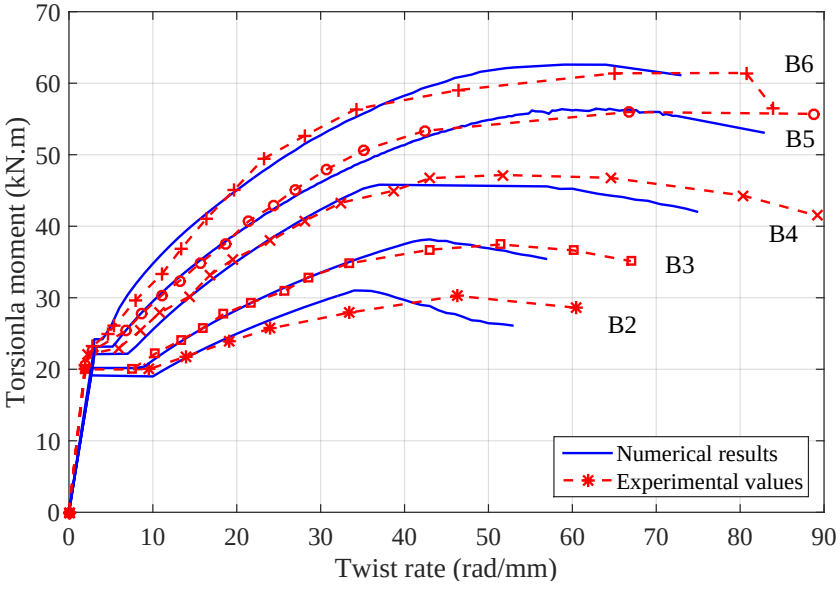

Figure 4-21 – Torsional moment versus Twist rate diagram for series B of Hsu's test. [45]

Concerning the test of Lee et al., in the series T1 (Figure 4-22a), good level of predicting for the ultimate torsional moment and post cracking stiffness were achieved. For the series T2 (Figure 4-22b), some slight gaps were noticed in the cracking phase, especially in the specimens T2-2 in which the horizontal plateau between the two phases before and after cracking was not recorded by the experimental data. However in general the predicting

torsional behavior obtained by the proposed model were reasonable and satisfactory.

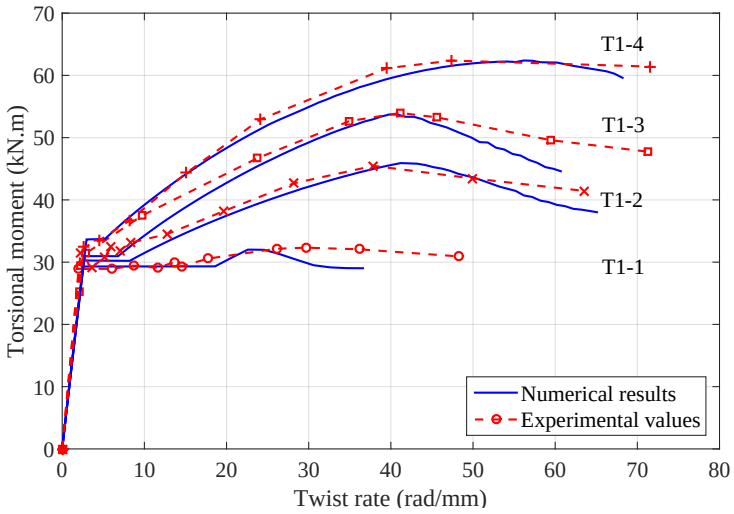

(a) Series T1

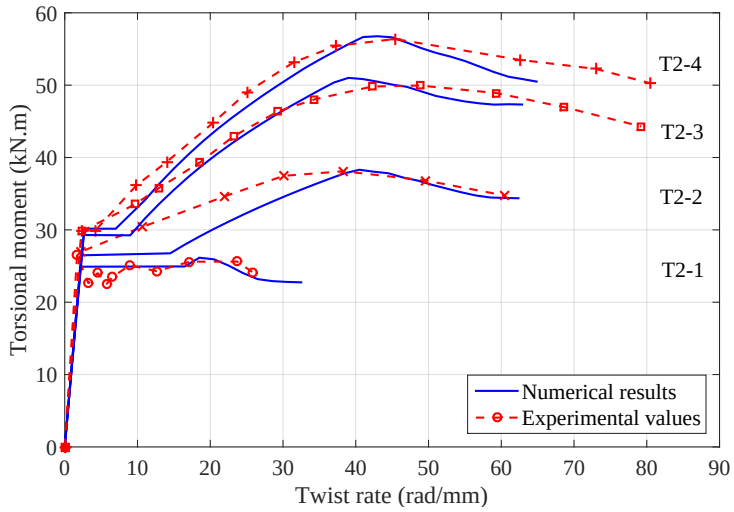

(b) Series T2

Figure 4-22 – Torsional moment versus Twist rate diagram for series T of Lee et al.'s test. [63]

4.6 Conclusions

A nonlinear multi-fiber finite element model has been developed for concrete and RC elements under pure torsional effect in this chapter. Through several numerical examples carefully executed above, the following remarks and conclusions can be draw:

- In the elastic material domain, good correlation has been obtained between the numerical results and the theoretical formulations. The influence of warping is significant and must be taken into account in order to obtain a correct torsional response. Besides the Saint-Venant warping function, the use of Lagrange polynomials to represent the warping effect can be also considered with very high level of

accuracy.

- The constitutive model based on the MCFT is suitable to be implemented in the multi-fiber finite element approach. In which, concerning the compression of concrete, the softening of concrete is a fundamental property and must be included in any loading conditions, so do the simulation of pure torsion, where the softening coefficient obtained from the shear tests can be applied without any modification. Therefore, the compressive relationship of concrete can be used from the one proposed on the original MCFT of existing formulations.

- However, under pure torsional effect, the tensile relationship proposed for shear effect is not suitable to predict correctly the torsional behavior of RC beam and a new relationship is required as a consequence. The modification proposed by the authors for the tensile behavior of concrete showed a reasonable and correct influence in predicting the torsional response of RC beam in the inelastic material domain.

- The section discretization in different zones following its stress state is very suitable to carrying the pure torsional effect, the parametric formulation developed by the authors for the effective wall thickness helps to complete this approach by giving a definition for the width of 2D-zone.

- From the numerical results obtained, the use of the proposed model is highly recommended to predict the cracking torque of RC beam under torsion and also for the cross-section in which the reinforcement bars are distributed with additional steel bar along the perimeter. Thanks to the specific constitutive model designed for this case of steel repartition, the proposed model shows its interest when giving a very good level of prediction, in comparison to other models and analytical formulations.

- The calibration method, presented by the authors to establish the formulation of the concrete tensile strength f_{cr} and the 2D-zone width t_e, allows to obtain a very good correlation between numerical and experimental results, as well as suggests an idea to the development of other formulations. However, it is obvious that some drawbacks of the calibration process should not be ignored, such as the dependency on the choice of the behavior constitutive law and on the size of experimental data. As a consequence, this method could become "sensitive" to any change of input data.

Chapter 5

Numerical analysis of RC members under Combined loading

The present chapter deals with the numerical analysis of RC members subjected to combined loadings of shear-bending-torsion. The enhanced multi-fiber 3D beam model formulation developed in Chapter 3 is used. The behavior of RC members considering the interaction between combined loading effects will be investigated in linear and non-linear regime of material behaviors. In case of elastic material, existing analytical solutions and numerical results are used as a reference to validate the model's ability and analyze the choice of mesh size. Also, two approaches proposed for the enhanced field of model are compared and discussed about their the advantage and inconveniences. While in inelastic material domain, the capacity of proposed model in predicting the behavior of RC members will be investigated by comparing with experimental test results.

According to the combined loading cases between shear, bending and torsion, the Chapter is organized as follows:

- Coupling of shear-bending: in Section 5.1, this typical combination of load cases of RC members is investigated in linear and non-linear regime of material behaviors. The numerical results are compared with the analytical solutions, other numerical models and the experimental values from three series of tests carried out by Bresler & Scordelis at the University of Berkeley [14].

- Coupling of bending-torsion: in Section 5.2, the interaction between bending and torsion is investigated and the numerical results are compared to the Collins et al.'s skew-bending theory and the experimental values from two tests carried out by McMullen & Warwaruk [72] and Onsongo [82].

- Coupling of shear-bending-torsion: in Section 5.3, the experimental test by McMullen & Warwaruk [72] is used as references in order to study the coupling of this completed combined loading cases of RC members.

- Finally, Section 5.4 summarizes the Chapter and offers some conclusions.

5.1 Elements subjected to combined shear and bending action

5.1.1 Elastic material

The numerical results are first validated in the domain of elastic linear material. In this section, the application of two formulations for the enhanced beam, using Saint-Venant warping function and Lagrange polynomials, will be investigated, in order to figure out the suitable approaches for the proposed model subjected to shear-bending action.

- Saint-Venant warping function approach: as developed in Section 3.3.2, the enhanced field using Saint-Venant warping function does not generate any additional normal strain (Equation (3.18)), while the axial warping displacement appears only under torsional effect (Equation (3.17)). Therefore, using this approach under shear-bending action, the proposed model is considered as a multifiber beam using plane-section beam theory.

- Lagrange polynomials approach: the enhanced field in this approach generates an additional normal strain (Equation 3.23a), while the axial displacements are also changed (Equation 3.21) and the cross section cannot maintain its plane shape under shear-bending action.

Two examples of cantilever beams subjected to vertical force at free-end, which were considered in the PhD thesis of Capdevielle [15] and Le Corvec [62], will be investigated hereafter. In both approaches, the numerical results obtained by the proposed models are compared in one hand with those of Capdevielle [15] and Le Corvec [62] and in other hand with the theoretical formulations (using plane-section beam theory such as Euler Bernoulli ou Timoshenko).

5.1.1.1 Numerical application using Saint-Venant warping function approach

A cantilever beam subjected to vertical force at the free end, which was used in the PhD thesis of Capdevielle [15], is studied firstly. The details of cross-section dimension, beam length and material properties are indicated in Figure 5-1. For the numerical modeling, in order to find the necessary number of elements and fibers, which ensure an adequate equilibrium between accuracy and calculation cost, different meshes are considered. Regarding the element discretization, three cases of meshing are used: 1, 4 and 8 elements. As for the cross-section, the following discretization is done: 10×5, 20×10, 40×20 and 100×50 square fibers.

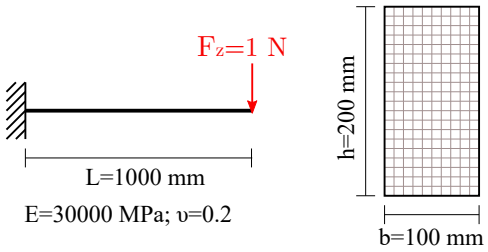

Figure 5-1 – Geometry and material properties for cantilever beam in the example of Capdevielle [15].

The values of deflection at free-end were computed and then compared to the theoretical formulation, which can be given by the following expressions according to the beam theory of Timoshenko (d_T), under the effect of vertical force F_z in z direction:

$$d_T = -\frac{F_z L^3}{3EI_z} - \frac{F_z L}{GA\kappa_y} = -171.47(mm) \tag{5.1}$$

with E is the Young modulus, A the cross-section area, I_z the moment of inertia about the z-axis, L the beam length and κ_y the shear correction factor in y direction. The numerical result for each case of mesh are presented in Table 5.1, accompanied with the relative error computed with respect to the theoretical formulation in Equation 5.1.

Table 5.1 – Tip deflection (mm) and corresponding relative different with respect to the theoretical formulation.

Beam Mesh \ Section Mesh	10×5	20×10	40×20	100×50
1	-173.15 / 0.98 %	-171.88 / 0.24 %	-171.57 / 0.06 %	-171.48 / 0 %
4	-173.15 / 0.98 %	-171.88 / 0.24 %	-171.57 / 0.06 %	-171.48 / 0 %
8	-173.15 / 0.98 %	-171.88 / 0.24 %	-171.57 / 0.06 %	-171.48 / 0 %

As can be seen from Table 5.1 , the number of element does not have any influence on the numerical results of this simple example. This can be explained by the constant distribution of shear force over element length in this loading configuration. Then, the more number of fibers, the more the numerical values are exact with respect to analytical solutions, and even a light system of 10×5 fibers over the cross-section can give satisfactory results with the relative error less than 1%. The elapsed times depend on the element number and fiber mesh, for example, 6 times differences can be remarked between the most-meshed model - 8 elements with 100×50 fibers in each section - (18 seconds) and a model of 4 elements with 40×20 fibers (less than 3 seconds). Even though, in compare to many finite element models, the elapsed times are relatively small.

The next parameter to evaluate is the distribution of shear strain over the cross-section, which are assumed parabolic in the model formulations (Equation (3.12)). Following the z direction, a parabolic distribution gives the following analytical solution of shear strain at a material point of cross-section situated at coordinate x of element axis:

$$\varepsilon_{xz}(x,z) = \frac{V_z(x)}{2GI_y}\left[\left(\frac{h}{2}\right)^2 - z^2\right] \tag{5.2}$$

with $V_z(x)$ is the shear force value in z direction at coordinate x, G is the shear modulus, I_y is the second moment of area with respect to th y-axis and h is the section height. At mid-span of the beam, the distribution of shear strain ε_{xz} over the cross-section are plotted in Figure 5-2. In this Figure, we can see that the values of shear strain calculated at the integration points (center of square fiber) are identical on the y direction, correspond to the analytical formulation in Equation (5.2).

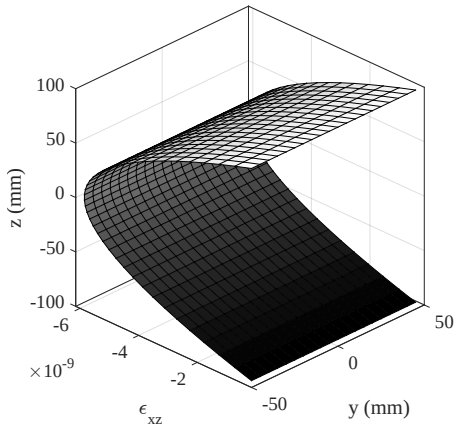

Figure 5-2 – Distribution of shear strain ε_{xz} over cross-section under shear-bending.

Because the values of shear strain are identical on the y direction, at an arbitrary

y coordinate, we will compare the values of shear strain ε_{xz} calculated by analytical formulation in Equation (5.2) and the ones obtained by the proposed model and the model of Capdevielle. In this case, the proposed model used a system of $20 \times 10 = 200$ square fibers, meaning 200 integration points over the cross-section and 20 fibers of identical y coordinate which give 20 different values of ε_{xz}, while the model of Capdevielle, with a system of 400 triangular mesh (Figure 5-3a), has 400 integration points over the cross-section and 40 fibers of identical y coordinate. However, of these 40 fibers, there are only 20 different values of ε_{xz}, because there are 20 pairs of fibers with different z coordinates but same values of ε_{xz}, due to the triangular mesh discretization. On Figure 5-3b, the numerical results given by the proposed model correlate perfectly with the analytical solutions, while there are small gaps between the numerical results of Capdevielle's model and the analytical solutions.

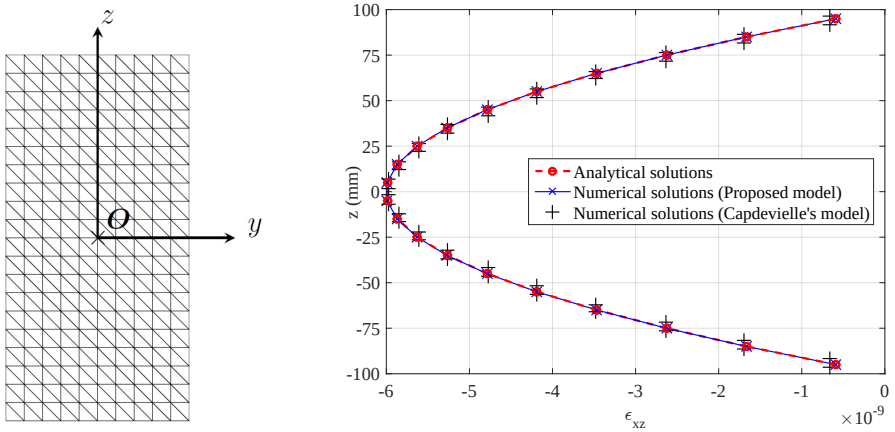

(a) (b)

Figure 5-3 – (a) System of FE mesh in the model of Capdevielle [15].; (b) Comparison of shear strain profile ε_{xz}.

5.1.1.2 Numerical applications using Lagrange polynomials approach

The example of Capdevielle in the previous section is re-used hereafter, the system of Lagrange interpolation points with 5 points along the element axis and a grid of (4×4) points over the cross-section are indicated in Figure 5-4.

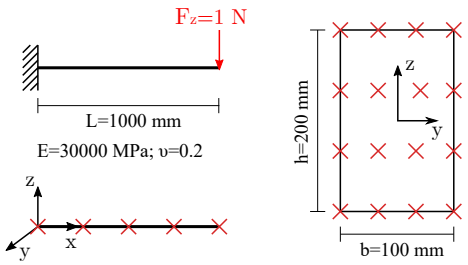

Figure 5-4 – System of Lagrange interpolation points (red cross sign).

The deflection at free-end are computed by the same models as in previous chapter. Because the number of element does not have any influence on the numerical results of this simple example, in this approach only different cases of fiber mesh are considered in a model of 8 elements. The numerical results are presented in Table 5.2.

Table 5.2 – Tip deflection, corresponding relative different with respect to the theoretical formulation and the elapsed times.

Approach \ Mesh	10×5	20×10	40×20	100×50
Saint-Venant	-173.15 mm	-171.88 mm	-171.57 mm	-171.48 mm
Warping	0.98 %	0.24 %	0.06 %	0 %
Function	1 s	1 s	3 s	18 s
Lagrange	-176.81 mm	-173.43 mm	-171.57 mm	-171.47 mm
polynomial	3.11 %	1.14 %	0.06 %	0 %
	3 s	14 s	33 s	211 s

As can be seen in Table 5.2, similar to the Saint-Venant warping function approach, the values of tip deflection obtained using the Lagrange polynomial approach tend to converge to the analytical solution. Ensuring a very reasonable result with relative error less than 0.1 % and a small elapsed time, the use of 40×20 fibers is recommended for the numerical modeling in both approach. In the other hands, using Lagrange polynomial approach, the elapsed times increase clearly, require 33 seconds on a model of 8 elements and 40×20 fibers (compared to 3 seconds in the Saint-Venant warping function approach), and up to 211 seconds with a system of 100×50 fibers (compared to 18 seconds).

The differences in the numerical results between two approaches in Table 5.1 and 5.2 can be explained by the appearance of the enhanced normal strains, leading to some slight changes in the element stiffness matrix $\mathbf{K}_e$. Using two numerical models constructed from 1 element and 40×20 fibers in each cross-section, the Saint-Venant warping function approach gave the following expression of $\mathbf{K}_e$:

$$\mathbf{K}_e = \begin{bmatrix}
6e5 & 0 & 0 & 0 & 0 & 0 & -6e5 & 0 & 0 & 0 & 0 & 0 \\
0 & 5.82e3 & 0 & 0 & 0 & 2.91e6 & 0 & -5.82e3 & 0 & 0 & 0 & 2.91e6 \\
0 & 0 & 2.15e4 & 0 & -1.08e7 & 0 & 0 & 0 & -2.15e4 & 0 & -1.08e7 & 0 \\
0 & 0 & 0 & 5.70e8 & 0 & 0 & 0 & 0 & 0 & -5.70e8 & 0 & 0 \\
0 & 0 & -1.08e7 & 0 & 7.38e9 & 0 & 0 & 0 & 1.08e7 & 0 & 3.38e9 & 0 \\
0 & 2.91e6 & 0 & 0 & 0 & 1.95e9 & 0 & -2.91e6 & 0 & 0 & 0 & 9.56e8 \\
-6e5 & 0 & 0 & 0 & 0 & 0 & 6e5 & 0 & 0 & 0 & 0 & 0 \\
0 & -5818 & 0 & 0 & 0 & -2.91e6 & 0 & 5818 & 0 & 0 & 0 & -2.91e6 \\
0 & 0 & -21509 & 0 & 1.08e7 & 0 & 0 & 0 & 21509 & 0 & 1.08e7 & 0 \\
0 & 0 & 0 & -5.70e8 & 0 & 0 & 0 & 0 & 0 & 5.70e8 & 0 & 0 \\
0 & 0 & -1.08e7 & 0 & 3.38e9 & 0 & 0 & 0 & 1.08e7 & 0 & 7.38e9 & 0 \\
0 & 2.91e6 & 0 & 0 & 0 & 9.56e8 & 0 & -2.91e6 & 0 & 0 & 0 & 1.95e9
\end{bmatrix} \tag{5.3}$$

While the expression obtained by Lagrange polynomial approach was:

$$\mathbf{K}_e = \begin{bmatrix}
6e5 & 0 & 0 & 0 & 0 & 0 & -6e5 & 0 & 0 & 0 & 0 & 0 \\
0 & 5.82e3 & 0 & 0 & 0 & 2.91e6 & 0 & -5.82e3 & 0 & 0 & 0 & 2.91e6 \\
0 & 0 & 2.15e4 & 0 & -1.08e7 & 0 & 0 & 0 & -2.15e4 & 0 & -1.08e7 & 0 \\
0 & 5.15e3 & -1.77e4 & 7.14e8 & 9.24e6 & 2.74e6 & 0 & -515e3 & 1.77e4 & -7.14e8 & 8.47e6 & 2.64e6 \\
0 & 0 & -1.08e7 & -9.65e4 & 7.38e9 & -7.93e3 & 0 & 0 & 1.08e7 & 9.65e4 & 3.38e9 & -8.13e3 \\
0 & 2.91e6 & 0 & 5.68e5 & 1.94e5 & 1.95e9 & 0 & -2.91e6 & 0 & -5.68e5 & 1.93e5 & 9.56e8 \\
-6e5 & 0 & 0 & 0 & 0 & 0 & 6e5 & 0 & 0 & 0 & 0 & 0 \\
0 & -5.82e3 & 0 & 0 & 0 & -2.91e6 & 0 & 5.82e3 & 0 & 0 & 0 & -2.91e6 \\
0 & 0 & -2.15e4 & 0 & 1.08e7 & 0 & 0 & 0 & 2.15e4 & 0 & 1.08e7 & 0 \\
0 & -5.15e3 & 1.77e4 & -7.14e8 & -9.24e6 & -2.74e6 & 0 & 5.15e3 & -1.77e4 & 7.14e8 & -8.47e6 & -2.64e6 \\
0 & 0 & -1.08e7 & -3.47e5 & 3.38e9 & 0 & 0 & 0 & 1.08e7 & 3.47e5 & 7.38e9 & 0 \\
0 & 2.91e6 & 0 & 2.76e5 & 6.57e4 & 9.56e9 & 0 & -2.91e6 & 0 & -2.76e5 & 6.53e5 & 1.95e8
\end{bmatrix} \tag{5.4}$$

In these two stiffness matrix, the terms whose value is zero in Equation (5.3) are marked in blue, while the stiffness values which are different between two approaches are marked in red. The appearance of new non-zero terms and the change of existing term (relative difference up to 25%) cause the differences in the numerical results between two approaches in Table 5.1 and 5.2. By increasing the mesh system to 100×50 fibers, the Saint-Venant warping function approach gave the following expression of $\mathbf{K}_e$:

$$\mathbf{K}_e = \begin{bmatrix}
6e5 & 0 & 0 & 0 & 0 & 0 & -6e5 & 0 & 0 & 0 & 0 & 0 \\
0 & 5.83e3 & 0 & 0 & 0 & 2.91e6 & 0 & -5.83e3 & 0 & 0 & 0 & 2.91e6 \\
0 & 0 & 2.15e4 & 0 & -1.08e7 & 0 & 0 & 0 & -2.15e4 & 0 & -1.08e7 & 0 \\
0 & 0 & 0 & 5.71e8 & 0 & 0 & 0 & 0 & 0 & -5.71e8 & 0 & 0 \\
0 & 0 & -1.08e7 & 0 & 7.38e9 & 0 & 0 & 0 & 1.08e7 & 0 & 3.38e9 & 0 \\
0 & 2.91e6 & 0 & 0 & 0 & 1.96e9 & 0 & -2.91e6 & 0 & 0 & 0 & 9.58e8 \\
-6e5 & 0 & 0 & 0 & 0 & 0 & -6e5 & 0 & 0 & 0 & 0 & 0 \\
0 & -5.83e3 & 0 & 0 & 0 & -2.91e6 & 0 & 5.83e3 & 0 & 0 & 0 & -2.91e6 \\
0 & 0 & -2.15e4 & 0 & 1.08e7 & 0 & 0 & 0 & 2.15e4 & 0 & 1.08e7 & 0 \\
0 & 0 & 0 & -5.71e8 & 0 & 0 & 0 & 0 & 0 & 5.71e8 & 0 & 0 \\
0 & 0 & -1.08e7 & 0 & 3.38e9 & 0 & 0 & 0 & 1.08e7 & 0 & 7.38e9 & 0 \\
0 & 2.91e6 & 0 & 0 & 0 & 9.58e9 & 0 & -2.91e6 & 0 & 0 & 0 & 1.96e9
\end{bmatrix} \tag{5.5}$$

and the Lagrange polynomials approach gave:

$$\mathbf{K}_e = \begin{bmatrix}
6e5 & 0 & 0 & 0 & 0 & 0 & -6e5 & 0 & 0 & 0 & 0 & 0 \\
0 & 5.83e3 & 0 & 0 & 0 & 2.91e6 & 0 & -5.83e3 & 0 & 0 & 0 & 2.91e6 \\
0 & 0 & 2.15e4 & 0 & -1.08e7 & 0 & 0 & 0 & -2.15e4 & 0 & -1.08e7 & 0 \\
0 & 0 & 1.11e4 & 5.89e8 & -7.82e6 & 3.05e5 & 0 & 0 & -1.11e4 & -5.89e8 & -3.26e6 & -1.05e6 \\
0 & 0 & -1.08e7 & 0 & 7.38e9 & 0 & 0 & 0 & 1.08e7 & 0 & 3.38e9 & 0 \\
0 & 2.91e6 & 0 & 0 & 0 & 1.96e9 & 0 & -2.91e6 & 0 & 0 & 0 & 9.58e8 \\
-6e5 & 0 & 0 & 0 & 0 & 0 & -6e5 & 0 & 0 & 0 & 0 & 0 \\
0 & -5.83e3 & 0 & 0 & 0 & -2.91e6 & 0 & 5.83e3 & 0 & 0 & 0 & -2.91e6 \\
0 & 0 & -2.15e4 & 0 & 1.08e7 & 0 & 0 & 0 & 2.15e4 & 0 & 1.08e7 & 0 \\
0 & 0 & -1.11e4 & -5.89e8 & 7.82e6 & -3.05e5 & 0 & 0 & 1.11e4 & 5.89e8 & 3.26e6 & 1.05e6 \\
0 & 0 & -1.08e7 & 0 & 3.38e9 & 0 & 0 & 0 & 1.08e7 & 0 & 7.38e9 & 0 \\
0 & 2.91e6 & 0 & 0 & 0 & 9.58e9 & 0 & -2.91e6 & 0 & 0 & 0 & 1.96e9
\end{bmatrix} \tag{5.6}$$

There are still some difference, however the number of new non-zero term decreases significantly, and the relative difference in the change of existing term reduces to only 3%. The similar numerical results between two approaches when increasing the mesh number can be therefore explained.

Another example which was in the PhD thesis of Le Corvec [62] was also investigated hereafter. The details of cross-section dimension, beam length, material properties and system of Lagrange interpolation points are indicated in Figure 5-5. Because of the high ratio between the section height and width, in this example over the cross-section only 4 Lagrange interpolation points were used for the numerical modeling.

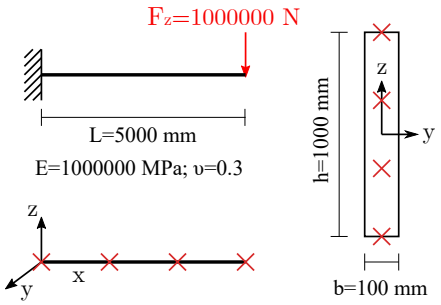

Figure 5-5 – Geometry, material properties and system of Lagrange interpolation points (red cross sign) for cantilever beam.

The values of tip deflection, given by the proposed model in both approaches (with 1 element accompanied by two mesh systems of 100×10 and 200×20 fibers on each cross-section), are shown in Table 5.3 and compared to the analytical solutions and the numerical result of Le Corvec's model. The result of the proposed model are in very good agreement with the ones given by the theoretical formulation. We can also remark that there are almost no gap in the numerical results between two proposed approaches, even with a light mesh system. This difference to the previous example of Capdevielle may be explained by the high ratio between the section height and width in this case study.

Table 5.3 – Tip deflection of cantilever beam with rectangular cross-section under vertical loading - Example of Le Corvec [62].

	Timoshenko Theory	Model of Le Corvec	Mesh	Proposed Model	
				Saint-Venant warping function	Lagrange polynomials
Tip deflection (mm)	-5.156	-5.156	10×1	-5.206	-5.207
			50×5	-5.158	-5.158
			100×10	-5.157	-5.157
			200×20	-5.156	-5.156

As a reminder, under shear-bending action, the enhanced field using Lagrange polynomials generates an additional axial displacement field. As a consequence, the cross-section is warped and cannot retain its plane shape. This warping displacement under

shear-bending action can be represented in Figure 5-6a, in which the parabolic shape is a result of the cubic interpolation polynomials over cross-section. We can also see that, similar to the profile of shear stress, under vertical shear force in z direction, the profile of warping displacement is constant following the y direction. However, the magnitude of this enhanced field is too small compared to that of the classical field, therefore the total displacement field is not much influenced and retains its plane shape (Figure 5-6b). The material strains and stresses are not influenced and as a result, there are no difference on the values of tip deflection in Table 5.3.

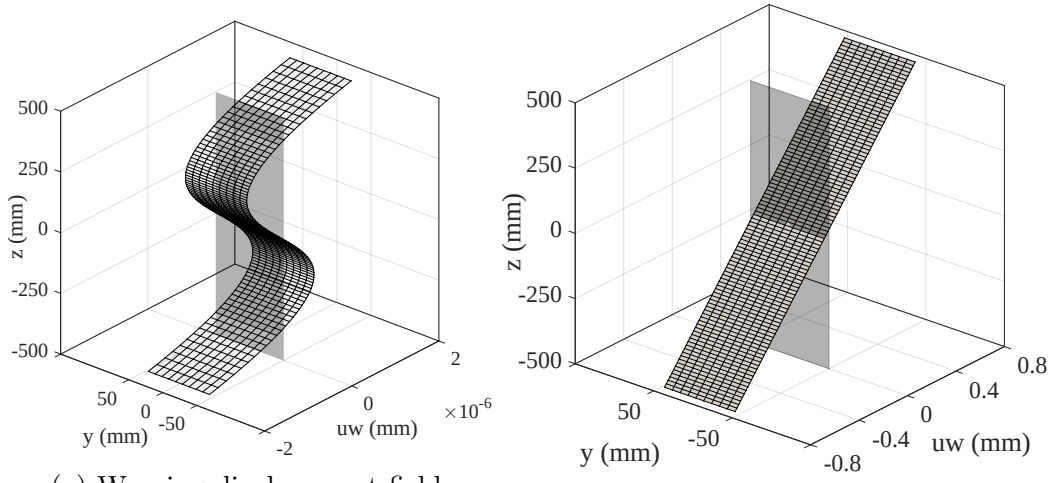

(a) Warping displacement field.

(b) Total displacement field.

Figure 5-6 – Distribution of displacement field over the free-end cross-section under shear-bending.

Along the element axis, this warping effect is not constant and is distributed proportionally according to the normal stress value: minimum at the fixed-end, then increase and reach the maximum at the free-end section (Figure 5-7).

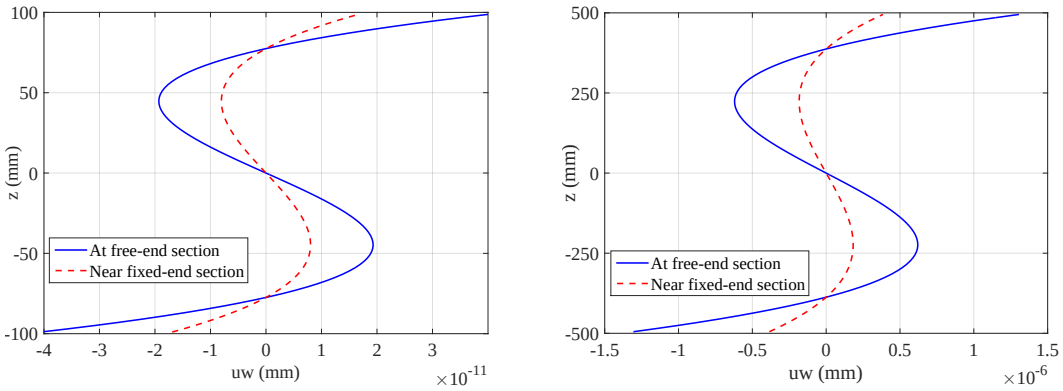

(a) Example by Capdevielle.

(b) Example by Le Corvec.

Figure 5-7 – Variation of the warping displacement profile along the beam axis.

5.1.2 Inelastic material

In this section, under shear-bending effect, the numerical model is simulated using the FE formulation presented in Chapter 3, while the model's material behavior is based on the MCFT, originally developed by Vecchio [110] and described in Section 2.4.1.1.

The RC beam tests conducted by Bresler & Scordelis at the University of Berkeley [14] is commonly taken as a benchmark reference and have been repeatedly used for the validation of various analytical and numerical models. For this reason, in this section the results of these test are used as references in order to investigate the capacity of the proposed model in predicting the behavior of reinforce concrete under shear-bending. Three series of test A, B and C are analyzed in this section. The details of beam sections in each series and the outline of test setup are showed in Figure 5-8.

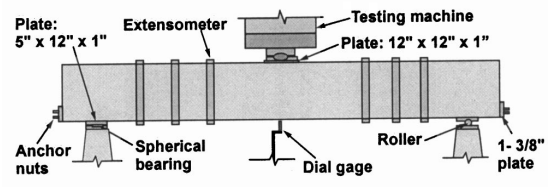

(a) Outline of test setup.

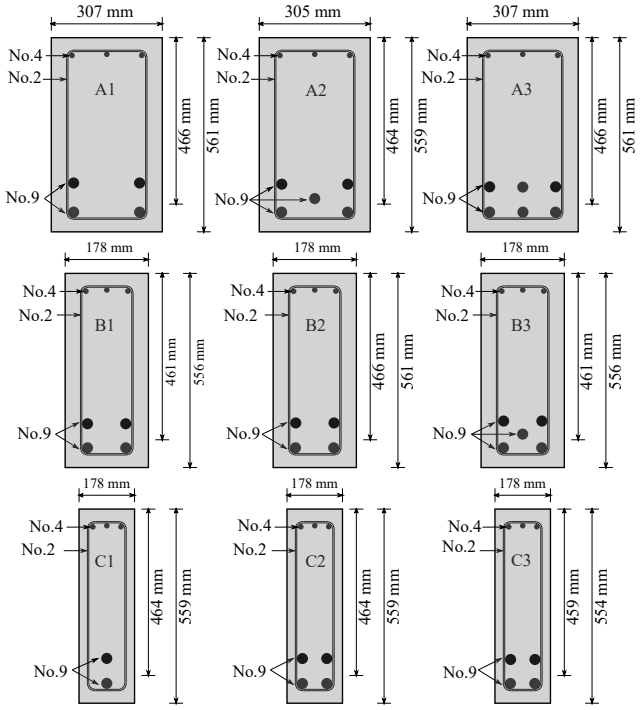

(b) Cross-section details.

Figure 5-8 – Bresler & Scordelis's shear bending test in 1963 [14].

In each series, the index number 1,2 and 3 correspond to three different types of specimen, each corresponds to a beam length indicated in Table 5.4a. According to the test result, the types of beam of intermediate length (A1, A2, B1, B2 and C1, C2) could

be characterized as shear-flexural behavior, correspond to a shear-compression failure mode, while the long-span beams of type 3 (A3, B3 and C3) generally exhibited a flexure-compression failure mode. In Table 5.4a we can also find the section dimensions and concrete properties, while the reinforcement details are given in Table 5.4b

Table 5.4 – Description of the RC beams tested by Bresler & Scordelis [14].

Beam	L (mm)	h (mm)	b (mm)	f'_c (MPa)	ε_o
A1	3658	561	307	24.1	0.002
A2	4572	559	305	24.3	0.002
A3	6400	561	307	35.1	0.002
B1	3658	556	231	24.8	0.002
B2	4572	561	229	23.2	0.002
B3	6400	556	229	38.8	0.002
C1	3658	559	155	29.6	0.002
C2	4572	559	152	23.8	0.002
C3	6400	554	155	35.1	0.002

(a) Section details and concrete properties.

Bar	d (mm)	f_y (MPa)	f_u (MPa)	E_s (MPa)
No. 2	6.4	325	430	189607
No. 4	12.7	345	542	201330
No. 9 (types 1,2)	28.7	555	958	217880
No. 9 (types 3)	28.7	552	933	205470

(b) Reinforcement details.

5.1.2.1 Numerical analysis of Beam A1

A detailed case study is analyzed in this section, the specimen A1 is modeled using 4 elements with 5 Gauss-Lobatto points and a system of 25 × 15 meshes over the cross-section. The interaction between shear and bending is investigated firstly. In order to point out the shear effect on the bending behavior, the deflections are determined by two different ways: using a model of combined bending and shear, and using a model in which shear is ignored. Figure 5-9 presents the mid-span deflection versus applied load curves.

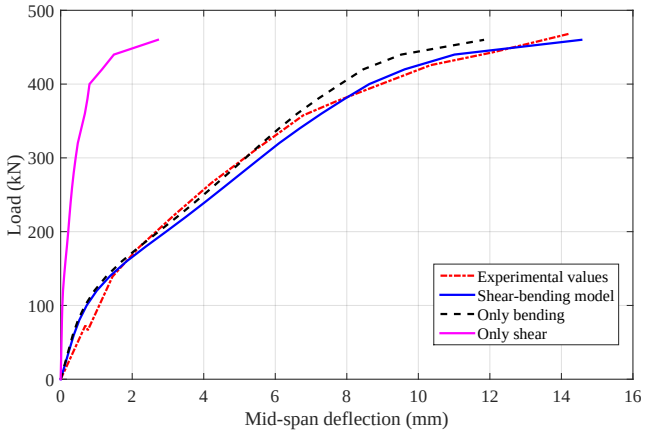

Figure 5-9 – Load-displacement diagram of beam A1.

It can be observed that shear effect on the beam deflection is not much pronounced in the elastic region (up to 100 kN). However, coupling between shear and flexural actions seems to give better results in terms of deflection when the beam gets in the nonlinear range. For instant, at the loading of 400 kN, the deflection due to shear is about 11 % of the total displacement. The deflection due to the shear increases with increasing of applied load. This situation can be explained by the appearance of shear crack pattern in the sectional stiffness matrix, which decreases the sectional stiffness and thus increases the displacement. Moreover, the numerical results obtained by the proposed model give quite good agreements with the experimental values in term of element stiffness, load bearing capacity (460 kN in compare to 468 kN of test value) and the maximum deflection (14.6 mm in compare to 14.2 mm of test value).

At ultimate loading, the crack orientation of concrete were illustrated in Figure 5-10a, for the left half of the beam. As can be seen, the numerical simulation gives logical results in terms of crack orientation. Indeed, the crack inclinations become higher towards the lower face of the beam and close to the mid-span - the point of load applications. This result is somehow in agreement with the experimental observations in Figure 5-10b.

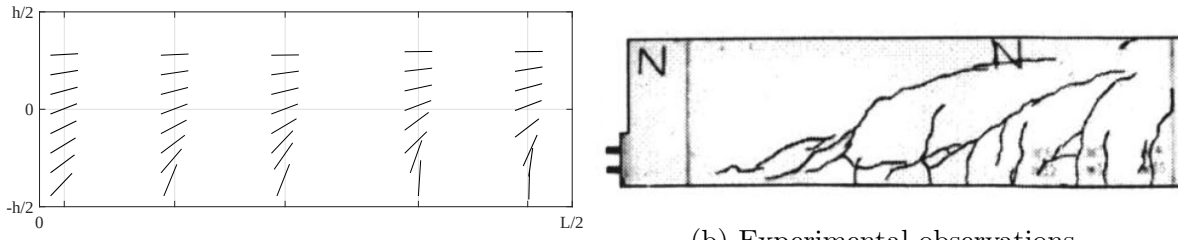

(a) Numerical simulation.

(b) Experimental observations.

Figure 5-10 – Crack distribution at ultimate loading for the left half of Beam A1.

The distributions of normal stress at different cross-sections are plotted in Figure 5-11 for the left half of the beam, just before the achievement of ultimate load. At mid of the left half (or at 1/4 of beam span), higher stress intensities are recorded in the compression zone because the appearance of crack limits the increase of normal stress in tension zone. At mid-span cross-section, where the strains are maximum, a higher ordinate of neutral axis than that at 1/4 span can be found because the cracks in tension zone become wider. Corresponding to the parabolic shape in the compressive relationship of the material constitutive model, in the compression zone the normal stresses reach its compressive strength and start to decrease at the top of the beam. In tension zone, the tension-stiffening phenomenon can be observed at the bottom of the beam.

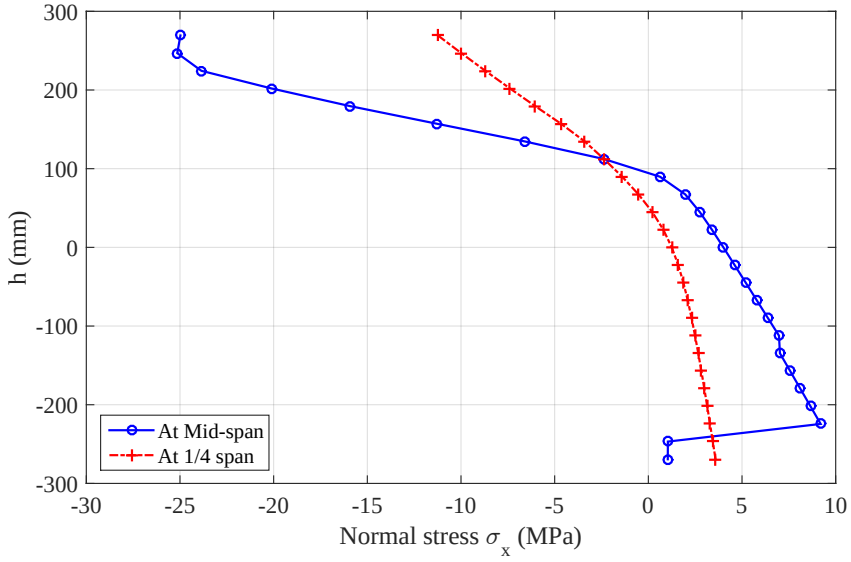

Figure 5-11 – Distribution of normal stress σ_x at different cross-section.

For the distribution of shear stresses, similar statement can also be remarked, as a parabolic profile corresponding to elastic regime is found at the left support where the applied load is at low level (Figure 5-12). Then, while shear stresses continue to increase with load level in compression zone, in the tension zone, because of cracks, the increment of shear stresses is considerably less than in the compression zone. From certain level of load, the propagation of flexural cracks forces the shear stresses to zeros, as sketched at the section near the mid-span. It is should be highlighted that the integration of the three curves, which correspond to the results of shear force distributions, are equal.

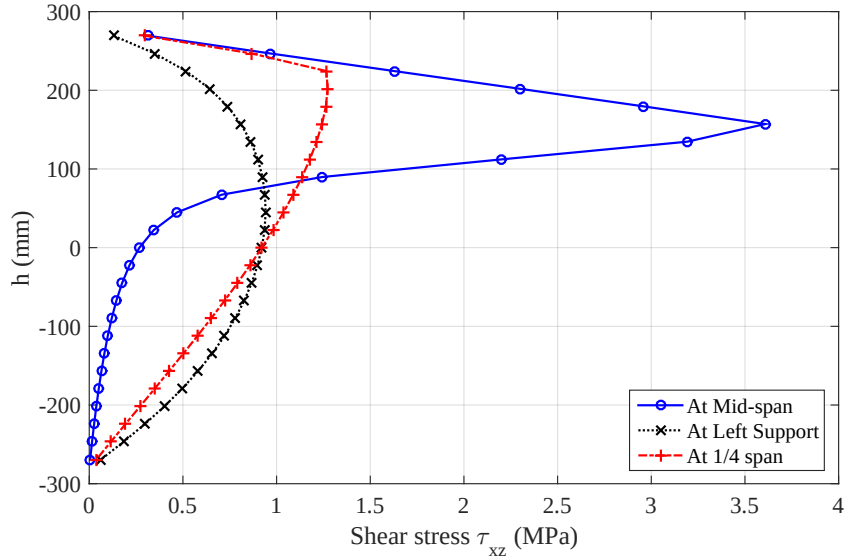

Figure 5-12 – Distribution of shear stress τ_{xz} at different cross-section.

5.1.2.2 Numerical results of others beams

Other simulation results for all specimens in the test of Bresler & Scordelis are represented hereafter. In Table 5.5, the ultimated loadings computed by the proposed model are compared to VecTor2, a finite element program developed at the University of Toronto. This program incorporate the behavior models and constitutive relations of the disturbed stress field model (DSFM) [108], a refinement of the MCFT [110]. Relative differences are computed with respect to the experimental values and the better results are highlighted in red. It can be seen that reasonable results have been obtained for both numerical models, but the proposed model generally gives better result of predicting than VecTor2 program, especially for the beams of series A and B. It is also interesting to note that the ultimate loading performed by both numerical models are typically under-estimated.

Table 5.5 – Ultimate Loading (in kN) and relative difference to the experimental result - Comparison between Proposed Model and VecTor2 program

Beam	Experimental	Proposed Model	VecTor2 Program
A1	468	461 / -1.5 %	**472 / 0.9 %**
A2	490	**442 / -9.8 %**	399 / -18.6 %
A3	468	**375 / -19.9 %**	366 / -21.8 %
B1	446	**441 / -1.1 %**	423 / -5.2 %
B2	400	**380 / -5.0 %**	327 / -18.3 %
B3	356	320 / -10.1 %	**355 / -0.3** %
C1	312	292 / -6.4 %	**307 / -1.6 %**
C2	324	**322 / -0.6 %**	258 / 5.5 %
C3	270	251 / -7.0 %	**255 / -5.5 %**

The load versus mid-span displacement curve obtained by the proposed model in compare to the experimental test data are plotted in Figure 5-13. For the beams of intermediate length (type 1 and 2), good agreements were obtained at all stages of loading, except in the case of beam C1 (Figure 5-13f), where the numerical and experimental curve did not correlate very well. For the long-span beam (type 3, although there are some difference at the early load stage, the beam stiffnesses were well represented, especially in beam B3 and C3 (Figure 5-13e and 5-13h), while the numerical result for beam A3 was a bit different to the experimental curve (Figure 5-13b). In general, very good correlations were obtained between the numerical result and the experimental values: the model is capable of well predicting the ultimate loading and maximum deflection (as shown in Table 5.5) as well as representing a very reasonable element stiffness in most cases of test.

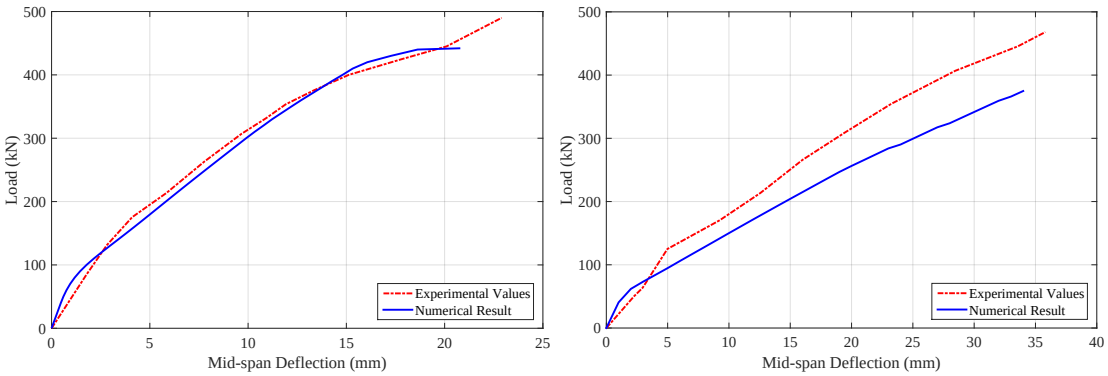

(a) Beam A2.

(b) Beam A3.

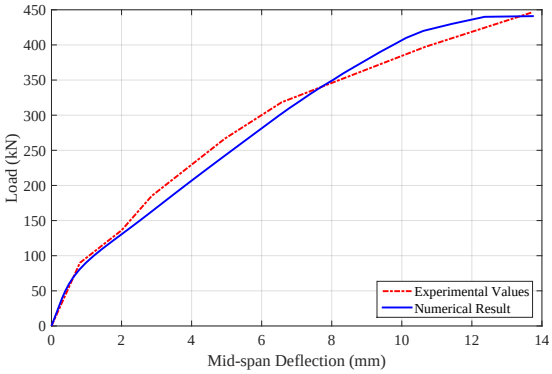

(c) Beam B1.

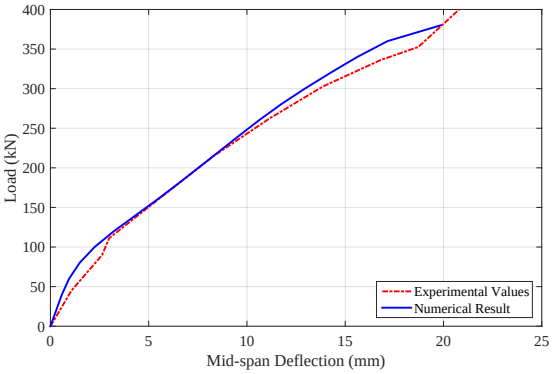

(d) Beam B2.

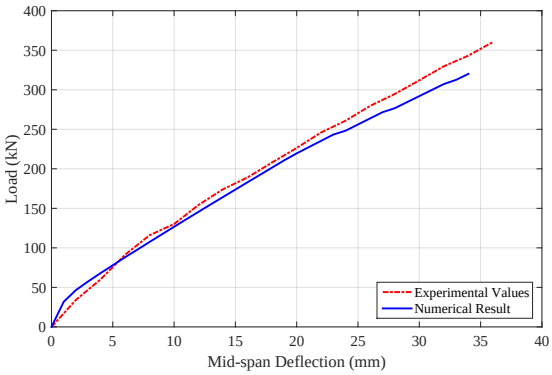

(e) Beam B3.

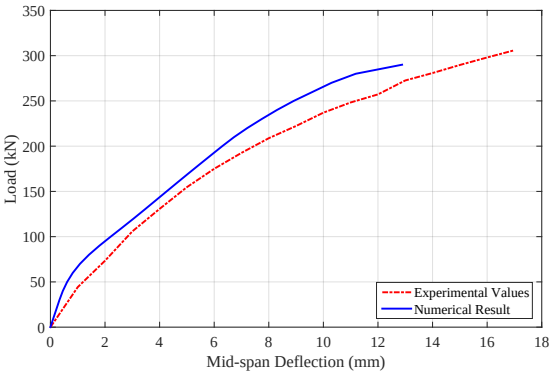

(f) Beam C1.

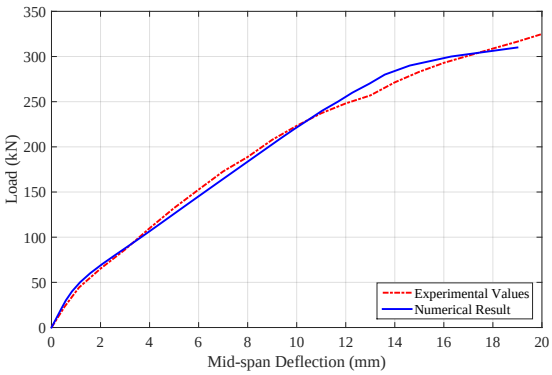

(g) Beam C2.

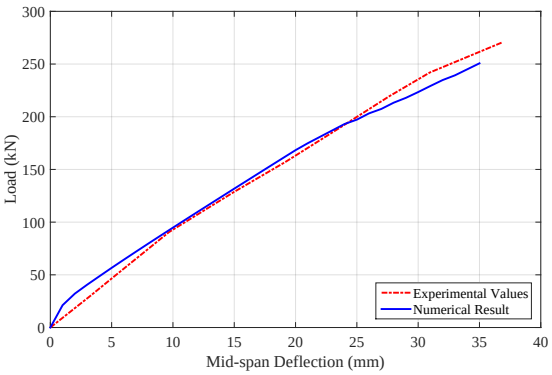

(h) Beam C3.

Figure 5-13 – Load versus mid-span displacement curve for series A,B and C.

5.2 Elements subjected to bending-torsion action

In this section, in order to analyze the suitability and accuracy of the developed three-dimensional formulation, the numerical results obtained by the proposed model are compared to various series of beam tested in combined bending-torsion carried out by McMullen & Warwaruk in 1967 [72] and by Onsongo in 1978 [82]. Although some modifications are required for the tensile relationship to correctly predict the torsional behavior of RC beam under pure torsion (as described in Chapter 4), in this section, the tensile relationship proposed for shear effect, originally developed by Vecchio [110] and described in Section 2.4.1.1, is used for the uniaxial tensile stress-strain behavior of concrete, for the following reasons:

- In the case of combined loading, the cracking of concrete might be due to a bending or torsional effect, knowing that the modified tensile relationship proposed in Chapter 4 has a greater concrete cracking strength than that proposed for shear effect, the use of this tensile law proposed for pure torsion could lead to an overestimation of the predicted values of cracking moment if cracking is due to bending.

- Even if cracking is due to torsion, it should be noted that under pure torsion, after cracking of concrete the sectional behavior is assumed to be carried out as a hollow section; however, in this case of combination loading, under the effect of bending moment, this assumption is no longer supported. In this multi-fiber approach, when the entire cross-section acts to resist torsional effect instead of a hollow cross-section, the proposed tensile relationship for pure torsion could also lead to overestimated predicted values of cracking moment.

5.2.1 Comparison with experimental data

5.2.1.1 McMullen & Warwaruk's beams [72]

McMullen & Warwaruk in 1967 [72] carried out a series of experimental test for rectangular RC members subjected to combined loading. The experimental program was divided into seven groups under bending and torsion (Group 1,2,3 and 4) and under shear, bending and torsion (Group 5,6,7). In this section, only the Group 1 and 2 were investigated in order to analyze the response of unsymmetrically and symmetrically RC members under bending - torsion combination. The outline of test setup and the internal forces diagrams are represented in Figure 5-14a, the cross-section dimensions along with the reinforcement

details are shown in Figure 5-14b while the concrete strength and the bending/torsional moments applied are indicated in Table 5.6. Because of big compressive strength, all the specimens in Group 2 are considered as design to fail on steel tension.

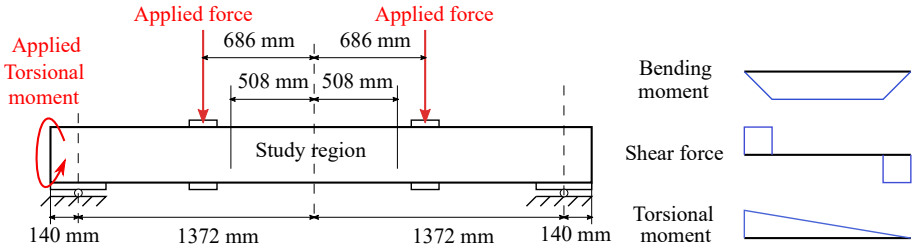

(a) Outline of test setup.

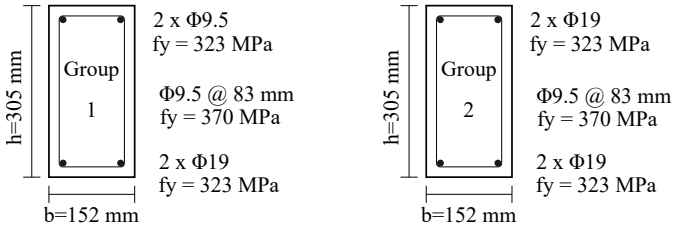

(b) Cross-section.

Figure 5-14 – McMullen & Warwaruk's bending and torsion test in 1967 [72].

In Table 5.6, the ultimate bending and torsional moments are also presented as well as the relative difference with respect to the experimental values. It is should to be noted that the loads were applied proportionally and the ratio between torsional and bending moments in each specimen is presented by the ratio R: $R = \dfrac{\text{Torsional moment}}{\text{Bending moment}}$. Reasonable results with relative difference less than 10 % can be found in most of the case.

Table 5.6 – Concrete strength, bending/torsional moments ratio and the ultimate loading values.

Beams	f_c (MPa)	R = T/M	Bending moment (kNm)			Torsional moment (kNm)		
			Exp values	Proposed Model	Relative difference	Exp values	Proposed Model	Relative difference
1-1	35.8	∞	0	0	0 %	13.8	13.6	-1.4 %
1-2	30.6	3.00	5.3	5.0	-5.7 %	15.6	14.6	-6.4 %
1-3	34.9	2.00	7.9	7.3	-7.6 %	15.8	14.5	-8.2 %
1-4	34.3	1.00	18.0	17.4	-3.3 %	18.0	17.4	-3.3 %
1-5	40.1	0.50	30.2	30.0	-0.7 %	14.8	15.0	1.4 %
1-6	38.2	0.25	40.9	38	-7.1 %	10.2	9.5	-6.9 %
2-1	39.6	∞	0	0	0 %	20.5	21.8	6.3 %
2-2	34.6	2.00	9.9	10.4	5.1 %	19.4	20.8	7.2 %
2-3	37.9	1.00	18.8	17.6	-6.4 %	18.8	17.6	-6.4 %
2-4	36.0	0.50	30.2	29.2	-3.3 %	15.1	14.6	-3.3 %
2-5	36.6	0.25	40.9	39.2	-4.2 %	10.2	9.8	-3.9 %

The load-deformation responses of specimens in Group 1 and 2 are simulated correctly in Figure 5-15. For the beam 1-2, the torsional moment - twist rate numerical curve gives a very good agreement with the experimental data, even though the cracking and ultimate torsional moment were a bit under-estimated (Figure 5-15a). For beam 2-2, the cracking torsional moment is correctly predicted, while the torsional stiffness after cracking is also well represented (Figure 5-15c). For beam 1-4, before cracking, very good correlation is obtained, while the torsional stiffnesses predicted by the proposed model after cracking are apparently correct with the experimental values (Figure 5-15b). In the case of beam 2-4, excellent behavior before and after cracking is simulated (Figure 5-15d).

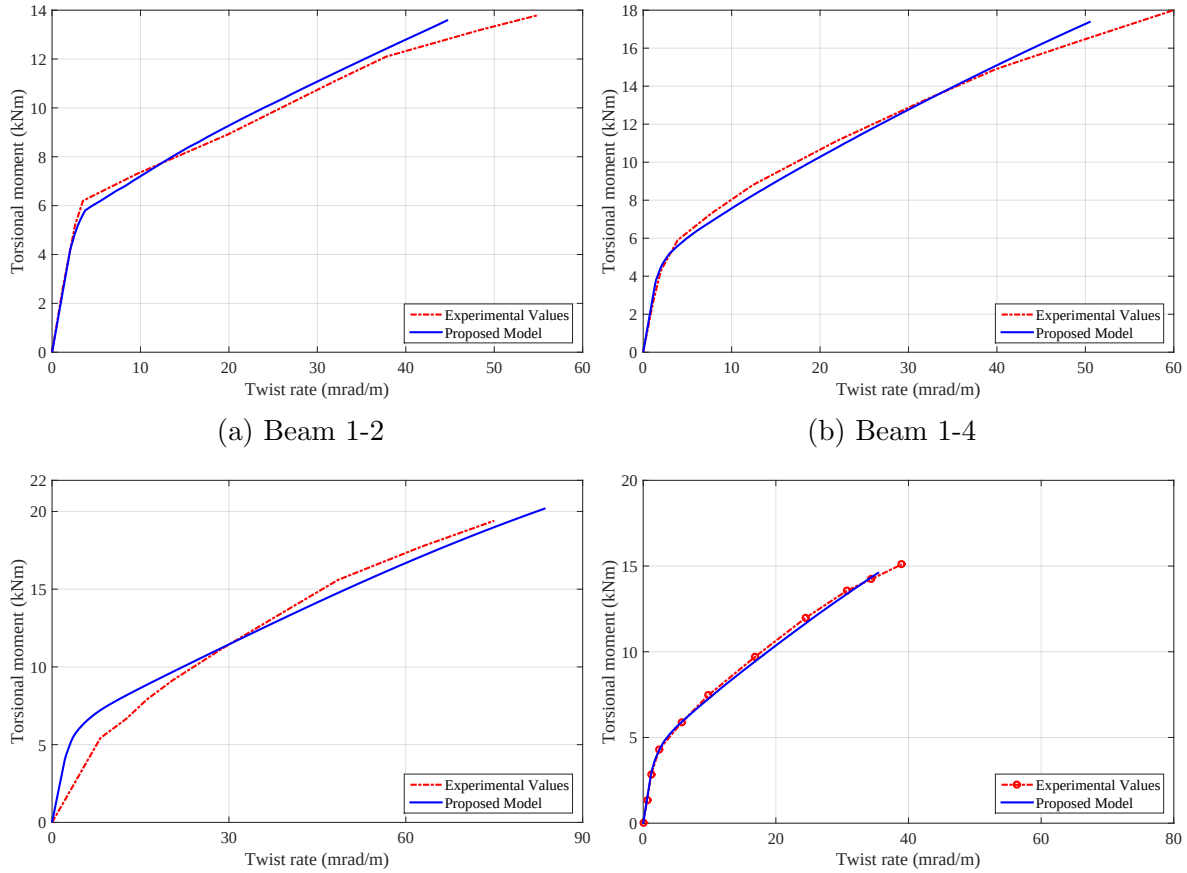

(a) Beam 1-2 (b) Beam 1-4

(c) Beam 2-2 (d) Beam 2-4

Figure 5-15 – Experimental and numerical Torsional moment - Twist rate diagrams for Group 2 of McMullen & Warwaruk's test of bending and torsion.

In the bending-displacement diagram in Figure 5-16, good correlations are also obtained at early load stage, in high load stage, the differences become bigger, however in general the numerical curve correlated well with the experimental values. It is important to note that in the test data, the displacement values were measured with an uncertainty 0.5 inches incertitude, which could make the experimental bending moment - displacement curve became less reliable, as observed in Figure 5-16.

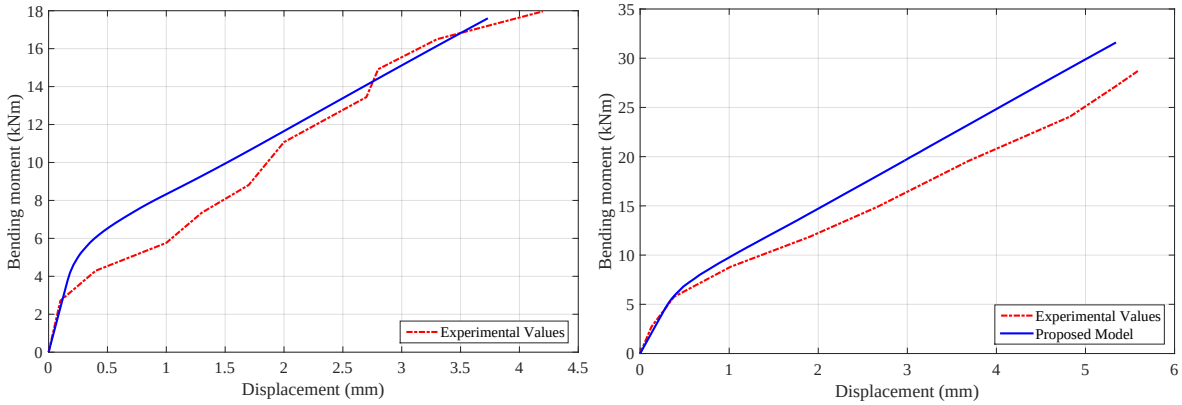

(a) Beam 2-3 (b) Beam 2-4

Figure 5-16 – Experimental and numerical Bending moment - mid-span displacement diagrams for Group 2 of McMullen & Warwaruk's test of bending and torsion.

5.2.1.2 Onsongo's beams [82]

In the test of Onsongo, two series of beam were investigated (Figure 5-17a). The first series named "torsion-bending-overreinforced" (TBO) series in which 5 specimens were over-reinforced designed to fail on concrete compression. In this series, concrete strengths were around $f_c = 20$ MPa, while the difference between each specimens were the ratio R of bending moment and torsional moment applied, which are indicated in Table 5.7. The second series named "torsion-bending-solid" (TBS) included 4 solid beams tested under the same R ratio but had different concrete compressive strengths ranging from 15.5 to 45.8 MPa (Table 5.7). The cross-section dimensions, as well as reinforcement distribution and properties, of these two series are detailed in Figure 5-17b.

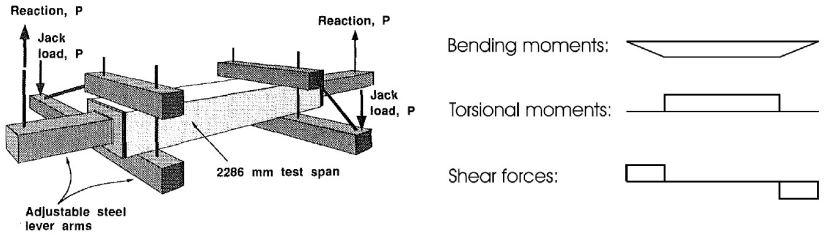

(a) Outline of test setup.

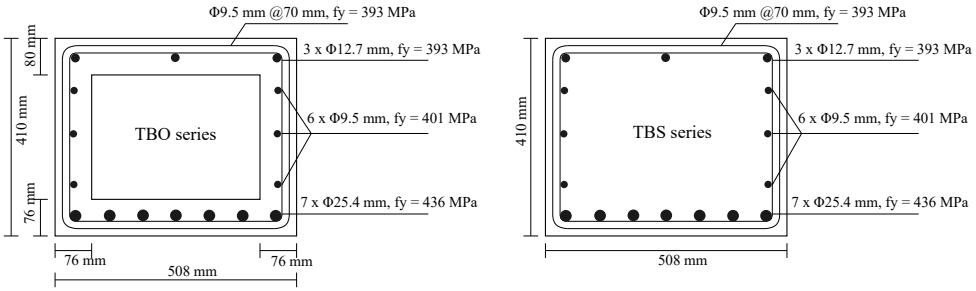

(b) Cross-section details.

Figure 5-17 – Onsongo's bending and torsion test in 1978 [82].

The ultimate bending and torsional moments are presented as well as the relative difference with respect to the experimental values in Table 5.7. Reasonable results with relative difference less than 10 % can be found in most of the case. It is also interesting to note that, similar to the numerical results in Section 5.2.1.1, in this test the proposed model give under-estimated numerical results in most of cases.

Table 5.7 – Concrete strength, bending/torsional moments ratio and the ultimate loading values.

Beams	f_c (MPa)	R = T/M	Bending moment (kNm)			Torsional moment (kNm)		
			Exp values	Proposed Model	Relative difference	Exp values	Proposed Model	Relative difference
TBO1	19.5	0	401	383	-4.5 %	0	0	0 %
TBO2	19.7	0.25	334	331	-0.9 %	78	74	-5.1 %
TBO3	19.1	0.70	232	238	2.6 %	143	143	0 %
TBO4	20.4	1.50	117	113	-3.4 %	149	147	-1.3 %
TBO5	20.6	5.00	35	36	2.9 %	143	137	-4.2 %
TBS1	28.0	1.50	164	159	-3.0 %	209	205	-1.9 %
TBS2	32.9	1.50	169	163	-3.6 %	216	211	-2.3 %
TBS3	45.8	1.50	186	185	-0.6 %	245	239	-2.4 %
TBS4	15.5	1.50	108	121	12.0 %	125	156	24.8 %

Good agreement can be also found in the torsional moment - twist rate diagram of series TBO of Onsongo's test (Figure 5-18). In this series, for beam TBO3, although there are some difference after cracking, the torsional stiffness predicted by the proposed model is apparently correct with the experimental values (Figure 5-18a). For beam TBO4, very good correlations are obtained at early load stage, in high load stage, the differences become slightly bigger, however in general the numerical torsional moment - twist rate curve represent well the torsional behavior in the series.

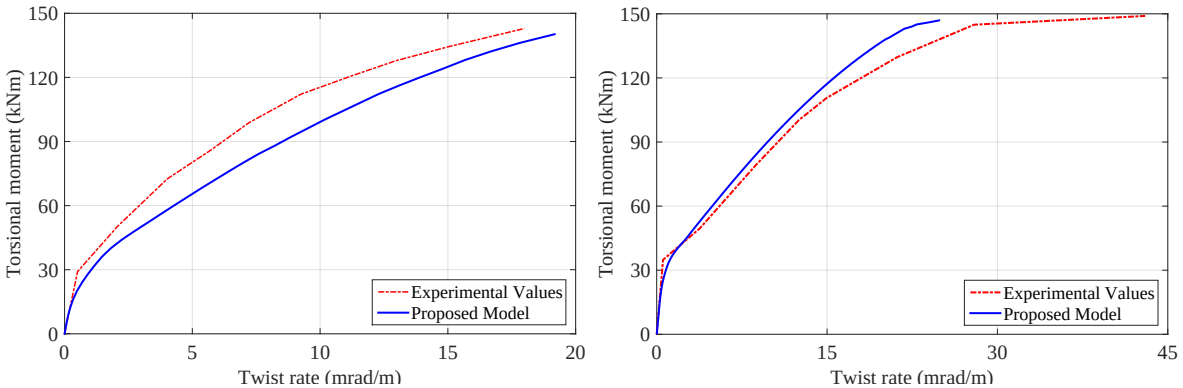

(a) Beam TBO3 (b) Beam TBO4

Figure 5-18 – Experimental and numerical Torsional moment - Twist rate diagrams for series TBO in the bending-torsion test of Onsongo.

In the TBS series, the behavior before cracking are well simulated for beam TBS1 (Figure 5-19a), while for the beam TBS3, very good correlation were obtained at all stages of loading (Figure 5-19b). In general, good correlations with experimental data are obtained by the proposed model in predicting the load-deformation responses.

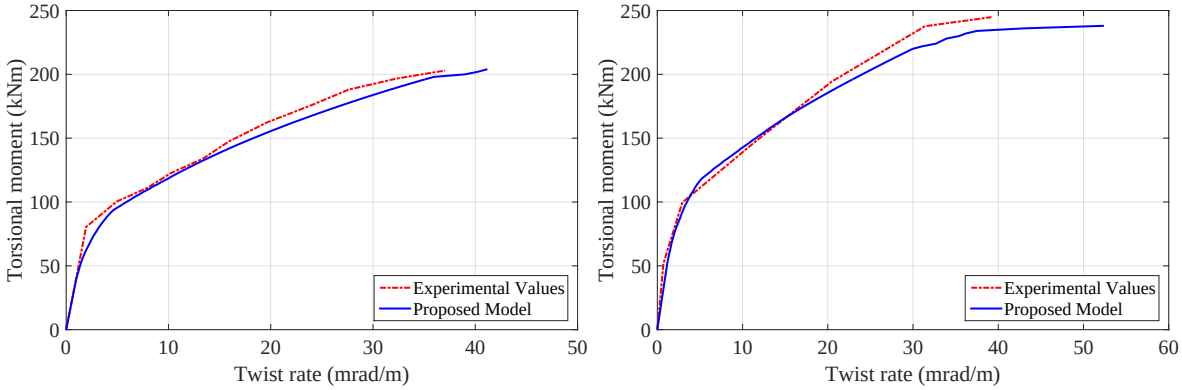

(a) Beam TBS1 (b) Beam TBS3

Figure 5-19 – Experimental and numerical Torsional moment - Twist rate diagrams for series TBS in the bending-torsion test of Onsongo.

The transverse strains were also measured in Onsongo's experimental test, using special strain gauge attached to the stirrups. The simulated strains in the stirrups can be therefore compared with the measured values from experimental test data. In Figure 5-20, the diagrams of torsional moments versus transverse strains at mid-depth of beam TBO4 and TB5 are represented with a good agreement between the numerical and experimental values, the slope of the curve and the maximum strain were obtained reasonably. In Figure 5-21, the torsional moment - transverse strain diagrams for different faces of beam TBO3 are showed and reasonable agreements were observed at mid-depth (Figure 5-21a) and at the bottom face of the beam (Figure 5-21b). In general, the transverse strain in the stirrups calculated and represented by the proposed model are satisfactory.

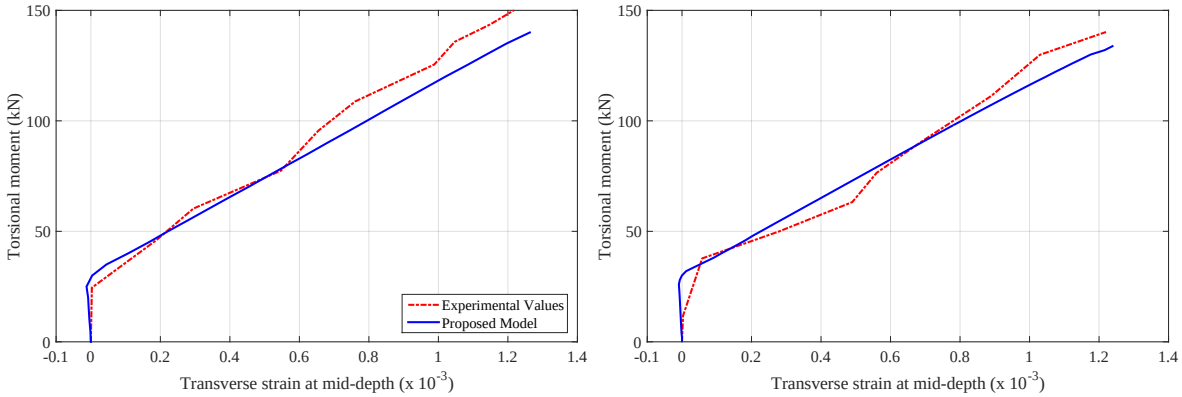

(a) Beam TBO4. (b) Beam TBO5.

Figure 5-20 – Experimental and numerical diagram of Torsional moment - Transverse strain at mid-depth of beams in series TBO of Onsongo's test.

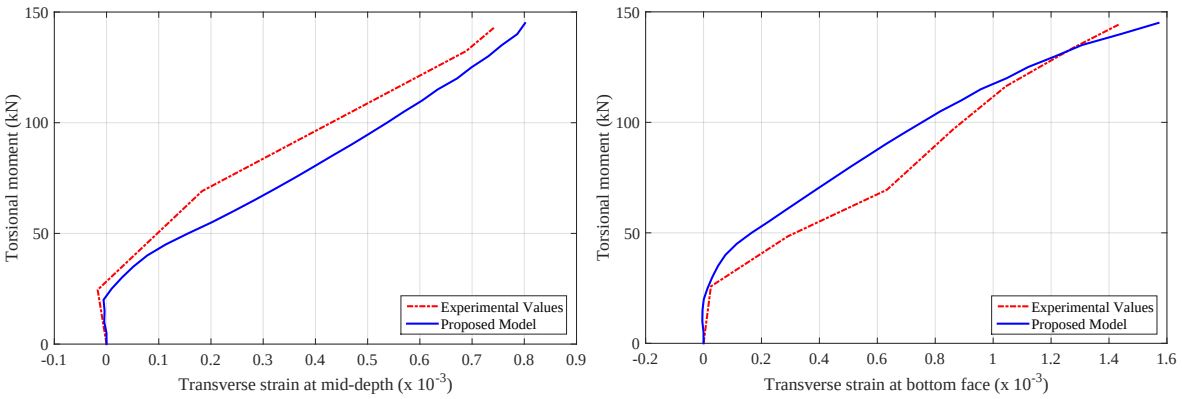

(a) At mid-depth of the beam. (b) Bottom face of the beam.

Figure 5-21 – Experimental and numerical diagram of Torsional moment - Transverse strain for different faces of beam TBO3.

It is interesting to remark that negative strains with respect to torsional moment are recorded in the experimental observation and by the proposed model when the gauge is placed at the mid-depth of the beam (Figure 5-20a, 5-21a). In fact, examining the case of a cross-section under bending and torsional moments as in Figure 5-22, at early load stage, in each side of cross-section, the combination of shear strains and stresses due to bending and torsional moments might have positive or negative relative values with respect to torsional moment. If the strain gauge is placed in the left side of cross-section, strain values recorded are always positive with respect to torsional moment. On the other hand, if the strain gauge is placed in the right side, strains values recorded might negative with respect to torsional moment at early load stage, when the shear strain due to bending dominates the one due to torsion.

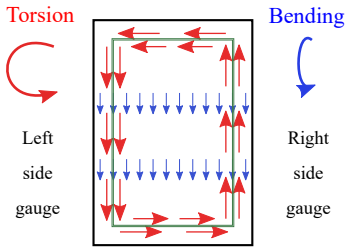

Figure 5-22 – Shear stress direction in cross-section under bending-torsion action.

5.2.2 Bending-Torsion interaction diagram

As mentioned in Chapter 2, Section 2.2, the bending-torsion interaction diagram can be plotted using the skew-bending theories, firstly proposed by Lessig [66] and then developed by Collins et al. [23], [24], Yudin [116] and Elfgren et al. [35]. Among these theories, the one proposed by Collins et al. is considered suitable for the analysis of Mc Mullen &

Wawaruk's experimental test, because it was developed for two case of symmetrically and unsymmetrically reinforcements disposition (Figure 5-23). In the interaction diagram, for both cases, the Mode 1 failure corresponds to the domination of bending moment, with a helical crack in which the failure surface is initiated at the top face of the beam, according to initial Skew-bending theory by Lessig [66] as indicated in Figure 2-1a. The Mode 2 failure produces when torsional moment becomes dominated and the failure surface is initiated by cracks on the side faces of the beam. For symmetrically rectangular RC members (equal quantity of top and bottom longitudinal reinforcements), only these two failures mode are recorded (Figure 5-23a), while in the case of unsymmetrically RC members (top longitudinal steel is less than the bottom), the Mode 3 failure occurs with a helical cracks initiated on the top of the beam (Figure 5-23b).

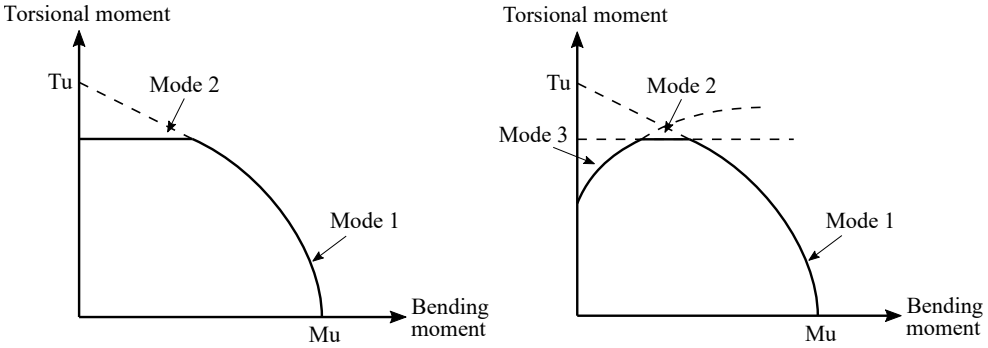

(a) Symmetrical RC members (b) Unsymmetrical RC members

Figure 5-23 – Collins et al.'s interaction diagram between bending and torsional moments [23].

Regarding the numerical results of ultimate loadings, for the case of symmetrically RC members concerning Group 2 of McMullen & Warwaruk's test, the bending-torsion interaction diagrams for this series are shown in Figure 5-24a, along with the experimental values and analytical solutions, which was calculated according to Collins et al.'s theory using an average concrete compressive strength of 5 specimens in Group 2. Good correlations between numerical results, experimental values and analytical solutions are achieved for the cases of beams 2-3, 2-4 and 2-5, when bending moment dominated torsional moment (The ratio R was less than 1). It is also interesting to note that in this stage, in compare to the experimental values, the numerical model gives conservative results while the analytical one gives unconservative results. However, when torsion became dominated (Ratio R became bigger than 1), the numerical and analytical ultimate values of torsional moment tends to over-estimated the experimental ones. It can be remarked that, compared to the experimentation, the skew-bending theory overestimates consider-

ably the pure torsional strength of symmetrically RC members, while the predicted values obtained by the proposed model are more reasonable with relative differences of about 6-7 % (Table 5.6). The numerical and experimental ultimate values of torsional moment of beams 2-3, 2-2 and 2-1 change slightly and are nearly constant between beams 2-1 and 2-2, which corresponds to a transition between Mode 1 and 2 in analytical solutions.

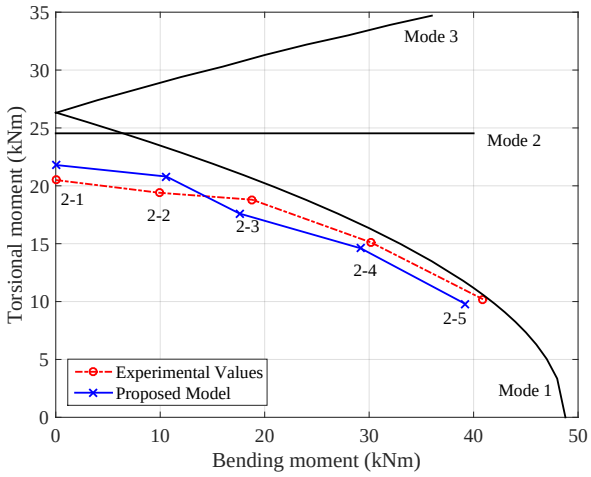

(a)

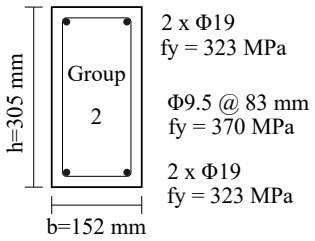

(b)

Figure 5-24 – (a) Interaction diagram between bending and torsional moments for the Group 2 of McMullen & Warwaruk's test. (b) Symmetrically cross-section of Group 2.

For the case of unsymmetrically RC members concerning Gr. 1 of McMullen & Warwaruk's test, a similar bending and torsional moments interaction diagrams are shown in Figure 5-25a. As in the case of symmetrically members, the analytical solutions continue to give conservative ultimate values, while the numerical model gives better agreements with experimental values, especially near the vicinity of the transitions between 3 failures modes.

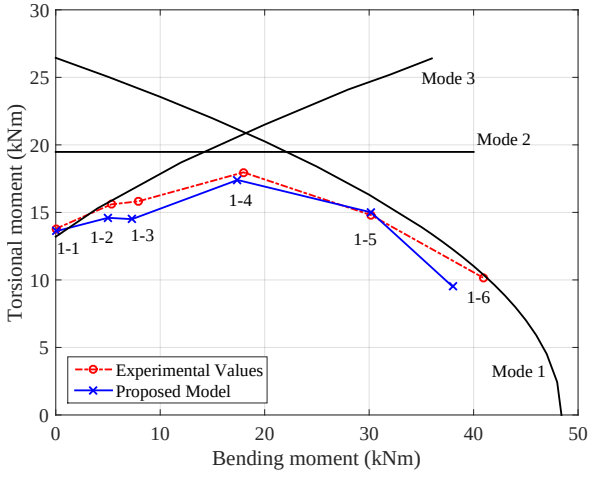

(a)

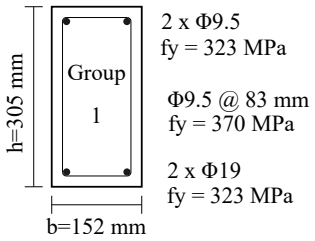

(b)

Figure 5-25 – (a) Interaction diagram between bending and torsional moments for the Group 1 of McMullen & Warwaruk's test. (b) Unsymmetrically cross-section of Group 1.

In the TBO series of Onsongo's test, good correlations were also obtained in the interaction diagrams of this series between numerical and experimental values (Figure 5-26a). Similar interaction curve than the Collins et al.'s theory in Figure 5-23b, with the appearance of the Mode 3 failure, were reproduced: in the Mode 1, the increase of torsional moment happens simultaneously with the decrease of bending moment (Beam TBO1, TBO2, TBO3); Until a value determined, when the ultimate value of bending moment continue to decrease but the ultimate values of torsional moment are still constant, the Mode 2 failure happens (Beam TBO3, TBO4). Then, when the ultimate value of bending moment becomes too small, the ultimate torsional moment decreases slowly, which corresponds to the failure Mode 3 (Beam TBO4 to TB5). Several numerical results obtained by others were also plotted in these interaction diagram with a good level of prediction obtained in most of specimens: the model of Bairan performed very well in the specimens with small ratio of bending/torsion (TBO1, TBO2, TBO3), the model of Vecchio gave good results in the specimens with big ratio of bending/torsion, while a good balance of accuracy between all 5 specimens can be obtained by the proposed model. In general, the ultimate values of bending and torsional moments are well predicted by the proposed model, especially for the case of higher ratio of torsion/bending. In Figure 5-26b, a new bending-torsion interaction curve was obtained with various values of the torsion/bending ratio R, using a numerical model based on the TBO series with a compressive strength of concrete $f_c = 20$ MPa. From this diagram, the Mode 1 failure can be considered for a value of R from 0 to 0.7 (Beam TBO3), the Mode 2 failure happens in a range of R from 0.7 to 2 and then the Mode 3 for a R larger than 2.

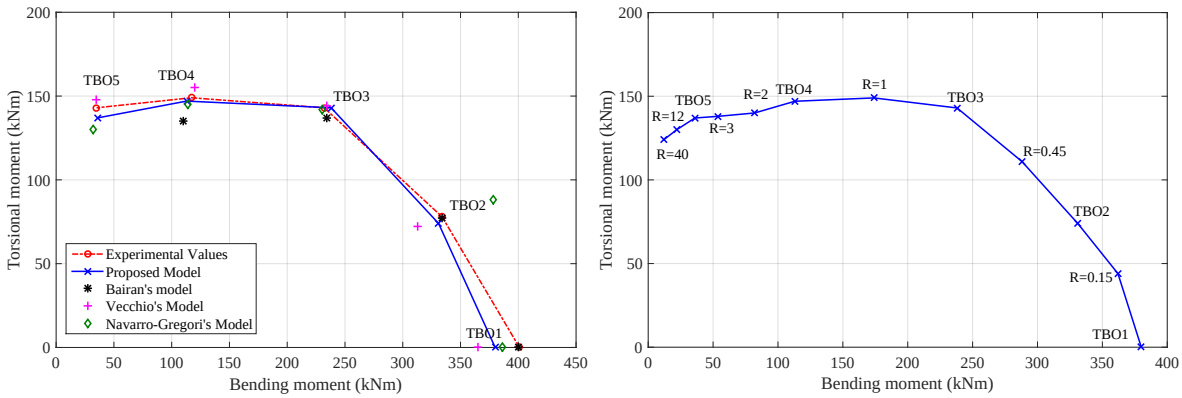

(a) In compare to others numerical models. (b) For different values of R.

Figure 5-26 – Interaction diagram between bending and torsional moments for the TBO series TBO of Onsongo's test.

5.2.3 Stirrup contribution on torsional resistance

This section aims to investigate the influence of the stirrup density on the bending-torsion interaction. To do so, let's consider a RC cantilever beam subjected to bending and torsional moments at the free-end as shown in Figure 5-27. The stirrup density is changed by varying the spacing of stirrups s_{st} along the beam length. During the simulation, bending and torsional moments are imposed simultaneously using a ratio $R = \dfrac{\text{Torsional moment}}{\text{Bending moment}}$.

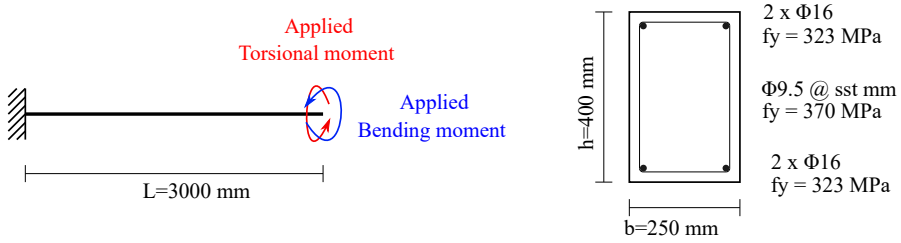

Figure 5-27 – Example of RC cantilever beam subjected to bending-torsion.

Figure 5-28 presents the bending-torsion interaction curves for different values of stirrup spacing. As we can see, when the torsion is minor compared to bending, for instant R=0.25, the stirrup density logically has almost no effect. The stirrup effect on the element resistance becomes more significant when the torsion dominates over the bending. In case of pure torsion, it can be seen that the torsional resistance increases about 34 % with increasing of stirrup density of 8 times. This numerical application highlights that the proposed FE formulation takes into account the transversal reinforcements in the predicting of the torsional resistance of RC members.

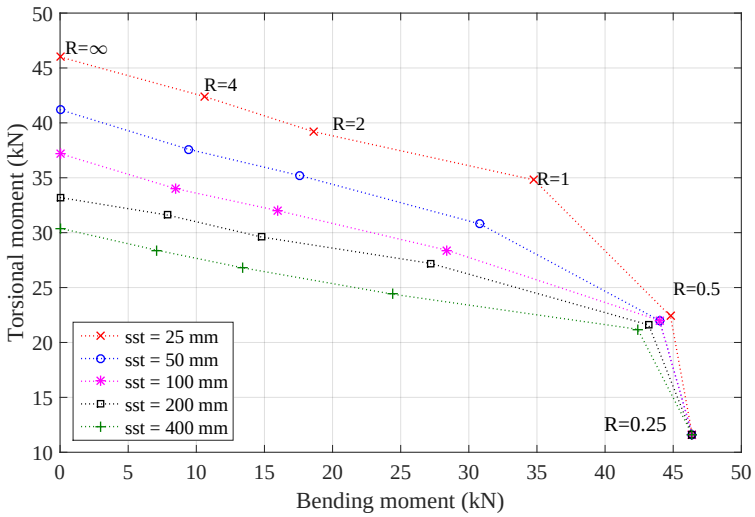

Figure 5-28 – Bending-Torsion diagrams in function of stirrup spacing.

Figure 5-29 presents the growth percent of the ultimate torsional moment for difference

cases of stirrup spacing, with respect to the case with the less amount of stirrup ($s_{st} = 400mm$). By increasing 2 times the transverse reinforcement amount, the ultimate value of bending moment increase only 10 %, while a 50 % of growth can be obtained by increasing 16 times the stirrup amount.

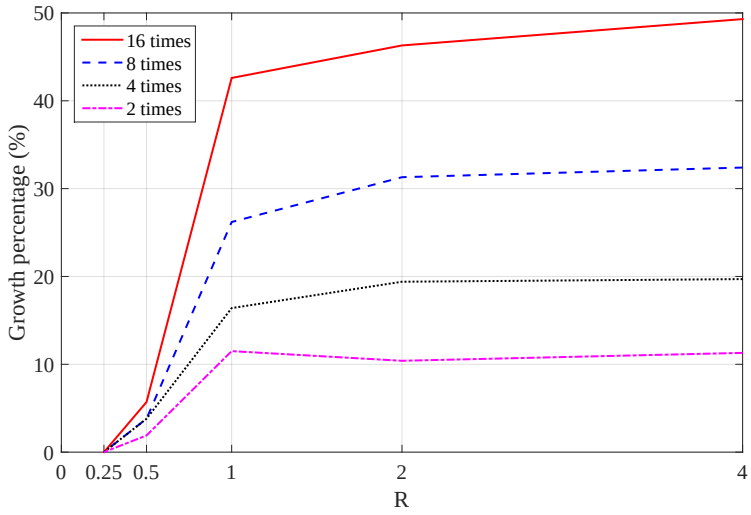

Figure 5-29 – Growth percent of the ultimate torsional moment when increasing the stirrup density.

5.2.4 Stress distribution

In this section, the distribution of normal and shear stresses of TBO series in Onsongo's test are studied in both elastic and inelastic material domains. In elastic range, the same outline and cross-section dimensions in Figure 5-17a are conserved, with an elastic modulus of 30 GPa, the Poisson's ratio of 0.2 and the ratio R of bending/torsional moments was 1.5 (beam TBO4). The distribution of stresses over the cross-section at torsional moment of 150 kNm and bending moment of 100 kNm are shown in Figure 5-30. The bending effect can be represented clearly by a constant distribution of normal stress in horizontal direction (Figure 5-30a). Because the cross-section is almost symmetric and crack is not considered in elastic range, σ_x distributions are also symmetrical. On the others hand, due to torsional effect, the shear stress flow creates opposite orientations of shear stresses in both vertical and horizontal directions (Figure 5-30b and 5-30c).

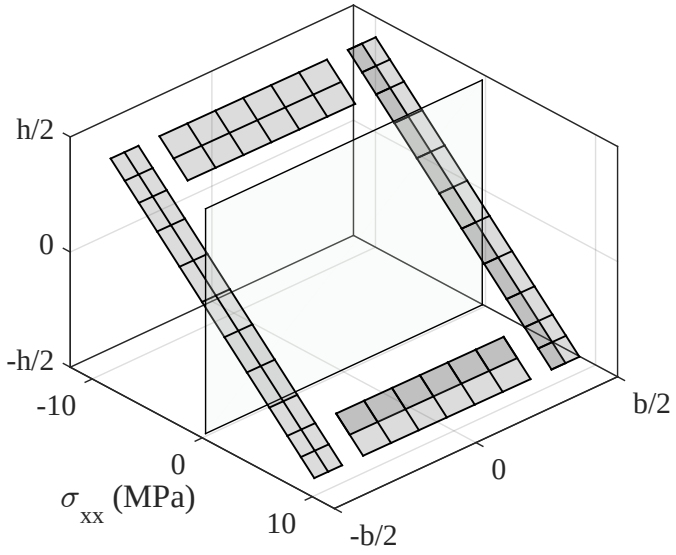

(a) Normal stress σ_x distribution.

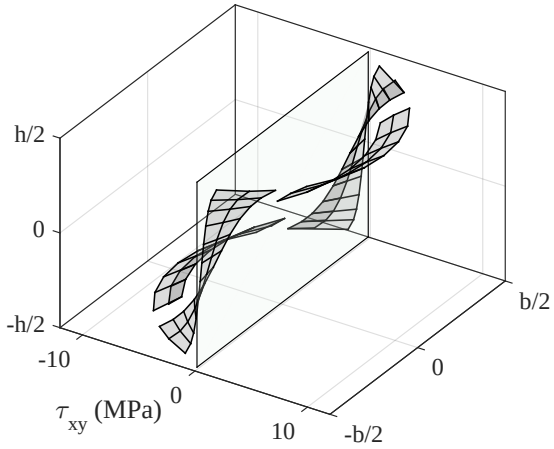

(b) Shear stress τ_{xy} distribution.

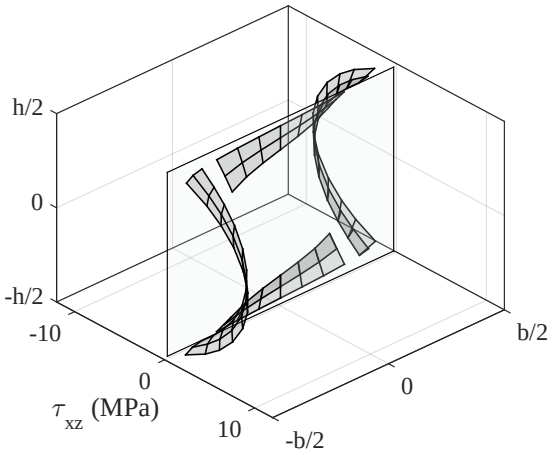

(c) Shear stress τ_{xz} distribution.

Figure 5-30 – Stress distribution over cross-section of beam TBO4 in elastic range.

Coupling between bending and torsional effect could be represented clearly in the inelastic range. For beam TBO4, the stresses distribution are shown in Figure 5-31 at load stage after cracking and close to the ultimate point. For a better illustration and analysis, the stresses distribution will be presented in 2D following four vertical and horizontal cuts at the Left and Right webs and the Top and Bottom flanges of the cross-section, as indicated in Figure 5-31a. In horizontal direction, the shear stress distribution are parabolic symmetrical (similar to that in elastic range) as seen in Figure 5-31c. However, in vertical direction, under bending effect and crack contribution, the increment of shear stresses in the tension zone is considerably less than in the compression zone, τ_{xz} distribution becomes unsymmetrical as seen in Figure 5-31d. The distributions of normal stresses are also unsymmetrical in vertical direction as consequence, while remaining constant in horizontal direction (Figure 5-31b). The numerical results achieved in Figure 5-31 are corresponding to the one obtained by Navarro-Gregori's model [76].

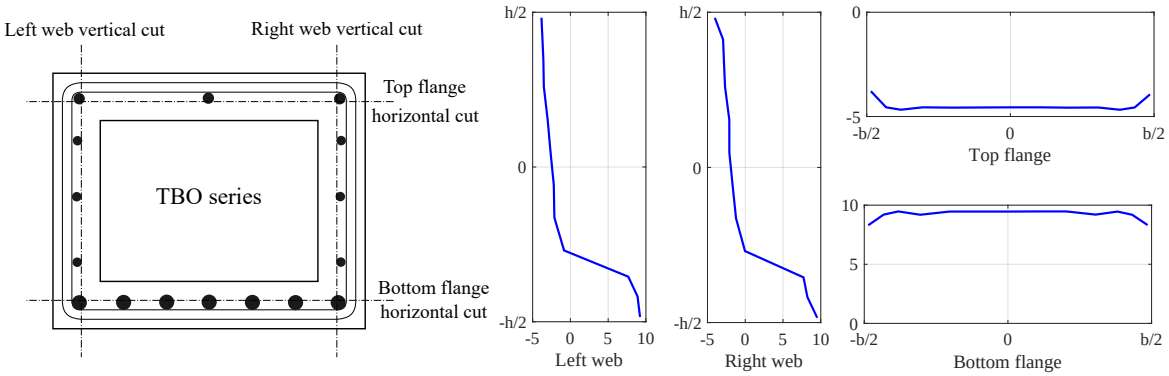

(a) Section cut position.

(b) Normal stress σ_x distribution.

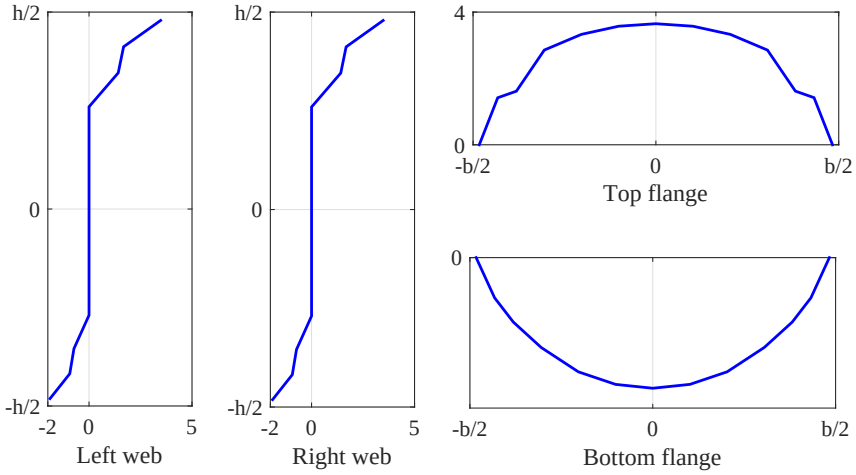

(c) Shear stress τ_{xy} distribution.

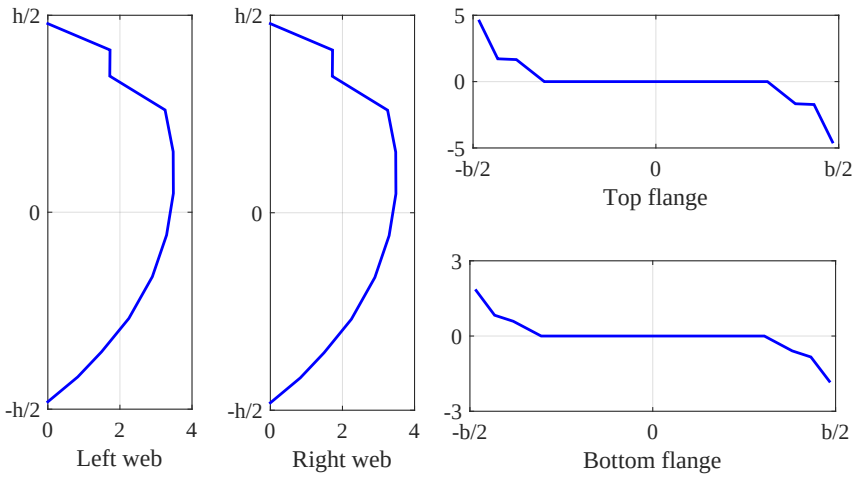

(d) Shear stress τ_{xz} distribution.

Figure 5-31 – Stress distribution over cross-section of beam TBO4 in inelastic range.

5.3 Elements subjected to shear-bending-torsion

In this section, the combined loading effect between shear, bending and torsional moments is analyzed by investigating several test series carried out by McMullen & Warwaruk [72]. The outline of test setup is shown in Figure 5-32a: a simple supported RC beam subjected to vertical force near to the mid-span, while torsional action is created by two steel arm at two beam's ends. Three groups of beams with 4 specimens in each were investigated: Group 5,6 with the same concrete properties and reinforcement distribution (Figure 5-32b), while the beams in Group 7 were provided with larger bottom longitudinal reinforcement steel bars and a large spacing of the stirrups in order to obtain a stronger strength in flexure but weaker in transverse shear. In this test setup, the distance A of study region, B between study region and the applied force, and C from vertical force to the right beam's support are different for various specimens and are indicated in Figure 5-32a.

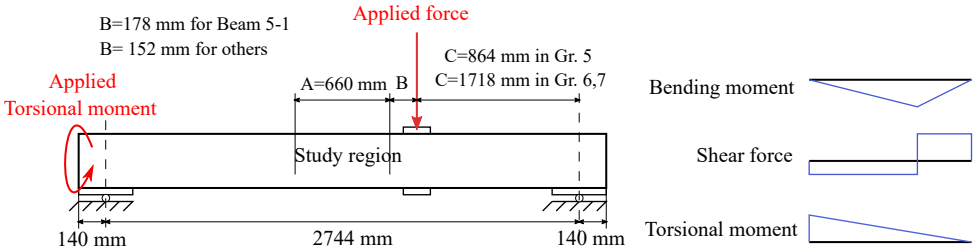

(a) Outline of test setup and diagrams of internal efforts.

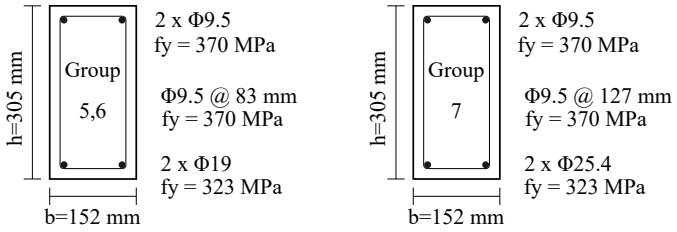

(b) Cross-section details of Group 5, 6 and 7.

Figure 5-32 – McMullen & Warwaruk's test [72] for combined shear-bending-torsion.

5.3.1 Comparison with experimental data

The ultimate shear force, bending and torsional moments of each specimen are presented for each concrete strength in Table 5.8, as well as the relative difference with respect to the experimental values. As can be seen, the proposed model gives the results more or less in good agreement with the experimental data. Indeed, the relative errors are most smaller than 6 %, except for the cases of beams 5-4 and 6-4, when the ratio R between

torsional and bending moments is small (R=0.25), and for the case of beam 7-2.

Table 5.8 – McMullen & Warwaruk's test [72] on shear-bending-torsion combining - Material properties and Ultimate loading.

Beams	f_c (MPa)	R = T/M	Bending moment (kNm)			Torsional moment (kNm)			Shear force (kN)		
			Exp values	Prop. Model	Rel. diff.	Exp values	Prop. Model	Rel. diff.	Exp values	Prop. Model	Rel. diff.
5-1	39.4	1.97	7.3	7.1	-2.7 %	14.5	14.0	-3.4 %	3.4	3.7	8.8 %
5-2	43.9	0.99	16.2	16.7	3.1 %	15.9	16.5	3.8 %	8.4	8.7	3.6 %
5-3	41.8	0.47	31.4	33.2	5.7 %	14.7	15.6	6.1 %	17.2	17.3	0.6 %
5-4	40.0	0.25	44.0	40.3	-8.4 %	11.2	10.1	-9.8 %	24.5	21.0	-14.3 %
6-1	40.4	1.98	7.3	7.2	-1.4 %	14.6	14.2	-2.7 %	8.1	8.2	1.2 %
6-2	40.9	0.97	16.8	17.3	3.0 %	16.4	16.7	1.8 %	19.0	19.7	3.7 %
6-3	39.3	0.50	29.8	31.2	4.7 %	14.9	15.6	4.7 %	34.1	35.6	4.4 %
6-4	39.4	0.25	48.3	41.3	-14.9 %	12.1	10.3	-14.9 %	55.4	46.9	-15.3 %
7-1	41.9	2.00	6.3	6.6	4.8 %	12.7	13.1	3.5 %	6.9	7.5	8.1 %
7-2	35.9	1.00	13.0	15.0	15.4 %	13.0	15.0	15.4 %	14.8	17.1	15.8 %
7-3	39.3	0.48	31.1	32.5	4.6 %	14.9	15.6	4.6 %	36.1	37.1	2.8 %
7-4	36.8	0.25	57.1	57.1	0 %	14.1	14.3	1.2 %	66.6	65.1	-2.2 %

The torsional moment - twist rate diagram of some specimens in these three groups are simulated correctly, as shown in Figure 5-15. The torsional stiffnesses predicted by the proposed model after cracking are in good agreement with the experimental values, especially for the cases of beam 5-4, 6-3 and 7-4 (Figure 5-33b, 5-33d and 5-33f). For beam 7-1, before cracking, very good correlation is obtained, while the torsional stiffnesses predicted by the proposed model after cracking are apparently correct with the experimental values (Figure 5-33e). For beam 5-2 and 6-2, there is a gap between numerical and experimental values in the inelastic regime, however the torsional stiffnesses are similar, while the cracking torsional moments are also well predicted (Figure 5-33a and 5-33c).

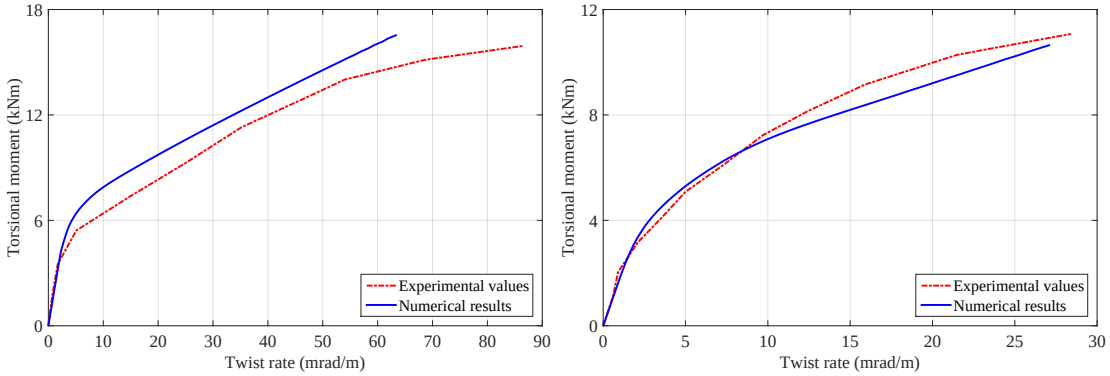

(a) Beam 5-2

(b) Beam 5-4

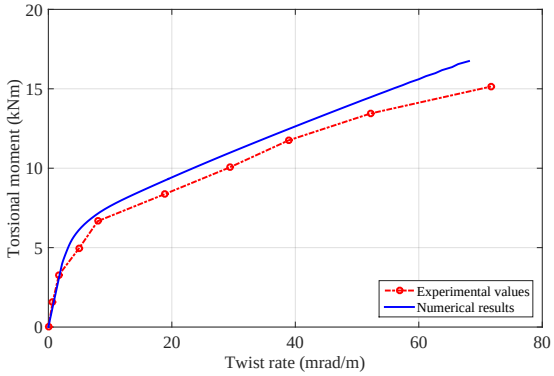

(c) Beam 6-2

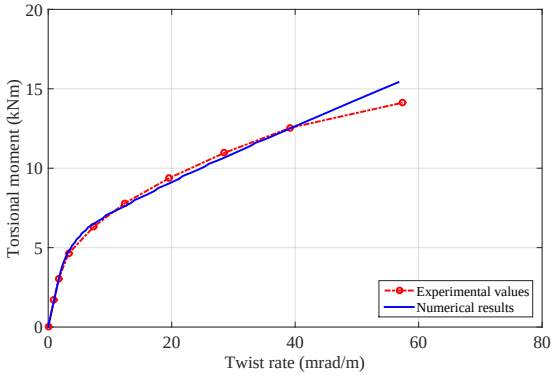

(d) Beam 6-3

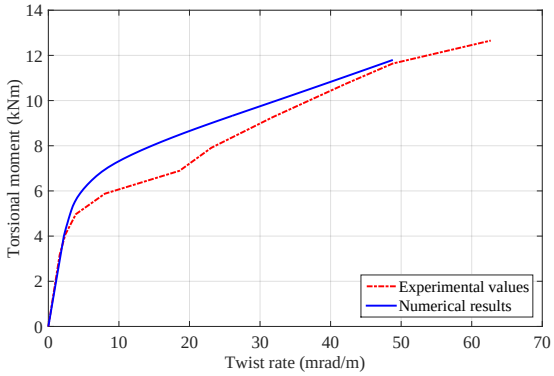

(e) Beam 7-1

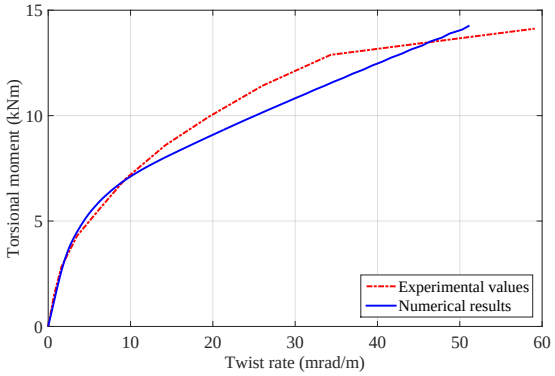

(f) Beam 7-4

Figure 5-33 – Torque-twist diagrams in McMullen & Warwaruk's test [72].

5.3.2 Bending-Torsion interaction diagram

The bending-torsion interaction diagrams of Group 5 and Group 6 are plotted in Figure 5-34. The analytical solutions given by the skew-bending theory by Collins et al. [23] are established with an average compressive strength of 41.3 MPa (in Group 5) and 40.0 MPa (in Group 6). Because of the same cross-section details and concrete strengths between two groups, similar results can be found: when the torsion/bending ratio R are bigger than 1 (beams 5-1, 5-2, 6-1, 6-2), the proposed model performs better than the skew-bending theory in predicting the ultimate loads; on the other hand, when R=0.5 (beams

5-3 and 6-3), the analytical solutions give better results. In particular, when bending moment becomes dominated torsional moments (R=0.25 for the cases of beams 5-4 and 6-4), the numerical results are very similar to the analytical solutions, but they are all too unconservative compared to the experimental values.

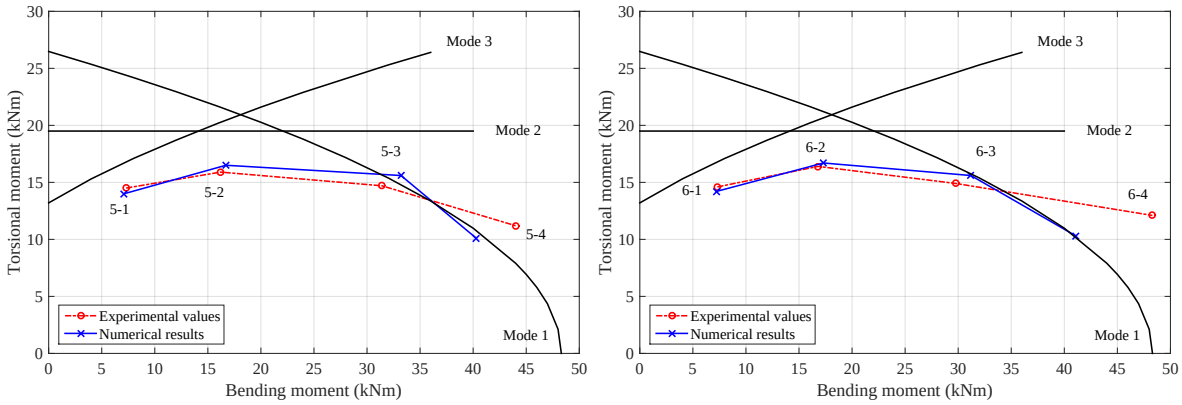

(a) Group 5. (b) Group 6.

Figure 5-34 – Bending-Torsion diagrams of Gr. 5, 6 in McMullen & Warwaruk's test [72].

In Figure 5-35, the bending-torsion interaction diagram of Group 7 is plotted. As mentioned above, the numerical results are conservative to the experimental ones. For the case of beam 7-1 and 7-4, the same level of accuracy compared to the experimentation is obtained for both proposed model and analytical solutions given by skew-bending theory. In the same way as the others bending-torsion interaction diagrams of Group 1, 2, 5 and 6, at the vicinity of transition between three failure modes, the skew-bending theory continues to give very conservative results.

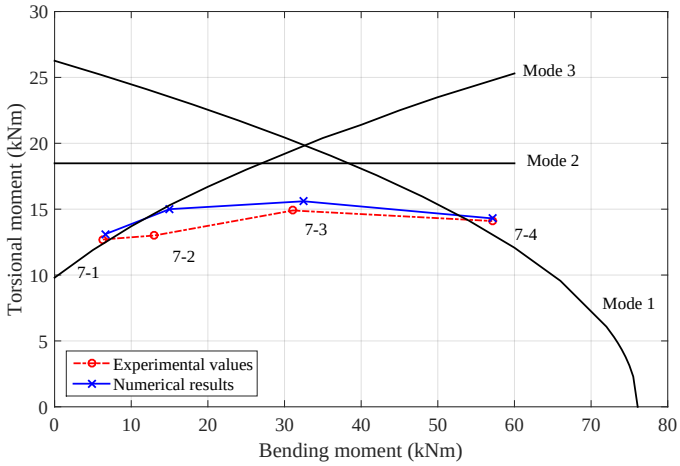

Figure 5-35 – Bending-Torsion diagram of Gr. 7 in McMullen & Warwaruk's test [72].

5.3.3 Shear-Torsion interaction diagram

In the same way as the bending-torsion interaction, in the skew-bending theory by Collins et al. [23], the shear-torsion interaction of rectangular RC members can also be illustrated for two cases of symmetrically and unsymmetrically cross-section. For symmetrically rectangular RC members (equal quantity of top and bottom longitudinal reinforcements), only the Mode 2 failure (corresponding to the predomination of torsional moment) is recorded (Figure 5-23a), while in the case of unsymmetrically RC members (top longitudinal steel is less than the bottom), the Mode 3 failure occurs while the torsional moment preponderant with respect to the shear force and bending moment (Figure 5-23b). Otherwise, in the Collins et al.'s interaction curve for torsion and shear, a shear failure mode can be included for member which fail in shear.

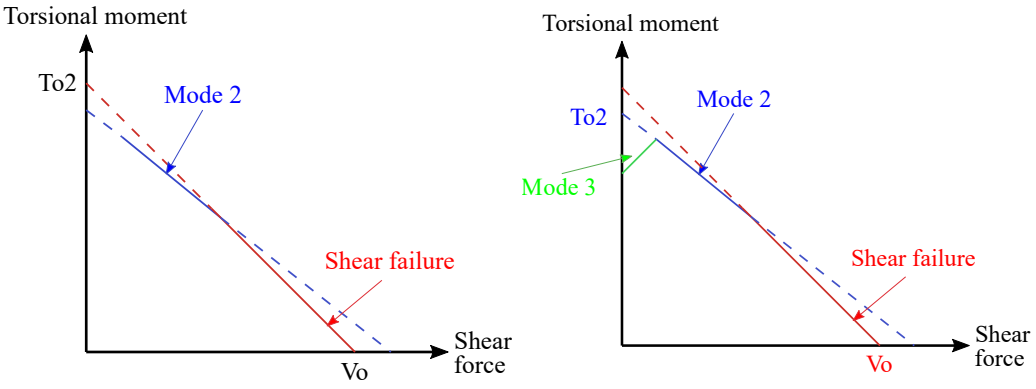

(a) Symmetrically RC members (b) Unsymmetrically RC members

Figure 5-36 – Collins et al.'s interaction diagram between shear force and torsional moment.

The shear-torsion interaction diagrams of Group 5, 6 and 7 are plotted in Figure 7-15. In Group 5 and 6, the experimental curve trend are somewhat correspondent to the skew-bending theory for unsymmetrically RC members, however, the analytical predictions are too conservative, especially in Group 5. In the other hand, different situation can be remarked for the shear-torsion interaction curve of Group 7 (Figure 5-37c). In this diagram, both the results given by the skew-bending theory and the proposed model are in good agreement with the experimentation. In the same way as the others bending-torsion and shear-torsion interaction curves have shown in this Chapter, the analytical solutions are quite conservative. This remark corresponds to the observation of Hsu [46] that the skew-bending theory overestimates considerably the pure torsional strength of RC members.

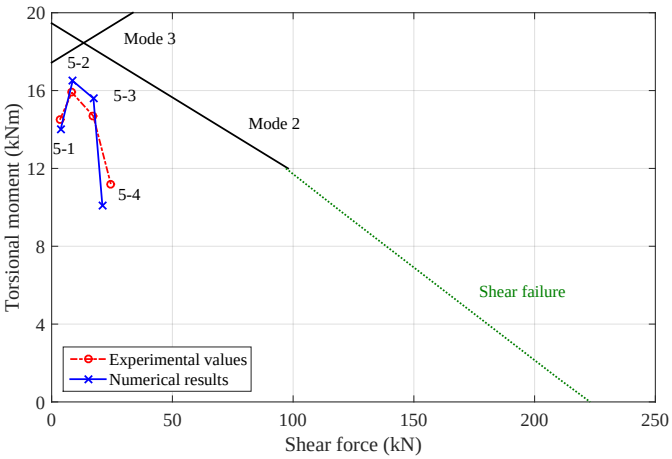

(a) Group 5

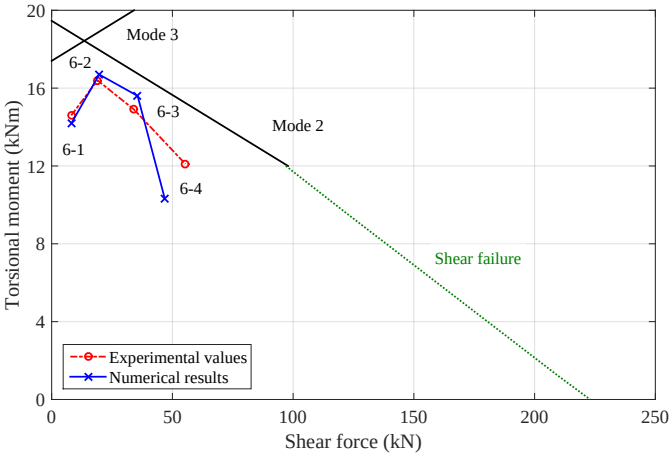

(b) Group 6

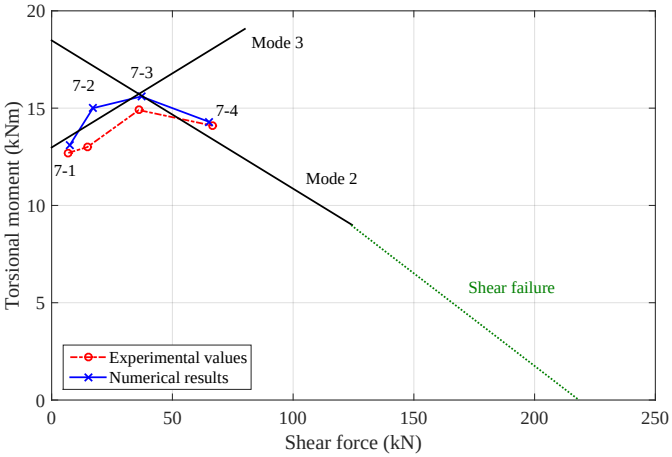

(c) Group 7

Figure 5-37 – Shear-Torsion diagrams of Group 5, 6 and 7 in McMullen & Warwaruk's test [72].

5.4 Conclusions

In this section, various numerical simulations have been done in order to assess the capability of the FE model developed in Chapter 3. Through these numerical examples, the following remarks and conclusions can be draw:

- In the elastic material regime, excellent correlations have been obtained between numerical results, theoretical formulations and analytical solutions. The multi-fiber approach has shown its advantage by ensuring an excellent balance between accuracy and calculation cost in this material regime. Deformation, strain and stress distributions can be computed and figured out with very high levels of accuracy by both approaches representing the enhanced displacement field (using Saint-Venant warping function and Lagrange polynomials).

- Between two enhanced approaches, Saint-Venant warping function is simpler and more practice with a lower computational cost, whereas the use of Lagrange polynomials approach is more general and presents a big advantage by obtaining the additional normal stresses and representing the distribution of warping displacement over cross-section under shear bending action, which can not be obtained by plane-section beam theory, as well as the Saint-Venant warping function approach.

- The proposed model is very efficient in simulating the inelastic coupling between shear and bending, in which every aspect of the beam analysis, including the load-displacement diagram, the crack propagation as well as the distribution of stresses, etc., could be represented and analyzed. Under shear-bending action, the use of proposed model for the modeling of RC beams is also appropriate by good levels of correlation obtained between numerical and experimental results in computing the ultimate loading and simulating the load-displacement diagrams of three beam series in the classic test of Bresler & Scordelis.

- The bending-torsion interaction diagrams indicates that the proposed model can provide reasonable coupling behavior of rectangular RC beams subjected to combined loading of bending and torsional moments. Indeed, the numerical results correlated well with the experimental tests of McMullen & Warwaruk and Onsongo, as well as with the analytical solutions of skew-bending theory proposed by Collins et al. Comparing to other numerical results, the proposed model gave a good balance of accuracy in predicting the ultimate values of bending and torsional moments. Not

only the load-displacement diagrams, but also the load-transverse strain diagram or the distribution of stresses over the cross-section can be correctly illustrated by the proposed model.

- Let recall that in Chapter 4, some modifications are required for the tensile relationship to predict correctly the torsional behavior of RC beams under pure torsion. However, in this Chapter, through the numerical results obtained by the proposed model, as well as by others, the tensile relationship proposed for shear effect (in Section 2.4.1.1) could be used efficiently to predict the coupling behavior including torsion. From these simulation results obtained, the use of the constitutive model based on the MCFT to representing the coupling between shear-bending-torsion is very appropriate.

- Finally, from the satisfactory results in Chapter 4 to this Chapter, the combination of MCFT based-constitutive model with the section discretization in different zones following its stress state is once again very suitable for the sectional approach model. The implementation of enhanced displacement field using Lagrange polynomials (or similar interpolation functions) in a displacement-based multi-fiber finite element approach can also be validated and applied in further studies.

Chapter 6

Geometric nonlinearity and Corotational formulation

Under extreme loads, structures may achieve large displacement conditions. Consequently, the linear geometric assumption becomes insufficient for the simulation of structural elements. The inclusion of nonlinear geometry effects is necessary in order to complete the competency of this 3D beam model. The present chapter deals with geometrically nonlinear finite element formulation for the analysis of RC members subjected to combined shear-bending-torsion actions. The co-rotational formulation is motivated by the fact that thin structures undergoing finite formulation are characterized by significant rigid body motions. The assumption of small strains but large displacements and rotations is adopted. The basic is an element-independent algorithm, where the rigid body motions (translations and rotations) are separated from the total deformation. In the corotational based, the reference configuration is split into base and corotated. Strains and stresses are measured from corotated to current, while base configuration is maintained as reference to measure rigid body motions. This formulation is recommended to use in case of solid and structural mechanics with arbitrarily large finite motions, but small strains and elastic material behavior. Extendible to nonlinear materials if inelasticity is localized so most of structure stays elastic.

The main advantage of a co-rotational approach is that it leads to an artificial separation of the material and geometric non-linearities when a linear strain definition in the local coordinate system is used: plastic deformations occur in the local coordinate system where geometrical linearity is assumed; geometric non-linearity is only present during the rigid rotation and translation of the undeformed beam. This leads to very simple ex-

pressions for the local internal force vector and tangent stiffness matrix. Even when a low-order geometrical non-linearity is included in the strain definition, the expressions for the local internal force vector and tangent stiffness matrix are still very simple. In this research, a Total Lagrangian-Corotational approach is employed for the development of beam and beam-column elements, in which an initial undeformed geometry, translated and rotated as a rigid body, is chosen as the reference configuration in the corotated frame. Moreover, the formulation is based on small deformations within the corotational (natural) frame.

6.1 3D rotation parametrization

Before expressing the co-rotational formulation, it is necessary to define the 3D finite rotations of a beam element, which is one of the key issues concerning the nonlinear geometric formulation.

6.1.1 Rotation tensor

Let $\mathbf{e} = \begin{pmatrix} e_1 & e_2 & e_3 \end{pmatrix}^T$ be a vector (or frame) that is rotated into the new position $\mathbf{t} = \begin{pmatrix} t_1 & t_2 & t_3 \end{pmatrix}^T$ (Figure 6-1a), a relation between these two vectors is obtained as follows:

$$\mathbf{t} = \mathbf{R}\mathbf{e} \tag{6.1}$$

These rotations are represented by an orthogonal tensor $\mathbf{R}$, which is an 3×3 matrix, but involving only three independent parameters, due to its ortho-normality ($\mathbf{R}\mathbf{R}^T = \mathbf{I}$). The rotation matrix $\mathbf{R}$ can be expressed as:

$$\mathbf{R} = \mathbf{I}_3 + \frac{\sin\theta}{\theta} Sp(\mathbf{\Theta}) + \frac{1-\cos\theta}{\theta^2} Sp(\mathbf{\Theta})^2 \tag{6.2}$$

where $\mathbf{I}_3$ is the 3×3 identity matrix; θ is the magnitude of the so-called *rotation vector* $\mathbf{\Theta} = \begin{pmatrix} \theta_1 & \theta_2 & \theta_3 \end{pmatrix}^T$; and $Sp(\mathbf{\Theta})$ is the spin of the rotation vector, defined as:

$$Sp(\mathbf{\Theta}) = \begin{bmatrix} 0 & -\theta_3 & \theta_2 \\ \theta_3 & 0 & -\theta_1 \\ -\theta_2 & \theta_1 & 0 \end{bmatrix} \tag{6.3}$$

6.1.2 Rotation increment

The finite rotation can be expressed with the rotation matrix $\mathbf{R}$ and the corresponding rotation vector $\mathbf{\Theta}$. Then, the incremental rotation of the moving vector/frame $\mathbf{t}$ is considered by generating a small variation $\delta\mathbf{t}$ from the rotated position $\mathbf{t}$ (Figure 6-1b):

$$\delta\mathbf{t} = \delta\mathbf{R}\mathbf{t} \tag{6.4}$$

The variation of the rotation matrix $\mathbf{R}$ is derived by defining a new parameter $\delta\mathbf{\Omega}$ as the *spatial angular variation* representing the infinitesimal rotation that is superimposed on the rotation matrix $\mathbf{R}$:

$$\delta\mathbf{R} = Sp(\delta\mathbf{\Omega})\mathbf{R} \tag{6.5}$$

In the numerical implementation, the spatial angular variation play a very important role in the incremental analysis for updating the rotation matrix $\mathbf{R}^i$ from i state to the rotation matrix $\mathbf{R}^{i+1}$ of $i+1$ state:

$$\mathbf{R}^{i+1}(\mathbf{\Theta}^{i+1}) = \mathbf{R}(\delta\mathbf{\Omega})\mathbf{R}^i(\mathbf{\Theta}^i) \tag{6.6}$$

Knowing that $\mathbf{R}^i$ is a function of $\mathbf{\Theta}^i$ and $\mathbf{R}^{i+1}$ is a function of $\mathbf{\Theta}^{i+1}$, however the addition of the vector $\delta\mathbf{\Omega}$ to $\mathbf{\Theta}^i$ does not give $\mathbf{\Theta}^{i+1}$: $\mathbf{\Theta}^{i+1} \neq \mathbf{\Theta}^i + \delta\mathbf{\Omega}$. This problem of multiplicative update for rotations in the incremental analysis is solved by projecting the spatial angular variation $\delta\mathbf{\Omega}$ onto the parameter space adopted for $\mathbf{R}$ and obtaining, as a result, a new parameter called admissible angular variation $\delta\mathbf{\Theta}$. The conversion between this two parameters, proposed by Battini & Pacoste [6], is represented by a complex relationship:

$$\delta\mathbf{\Omega} = \mathbf{T}_s(\mathbf{\Theta})\delta\mathbf{\Theta} \tag{6.7}$$

with

$$\mathbf{T}_s(\mathbf{\Theta}) = \frac{\sin\theta}{\theta}\mathbf{I} + \left(1 - \frac{\sin\theta}{\theta}\right)\mathbf{n}\mathbf{n}^T + \frac{1}{2}\left(\frac{\sin(\theta/2)}{(\theta/2)}\right)^2 Sp(\mathbf{\Theta}) \tag{6.8}$$

where $\mathbf{n}$ is an unit vector. The inverse relation is also available:

$$\delta\mathbf{\Theta} = \mathbf{T}_s^{-1}(\mathbf{\Theta})\delta\mathbf{\Omega} \tag{6.9}$$

with

$$\mathbf{T}_s^{-1}(\mathbf{\Theta}) = \frac{\theta/2}{\tan(\theta/2)}\mathbf{I} + \left(1 - \frac{\theta/2}{\tan(\theta/2)}\right)\mathbf{n}\mathbf{n}^T - \frac{1}{2}Sp(\mathbf{\Theta}) \tag{6.10}$$

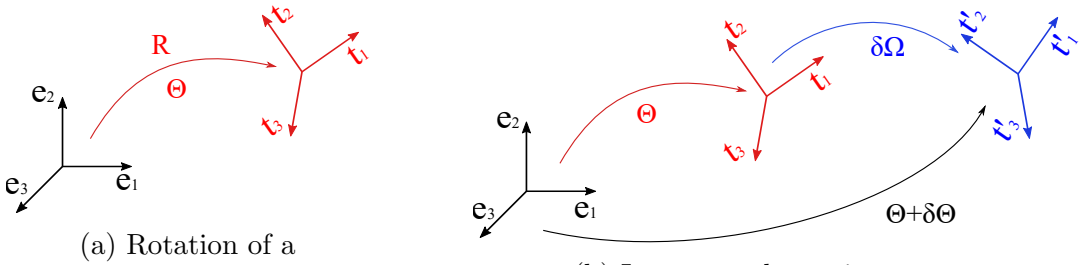

(a) Rotation of a vector/frame.

(b) Incremental rotation vector.

Figure 6-1

6.2 Coordinate systems and local reference frame definitions

As a reminder, in the context of co-rotational framework, the large displacement kinematics of 3D beam elements must be decomposed into a local rigid reference frame that follows the element deformations and the rigid body motion of this local frame. Knowing that in this local reference, the linear geometric assumption is still valid and the existing enhanced model formulations can be used accordingly, the key issue of the co-rotational formulation is to define the *local reference frame* and its nonlinear rigid body motion. Then, not only the proposed model in this work, but also different local formulations can be applied and compared in this co-rotational framework.

In this present work, a beam element is limited by two end nodes I and J. The motion of a beam element is attached to a local reference system and its rigid body motion is considered in a global reference system which is defined by a triad of unit orthogonal vectors $\mathbf{E}_i = \begin{pmatrix} E_1 & E_2 & E_3 \end{pmatrix}$. In the initial configuration (undeformed condition), the local reference system is defined by a triad of unit orthogonal vectors $\mathbf{e}_i^o = \begin{pmatrix} e_1^o & e_2^o & e_3^o \end{pmatrix}$. The rigid rotation relative to the global reference of this local frame is defined by a rotation matrix $\mathbf{R}_o$: $\begin{pmatrix} E_1 & E_2 & E_3 \end{pmatrix} \xrightarrow{\mathbf{R}^o} \begin{pmatrix} e_1^o & e_2^o & e_3^o \end{pmatrix}$ (Figure 6-2). The components of $\mathbf{R}^o$ are defined by the position of two beam nodes:

$$\mathbf{R}^o = \begin{bmatrix} \mathbf{R}_1^o & \mathbf{R}_2^o & \mathbf{R}_3^o \end{bmatrix} : \qquad R_1^o = \frac{\mathbf{x}_{J^o} - \mathbf{x}_{I^o}}{\|\mathbf{x}_{J^o} - \mathbf{x}_{I^o}\|}; \quad R_3^o = \frac{R_1^o \times [0,1,0]}{\|R_1^o \times [0,1,0]\|}; \quad R_2^o = \frac{R_3^o \times R_1^o}{\|R_3^o \times R_1^o\|} \tag{6.11}$$

with $\mathbf{x}_{I^o}$ and $\mathbf{x}_{J^o}$ are the nodal coordinates of nodes I, J at initial configuration. The term $\|\mathbf{x}_{J^o} - \mathbf{x}_{I^o}\| = l_o$ defines the initial beam length.

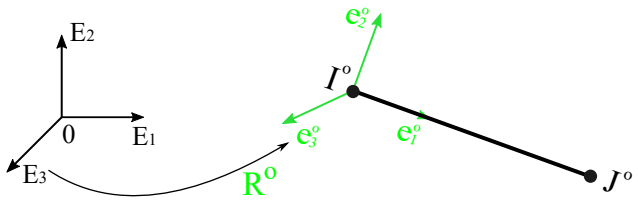

Figure 6-2 – Transition between global and local reference system at initial undeformed configuration.

Then, the beam is deformed and its rigid body motion is represented by the centroid displacement of a cross-section. This generalized displacement consists of two components: a vector of translations $\mathbf{d}$ relative to the global reference and a rotations vector $\mathbf{\Omega}$ about the axes of global triad. At local level, the translations vector is denoted by $\overline{\mathbf{d}}$ while the rotations vector about the local triad becomes $\overline{\mathbf{\Omega}}$. In the final configuration of the beam, it is recommended to define two local reference systems:

- Local reference system in semi-final configuration (translated but not rotated): defined by a triad of unit orthogonal vectors: $\mathbf{e}_i = \begin{pmatrix} e_1 & e_2 & e_3 \end{pmatrix}$ (Figure 6-3a). The rigid rotation relative to the global reference of this frame is defined by a rotation matrix $\mathbf{R}^r$: $\begin{pmatrix} E_1 & E_2 & E_3 \end{pmatrix} \xrightarrow{\mathbf{R}^r} \begin{pmatrix} e_1 & e_2 & e_3 \end{pmatrix}$.
- Local reference system in final configuration (totally deformed): defined by two triads of unit orthogonal vectors at each node: $\mathbf{t}_i^I = \begin{pmatrix} t_1^I & t_2^I & t_3^I \end{pmatrix}$ and $\mathbf{t}_i^J = \begin{pmatrix} t_1^J & t_2^J & t_3^J \end{pmatrix}$; or $\mathbf{t}_i^{IJ} = \begin{pmatrix} t_1^{IJ} & t_2^{IJ} & t_3^{IJ} \end{pmatrix}$ for the sake of generality (Figure 6-3b). As in the sequel, without any particular mention, the term *local frame* or *local reference system* is always considered to the local frame in final configuration $\mathbf{t}_i^{IJ}$.

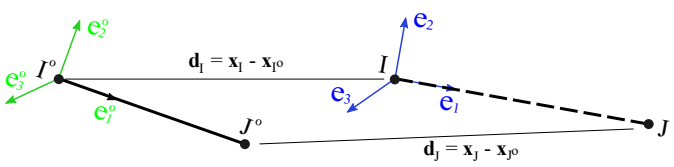

(a) Initial and semi-final configuration in local reference.

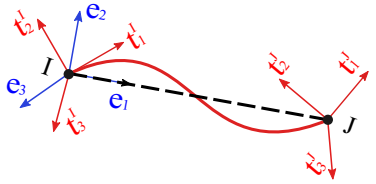

(b) Final configuration of beam element.

Figure 6-3

From these definitions of global and local coordinate systems, there are two ways to express the global rotation at end nodes of the beam element (Figure 6-4):

1. A rotation of the local axes relative to the global frame, defined by the rigid rotation matrix $\mathbf{R}^r$, followed by a rotation of the node relative to local axes, which is defined

by a local rotation matrix $\overline{\mathbf{R}}^{IJ}$:

$$\begin{pmatrix} E_1 & E_2 & E_3 \end{pmatrix} \xrightarrow{\mathbf{R}^r} \begin{pmatrix} e_1 & e_2 & e_3 \end{pmatrix} \xrightarrow{\overline{\mathbf{R}}^{IJ}} \begin{pmatrix} t_1^{IJ} & t_2^{IJ} & t_3^{IJ} \end{pmatrix} \tag{6.12}$$

2. A material rotation of the node relative to the global reference, defined by rotation matrices $\mathbf{R}^{gIJ}$, followed by a global rotation of the local frame at initial configuration (defined by the rotation matrix $\mathbf{R}^o$):

$$\begin{pmatrix} E_1 & E_2 & E_3 \end{pmatrix} \xrightarrow{\mathbf{R}_o} \begin{pmatrix} e_1^o & e_2^o & e_3^o \end{pmatrix} \xrightarrow{\mathbf{R}^{gIJ}} \begin{pmatrix} t_1^{IJ} & t_2^{IJ} & t_3^{IJ} \end{pmatrix} \tag{6.13}$$

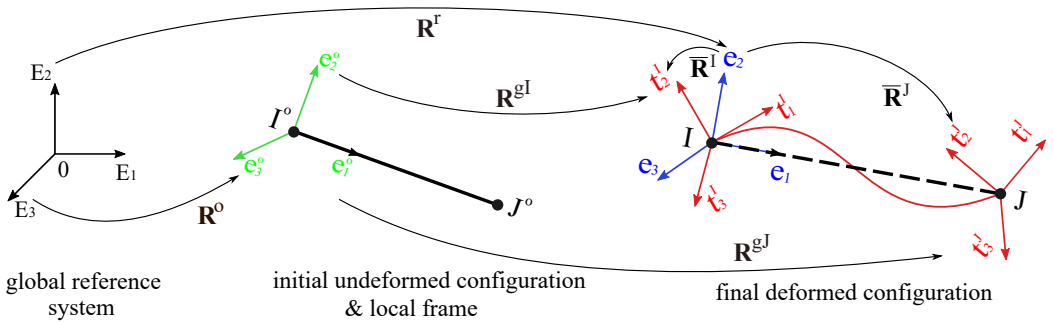

Figure 6-4 – Coordinate systems and beam kinematics.

The following relationship can be formulated between these rotation matrices:

$$\mathbf{R}^r \overline{\mathbf{R}}^{IJ} = \mathbf{R}^{gIJ} \mathbf{R}^o \tag{6.14}$$

As mentioned above in Equation (6.1), the expression of the material rotation matrix $\mathbf{R}^{gIJ}$ in the global reference can be expressed as:

$$\mathbf{R}^{gIJ} = \mathbf{I}_3 + \frac{\sin\theta}{\theta} Sp(\mathbf{\Theta}) + \frac{1-\cos\theta}{\theta^2} Sp(\mathbf{\Theta})^2 \tag{6.15}$$

While the rigid rotation matrix $\mathbf{R}^r$ is defined from the material rotation matrix $\mathbf{R}^{gIJ}$ in Equation (6.15) and the initial rotation matrix $\mathbf{R}^o$ in Equation (6.11):

$$\begin{aligned} \mathbf{R}^r &= \begin{bmatrix} \mathbf{R}_1^r & \mathbf{R}_2^r & \mathbf{R}_3^r \end{bmatrix} \\ \mathbf{R}_1^r &= \frac{\mathbf{x}_J + \mathbf{d}_J - \mathbf{x}_I - \mathbf{d}_I}{\|\mathbf{x}_J + \mathbf{d}_J - \mathbf{x}_I - \mathbf{d}_I\|}; \quad \mathbf{R}_3^r = \frac{R_1^r \times \mathbf{q}}{\|R_1^o \times \mathbf{q}\|}; \quad \mathbf{R}_2^r = \frac{R_3^r \times R_1^r}{\|R_3^r \times R_1^r\|} \end{aligned} \tag{6.16}$$

with $\mathbf{x}_I$ and $\mathbf{x}_J$ are the nodal coordinates of nodes I, J at final configuration; $\mathbf{d}_I$ and $\mathbf{d}_J$

denote the translation vectors of nodes I, J; the term $\|\mathbf{x}_J + \mathbf{d}_J - \mathbf{x}_I - \mathbf{d}_I\| = l_n$ defines the final beam length; $\mathbf{q}$ is an auxiliary vector defined as:

$$\mathbf{q} = \frac{\mathbf{q}_I + \mathbf{q}_J}{2}; \qquad \mathbf{q}_I = \mathbf{R}^{gI}\mathbf{R}^o \begin{bmatrix} 0 & 1 & 0 \end{bmatrix}^T; \qquad \mathbf{q}_J = \mathbf{R}^{gJ}\mathbf{R}^o \begin{bmatrix} 0 & 1 & 0 \end{bmatrix}^T \tag{6.17}$$

And the nodal rotation matrix can be evaluated from Equation (6.14)

$$\overline{\mathbf{R}}^{IJ} = \mathbf{R}^{rT}\mathbf{R}^{gIJ}\mathbf{R}^o \tag{6.18}$$

6.3 Change of variables

In the co-rotational framework, the generalized and nodal displacements of beam element are defined relative to the global reference system, while the existing element kinematics are determined relative to the local frame. Therefore, it is necessary to make a transformation of variables between global and local reference. For the shake of convenience, as in the sequel all the variables relative to the local frame in final configuration will be denoted with a bar. Moreover, as a reminder the incremental rotation of local frame needs a conversion from material angular variation $\delta\overline{\mathbf{\Theta}}$ to spatial angular variation $\delta\overline{\mathbf{\Omega}}$, thus two more changes of variables are required for this angular conversion, one in global and other in local level. In short, in the co-rotational formulation, there is a total of three transformations to be performed: Local variables (with material angular) $\xrightarrow{(1)}$ Local variables (with spatial angular) $\xrightarrow{(2)}$ Global variables (with spatial angular) $\xrightarrow{(3)}$ Global variables (with material angular).

It is important to note that, in this work, due to the particular separation of the local frame above, the local translations at node I will be zero and at node J, the only non-zero translation component is the axial translation along local axis e_1 (Figure 6-5). As a consequence, at local level the nodal displacements vector contains only 7 components, with 1 translation at node J, 3 rotations at node I and 3 rotations at node J: $\overline{\mathbf{q}}_e = \begin{pmatrix} \overline{u} & \overline{\mathbf{\Theta}}^I & \overline{\mathbf{\Theta}}^J \end{pmatrix}$ - for material angulars ; or $\overline{\mathbf{q}}_e^s = \begin{pmatrix} \overline{u} & \overline{\mathbf{\Omega}}^I & \overline{\mathbf{\Omega}}^J \end{pmatrix}$ - for spatial angulars. On the other hand, at global level, the nodal displacements vector contains 12 components with 3 translations and 3 rotations at each node: $\mathbf{q}_e^s = \begin{pmatrix} \mathbf{d}^I & \mathbf{\Omega}^I & \mathbf{d}^J & \mathbf{\Omega}^J \end{pmatrix}$ and $\mathbf{q}_e = \begin{pmatrix} \mathbf{d}^I & \mathbf{\Theta}^I & \mathbf{d}^J & \mathbf{\Theta}^J \end{pmatrix}$.

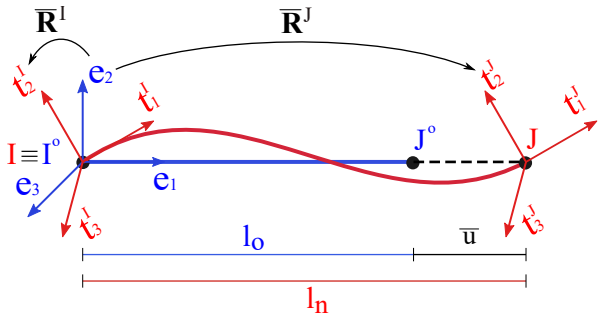

Figure 6-5 – Beam kinematics in local frame.

6.3.1 1st transformation: $\delta\overline{\mathbf{\Theta}} \rightarrow \delta\overline{\mathbf{\Omega}}$

Using Equation (6.9), we get:

$$\delta\overline{\mathbf{\Theta}}^{IJ} = \mathbf{T}_s^{-1}(\overline{\mathbf{\Theta}}^{IJ})\delta\overline{\mathbf{\Omega}}^{IJ} \tag{6.19}$$

Knowing that the translations vector is unchanged in this transformation, we get:

$$\delta\begin{pmatrix}\overline{u}\\ \overline{\mathbf{\Theta}}^{I}\\ \overline{\mathbf{\Theta}}^{J}\end{pmatrix} = \begin{bmatrix}1 & \mathbf{0}_{13} & \mathbf{0}_{13}\\ \mathbf{0}_{31} & \mathbf{T}_s^{-1}(\overline{\mathbf{\Theta}}^{I}) & \mathbf{0}_3\\ \mathbf{0}_{31} & \mathbf{0}_3 & \mathbf{T}_s^{-1}(\overline{\mathbf{\Theta}}^{J})\end{bmatrix}\delta\begin{pmatrix}\overline{u}\\ \overline{\mathbf{\Omega}}^{I}\\ \overline{\mathbf{\Omega}}^{J}\end{pmatrix} \Rightarrow \delta\overline{\mathbf{q}}_e = \mathbf{B}_\theta\delta\overline{\mathbf{q}}_e^s \tag{6.20}$$

with $\mathbf{0}_{13}$ is a 1×3 zero matrix; $\mathbf{0}_{31}$ is a 3×1 zero matrix and $\mathbf{0}_3$ is a 3×3 zero matrix. Then, the virtual work equation gives:

$$\overline{\mathbf{Q}}_e^s = \mathbf{B}_\theta^T\overline{\mathbf{Q}}_e \tag{6.21}$$

with $\overline{\mathbf{Q}}_e^s$ and $\overline{\mathbf{Q}}_e$ are the nodal forces vectors consistent with $\delta\overline{\mathbf{q}}_e^s$ and $\delta\overline{\mathbf{q}}_e$ respectively. The expression of theses local nodal vectors is expressed as:

$$\overline{\mathbf{Q}}_e^s = \begin{pmatrix}\overline{F}^s\\ \overline{\mathbf{M}}^{Is}\\ \overline{\mathbf{M}}^{Js}\end{pmatrix}; \qquad \overline{\mathbf{Q}}_e = \begin{pmatrix}\overline{F}\\ \overline{\mathbf{M}}^{I}\\ \overline{\mathbf{M}}^{J}\end{pmatrix} \tag{6.22}$$

with $\overline{F}$ and $\overline{F}^s$ are the axial forces, $\overline{\mathbf{M}}^{Is} = \begin{pmatrix}\overline{M}_1^{Is} & \overline{M}_2^{Is} & \overline{M}_3^{Is}\end{pmatrix}^T$, $\overline{\mathbf{M}}^{Js} = \begin{pmatrix}\overline{M}_1^{Js} & \overline{M}_2^{Js} & \overline{M}_3^{Js}\end{pmatrix}^T$, $\overline{\mathbf{M}}^{I} = \begin{pmatrix}\overline{M}_1^{I} & \overline{M}_2^{I} & \overline{M}_3^{I}\end{pmatrix}^T$ and $\overline{\mathbf{M}}^{J} = \begin{pmatrix}\overline{M}_1^{J} & \overline{M}_2^{J} & \overline{M}_3^{J}\end{pmatrix}^T$ are the moments vectors. In the assumption without any external uniform loading, the transformation for the local tangent

stiffness matrices is obtained by taking the variation of the nodal forces:

$$\overline{\mathbf{K}}_e^s = \frac{\delta \overline{\mathbf{Q}}_e^s}{\delta \overline{\mathbf{q}}_e^s} = \frac{\mathbf{B}_\theta^T \delta \overline{\mathbf{Q}}_e + \delta \mathbf{B}_\theta^T \overline{\mathbf{Q}}_e}{\delta \overline{\mathbf{q}}_e^s} = \frac{\mathbf{B}_\theta^T \overline{\mathbf{K}}_e \delta \overline{\mathbf{q}}_e + \delta \mathbf{B}_\theta^T \overline{\mathbf{Q}}_e}{\delta \overline{\mathbf{q}}_e^s} = \mathbf{B}_\theta^T \overline{\mathbf{K}}_e \mathbf{B}_\theta + \frac{\delta \mathbf{B}_\theta^T \overline{\mathbf{Q}}_e}{\delta \overline{\mathbf{q}}_e^s} \tag{6.23}$$

$$\Rightarrow \overline{\mathbf{K}}_e^s = \mathbf{B}_\theta^T \overline{\mathbf{K}}_e \mathbf{B}_\theta + \overline{\mathbf{K}}_e^h \tag{6.24}$$

with:

$$\overline{\mathbf{K}}_e^h = \frac{\delta \mathbf{B}_\theta^T \overline{\mathbf{Q}}_e}{\delta \overline{\mathbf{q}}_e^s} = \begin{bmatrix} 0 & \mathbf{0}_{13} & \mathbf{0}_{13} \\ \mathbf{0}_{31} & \overline{\mathbf{K}}_e^{Ih} & \mathbf{0}_{33} \\ \mathbf{0}_{31} & \mathbf{0}_{33} & \overline{\mathbf{K}}_e^{Jh} \end{bmatrix}$$

$$\overline{\mathbf{K}}_e^{Ih} = \left[\eta \left[\overline{\mathbf{\Theta}}^I \overline{\mathbf{M}}^{IT} - 2\overline{\mathbf{M}}^I \overline{\mathbf{\Theta}}^{IT} + \left(\overline{\mathbf{\Theta}}^{IT} \times \overline{\mathbf{M}}^I \right) \mathbf{I}_3 \right] + \mu Sp(\overline{\mathbf{\Theta}})^2 \left[\overline{\mathbf{M}}^I \overline{\mathbf{\Theta}}^{IT} \right] - \frac{1}{2} Sp(\overline{\mathbf{M}}^I) \right] \mathbf{T}_s^{-1}(\overline{\mathbf{\Theta}}^I)$$

$$\overline{\mathbf{K}}_e^{Jh} = \left[\eta \left[\overline{\mathbf{\Theta}}^J \overline{\mathbf{M}}^{JT} - 2\overline{\mathbf{M}}^J \overline{\mathbf{\Theta}}^{JT} + \left(\overline{\mathbf{\Theta}}^{JT} \times \overline{\mathbf{M}}^J \right) \mathbf{I}_3 \right] + \mu Sp(\overline{\mathbf{\Theta}})^2 \left[\overline{\mathbf{M}}^J \overline{\mathbf{\Theta}}^{JT} \right] - \frac{1}{2} Sp(\overline{\mathbf{M}}^J) \right] \mathbf{T}_s^{-1}(\overline{\mathbf{\Theta}}^J)$$

$$\eta = \frac{2\sin\alpha - \alpha(1+\cos\alpha)}{2\alpha^2 \sin\alpha}; \qquad \mu = \frac{\alpha(\alpha + \sin\alpha) - \sin^2(\alpha/2)}{4\alpha^4 \sin^2(\alpha/2)}; \alpha = \|\overline{\mathbf{\Theta}}\|$$

6.3.2 2nd transformation: local → global

In the local reference, the axial translation can be evaluated as:

$$\overline{u} = l_n - l_o \tag{6.25}$$

with l_o and l_n are the beam lengths in the initial and final configuration, respectively. From Equation (6.11) and (6.16), the variation of this axial translation gives:

$$\delta \overline{u} = \delta(l_n - l_o) = \begin{bmatrix} -\mathbf{R}_1^{rT} & \mathbf{0}_{13} & \mathbf{R}_1^{rT} & \mathbf{0}_{13} \end{bmatrix} \delta \begin{pmatrix} \mathbf{d}^I \\ \mathbf{\Omega}^I \\ \mathbf{d}_J \\ \mathbf{\Omega}^J \end{pmatrix} \Rightarrow \delta \overline{u} = \mathbf{r} \delta \mathbf{q}_e^s \tag{6.26}$$

In order to express the variation of the nodal material angular vector $\overline{\mathbf{\Theta}}^{IJ}$, it is necessary to obtain the variation of nodal rotation matrix $\overline{\mathbf{R}}^{IJ}$, from Equation (6.18) we get:

$$\delta \overline{\mathbf{R}}^{IJ} = \delta \mathbf{R}^{rT} \mathbf{R}^{gIJ} \mathbf{R}^o + \mathbf{R}^{rT} \delta \mathbf{R}^{gIJ} \mathbf{R}^o \tag{6.27}$$

From Equation (6.5) the variation of rotation matrices above can be expressed as follows:

$$\delta\overline{\mathbf{R}}^{IJ} = Sp(\delta\overline{\mathbf{\Omega}}^{IJ})\overline{\mathbf{R}}^{IJ} \tag{6.28a}$$

$$\delta\mathbf{R}^{r} = Sp(\delta\mathbf{\Omega}^{gr})\mathbf{R}^{r} \tag{6.28b}$$

$$\delta\mathbf{R}^{gIJ} = Sp(\delta\mathbf{\Omega}^{gIJ})\mathbf{R}^{gIJ} \tag{6.28c}$$

with $\delta\mathbf{\Omega}^{gr}$ is defined as the variation of the angular vector attached to the local reference system in semi-final configuration $\mathbf{e}_i$, relative to the global reference; while $\delta\mathbf{\Omega}^{gIJ}$ is the variation of the nodal angular vector in final configuration $\mathbf{t}_i^{IJ}$, relative to the global reference. These two variations can be expressed relatively to the local frame $\mathbf{e}_i$ by the rigid rotation matrix $\mathbf{R}^r$ as follows:

$$\left\{\begin{array}{l} \mathbf{\Omega}^{er} = \mathbf{R}_r^T\mathbf{\Omega}^{gr} \\ \mathbf{\Omega}^{eIJ} = \mathbf{R}_r^T\mathbf{\Omega}^{gIJ} \end{array}\right. \Rightarrow \left\{\begin{array}{l} Sp(\mathbf{\Omega}^{er}) = \mathbf{R}_r^T Sp(\mathbf{\Omega}^{gr})\mathbf{R}_r \\ Sp(\mathbf{\Omega}^{eIJ}) = \mathbf{R}_r^T Sp(\mathbf{\Omega}^{gIJ})\mathbf{R}_r \end{array}\right. \tag{6.29}$$

It is also important to distinct the difference between $\delta\overline{\mathbf{\Omega}}^{IJ}$ and $\delta\mathbf{\Omega}^{eIJ}$, these all expressed the nodal angular vector of beam element relatively to the local frame, however $\delta\overline{\mathbf{\Omega}}^{IJ}$ is attached to the local frame in final configuration $\mathbf{t}_i^{IJ}$, while $\delta\mathbf{\Omega}^{eIJ}$ is attached to the local frame in semi-final configuration $\mathbf{e}_i$. Another important remark is the orthogonality condition of rigid rotation matrix $\mathbf{R}^r$ gives the following relationship:

$$\delta\mathbf{R}^{rT} = -\mathbf{R}^{rT}Sp(\delta\mathbf{\Omega}^{gr}) \tag{6.30}$$

So, from equations (6.18), (6.29), (6.30), Equation (6.27) can be rewritten as:

$$\begin{array}{rcl} Sp(\delta\overline{\mathbf{\Omega}}^{IJ})\overline{\mathbf{R}}^{IJ} & = & -\mathbf{R}^{rT}Sp(\delta\mathbf{\Omega}^{gr})\mathbf{R}^{gIJ}\mathbf{R}^{o} + \mathbf{R}^{rT}Sp(\delta\mathbf{\Omega}^{gIJ})\mathbf{R}^{gIJ}\mathbf{R}^{o} \\ & = & \left(Sp(\delta\mathbf{\Omega}^{eIJ}) - Sp(\delta\mathbf{\Omega}^{er})\right)\overline{\mathbf{R}}^{IJ} \end{array} \tag{6.31}$$

Thus we obtain the following relationship between the angular variations:

$$\delta\overline{\mathbf{\Omega}}^{IJ} = \delta\mathbf{\Omega}^{eIJ} - \delta\mathbf{\Omega}^{er} \tag{6.32}$$

Knowing that two local reference are used in this section, it is necessary to define the

nodal displacement vectors in these references:

$$\overline{\mathbf{q}}_e^s = \begin{pmatrix} \overline{u} \\ \overline{\mathbf{\Omega}}^I \\ \overline{\mathbf{\Omega}}^J \end{pmatrix}; \qquad \mathbf{q}_e^e = \begin{pmatrix} \mathbf{d}^{eI} \\ \mathbf{\Omega}^{eI} \\ \mathbf{d}^{eJ} \\ \mathbf{\Omega}^{eJ} \end{pmatrix}; \qquad \mathbf{q}_e^s = \begin{pmatrix} \mathbf{d}^I \\ \mathbf{\Omega}^I \\ \mathbf{d}^J \\ \mathbf{\Omega}^J \end{pmatrix} \tag{6.33}$$

with $\overline{\mathbf{q}}_e^s$, $\mathbf{q}_e^e$ and $\mathbf{q}_e^s$ are the nodal displacement vector in local frame, in local reference system in semi-configuration and in global reference, respectively. The change of variables between $\mathbf{q}_e^e$ and $\mathbf{q}_e^s$ can be done by the rigid rotation matrix $\mathbf{R}^r$:

$$\delta\mathbf{q}_e^e = \mathbf{B}_r^T \delta\mathbf{q}_e^s \quad \text{with} \quad \mathbf{B}_r = \begin{bmatrix} \mathbf{R}^r & \mathbf{0}_3 & \mathbf{0}_3 & \mathbf{0}_3 \\ \mathbf{0}_3 & \mathbf{R}^r & \mathbf{0}_3 & \mathbf{0}_3 \\ \mathbf{0}_3 & \mathbf{0}_3 & \mathbf{R}^r & \mathbf{0}_3 \\ \mathbf{0}_3 & \mathbf{0}_3 & \mathbf{0}_3 & \mathbf{R}^r \end{bmatrix} \tag{6.34}$$

In order to establish a change of variables between $\overline{\mathbf{q}}_e^s$ and $\mathbf{q}_e^s$, the spatial angular variation $\delta\overline{\mathbf{\Omega}}^{IJ}$ should be expressed with respect to the variation of $\mathbf{q}_e^s$:

$$\frac{\delta\overline{\mathbf{\Omega}}^{IJ}}{\delta\mathbf{q}_e^s} = \frac{\partial\overline{\mathbf{\Omega}}^{IJ}}{\partial\mathbf{q}_e^e}\frac{\partial\mathbf{q}_e^e}{\partial\mathbf{q}_e^s} = \frac{\partial\mathbf{\Omega}^{eIJ} - \partial\mathbf{\Omega}^{er}}{\partial\mathbf{q}_e^e}\mathbf{B}_r^T \tag{6.35}$$

with:

$$\frac{\partial\mathbf{\Omega}^{eIJ}}{\partial\mathbf{q}_e^e} = \begin{bmatrix} \dfrac{\partial\mathbf{\Omega}^{eI}}{\partial\mathbf{q}_e^e} \\ \dfrac{\partial\mathbf{\Omega}^{eJ}}{\partial\mathbf{q}_e^e} \end{bmatrix} = \begin{bmatrix} \mathbf{0}_3 & \mathbf{I}_3 & \mathbf{0}_3 & \mathbf{0}_3 \\ \mathbf{0}_3 & \mathbf{0}_3 & \mathbf{0}_3 & \mathbf{I}_3 \end{bmatrix} \tag{6.36}$$

and from Equation (6.28b), (6.29):

$$\begin{aligned} Sp(\delta\mathbf{\Omega}^{er}) = \mathbf{R}^{rT}\delta\mathbf{R}^r \quad &\Leftrightarrow \quad \delta\begin{bmatrix} 0 & -\Omega_3^{er} & \Omega_2^{er} \\ \Omega_3^{er} & 0 & -\Omega_1^{er} \\ -\Omega_2^{er} & \Omega_1^{er} & 0 \end{bmatrix} = \begin{bmatrix} \mathbf{R}_1^{rT} \\ \mathbf{R}_2^{rT} \\ \mathbf{R}_3^{rT} \end{bmatrix} \delta\begin{bmatrix} \mathbf{R}_1^r & \mathbf{R}_2^r & \mathbf{R}_3^r \end{bmatrix} \\ &\Rightarrow \quad \delta\begin{pmatrix} \Omega_1^{er} \\ \Omega_2^{er} \\ \Omega_3^{er} \end{pmatrix} = \begin{pmatrix} -\mathbf{R}_2^{rT}\delta\mathbf{R}_3^r \\ -\mathbf{R}_3^{rT}\delta\mathbf{R}_1^r \\ \mathbf{R}_2^{rT}\delta\mathbf{R}_1^r \end{pmatrix} \end{aligned} \tag{6.37}$$

Therefore, the following relationship can be obtained for the variation of $\mathbf{\Omega}^{er}$:

$$\Rightarrow \frac{\partial \mathbf{\Omega}^{er}}{\partial \mathbf{q}_e^e} = \mathbf{G}; \tag{6.38}$$

with the expression of matrix $\mathbf{G}$:

$$\mathbf{G} = \begin{bmatrix} 0 & 0 & \nu/l_n & \nu_{I2}/2 & -\nu_{I1}/2 & 0 & 0 & 0 & -\nu/l_n & \nu_{J2}/2 & -\nu_{J1}/2 & 0 \\ 0 & 0 & 1/l_n & 0 & 0 & 0 & 0 & 0 & -1/l_n & 0 & 0 & 0 \\ 0 & -1/l_n & 0 & 0 & 0 & 0 & 0 & 1/l_n & 0 & 0 & 0 & 0 \end{bmatrix} \tag{6.39}$$

$$\nu = \frac{q_1}{q_2}; \qquad \nu_{I1} = \frac{q_{I1}}{q_2}; \qquad \nu_{I2} = \frac{q_{I2}}{q_2}; \qquad \nu_{J1} = \frac{q_{J1}}{q_2}; \qquad \nu_{J2} = \frac{q_{J2}}{q_2};$$

$$\begin{pmatrix} q_1 & q_2 & q_3 \end{pmatrix}^T = \mathbf{R}^{rT}\mathbf{q}$$

where $\mathbf{q}$ is the auxiliary vector in Equation (6.17) and q_{I1}, q_{I2}, q_{J1}, q_{J2} are the component of auxiliary vector $\mathbf{q}_I$ and $\mathbf{q}_J$.

Thus, from Equation (6.36) and (6.38), Equation (6.35) can be rewritten as follows:

$$\delta \begin{pmatrix} \overline{\mathbf{\Omega}}^I \\ \overline{\mathbf{\Omega}}^J \end{pmatrix} = \left(\begin{bmatrix} \mathbf{0}_3 & \mathbf{I}_3 & \mathbf{0}_3 & \mathbf{0}_3 \\ \mathbf{0}_3 & \mathbf{0}_3 & \mathbf{0}_3 & \mathbf{I}_3 \end{bmatrix} - \begin{bmatrix} \mathbf{G}^T \\ \mathbf{G}^T \end{bmatrix} \right) \mathbf{B}_r^T \delta \mathbf{q}_e^s = \mathbf{P}\mathbf{B}_r^T \delta \mathbf{q}_e^s \tag{6.40}$$

And from Equation (6.26) and (6.40), the transformation between $\delta\overline{\mathbf{q}}_e^s$ and $\delta\mathbf{q}_e^s$ can be expressed as:

$$\delta\overline{\mathbf{q}}_e^s = \mathbf{B}_s \delta\mathbf{q}_e^s \qquad \text{with} \qquad \mathbf{B}_s = \begin{bmatrix} \mathbf{r} \\ \mathbf{P}\mathbf{B}_r^T \end{bmatrix} \tag{6.41}$$

As a consequence, the transformation between nodal forces vectors and the element stiffness matrix can be expressed as follows:

$$\mathbf{Q}_e^s = \mathbf{B}_s^T \overline{\mathbf{Q}}_e^s \tag{6.42a}$$

$$\mathbf{K}_e^s = \frac{\delta \mathbf{Q}_e^s}{\delta \mathbf{q}_e^s} = \frac{\mathbf{B}_s^T \delta \overline{\mathbf{Q}}_e^s + \delta \mathbf{r}^T \overline{F}^s + \delta \mathbf{B}_r \mathbf{P}^T \overline{\mathbf{M}}^s}{\delta \mathbf{q}_e^s} \tag{6.42b}$$

with $\overline{\mathbf{M}}^s = \begin{pmatrix} \overline{\mathbf{M}}^{IsT} & \overline{\mathbf{M}}^{JsT} \end{pmatrix}$, after some algebra the expression of $\mathbf{K}_e^s$ becomes:

$$\mathbf{K}_e^s = \mathbf{B}_s^T \overline{\mathbf{K}}_e^s \mathbf{B}_s + \mathbf{K}_m \tag{6.43}$$

with:

$$\mathbf{K}_m = \mathbf{D}\overline{F}^s - \mathbf{B}_r\mathbf{Q}\mathbf{G}\mathbf{B}_r^T + \mathbf{B}_r\mathbf{G}\mathbf{a}\mathbf{r}; \qquad \mathbf{a} = \begin{bmatrix} 0 \\ \eta\left(\overline{M}_1^{Is} + \overline{M}_1^{Js}\right)/l_n - \left(\overline{M}_2^{Is} + \overline{M}_2^{Js}\right)/l_n \\ \left(\overline{M}_3^{Is} + \overline{M}_3^{Js}\right) \end{bmatrix}$$

$$\mathbf{D} = \begin{bmatrix} \mathbf{D}_3 & \mathbf{0}_3 & \mathbf{D}_3 & \mathbf{0}_3 \\ \mathbf{0}_3 & \mathbf{0}_3 & \mathbf{0}_3 & \mathbf{0}_3 \\ -\mathbf{D}_3 & \mathbf{0}_3 & \mathbf{D}_3 & \mathbf{0}_3 \\ \mathbf{0}_3 & \mathbf{0}_3 & \mathbf{0}_3 & \mathbf{0}_3 \end{bmatrix}; \qquad \mathbf{D}_3 = \frac{1}{l_n}\left(\mathbf{I}_3 - \mathbf{R}_1^r\mathbf{R}_1^{rT}\right); \qquad \mathbf{Q} = \begin{bmatrix} Sp(\mathbf{Q}_1) \\ Sp(\mathbf{Q}_2) \\ Sp(\mathbf{Q}_3) \\ Sp(\mathbf{Q}_4) \end{bmatrix}; \qquad \begin{bmatrix} \mathbf{Q}_1 \\ \mathbf{Q}_2 \\ \mathbf{Q}_3 \\ \mathbf{Q}_4 \end{bmatrix} = \mathbf{P}^T\overline{\mathbf{M}}^s$$

6.3.3 3rd transformation: $\delta\boldsymbol{\Omega} \rightarrow \delta\boldsymbol{\Theta}$

In this last transformation, the conversion between spatial angular and material angular in global reference will be established. Using the relationship in Equation (6.7), we obtain:

$$\delta\begin{pmatrix} \mathbf{d}^I \\ \boldsymbol{\Omega}^I \\ \mathbf{d}^J \\ \boldsymbol{\Omega}^J \end{pmatrix} = \begin{bmatrix} \mathbf{I}_3 & \mathbf{0}_3 & \mathbf{0}_3 & \mathbf{0}_3 \\ \mathbf{0}_3 & \mathbf{T}_s(\boldsymbol{\Theta}^I) & \mathbf{0}_3 & \mathbf{0}_3 \\ \mathbf{0}_3 & \mathbf{0}_3 & \mathbf{I}_3 & \mathbf{0}_3 \\ \mathbf{0}_3 & \mathbf{0}_3 & \mathbf{0}_3 & \mathbf{T}_s(\boldsymbol{\Theta}^J) \end{bmatrix} \delta\begin{pmatrix} \mathbf{d}^I \\ \boldsymbol{\Theta}^I \\ \mathbf{d}^J \\ \boldsymbol{\Theta}^J \end{pmatrix} \Rightarrow \delta\mathbf{q}_e^s = \mathbf{B}_h\delta\mathbf{q}_e \tag{6.44}$$

The global nodal force vector and the global stiffness matrix consistent with $\mathbf{q}_e$ are given as follows:

$$\mathbf{Q}_e = \mathbf{B}_h^T\mathbf{Q}_e^s \tag{6.45a}$$

$$\mathbf{K}_e = \frac{\partial\mathbf{Q}_e}{\partial\mathbf{q}_e} = \mathbf{B}_h^T\mathbf{K}_e^s\mathbf{B}_h + \mathbf{K}_h \tag{6.45b}$$

with:

$$\mathbf{K}_h = \begin{bmatrix} \mathbf{0}_3 & \mathbf{0}_3 & \mathbf{0}_3 & \mathbf{0}_3 \\ \mathbf{0}_3 & \mathbf{K}_h^I & \mathbf{0}_3 & \mathbf{0}_3 \\ \mathbf{0}_3 & \mathbf{0}_3 & \mathbf{0}_3 & \mathbf{0}_3 \\ \mathbf{0}_3 & \mathbf{0}_3 & \mathbf{0}_3 & \mathbf{K}_h^J \end{bmatrix}$$

$$\begin{aligned}
\mathbf{K}_h^I &= -\left(\frac{\sin\theta^I}{\theta^I} - \left(\frac{\sin(\theta^I/2)}{\theta^I/2}\right)^2\right)\left(\mathbf{e}^I \times \mathbf{M}^{Is}\right)\mathbf{e}^{IT} + \frac{1}{2}\left(\frac{\sin(\theta^I/2)}{\theta^I/2}\right)^2 Sp(\mathbf{M}^{Is}) \\
&+ \left(\cos\theta^I - \frac{\sin\theta^I}{\theta^I}\right)\frac{1}{\theta^I}\left[\mathbf{M}^{IsT} - \left(\mathbf{e}^{IT}\mathbf{M}^{Is}\right)\mathbf{e}^I\mathbf{e}^{IT}\right] \\
&+ \left(1 - \frac{\sin\theta^I}{\theta^I}\right)\frac{1}{\theta^I}\left[\mathbf{e}^I\mathbf{M}^{IsT} - 2\left(\mathbf{e}^{IT}\mathbf{M}^{Is}\right)\mathbf{e}^I\mathbf{e}^{IT} + \left(\mathbf{e}^{IT}\mathbf{M}^{Is}\right)\mathbf{I}_3\right] \\
\mathbf{K}_h^J &= -\left(\frac{\sin\theta^J}{\theta^J} - \left(\frac{\sin(\theta^J/2)}{\theta^J/2}\right)^2\right)\left(\mathbf{e}^J \times \mathbf{M}^{Js}\right)\mathbf{e}^{JT} + \frac{1}{2}\left(\frac{\sin(\theta^J/2)}{\theta^J/2}\right)^2 Sp(\mathbf{M}^{Js}) \\
&+ \left(\cos\theta^J - \frac{\sin\theta^J}{\theta^J}\right)\frac{1}{\theta^J}\left[\mathbf{M}^{JsT} - \left(\mathbf{e}^{JT}\mathbf{M}^{Js}\right)\mathbf{e}^J\mathbf{e}^{JT}\right] \\
&+ \left(1 - \frac{\sin\theta^J}{\theta^J}\right)\frac{1}{\theta^J}\left[\mathbf{e}^J\mathbf{M}^{JsT} - 2\left(\mathbf{e}^{JT}\mathbf{M}^{Js}\right)\mathbf{e}^J\mathbf{e}^{JT} + \left(\mathbf{e}^{JT}\mathbf{M}^{Js}\right)\mathbf{I}_3\right] \\
&\omega^{I/J} = \|\mathbf{\Theta}^{I/J}\|; \qquad \mathbf{e}^{I/J} = \frac{\mathbf{\Theta}^{I/J}}{\theta^{I/J}}
\end{aligned}$$

6.4 Local beam formulation

According to Battini & Pacoste, most of the co-rotational elements found in the literature are based on local linear strain assumptions, except when the torsional effects are important [6]. In this case, for members under torsional effects the geometrical nonlinearity is generated by a term included in the local strain definition, which is defined by a second-order approximation of the Green Lagrange strains. A second-order approximation of the displacement field is therefore necessary to obtain the second-order of the strains. In this section, the second-order approximation of Green-Lagrange strains will be constructed at the local level, in order to describe the local kinematic of beam element in a co-rotational framework under combined loadings and pure torsion. For the shake of simplicity, only the approach using Saint-Venant warping function has been developed.

The kinematic model proposed by Gruttmann et al. [41] is adopted for a general case of classical beam in which the centroid G and the shear center C are not coincident (Figure 6-6). The position of an arbitrary point P is defined by vector $\mathbf{x}_P^o(x, y, z)$ in the initial

configuration and by vector $\mathbf{x}_P(x,y,z)$ in the current configuration:

$$\begin{aligned} \mathbf{x}_P^o(x,y,z) &= \mathbf{x}_G^o(x) + y\mathbf{e}_y + z\mathbf{e}_z \\ \mathbf{x}_P(x,y,z) &= \mathbf{x}_G(x) + y\mathbf{a}_y + z\mathbf{a}_z + \alpha(x)\bar{\psi}(y,z)\mathbf{a}_x \end{aligned} \tag{6.46}$$

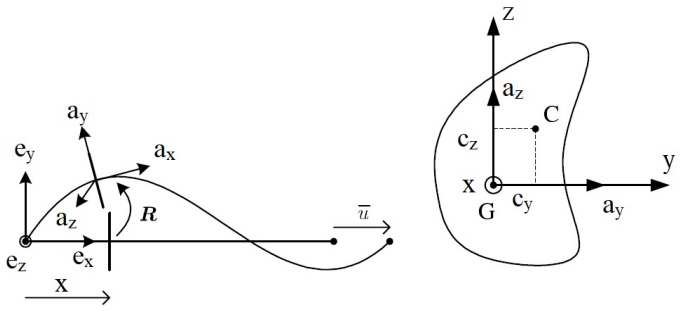

Figure 6-6 – Kinematic model proposed by Gruttmann et al. [41].

with $\mathbf{x}_G^o(x)$ and $\mathbf{x}_G(x)$ denote the position vectors of the centroid G in the initial and current configuration, respectively; $\alpha(x)$ is the parameters representing the distribution of warping as defined in Section 3.3.2; $\bar{\psi}(y,z)$ is the Saint-Venant warping function refers to the centroid G:

$$\bar{\psi}(y,z) = \psi(y,z) - c_y z + c_z y \tag{6.47}$$

where $\psi(y,z)$ is the Saint-Venant warping function refers to the shear center C. $\mathbf{e} = \begin{pmatrix} \mathbf{e}_x & \mathbf{e}_y & \mathbf{e}_z \end{pmatrix}$ is the triad of three unit vector of local reference, while $\mathbf{a} = \begin{pmatrix} \mathbf{a}_x & \mathbf{a}_y & \mathbf{a}_z \end{pmatrix}$ is an orthonormal triad which specifies the orientation of the current cross-section. These two triads are related by an orthogonal matrix $\bar{\mathbf{R}}$ defining the finite 3D rotation of beam element under non-linear geometric conditions:

$$\mathbf{a} = \bar{\mathbf{R}}\mathbf{e} \tag{6.48}$$

and

$$\bar{\mathbf{R}} = \mathbf{I}_3 + Sp(\theta) + \frac{1}{2}Sp(\theta)^2; \qquad Sp(\theta) = \begin{bmatrix} 0 & -\theta_z & \theta_y \\ \theta_z & 0 & -\theta_x \\ -\theta_y & \theta_x & 0 \end{bmatrix} \tag{6.49}$$

where θ_x, θ_y and θ_z are the material rotation of point P. The definition of rotation matrix $\bar{\mathbf{R}}$ will be detailed in Section 6.1.1. With the aid from Equation (6.49), the second-order

approximation of the displacement field can be expressed as follows:

$$\mathbf{d}_s(x,y,z) = \mathbf{x}_P - \mathbf{x}_P^o \tag{6.50}$$

so we obtain the following components of $\mathbf{d}_s(x,y,z)$, for the case of solid cross-section in which the centroid G and the shear center C are coincident:

$$\begin{aligned}
\overline{U}(x,y,z) &= u - y\theta_z + z\theta_y + \psi\frac{\partial\theta_x}{\partial x} + \frac{1}{2}y\theta_x\theta_y + \frac{1}{2}z\theta_x\theta_z \\
\overline{V}(x,y,z) &= v - z\theta_x - \frac{1}{2}y\left(\theta_x^x + \theta_z^2\right) + \frac{1}{2}z\left(\theta_y\theta_z\right) + \psi\frac{\partial\theta_x}{\partial x}\theta_z \\
\overline{W}(x,y,z) &= w + y\theta_x - \frac{1}{2}z\left(\theta_x^x + \theta_y^2\right) + \frac{1}{2}y\left(\theta_y\theta_z\right) - \psi\frac{\partial\theta_x}{\partial x}\theta_y
\end{aligned} \tag{6.51}$$

Unlike the material strains expressed in Equation (3.9), the second order Green-Lagrange strains are derived as follows:

$$\begin{aligned}
\varepsilon_{xx}^{GL} &= \frac{\partial\overline{U}}{\partial x} + \boldsymbol{\frac{1}{2}\left(\frac{\partial\overline{U}}{\partial x}\right)^2} + \boldsymbol{\frac{1}{2}\left(\frac{\partial\overline{V}}{\partial x}\right)^2} + \boldsymbol{\frac{1}{2}\left(\frac{\partial\overline{W}}{\partial x}\right)^2} \\
\gamma_{xy}^{GL} &= \frac{\partial\overline{U}}{\partial y} + \frac{\partial\overline{V}}{\partial x} + \boldsymbol{\frac{\partial\overline{U}}{\partial x}\frac{\partial\overline{U}}{\partial y}} + \boldsymbol{\frac{\partial\overline{V}}{\partial x}\frac{\partial\overline{V}}{\partial y}} + \boldsymbol{\frac{\partial\overline{W}}{\partial x}\frac{\partial\overline{W}}{\partial y}} \\
\gamma_{xz}^{GL} &= \frac{\partial\overline{U}}{\partial z} + \frac{\partial\overline{W}}{\partial x} + \boldsymbol{\frac{\partial\overline{U}}{\partial x}\frac{\partial\overline{U}}{\partial z}} + \boldsymbol{\frac{\partial\overline{V}}{\partial x}\frac{\partial\overline{V}}{\partial z}} + \boldsymbol{\frac{\partial\overline{W}}{\partial x}\frac{\partial\overline{W}}{\partial z}}
\end{aligned} \tag{6.52}$$

In order to distinct the Green-Lagrange strain and the linear strain in Section 3.3, in this section all the nonlinear terms are highlighted in bold. With the assumption that the term $\frac{1}{2}\left(\frac{\partial\overline{U}}{\partial x}\right)^2$ in the expression of ε_{xx}^{GL} is neglected and the non-linear strain components generated by the warping function are omitted, the following expressions of Green-Lagrange strains in equation 6.52 can be obtained:

$$\begin{aligned}
\varepsilon_{xx}^{GL} &= \varepsilon_x - y\kappa_z + z\kappa_y + \boldsymbol{\frac{1}{2}r^2\left(\frac{\partial\theta_x}{\partial x}\right)^2} \\
\gamma_{xy}^{GL} &= \gamma_y - z\kappa_x + \frac{\partial\psi}{\partial y}\frac{\partial\theta_x}{\partial x} \\
\gamma_{xz}^{GL} &= \gamma_z + y\kappa_x + \frac{\partial\psi}{\partial z}\frac{\partial\theta_x}{\partial x}
\end{aligned} \tag{6.53}$$

with the new definition of generalized strains:

$$
\begin{aligned}
r^2 &= y^2 + z^2 \\
\varepsilon_x^{GL} &= \frac{\partial u}{\partial x} + \frac{\mathbf{1}}{\mathbf{2}}\left(\left(\frac{\boldsymbol{\partial v}}{\boldsymbol{\partial x}}\right)^{\mathbf{2}} + \left(\frac{\boldsymbol{\partial w}}{\boldsymbol{\partial x}}\right)^{\mathbf{2}}\right) \\
\gamma_y^{GL} &= \frac{\partial v}{\partial x} - \theta_z + \frac{\mathbf{1}}{\mathbf{2}}\boldsymbol{\theta_x}\boldsymbol{\theta_y} + \frac{\boldsymbol{\partial w}}{\boldsymbol{\partial x}}\boldsymbol{\theta_x} - \frac{\boldsymbol{\partial x}}{\boldsymbol{\partial x}}\boldsymbol{\theta_z} \\
\gamma_z^{GL} &= \frac{\partial w}{\partial x} + \theta_y + \frac{\mathbf{1}}{\mathbf{2}}\boldsymbol{\theta_x}\boldsymbol{\theta_z} - \frac{\boldsymbol{\partial v}}{\boldsymbol{\partial x}}\boldsymbol{\theta_x} - \frac{\boldsymbol{\partial x}}{\boldsymbol{\partial x}}\boldsymbol{\theta_y} \\
\kappa_x^{GL} &= \frac{\partial \theta_x}{\partial x} + \frac{\mathbf{1}}{\mathbf{2}}\left(\frac{\boldsymbol{\partial \theta_y}}{\boldsymbol{\partial x}}\boldsymbol{\theta_z} - \frac{\boldsymbol{\partial \theta_z}}{\boldsymbol{\partial x}}\boldsymbol{\theta_y}\right) \\
\kappa_y^{GL} &= \frac{\partial \theta_z}{\partial x} - \frac{\mathbf{1}}{\mathbf{2}}\left(\frac{\boldsymbol{\partial \theta_x}}{\boldsymbol{\partial x}}\boldsymbol{\theta_y} + \boldsymbol{\theta_x}\frac{\boldsymbol{\partial \theta_y}}{\boldsymbol{\partial x}}\right) - \frac{\boldsymbol{\partial w}}{\boldsymbol{\partial x}}\frac{\boldsymbol{\partial \theta_x}}{\boldsymbol{\partial x}} \\
\kappa_z^{GL} &= \frac{\partial \theta_y}{\partial x} + \frac{\mathbf{1}}{\mathbf{2}}\left(\frac{\boldsymbol{\partial \theta_x}}{\boldsymbol{\partial x}}\boldsymbol{\theta_z} + \boldsymbol{\theta_x}\frac{\boldsymbol{\partial \theta_z}}{\boldsymbol{\partial x}}\right) - \frac{\boldsymbol{\partial v}}{\boldsymbol{\partial x}}\frac{\boldsymbol{\partial \theta_x}}{\boldsymbol{\partial x}}
\end{aligned}
\tag{6.54}
$$

However, the numerical tests show that the expressions in Equation (6.53) can be simplified by neglecting the non-linear terms in the expressions of generalized strains in Equation (6.54), without affecting the results [5]. Hence, the strains in Equation (6.54) can be rewritten as:

$$
\begin{aligned}
\varepsilon_{xx}^{GL} &= \frac{\partial u}{\partial x} - y\frac{\partial \theta_y}{\partial x} + z\frac{\partial \theta_z}{\partial x} + \frac{\mathbf{1}}{\mathbf{2}}\boldsymbol{r^2}\left(\frac{\boldsymbol{\partial \theta_x}}{\boldsymbol{\partial x}}\right)^{\mathbf{2}} \\
\gamma_{xy}^{GL} &= \frac{\partial v}{\partial x} - \theta_z + \frac{\partial \psi}{\partial y}\frac{\partial \theta_x}{\partial x} - z\frac{\partial \theta_x}{\partial x} \\
\gamma_{xz}^{GL} &= \frac{\partial w}{\partial x} + \theta_y + \frac{\partial \psi}{\partial z}\frac{\partial \theta_x}{\partial x} + y\frac{\partial \theta_x}{\partial x}
\end{aligned}
\tag{6.55}
$$

Comparing to the linear material strain in Equation (3.18), the only nonlinear term of the Green-Lagrange strain approximation is $\frac{1}{2}r^2\left(\frac{\partial \theta_x}{\partial x}\right)^2$. This term, called *Wagner term*, describes the interaction between axial and torsional strain. Using the same definition of generalized strains as in Equation (3.11), the following kinematic relationship can be

obtained between Green-Lagrange strains and the generalized strains vector:

$$\begin{pmatrix} \varepsilon_{xx}^{GL} \\ \gamma_{xy}^{GL} \\ \gamma_{xz}^{GL} \end{pmatrix} = \begin{bmatrix} 1 & 0 & 0 & \frac{1}{2}\boldsymbol{r^2\kappa_x} & z & -y \\ 0 & 1 & 0 & \frac{\partial\psi}{\partial y} - z & 0 & 0 \\ 0 & 0 & 1 & \frac{\partial\psi}{\partial z} + y & 0 & 0 \end{bmatrix} \begin{pmatrix} \varepsilon_x \\ \gamma_y \\ \gamma_z \\ \kappa_x \\ \kappa_y \\ \kappa_z \end{pmatrix} \Rightarrow \mathbf{e}_f^{GL}(x,y,z) = \mathbf{a}_f^{GL}(x,y,z)\mathbf{e}_s(x) \quad (6.56)$$

As in the sequel, for the shake of simplicity in establishing the numerical implementation, the above expression (and others) will be decomposed into 2 parts: one represents the linear/ordinary part following the local linear strain assumption $\mathbf{e}_f$, and another resulting from the second order Green-Lagrange approximation $\mathbf{e}_f^*$:

$$\begin{aligned} \mathbf{e}_f^{GL}(x,y,z) &= \left(\begin{bmatrix} 1 & 0 & 0 & 0 & z & -y \\ 0 & 1 & 0 & \frac{\partial\psi}{\partial y} - z & 0 & 0 \\ 0 & 0 & 1 & \frac{\partial\psi}{\partial z} + y & 0 & 0 \end{bmatrix} + \begin{bmatrix} 0 & 0 & 0 & \frac{1}{2}\boldsymbol{r^2\kappa_x} & 0 & 0 \\ 0 & 0 & 0 & 0 & 0 & 0 \\ 0 & 0 & 0 & 0 & 0 & 0 \end{bmatrix} \right) \mathbf{e}_s(x) \\ &= \left(\mathbf{a}_f(y,z) + \mathbf{a}_f^*(x,y,z)\right)\mathbf{e}_s(x) = \mathbf{e}_f(x,y,z) + \mathbf{e}_f^*(x,y,z) \end{aligned} \quad (6.57)$$

The expression of $\mathbf{e}_f(x,y,z)$ is similar to the existing one in Section 3.3, while for $\mathbf{e}_f^*$ the only non zero components is the axial strain: $\mathbf{e}_f^* = \begin{pmatrix} \frac{1}{2}r^2\kappa_x^2 & 0 & 0 \end{pmatrix}^T$; $\mathbf{a}_f(x,y,z)$ and $\mathbf{a}_f^*(x,y,z)$ are respectively the linear/ordinary and the second order compatibility matrix.

Then, the following constitutive relationship can be established:

$$\mathbf{s}_f^{GL} = \mathbf{k}_f\mathbf{e}_f^{GL} = \mathbf{k}_f\left(\mathbf{e}_f + \mathbf{e}_f^*\right) = \mathbf{s}_f + \mathbf{s}_f^* \quad (6.58)$$

where $\mathbf{k}_f$ is the material stiffness matrix. In this section, for the shake of simplicity, we consider that $\mathbf{k}_f$ is approximated as a consistent tangent operator as follows:

$$\mathbf{k}_f = \begin{bmatrix} E & 0 & 0 \\ 0 & G_y & 0 \\ 0 & 0 & G_z \end{bmatrix} \quad (6.59)$$

As a consequence, the normal stress becomes the only non-zero component of the non-

linear stress vector: $\mathbf{s}_f^* = \begin{pmatrix} \frac{1}{2}Er^2\kappa_x^2 & 0 & 0 \end{pmatrix}^T$. From Equation (3.40) in Section 3.4.1, the sectional forces vector consistent to the Green-Lagrange strains can be expressed as follows:

$$\mathbf{D}_s^{GL}(x) = \iint_A \mathbf{a}_f^{GL^T} \mathbf{s}_f^{GL} dA = \begin{pmatrix} N_x \\ V_y \\ V_z \\ M_x \\ M_y \\ M_z \end{pmatrix} = \begin{pmatrix} \iint_A \sigma_{xx}^{GL} dA \\ \iint_A \tau_{xy}^{GL} dA \\ \iint_A \tau_{xz}^{GL} dA \\ \iint_A \left[\left(y + \frac{\partial \psi}{\partial z} \right) \tau_{xz}^{GL} - \left(z - \frac{\partial \psi}{\partial y} \right) \tau_{xy}^{GL} + \frac{1}{2} \boldsymbol{r^2 \kappa_x \sigma_{xx}^{GL}} \right] dA \\ \iint_A z \sigma_{xx}^{GL} dA \\ -\iint_A y \sigma_{xx}^{GL} dA \end{pmatrix} \tag{6.60}$$

From Equation (6.58), the decomposition of this sectional forces results as:

$$\mathbf{D}_s^{GL}(x) = \begin{pmatrix} \iint_A \sigma_{xx} dA \\ \iint_A \tau_{xy} dA \\ \iint_A \tau_{xz} dA \\ \iint_A \left[\left(y + \frac{\partial \psi}{\partial z} \right) \tau_{xz} - \left(z - \frac{\partial \psi}{\partial y} \right) \tau_{xy} \right] dA \\ \iint_A z \sigma_{xx} dA \\ -\iint_A y \sigma_{xx} dA \end{pmatrix} + \begin{pmatrix} \iint_A \sigma_{xx}^* dA \\ 0 \\ 0 \\ \iint_A \frac{1}{2} r^2 \kappa_x \sigma_{xx}^{GL} dA \\ \iint_A z \sigma_{xx}^* dA \\ -\iint_A y \sigma_{xx}^* dA \end{pmatrix} = \mathbf{D}_s(x) + \mathbf{D}_s^*(x) \tag{6.61}$$

As we can see, the nonlinear Wagner term influences not only on the torsional moment but also the axial force and bending moments. However, for the case of a solid symmetric section as considered in this present work, the expression of $\mathbf{D}_s^*(x)$ becomes:

$$\mathbf{D}_s^*(x) = \begin{pmatrix} \iint_A \frac{1}{2} Er^2 dA \\ 0 \\ 0 \\ \iint_A \frac{1}{2} r^2 \kappa_x \sigma_{xx}^{GL} dA \\ \iint_A \frac{1}{2} Ezr^2 dA \\ -\iint_A \frac{1}{2} Eyr^2 dA \end{pmatrix} = \begin{pmatrix} \iint_A \frac{1}{2} Er^2 dA \\ 0 \\ 0 \\ \iint_A \frac{1}{2} Er^2 \kappa_x \left(\varepsilon_x + \frac{1}{2} r^2 \kappa_x^2 \right) dA \\ 0 \\ 0 \end{pmatrix} \tag{6.62}$$

The vector of nodal forces in local coordinates can be given by:

$$\mathbf{Q}_e^{GL} = \int_L \mathbf{B}_s^T \mathbf{D}_s^{GL} dx = \int_L \mathbf{B}_s^T \left(\mathbf{D}_s + \mathbf{D}_s^* \right) dx = \mathbf{Q}_e + \mathbf{Q}_e^* \tag{6.63}$$

with $\mathbf{B}_s$ the matrix of shape functions in Equation (3.15). The ordinary part has already been implemented in the existing beam element formulation, while the nonlinear part can

be expressed as:

$$\mathbf{Q}_e^* = \int_L \mathbf{B}_s^T \mathbf{D}_s^* dx = \begin{bmatrix} N_x^{*I} & 0 & 0 & M_x^{*I} & 0 & 0 & N_x^{*J} & 0 & 0 & M_x^{*J} & 0 & 0 \end{bmatrix} \tag{6.64}$$

where the expressions of the axial force and the nodal torsional moment are:

$$N_x^{*J} = -N_x^{*J} = -\int_L \frac{1}{L} \left(\iint_A \frac{1}{2} E r^2 dA \right) dx \tag{6.65a}$$

$$M_x^{*J} = -M_x^{*J} = -\int_L \frac{1}{L} \left(\iint_A \frac{1}{2} E r^2 \kappa_x \left(\varepsilon_x + \frac{1}{2} r^2 \kappa_x^2 \right) dA \right) dx \tag{6.65b}$$

For the sectional stiffness matrix, from Equation (3.43) we get:

$$\mathbf{K}_s^{GL}(x) = \iint_A \mathbf{a}_f^{GL^T} \mathbf{k}_f \mathbf{a}_f^{GL} dA \tag{6.66}$$

Using the consistent tangent operator for $\mathbf{k}_f$ as in equation 6.59, for a rectangular symmetric section, the following expression of sectional stiffness matrix has been obtained:

$$\mathbf{K}_s^{GL} = \iint_A \begin{bmatrix} E & 0 & 0 & \frac{\mathbf{1}}{\mathbf{2}} \boldsymbol{E r^2 \kappa_x} & 0 & 0 \\ 0 & G_y & 0 & 0 & 0 & 0 \\ 0 & 0 & G_z & 0 & 0 & 0 \\ \frac{\mathbf{1}}{\mathbf{2}} \boldsymbol{E r^2 \kappa_x} & 0 & 0 & G_y \left(\frac{\partial \psi}{\partial y} - z \right)^2 + G_z \left(\frac{\partial \psi}{\partial z} + y \right)^2 + \frac{\mathbf{1}}{\mathbf{4}} \boldsymbol{E r^4 \kappa_x^2} & 0 & 0 \\ 0 & 0 & 0 & 0 & Ez^2 & 0 \\ 0 & 0 & 0 & 0 & 0 & Ey^2 \end{bmatrix} dA \tag{6.67}$$

As mentioned above, the expression of $\mathbf{K}_s^{GL}$ can be decomposed into the linear/ordinary part $\mathbf{K}_s$ and the nonlinear part $\mathbf{K}_s^*$ containing only the bold terms in the expression of $\mathbf{K}_s^{GL}$ in Equation (6.67). It is worth to note that, for a symmetric section, at local level in the framework of co-rotational formulation, the second order approximation, through the Wagner term, influences strongly on the torsional response and the interaction between axial-torsion. Then, according to Equation (3.48), when considering the element equilibrium, the element stiffness matrix can also be decomposed into the linear and nonlinear part:

$$\mathbf{K}_e^{GL} = \int_L \mathbf{B}_s^T \mathbf{K}_s^{GL} \mathbf{B}_s dx = \int_L \mathbf{B}_s^T \left(\mathbf{K}_s + \mathbf{K}_s^* \right) \mathbf{B}_s dx = \mathbf{K}_e + \mathbf{K}_e^* \tag{6.68}$$

Where the nonlinear part can be expressed as:

$$\mathbf{K}_e^* = \int_L \mathbf{B}_s^T \mathbf{K}_s^* \mathbf{B}_s dx = \begin{bmatrix} 0 & 0 & 0 & K_1^* & 0 & 0 & 0 & 0 & 0 & -K_1^* & 0 & 0 \\ 0 & 0 & 0 & 0 & 0 & 0 & 0 & 0 & 0 & 0 & 0 & 0 \\ 0 & 0 & 0 & 0 & 0 & 0 & 0 & 0 & 0 & 0 & 0 & 0 \\ K_1^* & 0 & 0 & K_2^* & 0 & 0 & -K_1^* & 0 & 0 & -K_2^* & 0 & 0 \\ 0 & 0 & 0 & 0 & 0 & 0 & 0 & 0 & 0 & 0 & 0 & 0 \\ 0 & 0 & 0 & 0 & 0 & 0 & 0 & 0 & 0 & 0 & 0 & 0 \\ 0 & 0 & 0 & -K_1^* & 0 & 0 & 0 & 0 & 0 & K_1^* & 0 & 0 \\ 0 & 0 & 0 & 0 & 0 & 0 & 0 & 0 & 0 & 0 & 0 & 0 \\ 0 & 0 & 0 & 0 & 0 & 0 & 0 & 0 & 0 & 0 & 0 & 0 \\ -K_1^* & 0 & 0 & -K_2^* & 0 & 0 & K_1^* & 0 & 0 & K_2^* & 0 & 0 \\ 0 & 0 & 0 & 0 & 0 & 0 & 0 & 0 & 0 & 0 & 0 & 0 \\ 0 & 0 & 0 & 0 & 0 & 0 & 0 & 0 & 0 & 0 & 0 & 0 \end{bmatrix} \tag{6.69}$$

with the following definition of K_1^* and K_2^*:

$$K_1^* = \int_L \frac{1}{L^2} \left(\iint_A \frac{1}{2} E r^2 \kappa_x dA \right) dx \tag{6.70a}$$

$$K_2^* = \int_L \frac{1}{L^2} \left(\iint_A \frac{1}{4} E r^4 \kappa_x^2 dA \right) dx \tag{6.70b}$$

6.4.1 Case of Pure torsion

In the case of pure torsion for a rectangular cross-section, the material displacements in Equation (6.51) becomes:

$$\overline{U}_t(x, y, z) = \kappa_x(x)\psi(y, z) \tag{6.71a}$$

$$\overline{V}_t(x, y, z) = -z\theta_x(x) - \frac{1}{2} z\theta_x^2(x) \tag{6.71b}$$

$$\overline{W}_t(x, y, z) = y\theta_x(x) - \frac{1}{2} y\theta_x^2(x) \tag{6.71c}$$

where $\kappa_x(x) = \dfrac{\partial \theta_x}{\partial x}$ and the subindex t denoted for the case of pure torsion. Comparing to the expression in Equation (4.6), the appear of second-order terms in the transversal displacements make the non-linearity geometric. The Green-Lagrange strain components

are then given by:

$$\varepsilon_{xx,t}^{GL} = \frac{\partial \overline{U}}{\partial x} + \frac{1}{2}\left(\left(\frac{\partial U}{\partial x}\right)^2 + \left(\frac{\partial V}{\partial x}\right)^2 + \left(\frac{\partial \mathrm{W}}{\partial x}\right)^2\right) \tag{6.72a}$$

$$\gamma_{xy,t}^{GL} = \frac{\partial \overline{U}}{\partial y} + \frac{\partial \overline{V}}{\partial x} + \frac{\partial \overline{U}}{\partial x}\frac{\partial \overline{U}}{\partial y} + \frac{\partial \overline{V}}{\partial x}\frac{\partial \overline{V}}{\partial y} + \frac{\partial \overline{W}}{\partial x}\frac{\partial \overline{W}}{\partial y} \tag{6.72b}$$

$$\gamma_{xz,t}^{GL} = \frac{\partial \overline{U}}{\partial z} + \frac{\partial \overline{V}}{\partial x} + \frac{\partial \overline{U}}{\partial x}\frac{\partial \overline{U}}{\partial z} + \frac{\partial \overline{V}}{\partial x}\frac{\partial \overline{V}}{\partial z} + \frac{\partial \overline{W}}{\partial x}\frac{\partial \overline{W}}{\partial z} \tag{6.72c}$$

Using Equation (6.71), Equation (6.72) becomes:

$$\varepsilon_{xx,t}^{GL} = \frac{1}{2}(y^2 + z^2)\kappa_x^2 \tag{6.73a}$$

$$\gamma_{xy,t}^{GL} = \left(-z + \frac{\psi(y,z)}{y}\right)\kappa_x \tag{6.73b}$$

$$\gamma_{xz,t}^{GL} = \left(y + \frac{\psi(y,z)}{z}\right)\kappa_x \tag{6.73c}$$

Unlike the material strain in linear geometry condition in Equation (4.7), the axial strain under large displacements is not zero and is called *Wagner term* which causes a non linearity in the response in pure torsion. Because of this term, the local strain can not be related to the generalized twist κ_x in a compact form as in the above section. Instead, the nodal torsional moments and element stiffness matrix in a finite element framework will be derived from the strain energy function.

The strain energy is expressed as a function of the local strains:

$$\begin{aligned}\Phi = \int_0^L \Phi_A dx &= \int_0^L \left(\frac{1}{2}\iint_A E\varepsilon_{xx}^2 dA + \frac{1}{2}\iint_A G\left(\gamma_{xy}^2 + \gamma_{xz}^2\right) dA\right) dx \\ &= \frac{1}{2}\int_0^L \left(EI_{rr}\kappa_x^4 + GJ\kappa_x^2\right) dx\end{aligned} \tag{6.74}$$

With:

$$EI_{rr} = \iint_A E(y,z)\frac{1}{4}(y^2 + z^2) dA$$

$$GJ = \iint_A \left[G(y,z)\left(\frac{\partial \psi}{\partial y} - z\right)^2 + \left(\frac{\partial \psi}{\partial z} + y\right)^2\right] dA$$

Using Equation (3.14), Equation (6.74) becomes:

$$\begin{aligned}\Phi &= \frac{1}{2}\int_0^L \left(EI_{rr}\kappa_x^4 + GJ\kappa_x^2\right) dx \\ &= \frac{1}{2}\left(EI_{rr}\int_0^L \kappa_x^4 dx + GJ\int_0^L \kappa_x^2 dx\right) \\ &= \frac{1}{2}\left(EI_{rr}\int_0^L \left(-\frac{\theta_x^I}{L} + \frac{\theta_x^J}{L}\right)^4 dx + GJ\int_0^L \left(-\frac{\theta_x^I}{L} + \frac{\theta_x^J}{L}\right)^2 dx\right) \\ &= \frac{1}{2}\left(\frac{EI_{rr}}{L^3}(\theta_x^J - \theta_x^I)^4 + \frac{GJ}{L}(\theta_x^J - \theta_x^I)^2\right)\end{aligned} \tag{6.75}$$

The nodal torsional moment in each element is then evaluated by:

$$\mathbf{M}_{x,e} = \frac{\partial \Phi}{\partial \mathbf{q}_e} = \begin{pmatrix} \dfrac{\partial \Phi}{\partial \theta_x^I} \\ \dfrac{\partial \Phi}{\partial \theta_x^J} \end{pmatrix} = \begin{pmatrix} -2\dfrac{EI_{rr}}{L^3}(\theta_x^J - \theta_x^I)^3 - \dfrac{GJ}{L}(\theta_x^J - \theta_x^I) \\ 2\dfrac{EI_{rr}}{L^3}(\theta_x^J - \theta_x^I)^3 + \dfrac{GJ}{L}(\theta_x^J - \theta_x^I) \end{pmatrix} = \begin{pmatrix} M_x^I \\ \\ M_x^J \end{pmatrix} \tag{6.76}$$

And the element stiffness matrix:

$$\mathbf{K}_e = \frac{\partial \mathbf{M}_{x,e}}{\partial \mathbf{q}_e} = \begin{bmatrix} \dfrac{\partial M_x^I}{\partial \theta_x^I} & \dfrac{\partial M_x^I}{\partial \theta_x^J} \\ \dfrac{\partial M_x^J}{\partial \theta_x^I} & \dfrac{\partial M_x^J}{\partial \theta_x^J} \end{bmatrix} = \begin{bmatrix} 6\dfrac{EI_{rr}}{L^3}(\theta_x^J - \theta_x^I)^2 + \dfrac{GJ}{L} & -6\dfrac{EI_{rr}}{L^3}(\theta_x^J - \theta_x^I)^2 - \dfrac{GJ}{L} \\ -6\dfrac{EI_{rr}}{L^3}(\theta_x^J - \theta_x^I)^2 - \dfrac{GJ}{L} & 6\dfrac{EI_{rr}}{L^3}(\theta_x^J - \theta_x^I)^2 + \dfrac{GJ}{L} \end{bmatrix} \tag{6.77}$$

6.5 Analysis algorithm

In this work, the proposed model developed in Chapter 3 is a two-node displacement-based formulation in which the primary input is the nodal displacements vector $\mathbf{q}_e$ of 12 components. Under linear geometric condition, $\mathbf{q}_e$ can be used directly in the beam formulation, however, under non-linear geometric assumptions using co-rotational framework, $\mathbf{q}_e$ is related to the global reference so it is necessary to transform it into $\overline{\mathbf{q}}_e$, which is related to the local reference frame and corresponds to the beam formulation developed in Chapter 3 and Section 6.4. As mentioned above, the local displacements vector $\overline{\mathbf{q}}_e$

contains 7 components: $\overline{\mathbf{q}}_e = \begin{pmatrix} \overline{u} & \overline{\theta}_x^I & \overline{\theta}_y^I & \overline{\theta}_z^I & \overline{\theta}_x^J & \overline{\theta}_y^J & \overline{\theta}_z^J \end{pmatrix}^T$, in which:

$$\overline{u} = l_n - l_o; \qquad \begin{pmatrix} \overline{\theta}_x^I \\ \overline{\theta}_y^I \\ \overline{\theta}_z^I \end{pmatrix} = \log(\overline{\mathbf{R}}^I); \qquad \begin{pmatrix} \overline{\theta}_x^J \\ \overline{\theta}_y^J \\ \overline{\theta}_z^J \end{pmatrix} = \log(\overline{\mathbf{R}}^J)$$

where the rotation matrices $\overline{\mathbf{R}}^{I/J}$ are computed using Equation (6.18). Knowing that $\overline{\mathbf{q}}_e$ has only 7 components, while the nodal displacements vector using in the local beam formulation in section 6.4 has 12 components, one auxiliary transformation is required:

$$\mathbf{q}_e = \mathbf{T}^T \overline{\mathbf{q}}_e \tag{6.78}$$

where $\mathbf{T} = \mathbf{T}_d \mathbf{T}_r$ is a transformation matrix defined as a multiplication of two sub-matrices of transformation: $\mathbf{T}_d$ is the translated-transformation matrix while $\mathbf{T}_r$ is the rotate-transformation matrix.

$$\mathbf{T}_d = \begin{bmatrix} -1 & 0 & 0 & 0 & 0 & 0 & 1 & 0 & 0 & 0 & 0 & 0 \\ 0 & 0 & 0 & 1 & 0 & 0 & 0 & 0 & 0 & 0 & 0 & 0 \\ 0 & 0 & -1/l_n & 0 & 1 & 0 & 0 & 0 & 1/l_n & 0 & 0 & 0 \\ 0 & 1/l_n & 0 & 0 & 0 & 1 & 0 & -1/l_n & 0 & 0 & 0 & 0 \\ 0 & 0 & 0 & 0 & 0 & 0 & 0 & 0 & 0 & 1 & 0 & 0 \\ 0 & 0 & -1/l_n & 0 & 1 & 0 & 0 & 0 & 1/l_n & 0 & 0 & 0 \\ 0 & 1/l_n & 0 & 0 & 0 & 1 & 0 & -1/l_n & 0 & 0 & 0 & 0 \end{bmatrix}; \quad \mathbf{T}_r = \begin{bmatrix} \mathbf{C} & \mathbf{0}_3 & \mathbf{0}_3 & \mathbf{0}_3 \\ \mathbf{0}_3 & \mathbf{C} & \mathbf{0}_3 & \mathbf{0}_3 \\ \mathbf{0}_3 & \mathbf{0}_3 & \mathbf{C} & \mathbf{0}_3 \\ \mathbf{0}_3 & \mathbf{0}_3 & \mathbf{0}_3 & \mathbf{C} \end{bmatrix} \tag{6.79}$$

the component $\mathbf{C}$ of $\mathbf{T}_r$ contains the direction cosines defined as follows:

$$\mathbf{C} = \begin{bmatrix} C_x & C_y & C_z \\ -(C_x C_y \cos\alpha + C_z \sin\alpha)/C_{xz} & C_{xz}\cos\alpha & -(C_y C_z \cos\alpha + C_x \sin\alpha)/C_{xz} \\ (C_x C_y \sin\alpha - C_z \cos\alpha) & -C_x z \sin\alpha & (C_y C_z \sin\alpha + C_x \cos\alpha)/C_{xz} \end{bmatrix}$$

$$C_x = (x^J - x^I)/l; \qquad C_y = (y^J - y^I)/l; \qquad C_x = (z^J - z^I)/l; \qquad C_{xz} = \sqrt{C_x^2 + C_z^2};$$

$$l = \sqrt{(x^J - x^I)^2 + (y^J - y^I)^2 + (z^J - z^I)^2} \tag{6.80}$$

and $\mathbf{x}^{IJ} = \begin{pmatrix} x^{IJ} & y^{IJ} & z^{IJ} \end{pmatrix}^T$ are the nodal coordinates of nodes I,J in global reference.

Now the displacements vector $\overline{\mathbf{q}}_e$ can be implemented in the local beam formulation, and as a result the nodal forces vector $\overline{\mathbf{Q}}_e$ and the element stiffness matrix $\overline{\mathbf{K}}_e$ will be obtained. Then, 3 successive transformations described in section 6.3 will be applied in order to transform these variables from the local frame into global reference. The algorithm and implementation of co-rotational formulation in the proposed model is resumed and shown in Figure 6-7.

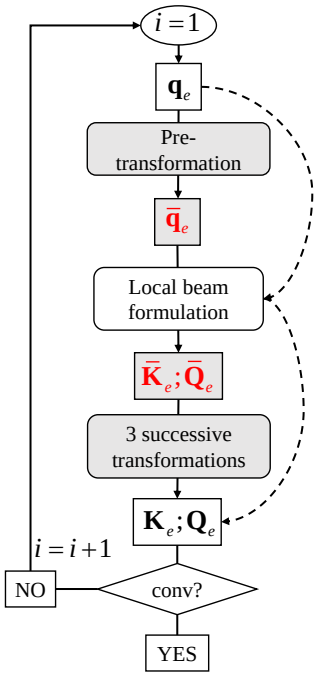

Figure 6-7 – Implementation of co-rotational formulation into the proposed model. The dashed line represents the algorithm in linear geometric conditions.

6.6 Numerical examples

In this section, some numerical examples are first simulated using cross-section dimensions and material properties of steel structures in order to validate the implementation of co-rotational framework in the proposed model formulation. Then other cases studies were investigated for reinforced concrete members. As mentioned in Section 6.4, the linear geometric conditions of the beam formulation in the local reference are ensured by using a big number of finite element and cross-section mesh.

6.6.1 Cases of elastic material

The geometrical non-linearity in the elastic material range is discussed in this section. Let's consider an elastic cantilever beam as shown in Figure 6-8. Note that this beam was

used as reference in Battini's PhD Thesis [5]. The beam model has been simulated using 10 elements with a system of 50×5 square mesh, subjected to two loading cases: pure torsion (Figure 6-8a) and combined shear-bending-torsion (Figure 6-8b). In this example, the cross-section profile is a thin-type usually found in steel structure.

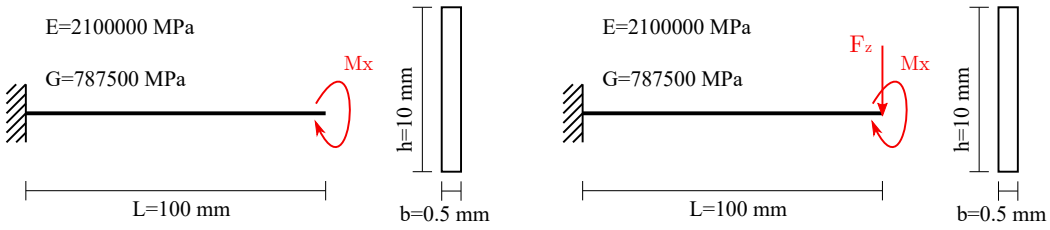

(a) Exam. 1: Pure torsion. (b) Exam. 2: Shear-bending-torsion.

Figure 6-8 – Example 1 & 2: Cantilever beam under nonlinear geometrical conditions, subjected to different loading cases.

6.6.1.1 Example 1: Cantilever elastic beam under pure torsion

In this first example, the case of pure torsion is investigated. The formulation proposed in Section 6.4.1 is validated by the results against the ones obtained by analytical model and other numerical model. Figure 6-9 presents the torsional moment versus end twist angle curves. Compared to the analytical solution based on Vlasov's beam theory [113] and the numerical one of Battini's model, the results obtained by the proposed model, taking into account the contribution of the Wagner term in the model formulation, show a very good correlation. It can be seen that, although simulated in the elastic material range, the relationship between torsional moment and twist angle was no longer linear, due to the geometrical non-linearity caused by the introduction of Wagner term, as explained in Section 6.4.1. It is evident that without taking into account the Wagner term, the model is considered as a linear geometry model which gave a purely linear response.

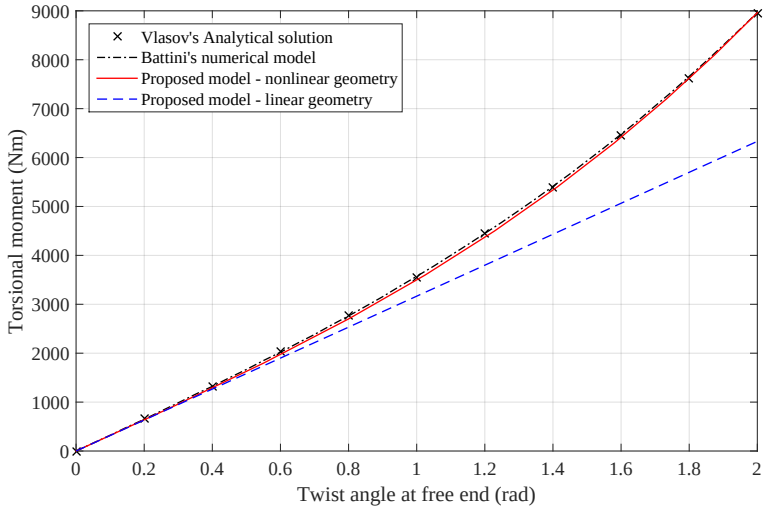

Figure 6-9 – Example 1: Elastic torsional response under nonlinear geometric conditions.

6.6.1.2 Example 2: Cantilever elastic beam subjected to shear-bending-torsion

This numerical example is to study the influence of shear and bending on the torsional behavior of the elastic beam in large rotation. Figure 6-10 presents the torsional moment versus end twist angle curves for four torsion-bending moment ratios: $R = \infty$; $R = 1$; $R = 1/2$ and $R = 1/5$. As can be seen, in elastic material regime, the torsional behavior is not affected by the bending and shear actions when the geometrical nonlinearity is neglected. However, the numerical results show that the torsional stiffness decreases significantly with increasing of torsion-bending moment ratios when the beam is in geometrical nonlinear regime. Further, experimentation test needs to be conducted to confirm this statement.

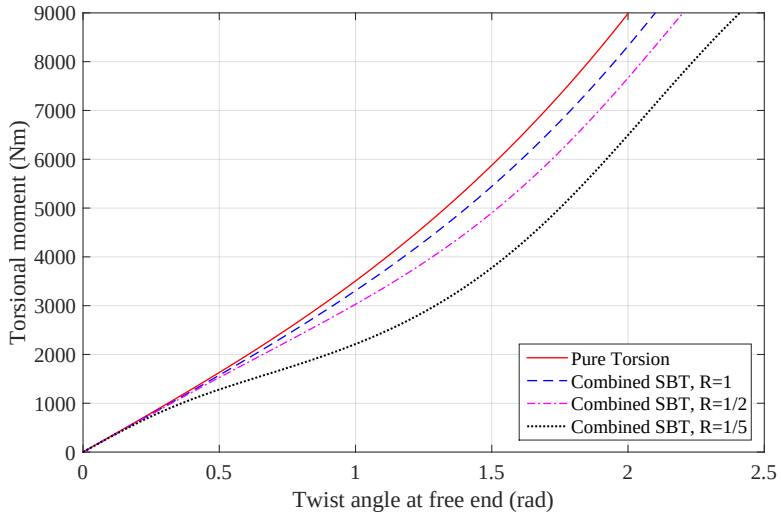

Figure 6-10 – Example 2: Torsional moment versus twist angle diagrams of elastic material beam subjected to shear-bending-torsion effect under nonlinear geometric conditions, with different ratio of torsional versus bending moment.

6.6.2 Cases of inelastic material

This section deals with several numerical examples of beam under inelastic material regime: an elasto-plastic cantilever beam subjected to shear-bending and torsion, and a simply supported RC beam subjected to pure torsion. Through these examples, the implementation of the corotational framework in the proposed model formulation as described in previous sections can be validated in inelastic material regime.

6.6.2.1 Example 3: Cantilever inelastic beam subjected to shear-bending and torsion

The third example concerns an elasto-plastic thin-walled cross-section cantilever beam, subjected to vertical load at the free-end, which was also investigated by Kondoh & Atluri

[55], using a numerical model based on Euler-Benoulli assumption. The beam dimensions, material properties and the elasto-plastic material behavior are shown in Figure 6-11.

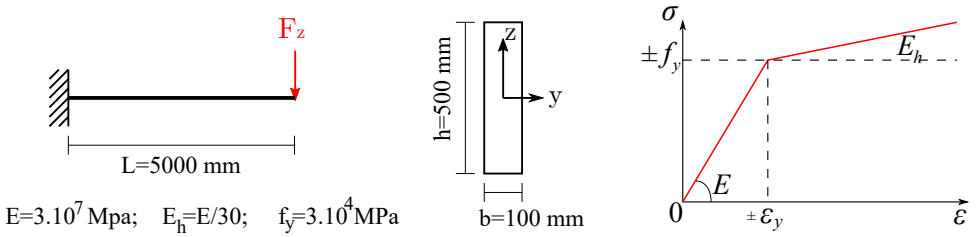

Figure 6-11 – Example 3: Cantilever beam in the example of Kondoh & Atluri [55].

Using 10 beam elements with a mesh of 50×10 square fibers, the simulation results obtained by the proposed model are shown in Figure 6-12. The effect of nonlinear geometric assumptions, bring up by corotational framework, can be easily noticed, as the element stiffness increases significantly in the plastic material range. Compared to the Kondoh & Atlure's model, a good correlation is achieved. Regarding the high ratio between beam length and height, although the two numerical models use different kinematic conditions in its beam formulation (Euler-Bernoulli in Kondoh & Atlure's model and Timoshenko in the proposed model), the shear effect can be generally neglected, except a slight gap observed at high load stage.

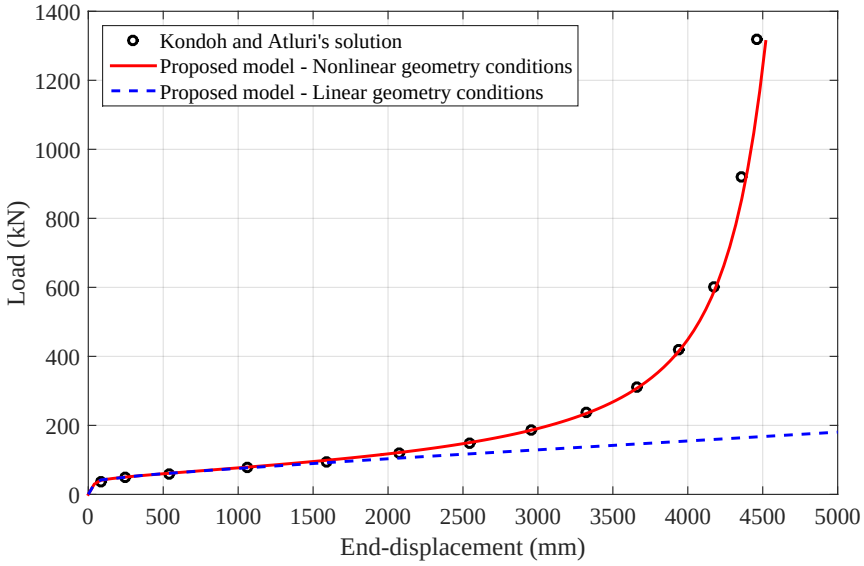

Figure 6-12 – Example 3: Load-displacement diagrams of elasto-plastic beam subjected to shear-bending under nonlinear geometrical conditions.

Using the same outline of beam as in Figure 6-11, but instead of vertical load, a torsional moment is applied at the free end. Simulation result can be found in Figure 6-13, concerning two numerical models: one with the implementation of the Wagner term

in the model formulation (nonlinear geometry model), and another without this nonlinear term (linear geometry model). Similar to the above case subjected to shear-bending effect, the torsional stiffness given by the nonlinear geometry model increases significantly compared to the response of the linear geometry model. The effect of second-order Wagner term continues to give a significant influence on the torsional response of elasto-plastic material beam.

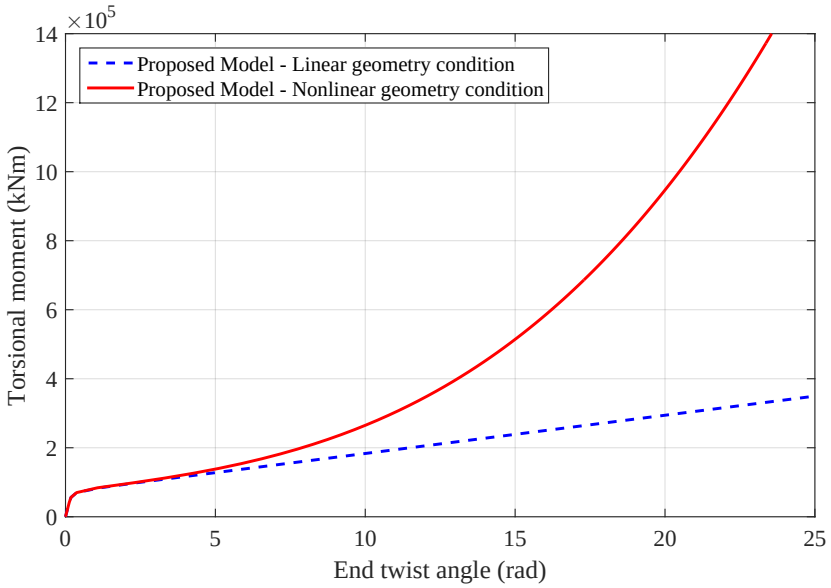

Figure 6-13 – Example 3: Torsional moment - twist angle diagrams of elasto-plastic beam subjected to pure torsion effect under linear and nonlinear geometric conditions.

When torsional moment is accompanied by the vertical load, the beam is subjected to combined shear-bending-torsion. Figure 6-14 presents the torsional moment versus end twist angle curve for different torsion-bending moment ratios: $R = \infty$, $R = 10$, $R = 1$, $R = 1/5$ and $R = 1/20$. When torsional moment dominates bending moment (R is bigger than 1), the material yielding is due to torsional effect as in the above case of pure torsion, and no difference is recorded in the plastic material regime. When bending moment becomes bigger and dominated, the yielding point is changed, depending on the value of bending moment, and the torque-twist diagram becomes different as a consequence. In this example of combined loadings under elasto-plastic material regime, the fact that torsional behavior depends on the yielding point limits the study of coupling actions. One statement can be draw is that there is no significant influence of shear-bending actions to torsional response when torsional moment dominates bending moment.

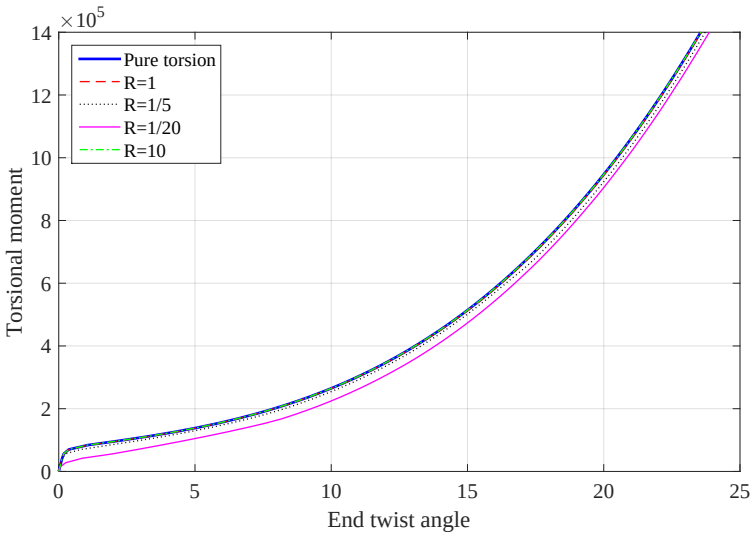

Figure 6-14 – Example 3: Torsional moment versus twist angle diagrams of elasto-plastic material beam subjected to shear-bending-torsion effect under nonlinear geometric conditions, with different ratio of torsional versus bending moment.

6.6.2.2 Example 4: simply-supported RC beam subjected to pure torsion

Although making a great influence in the torque-twist diagram of beam under torsion, in practice, the necessary of including this nonlinear geometric effect due to Wagner term in an ordinary RC beam might be under question. In this section, another example is carried out in the field of inelastic material, in order to clarify the statement of negligence of nonlinear geometric conditions for concrete and/or RC beams. Specimen G5, a simply supported beam in the torsion test of Hsu [45], is simulated in two cases of two different local formulations: linear geometric model (LGM - without Wagner term) and nonlinear geometric model (NLGM - Wagner term included). Section details and material properties of specimen G5 are cited in Figure 6-15.

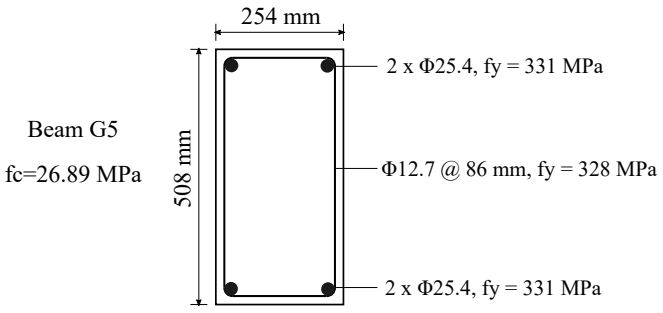

Figure 6-15 – Example 4: Details of Beam G5 .

No significant difference between the linear and nonlinear geometric model could be observed in the torque-twist diagram in Figure 6-16. Using a displacement imposed approach

during the simulation, the cracking torque was reached at 2.5 mrad/m, corresponding to the same value of 29.26 kN in both models, no difference was therefore remarked between two models in the phase before cracking of concrete. In the phase after cracking, the ultimate torsional moment was achieved at 55 mm for both two models and gave a value of 73.51 kN for the LGM and 73.55 kN for the NLGM. Only a very minor relative difference of 0.05 % was recorded.

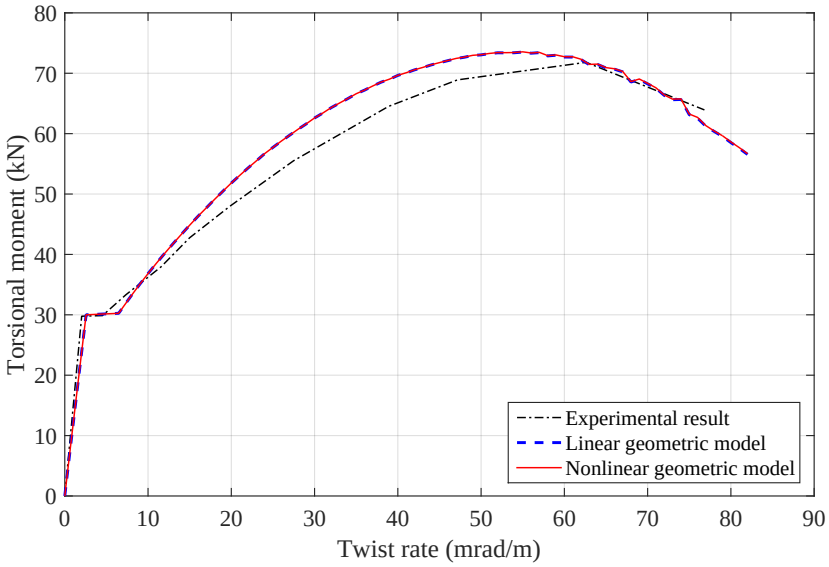

Figure 6-16 – Example 7: Torsional moment versus twist angle diagrams of beam G5 subjected to pure torsion under linear and nonlinear geometric conditions.

Table 6.1 indicates the values of cracking and ultimate torsional moment in each specimen of series G in Hsu's test, obtained by the LGM and the NLGM. At the same twist rate value, the cracking and ultimate torsional moments obtained by the LGM were always smaller (or similar) than those of the NLGM. This observation corresponds to the result obtained in Section 6.6.1.1 and 6.6.2.1, in which the nonlinear geometric effect makes the torsional stiffness stronger in both the elastic and inelastic material regime. However, knowing that concrete is a brittle material and its cracking and failure deformation is small, the RC beams were failure before any significant differences could be remarked. Indeed, in Table 6.1, minor differences were recorded in all the cases.

Table 6.1 – Series G of Hsu's torsion test: Cracking and ultimate torsional model obtained by the LGM and NLGM.

Beams	T_{cr} (kN)			T_u (kN)		
	LGM	NLGM	Difference	LGM	NLGM	Difference
G2	29.40	29.44	0.14 %	37.75	37.76	0.03 %
G3	26.72	26.72	0 %	49.60	49.62	0.04 %
G4	27.94	27.94	0 %	65.72	65.74	0.02 %
G5	29.26	29.26	0 %	73.51	73.55	0.05 %
G6	29.79	29.84	0.17 %	40.46	40.49	0.07 %
G7	32.13	32.13	0 %	53.79	53.80	0.02 %
G8	32.77	32.78	0.03 %	72.12	72.14	0.03 %

6.7 Conclusions

In this Chapter, using the corotational formulation, the nonlinear geometry of the proposed beam model under large displacement conditions has been investigated. Through several numerical examples carefully executed above, the following remarks and conclusions can be draw:

- By validating with some existing example in the literature under the loading case of shear-bending and pure torsion, the corotational formulation can be considered as successfully implemented in the proposed model formulation.
- When considering the torsional effect, the contribution of the Wagner term is very significant, in both elastic and inelastic material regime, knowing that the torsional rigidity could be considerably increased under the influence of this nonlinear term.
- In the elastic material regime, when the beam is in geometrical non linear conditions, the combination of shear, bending and torsional moments could make some significants impact on the torsional behavior, compared to the case of pure torsion. This statement is interesting because no difference can be recorded between these two loading cases in elastic material regime under geometrical linear conditions.
- However, in the elasto-plastic material regime, when torsional moment dominates bending moment, no significant influence of shear-bending actions to torsional response could be observed. Otherwise, in practice, the nonlinear geometric effect could be neglected for a simply supported RC beam of ordinary length.

Chapter 7

Conclusions and Perspectives

7.1 Summary and Conclusions

The main objective of this PhD thesis was the development of an efficient finite element model for the nonlinear analysis of reinforced concrete members taking into account the coupling effect of multi-stresses resultants under bending, shear and torsional loadings. Indeed, using a multi-fiber discretization and sectional analysis approach, the developed 3D beam element is capable of describing the sectional responses and representing the non-uniform stress/strain distributions due to warping deformation of the cross-section. Although developed primarily in this work for rectangular cross-section, the model formulation in Chapter 3 is generally expressed to be applied to any arbitrary cross-section.

According to the prior discussion in the state of the art (Chapter 2), although various researches have successfully applied the Lagrange polynomial approach to the mixed-based formulation in order to take into account the warping displacement, this approach has not yet been implemented in any displacement-based model of reinforced concrete. In present work, the Lagrange polynomial approach has been completely implemented in the proposed displacement-based model, as well as a comparison with the use of Saint-Venant warping function when accounting for torsional effect. The numerical examples in Chapter 5 gave good results and showed reasonable correlations between the two approaches. Thanks to its generality, the successful implementation of Lagrange polynomials in the proposed model also offers more possibilities for further research on different cross-section shapes, such as T or L.

The satisfactory results obtained in the inelastic material domain ensured the adaptation of the Modified Compression Field Theory (MCFT) to the constitutive material model for concrete. In this PhD thesis, based on MCFT, a consistent constitutive model, suitable for the use in the 2D multi-fiber beam formulation, has been developed for reinforced concrete in case of pure torsion. The discretization of the cross-section into different regions following the stress state (i.e. 1D-zone, 2D-zone and 3D-zone) which was proposed by others researchers in literature, has been used and improved in this work. A new formulation to determinate the width of the 2D-zone has been proposed. The calibration process carried out by the author in this work, which used the *engineering* parameters in order to increase the ability to apply the proposed model in practical simulations, can also offer some ideas and recommendations to other researchers in similar studies.

The case of RC members subjected to combined shear-bending-torsion actions under non-linear geometric conditions has also been treated in the present work. A Total Lagrangian-Corotational approach has been employed for the development of beam and beam-column elements, in which an initial undeformed geometry, translated and rotated as a rigid body, was chosen as the reference configuration in the corotated frame. The formulation is based on small deformations within the corotational (natural) frame. The satisfactory results obtained through several examples from the literature showed that the corotational framework had been successfully implemented in the proposed model. Under the assumption of large displacement, the coupling between the actions due to the torsional effect was carefully developed in the local beam formulation and evaluated with the help of some numerical examples.

7.2 Perspectives

The proposed model has been developed in a general way in order to open many possibilities to extend the range of applications and studies. Several of additional developments can be suggested and some aspects of the proposed model could be more developed in future researches, such as:

- The model formulation could be extended for the case of high-strength concrete, prestressed concrete, concrete with fibers or self-compacting concrete, etc.
- The model formulation could also be extended to the case of curved and/or tapered

beam, in order to investigate the application of model in usual case of shear and torsional effects.

- The material behavior could be more developed by including the confinement effect of concrete and/or stirrups. The cyclic loading behavior of concrete and steel could also be implemented in the constitutive model.

- Regarding the calibration process, more test data can be used and other engineering parameters can be served as input, in order to develop a new, and possibly more exact formulation for the constitutive behavior law and the 2D-zone's width.

- The inclusion of distortion deformation in the model formulation could be represented with the implementation of two enhanced transversal displacements in the enhanced field.

- Concerning the warping and distortion deformations, other kinds of interpolation functions could be explored over the cross-section and along the beam axis, such as Hermite polynomials or Spline functions.

- The inclusion of Wagner term in the local formulation of corotational framework could be expressed in a more consistent and rational way, instead of using an approximate tangent operator as in the proposed model.

INSA de RENNES
Service des Formations

AVIS DU JURY SUR LA REPRODUCTION DE LA THESE SOUTENUE

Titre de la thèse:
Développement d'un modèle d'élément fini 3D pour des poutres en béton armé soumis à des sollicitations M-N-V-T

Nom Prénom de l'auteur : NGUYEN TUAN ANH

Membres du jury :
- Monsieur RAGUENEAU Frédéric
- Monsieur LE GROGNEC Philippe
- Madame COMBESCURE Christelle
- Monsieur MARTINELLI Enzo
- Monsieur KOTRONIS Panagiotis
- Monsieur NGUYEN Quang Huy

Président du jury : Panagiotis Kotronis

Date de la soutenance : 28 Novembre 2019

Reproduction de la these soutenue

☒ Thèse pouvant être reproduite en l'état
☐ Thèse pouvant être reproduite après corrections suggérées

Fait à Rennes, le 28 Novembre 2019

Signature du président de jury

Le Directeur,

M'hamed DRISSI

Résumé étendu en français

Problématique

La plupart des ouvrages de génie civil est soumise à des actions multiaxiales, incluant des efforts normaux et des efforts tangentiels. Même si les effets du cisaillement et de la torsion ont déjà été mis en œuvre dans plusieurs théories et modèles d'analyse structurelle, il manque toujours une théorie scientifique rationnelle. Afin de contribuer à ce domaine de recherche, ce travail de recherche porte sur le développement d'un modèle d'éléments finis non linéaire pour les éléments en béton armé soumis à des sollicitations complexes et en particulier la torsion.

Parmi les principales sollicitations, l'effort axial et le moment de flexion sont largement étudiés et modélisés par plusieurs modèles théoriques et numériques. Les théories d'analyse des structures sous sollicitations de cisaillement et de torsion sont également développées par plusieurs chercheurs par contre, il n'y a pas beaucoup de modèle qui considère la combinaison de toutes les types de sollicitation (traction-compression; flexion; cisaillement; et torsion). De plus, étant l'un des principales sollicitations soumises aux structures en génie civil, la torsion est souvent négligée devant les autres dans le contexte des structures en béton armé courantes. Cependant, dans certains cas particuliers, par exemple le cas dans le cadre de la tenue des balcons dans les bâtiments isolés par l'intérieur, la torsion peut jouer un rôle déterminant dans la stabilité des structures.

En effet, les règlementations thermiques en vigueur imposent de traiter le pont thermique qui se crée au niveau du plancher. Ce pont thermique perturbe la continuité de l'isolation thermique et doit être traité par un disjoncteur de pont thermique (Figure 7-1a). Dans le cadre de la tenue du balcon, la transmission du poids de plancher aux murs fait appel à la contribution du *linteau*, qui est préférablement fabriqué en acier grâce à sa légèreté afin de minimiser les éléments structuraux (Figure 7-1b). Cependant, en sachant que le rupteur du pont thermique est attaché au linteau, son efficacité peut être réduite si

le dernier est fabriqué en acier. C'est la raison pour laquelle, le linteau est conçu comme une poutre en béton armé de section rectangulaire, qui est dans un état combiné de flexion, de cisaillement et de torsion, pour laquelle les modèles théoriques et numériques sont peu nombreux dans la littérature.

(a) (b)

Figure 7-1 – (a) Rupteur du pont thermique. (b) Disposition du linteau dans le cadre de la tenue des balcons pour des bâtiments isolés par l'intérieure.

A cause des différences entre les déformations extensionnelles des fibres longitudinales dans l'élément, sous l'effet de torsion la section transversale est gauchie et sort de leur plan initial. Cette action s'appelle le gauchissement et se produit pour tout type de section transversale, excepte celui circulaire, sous chargement de torsion (Figure 7-2). Ce phénomène de gauchissement fait nier l'hypothèse de section plane en considération l'équilibre cinématique de section, de plus influence fortement sur le calcul de l'angle de torsion et des contraintes normales sous sollicitations de torsion. L'étude de ce phénomène fait donc une partie importante dans ce travail de recherches.

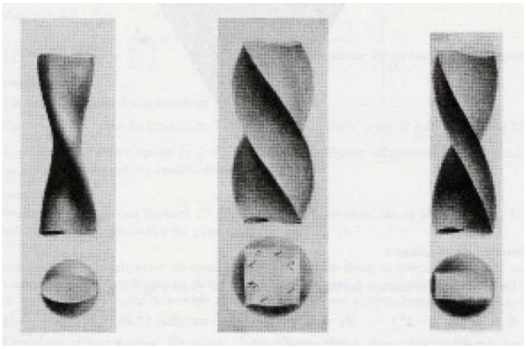

Figure 7-2 – Dessin originaux de Saint-Venant pour les poutres soumises à torsion de section elliptique, carrée et rectangulaire [97].

Objectifs

L'objectif principal de cette thèse de doctorat est de développer un modèle enrichi de poutre en éléments finis pour l'analyse non linéaire des éléments en béton armé soumis

à des sollicitations combinées: l'effort axial, la flexion, le cisaillement et la torsion. Les objectifs spécifiques sont les suivants:

- Le développement d'un élément de poutre 3D pour les éléments en BA utilisant une approche "multifibres". Dans cette étude, le modèle est développé principalement pour une section droite rectangulaire, mais la formulation est exprimée de manière générale pour tous types de sections droites arbitraires.

- L'implémentation d'un champ de déplacement enrichi dans les équations cinématiques afin d'inclure le déplacement de gauchissement de section droite sous l'effet de cisaillement et de torsion. Ensuite, une analyse numérique est réalisée pour étudier l'influence du gauchissement sur l'état de contrainte.

- L'adaptation de la théorie du champ de compression modifié (Modified Compression Field Theory – MCFT [110]) à la loi de comportement du béton.

- L'adaptation de la discrétisation de section en différentes régions selon l'état de contrainte (1D, 2D et 3D) afin de prendre en compte l'impact des armatures transversales et du confinement du béton. Une nouvelle formulation paramétrique permettant de déterminer la règle de cette discrétisation est également proposée.

- La mise en œuvre et la dérivation d'un concept général et cohérant de co-rotationnel dans la formulation 3D de poutre afin de prendre en compte la condition géométrique non linéaire.

Développement du modèle numérique pour les éléments BA

Introduction de l'élément multifibre

En utilisant l'approche transversale de section et la formulation en déplacement, un élément 3D multifibre enrichi est développé pour déterminer le comportement des membranes en BA soumis à des chargements arbitraires (cisaillement, flexion et / ou torsion). Basée sur le principe de la modélisation en éléments finis discret, l'approche de multifibres représente un équilibre parfait entre la précision des résultats, la rapidité du calcul et l'ergonomie. Il s'agit d'un système de points d'intégrations (appellé fibre) est obtenu à l'intersection des fibres longitudinales et des sections transversales sur le long d'élément

(Figure 7-3). A chaque fibre, les déformations et déplacements sont liés aux déplacements nodaux (définis comme dégrée de liberté d'un élément) par des équilibres cinématiques. Pour chaque fibre, une loi de comportement approprié est affectée afin de déterminer les contraintes à partir des déformations qui sont obtenues par la cinématique de section. Ensuite, à l'aide du Principe du Travail Virtuel et les fonctions de forme, les efforts nodaux et les matrices de rigidité au niveau d'élément sont déterminés par des calculs d'intégrations numériques.

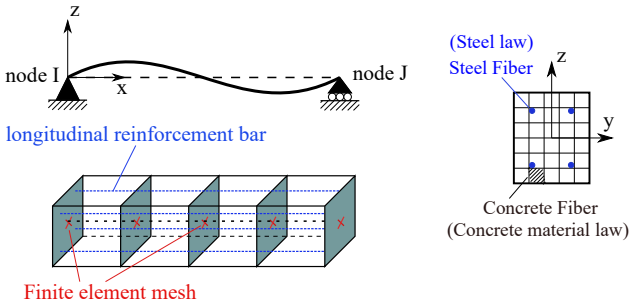

Figure 7-3 – Approache de multifibre pour les éléments en BA et des coordonées d'élément locals dans cette recherche.

Cinématique de section

La cinématique de section est basée sur l'enrichissement des hypothèses de cinématique de poutre de Timoshenko. A cause du phénomène de gauchissement, l'hypothèse de section plane devient insuffisante pour représenter la forme de déformation complète de section sous sollicitation composée de cisaillement et de torsion (Figure 7-4a). C'est la raison pour laquelle, en considérant l'équilibre cinématique d'un point matériel de la section, le champ cinématique d'un corps rigide doit être enrichi par un champ de déplacement supplémentaire (Figure 7-4b):

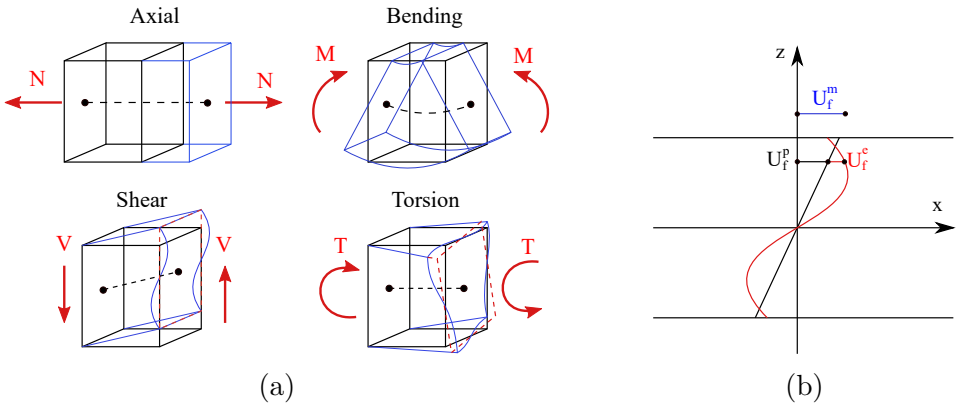

Figure 7-4 – (a) Déformation de section transversale sous efforts normaux (axiale force, flexion) et tangentiels (cisaillement, torsion). (b) Décomposition du déplacement axial d'un point matériel.

$$\mathbf{d}_f^m(x,y,z) = \mathbf{d}_f^p(x,y,z) + \mathbf{d}_f^e(x,y,z) = \begin{pmatrix} U^p(x,y,z) \\ V^p(x,y,z) \\ W^p(x,y,z) \end{pmatrix} + \begin{pmatrix} U^e(x,y,z) \\ V^e(x,y,z) \\ W^e(x,y,z) \end{pmatrix} = \begin{pmatrix} U^m(x,y,z) \\ V^m(x,y,z) \\ W^m(x,y,z) \end{pmatrix} \tag{7.1}$$

Le champ classique $\mathbf{d}_f^p(x,y,z)$ porté sous l'hypothèse de section plane dans la théorie de poutre de Timoshenko, dont la relation cinématique suivante est établie entre $\mathbf{d}_f^p(x,y,z)$ et le vecteur de déplacements généralisés $\mathbf{d}_s(x)$:

$$\left.\begin{aligned} U^p(x,y,z) &= u(x) - y\theta_z(x) + z\theta_y(x) \\ V^p(x,y,z) &= v(x) - z\theta_x(x) \\ W^p(x,y,z) &= w(x) + y\theta_x(x) \end{aligned}\right\} \quad \Rightarrow \mathbf{d}_f^p(x,y,z) = \mathbf{a}_f^p(y,z)\mathbf{d}_s(x) \tag{7.2}$$

Dans le cadre de ces travaux de recherche, deux approaches sont utilisées pour représenter le champ enrichi $\mathbf{d}_f^e(x,y,z)$, la première concernant l'application de la théorie de poutre de Saint-Venant, avec la définition de la fonction de gauchissement $\psi(y,z)$ et la distribution de gauchissement $\alpha(x)$. Dans le cas d'une section solide, $\alpha(x)$ peut prendre la valeur de la dérivation de l'angle de torsion κ_x. Par conséquence, le champ de déplacement total $\mathbf{d}_f^p(x,y,z)$ dans l'Equation (7.1) devient:

$$\begin{aligned} U^m(x,y,z) &= u(x) - y\theta_z(x) + z\theta_y(x) + \kappa_x\psi(y,z) \\ V^m(x,y,z) &= v(x) - z\theta_x(x) \\ W^m(x,y,z) &= w(x) + y\theta_x(x) \end{aligned} \tag{7.3}$$

La deuxième approche enrichie concerne l'utilisation des fonctions d'interpolation comme Lagrange pour représenter le champ enrichi. Il s'agit d'un système de points fixes créés et interpolés par des fonctions et des polynômes de Lagrange (Figure 7-5), qui conduisent à l'introduction de degrés de liberté supplémentaires à chaque section transversale (Figure 7-6). Le champ de déplacement enrichi est établi à l'aide des matrices de polynômes de Lagrange:

$$U^e(x,y,z) = \sum_{i=1}^{n_w} L_i(x)U^e(x_i,y,z) = \hat{\mathbf{L}}(x)\hat{\mathbf{S}}(y,z)\mathbf{U}^e \tag{7.4a}$$

$$V^e(x,y,z) = \sum_{i=1}^{n_w} L_i(x)V^e(x_i,y,z) = \hat{\mathbf{L}}(x)\hat{\mathbf{S}}(y,z)\mathbf{V}^e \tag{7.4b}$$

$$W^e(x,y,z) = \sum_{i=1}^{n_w} L_i(x)W^e(x_i,y,z) = \hat{\mathbf{L}}(x)\hat{\mathbf{S}}(y,z)\mathbf{W}^e \tag{7.4c}$$

où $\hat{\mathbf{L}}(x)$ est une vecteur contenant des polynômes d'interpolation 1D; $\hat{\mathbf{S}}(y,z)$ est une matrice contenant des polynômes d'interpolation 2D; $\mathbf{U}^e$, $\mathbf{V}^e$ et $\mathbf{W}^e$ sont des vecteur contenant les déplacements nodaux enrichis définis comme les dégrées de liberté supplémentaires (Figure 7-6).

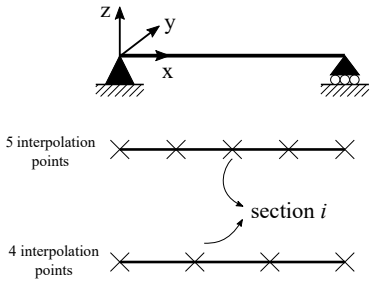

(a) Système de point d'interpolation longitudinal sur l'axe d'élément.

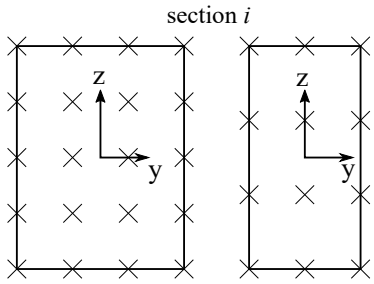

(b) Système de point d'interpolation sur la section transversale.

Figure 7-5 – System de point d'interpolation de l'élément.

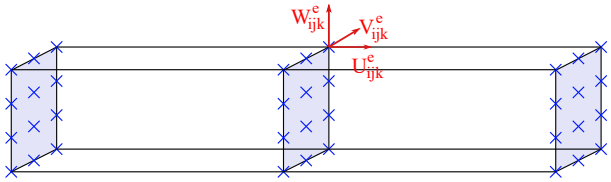

Figure 7-6 – Les déplacements enrichis définis comme les dégrées de liberté supplémentaires indépendantes.

Organigramme de formulations

La Figure 7-7 résume la formulation en déplacement pour l'élément fini multifibre selon deux approches enrichies dans le cadre de ce recherche.

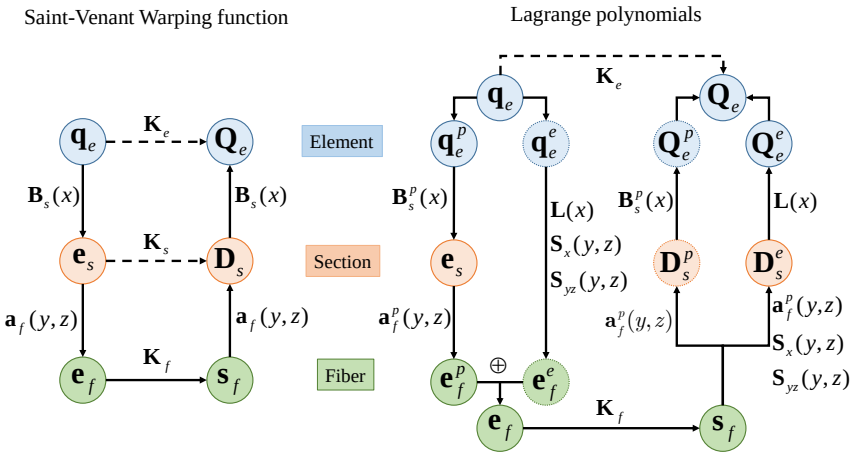

Figure 7-7 – Organigramme de la formulation en déplacement pour l'élément fini multifibre selon deux approches enrichies.

Les efforts généralisés de section $\mathbf{D}_s$ ou $\mathbf{D}_s^p$, $\mathbf{D}_s^e$ sont calculés par l'intégration numérique sur la section, tandis que les efforts nodaux d'élément $\mathbf{Q}_e$ ou $\mathbf{Q}_e^p$, $\mathbf{Q}_e^e$ sont déterminés selon la méthode de quadrature de Gauss-Lobatto. La formulation du modèle est programmée en Matlab grâce à son compétence en manipulant des matrices.

Modèle pour le comportement de l'élément en béton armé

Dans la formulation en déplacement de l'élément fini multifibre, le calcul à l'échelle fibre (ou point d'intégration) concernant la relation constitutive entre les contraintes-déformations demande une équation constitutive adéquat et une loi de comportement appropriée. Dans cette thèse, le modèle développé doit être capable de représenter les effets typiques du membrane en BA, comme la fissuration, l'effet de raidissement de contraintes (stress-stiffening effect) ou l'effet adoucissant de compression (compression softening effect). C'est la raison pour laquelle, le modèle proposé est basé sur la théorie modifiée du champ de compression by Vecchio [110] (Modified Compression Field Theory - MCFT). Dans cette théorie, l'idée principale est de remplacer la loi de comportement biaxiale du béton par une loi de comportement uniaxiale, dans laquelle la relation contrainte-déformation est formulée dans la direction principale de fissure du béton. L'hypothèse principale est la coincidence des directions principales des contraintes et des déformations. Les équation d'équilibre et de compatibilité sont évaluées par la valeur moyenne de contrainte et de déformation dans le plan de fissures, tandis que la contribution du béton et de l'acier peut être ajoutée séparément dans l'expression de contrainte totale et dans la matrice de rigidité (Figure 7-8).

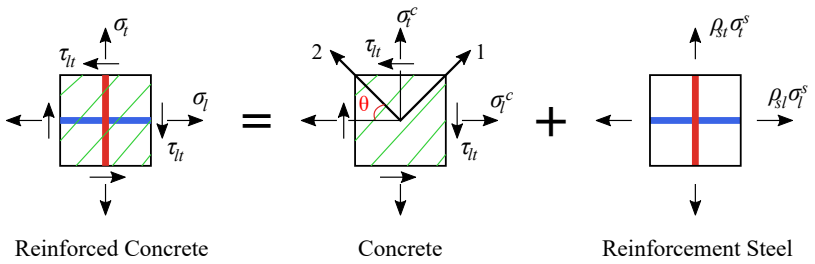

Figure 7-8 – Composition de contrainte pour l'élément BA selon la théorie de MCFT [110].

Dans le cadre de ce travail de recherche, le comportement uniaxial du béton selon la direction principale est celui proposé dans la théorie originale de Vecchio [110] (Figure 7-9). Cependant, d'autres relations peuvent être empruntées pour exploiter la recherche.

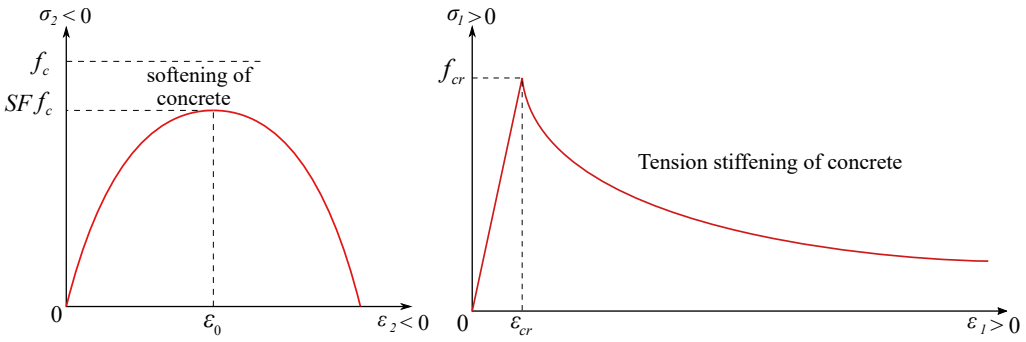

(a) En compression [110] (b) En traction

Figure 7-9 – Comportement uniaxial du béton dans la direction principale.

Dans l'approche multifibre pour des éléments en béton armé, la prise en compte de la contribution des armatures transversales dans la résistance et la rigidité est loin d'être simple. Comme montré sur la figure 7-3, alors que le béton et l'armature longitudinale sont répartis longitudinalement dans l'élément, la distribution des armatures transversalles est interrompue dans cette direction par un espacement s. Pour cela, basé sur l'idée de Navarro-Gregori [76], la section transversale est discrétisée en plusieurs régions selon son comportement matériel et de son état de contrainte (Figure 7-10a):

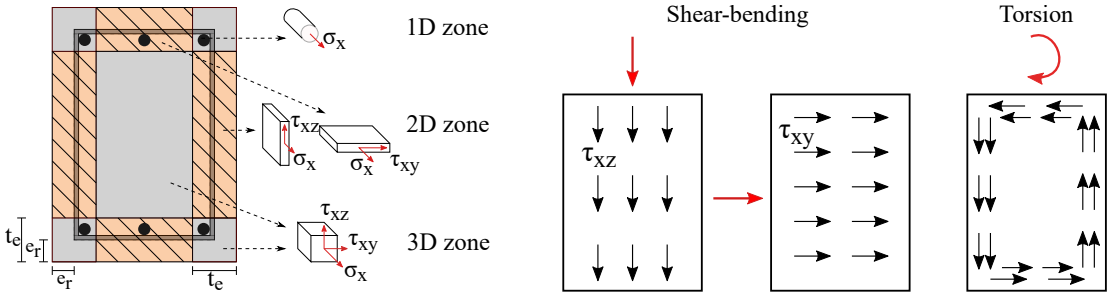

Figure 7-10 – (a) Discrétisation de la section selon l'état de contrainte dans le modèle de Navarro-Gregori et al. [76]. (b) Directions de contrainte de cisaillement sous les effets de flexion-cisaillement et de torsion.

- Zone 1D: cette zone ne contient que les armatures longitudinales, où l'on fait l'hypothèse que la contrainte normale dans la direction des armatures est la seul contrainte à tenir en compte. La loi de comportement appliqué dans cette zone est celle de l'acier.

- Zone 2D: cette zone est définie par la région où se trouve les armatures transversales dans une seule direction et le béton l'entouré. Dans cette zone, sous les effets de cisaillement, de flexion ou de torsion, la direction de contrainte normale dans les étriers coïncide à celle dans le béton (τ_{xz} dans la zone verticale ou τ_{xy} dans la zone horizontale) (Figure 7-10b). Par conséquent, à chaque fibre, on ne considère que

l'état des contraintes planes avec deux composants: une normale et une transversale. La prise en compte des effets des armatures transversales est réalisée par un processus d'itération satisfaisant l'équilibre interne entre le béton et les armatures transversales. La loi de comportement est celle de la théorie de MCFT [110].

- Zone 3D: où se trouvent les armatures transversales en deux directions et dans le noyau en béton de la section, cette zone est définie avec un état de contrainte complet : une normale et deux cisaillements, dans chaque fibre. Le modèle de comportement appliqué est une extension de la théorie de MCFT pour l'élément fini 3D [112]. Dans cette zone, ainsi que dans la zone 2D, l'équilibre interne et le couplage des efforts sont assurée par des condensations statiques de contrainte dans chaque fibre.

Modélisation numérique des éléments BA soumis à des sollicitations complexes

Un exemple évalué par Le Corvec [62] dans sa thèse est étudié ci-dessous afin de valider le modèle EF développé dans la régime de matériaux élastiques: une poutre cantilever de section mince soumise à l'effort de flexion-cisaillement (Figure 7-11). Les valeurs des déplacements à l'extrémité de la poutre, obtenue par les deux approaches enrichies, sont montrées dans le Tableau 7.1 et comparées aux solutions analytiques et aux résultats numériques de Le Corvec. Les résultats numériques donnés par le modèle proposé sont satisfaisant, et les différences entre deux approches enrichies ne sont pas importantes.

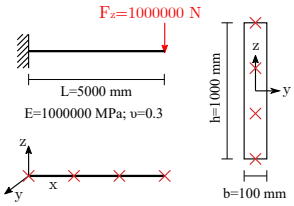

Figure 7-11 – Système des points d'interpolation dans l'exemple de Le Corvec [62].

Table 7.1 – Déplacement à l'extrémité d'une poutre cantilever de section rectangulaire sous l'effet de flexion-cisaillement - Exemple de Le Corvec [62].

	Théorie de Timoshenko	Modèle de Le Corvec	Maillage	Modèle Proposé	
				Théorie de Saint-Venant	Polynôme de Lagrange
Déplacement à l'extrémité (mm)	-5.156	-5.156	10×1	-5.206	-5.207
			50×5	-5.158	-5.158
			100×10	-5.157	-5.157
			200×20	-5.156	-5.156

Pour rappel, sous l'effet de flexion-cisaillement, l'approche enrichie des polynômes de Lagrange génère un champ de déplacement axial supplémentaire. Par conséquence, la section droite se gauchit et ne peut pas conserver sa forme plane. Ce déplacement de gauchissement sous l'effet de flexion-cisaillement est présenté à la Figure 7-12a. On peut observer que la forme parabolique est le résultat des polynômes d'interpolation cubique sur la section droite. Cependant, la magnitude de ce champ enrichi est très faible en comparant à celle du champ classique. Cela dit que le champ de déplacement total est donc peu influencé et conserve sa forme plane (Figure 7-12b). Les impacts sur les déformations et les contraintes sont donc limités et par conséquent, il n'y a pas de différence entre les valeurs de déplacement à l'extrémité dans le Tableau 7.1.

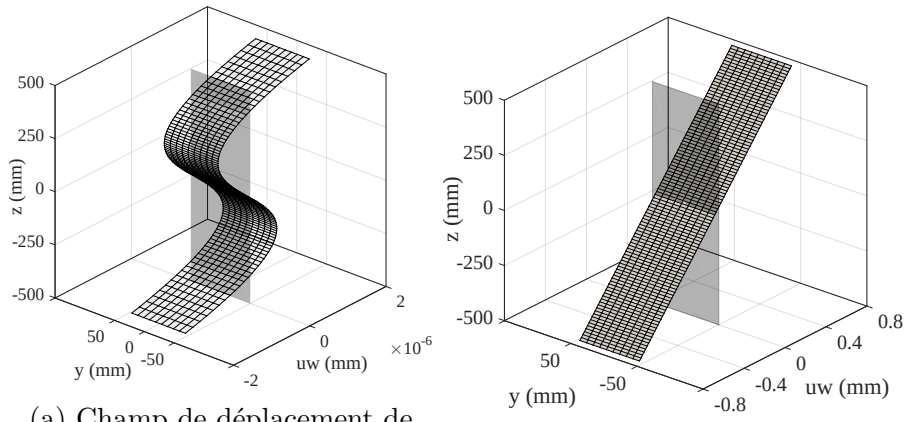

(a) Champ de déplacement de gauchissement.

(b) Champ de déplacement total.

Figure 7-12 – Distribution du champ de déplacement sur la section droite à l'extrémité de poutre sous l'effet de flexion-cisaillement.

L'intéraction des efforts flexion-torsion est évaluée en étudiant la simulation numérique quelques spécimens dans le test expérimental de McMullen & Warwaruk [72]. Les diagrammes d'intéraction de flexion-torsion concernant les résultats numériques des valuers ultimes de moment fléchissant et de moment de torsion sont montrés sur la Figure 7-13 et comparés aux solutions analytiques obtenue par la théorie de Skew-bending proposée par

Collins et al. [23, 24]. D'après cette théorie, pour une poutre en BA de section symétrique, il existe 2 modes de rupture: rupture par flexion, rupture par torsion. Dans le cas de section asymétrique, il existe une 3ème mode accompagné par des initiations de fissures sur la surface haut de poutre. On peut observer à la Figure 7-13 concernant les résultats de deux groupes de section asymétrique et symétrique, en comparant aux résulats expérimentaux, les solutions analytiques sont toujours conservatives tandis que les résultats numériques donnés par le modèle proposé sont au meilleurs corrélations, notamment au voisinage des transitions entre 3 modes de défaillance.

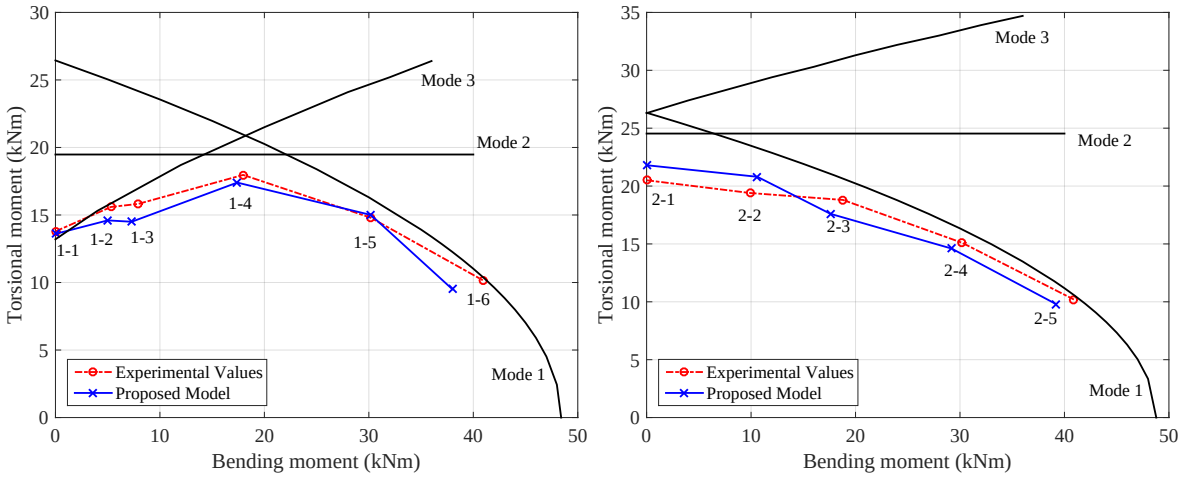

(a) Groupe 1: section droite asymétrique. (b) Groupe 2: section droite symétrique.

Figure 7-13 – Diagramme d'intéraction entre flexion-torsion dans le test de McMullen & Warwaruk's [72].

En effectuant une simulation numérique pour une poutre cantilever en BA soumise à combinaison de flexion-torsion à l'extrémité, l'impact des armatures transversales sur la résistance en flexion-torsion est étudié et représenté sur la Figure 7-14. Sur cette figure, différents diagrammes d'intéraction sont établis pour différents valuers d'espacements d'étries. Comme on peut le constater, lorsque la torsion est faible par rapport à la flexion, par exemple R = 0,25, la densité de l'étrier n'a logiquement presque aucun effet. L'effet de l'étrier sur la résistance des éléments devient plus important lorsque la torsion domine la flexion. En cas de torsion pure, on peut constater que la résistance à la torsion augmente d'environ 34 % avec une augmentation de 8 fois de la densité de l'étrier. Cette application numérique met en évidence le fait que la formulation EF proposée prend en compte les armatures transversales dans la prédiction de la résistance à la torsion des éléments BA.

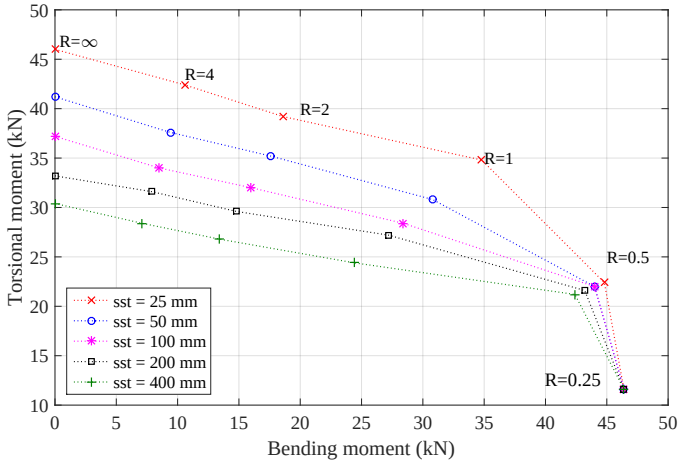

Figure 7-14 – Diagramme d'intéraction de flexion-torsion en fonction d'espacement des étriers.

L'intéraction entre flexion-cisaillement-torsion est aussi étudiée dans la simulation numérique concernant le test expérimental des poutres en BA soumise aux effets de flexion-cisaillement-torsion de McMullen & Warwaruk [72]. Pour le Groupe 7, le diagramme d'intéraction de flexion-torsion est présenté à la Figure 7-15a avec un bon niveau de corrélation entre les résultats numériques et ceux expérimentaux. Concernant le diagramme d'intéraction de cisaillement-torsion (Figure 7-15b), les résultats donnés par la théorie de Skew-bending et par le modèle proposé sont en bon accord avec l'expérimentation. De la même manière que les autres courbes d'interaction flexion-torsion et cisaillement-torsion présentées ci-dessus, les solutions analytiques sont plutôt conservatrices. Cette remarque correspond à l'observation de Hsu [46] selon laquelle la théorie de skez-bending surestime considérablement la résistance à la torsion pure des membres BA.

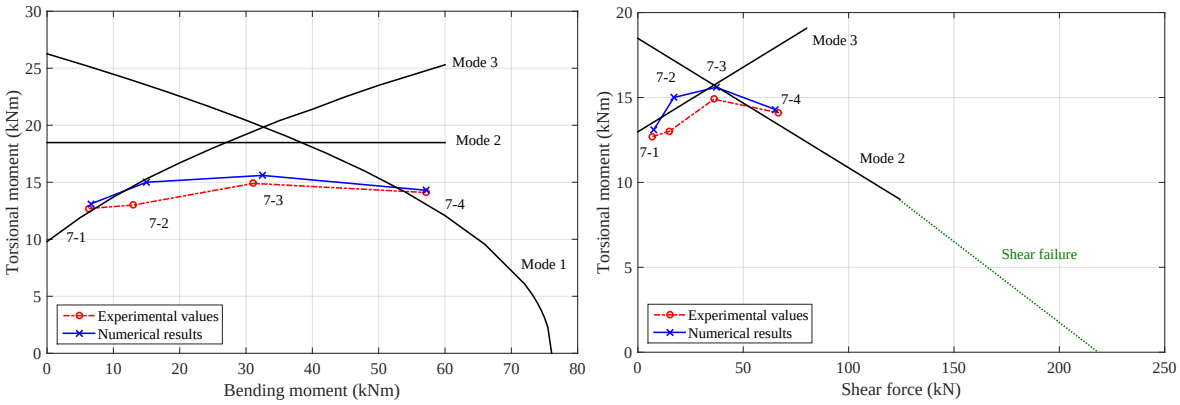

(a) Intéraction de flexion-torsion (b) Intéraction de cisaillement-torsion

Figure 7-15 – Diagramme d'intéraction du Groupe 7 dans le test de McMullen & Warwaruk [72].

Les éléments BA soumis à la torsion pure

Modèle constitutif proposé pour le béton

Sous l'effet de torsion pure, en utilisant la théorie de MCFT comme le modèle constitutif du béton, la valeur numériques du moment de torsion à la fissuration est réduite environ la moitié des valeurs expérimentales. Cela est expliqué par le fait que dans la théorie de MCFT, la relation en traction est basée sur des tests expérimentaux de panneaux soumis à l'effet de cisaillement, donc pas vraiment adapté au comportement en torsion. Une modification du comportement en traction est donc nécessaire.

De plus, une deuxième remarque pour le modèle constitutif du béton à torsion pure est à retirer en regardant sur le comportement du membrane BA soumis à torsion pure, qui est divisé en 2 phases différentes:

- Avant fissuration, la réponse de la section est considérée comme élastique et le comportement est très similaire à celui d'un élément en béton pure, ce qui peut être prédit par la théorie de la torsion de Saint-Venant.

- Après fissuration, le matériau n'est plus continu, la théorie de l'élasticité devient inutile et un nouveau mécanisme est nécessaire pour interpréter la réponse en torsion dans cette phase. A partir du concept de treillis [93] et des résultats des tests expérimentaux de Hsu [45] et de Onsongo [82], on peut supposer que le comportement d'éléments BA après fissuration est considéré comme un tube de section creuse.

Ce comportement spécial conduit à la deuxième modification du modèle mécanique pour les éléments BA en torsion pure: le comportement de la zone 3D du béton dans le noyau de section est mis à zéro après la fissuration. La réponse en torsion non linéaire après la fissuration dépend donc uniquement du comportement de la zone 2D et de la zone 3D aux quatre coins de la section, et la largeur de la zone 2D, appelée *épaisseur effective*, joue un rôle déterminant.

Une troisième remarque aussi importante est l'impact de la distribution des armatures longitudinales dans la section sur la résistance en torsion pure du membre en BA. En effet, d'après l'analyse des tests expérimentaux par Hsu [45], pour les éléments en BA, la valeur à la fissuration du moment de torsion est en fonction du pourcentage total des armatures. De plus, Hsu a remarqué également qu'une meilleure répartition (ou distribution) des armatures longitudinales sur la section augmenterait légèrement le moment de torsion à

la fissuration: c'est le cas des poutres G6, G7 et G8 dans lesquelles les barres longitudinales sont également situées au centre de la section (Figure 7-16).

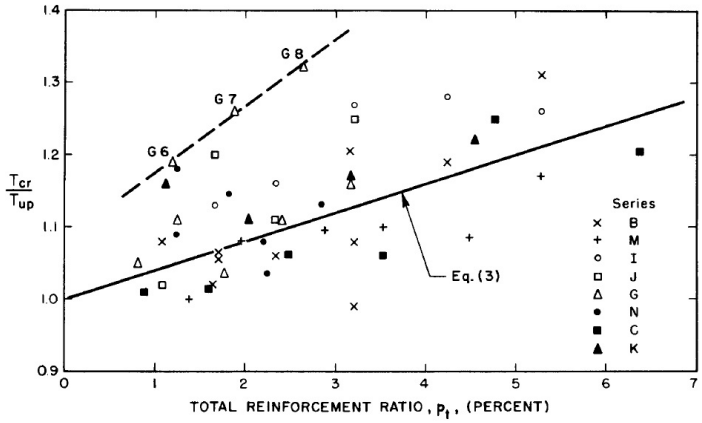

Figure 7-16 – Moment de torsion à la fissuration en fonction des pourcentages totals des armatures dans le test de Hsu (1963) [45].

A partir de ces trois remarques ci-dessus, en faisant une étude paramétrique et une calibration sur plusieurs tests expérimentaux en torsion (par Hsu [45], par Csikos & Hegedus [29] et par Lee et al. [63]), basée sur l'idée de Jeng & Hsu [53], une nouvelle loi de comportement en traction est proposée (Figure 7-18):

- Pour le module élastique:

$$E_{cr} = 5620\sqrt{f_c} \quad (f_c \text{ in MPa}) \tag{7.5}$$

dont f_c est la résistance en compression du béton, 5620 est un coefficient calibré par Jeng & Hsu [53].

- Pour la résistance en traction à la fissuration du béton, il existe deux formulation correspondant à deux cas différents de distribution des armatures longitudinales dans la section:

Pour une distribution habituelle (Figure 7-17a)

$$f_{cr} = f_{cr}^{PC}\left(0.38\frac{b}{h}\rho_s + 1\right) \tag{7.6}$$

Pour une distribution avec des barres additionnelles sur le long du périmètre (Figure 7-17b):

$$f_{cr} = f_{cr}^{PC}\left(0.22\frac{b}{h}\rho_s + 1.3\right) \tag{7.7}$$

où f_{cr}^{PC} est la résistance en traction à la fissuration d'un member en béton pure, b est la largeur et h la hauteur de la section, ρ_s est le pourcentage total des armatures.

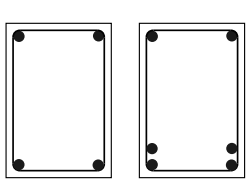

(a) Distribution habituelle.

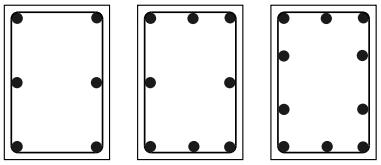

(b) Distribution avec des barres additionnelles sur le long du périmètre.

Figure 7-17 – Deux cas de distribution des armatures longitudinales.

- Pour la déformation à la fissuration:

$$\varepsilon_{cr} = \frac{f_{cr}}{E_{cr}} \tag{7.8}$$

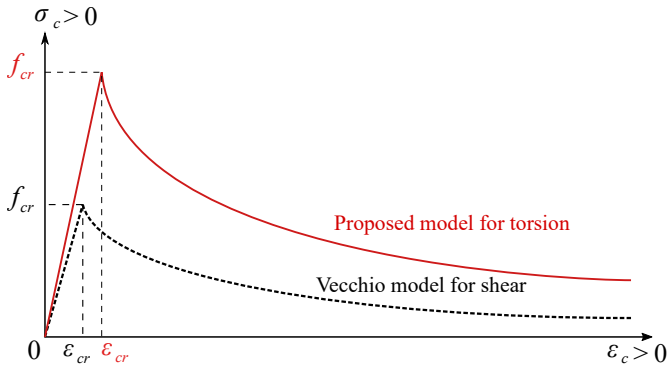

Figure 7-18 – La relation en traction proposée pour la torsion en comparée à celle dans la théorie de MCFT par Vecchio [110].

Des formulations paramétriques pour déterminer l'épaisseur effective de la zone 2D sont également proposées grâce à la procédure de calibration mentionnée ci-dessus:

- Pour une distribution habituelle:

$$t_e = b\left(0.0130\frac{h}{b}m\rho_s + 0.1\right) \tag{7.9}$$

- Pour une distribution avec des barres additionnelles sur le long du périmètre:

$$t_e = b\left(0.0088\frac{h}{b}m\rho_s + 0.1\right) \tag{7.10}$$

b est la largeur et h la hauteur de la section; m est le ratio entre le pourcentage des armatures longitudinales et transversales; ρ_s est le pourcentage total des armatures.

Résultats numériques

Dans le régime de matériaux élastique, les résultats numériques obtenus par le modèle proposé sont comparés aux formulations théoriques et aux résultats d'autres modèles. Une poutre cantilever soumise à une torsion pure à l'extrémité, qui a également été simulée par Le Corvec dans sa thèse de doctorat [62], est étudiée (Figure 7-19a). Les résultats numériques pour l'angle de torsion à l'extrémité de la poutre calculés par le modèle de Le Corvec et le modèle proposé (selon deux approches enrichies) sont donnés dans le Tableau 7.2. Bonnes corrélations sont obtenues et de plus, cela confirme que le fait de négliger l'effet du gauchissement peut provoquer une forte influence sur la valeur de l'angle de torsion. Le profil de gauchissement de la section est représenté dans la Figure 7-19b. Cela donne une bonne illustration du phénomène: sous l'effet de torsion, les sections se gauchissent et sortent de leur propre plan. En conséquence, la rigidité de la section est modifiée et la déformation en torsion est fortement influencée.

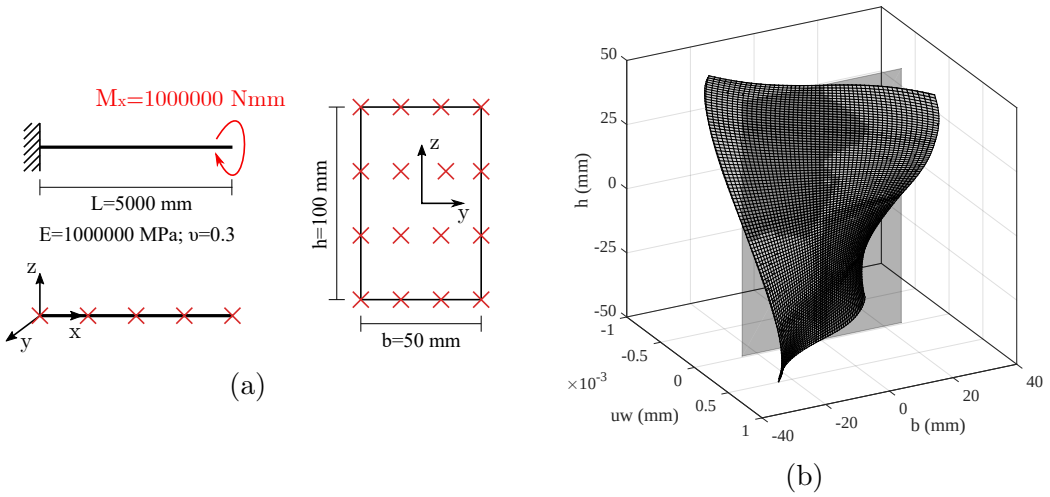

Figure 7-19 – (a) Poutre cantilever soumise à la torsion pure et système de points d'interpolation.; (b) Gauchissement de la section droite soumise à la torsion.

Table 7.2 – End twist angle for cantilever beam under mid span torque

	Théorie	Modèle de Le Corvec	Modèle Proposé		
			Sans gauchissement	Théorie de Saint-Venant	Polynôme de Lagrange
Angle de torsion (10^{-3} rad)	4.548	4.554	2.496	4.550	4.566
Erreur relative (%)		0.13	45.11	0.04	0.39
Temps de calcul (seconde)			9	9	18

La courbe moment de torsion - angle de torsion linéaire obtenue par le modèle proposé est comparée aux résultats expérimentaux des spécimens M2 et M3 dans le test

de Hsu (Figure 7-20), avec et sans les modifications proposées pour le comportement en traction du béton. Un très bon accord a été obtenu entre les résultats expérimentaux et numériques: le moment de torsion ultime et à la fissuration ont des mêmes amplitudes, les pentes aux phases post-fissuration sont quasiment identiques et le plateau horizontal caractéristique manifestant par la transition entre les deux phases avant et après la fissuration est bien représenté. De plus, nous pouvons constater que, sans la modification proposée du comportement en traction, le moment de torsion à fissuration est environ la moitié de celui du test expérimental et, par conséquent, la courbe moment de torsion - angle de torsion linéaire ne peut pas être similaire à celle expérimentale.

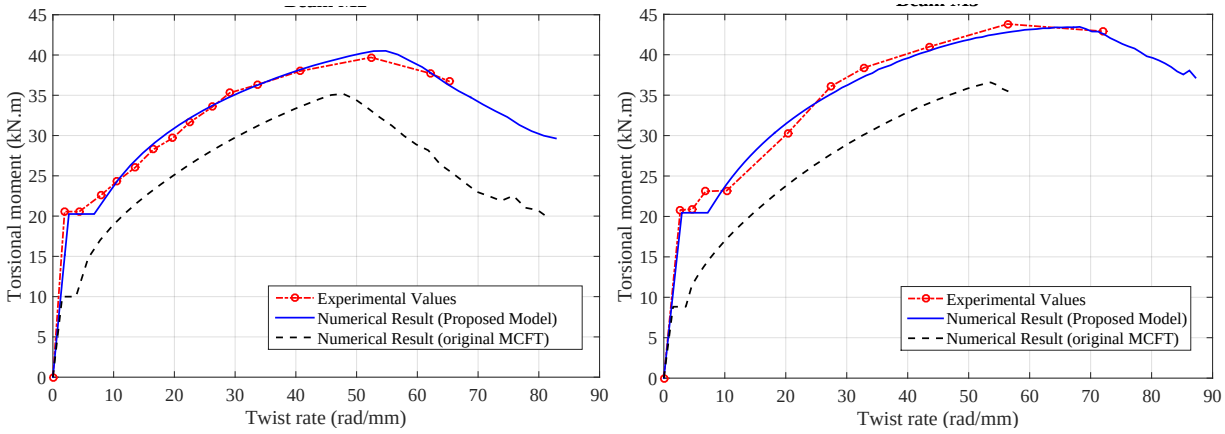

(a) Beam M2 (b) Beam M3

Figure 7-20 – Courbe moment de torsion - angle de torsion linéaire pour deux spécimens M2 et M3 dans le test de Hsu [45].

Un bon niveau de prédiction du moment de torsion ultime et de la rigidité post-fissuration est aussi atteints dans la simulation numérique du test de Lee et al. [63] (Figure 7-21).

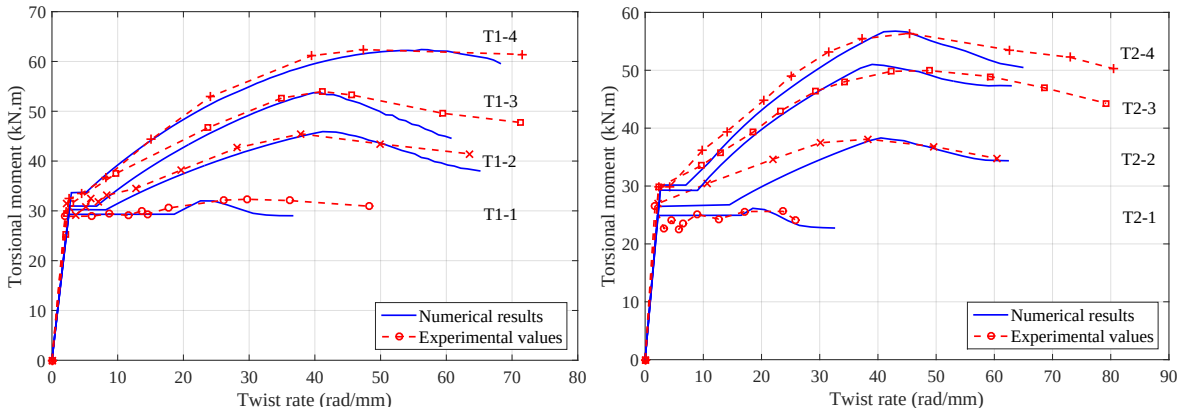

(a) Series T1 (b) Series T2

Figure 7-21 – Courbe moment de torsion - angle de torsion linéaire pour la série T dans le test de Lee et al.'s. [63]

Développemnt de formulation proposée dans les conditions géométriques non linéaire

Le cas d'éléments BA soumis à des actions combinées cisaillement-flexion-torsion dans des conditions géométriques non linéaires a également été traité dans ce travail de recherche. Une approche totale Lagrangienne-Corotationnelle a été utilisée pour développer des éléments de poutre, dans laquelle une géométrie initiale non déformée, translation et tournée en tant que corps rigide, a été choisie comme la configuration de référence dans le concept de co-rotationnelle. La formulation est basée sur de petites déformations dans le concept de co-rotationnelle (ou de naturel). Au niveau local, sous l'effet de torsion, un term non-linéaire, appelé terme de Wagner, génère la non linéarité et doit être pris en compte. Des couplages entre des efforts de flexion-cisallement-torsion sont aussi à considérer et développer dans le formulation locale.

Une poutre cantilever de section solide, qui a été utilisée dans la thèse de Battini [3], est simulée pour étudier le cas de torsion pure en grand déplacement. La Figure 7-22 présente les courbes du moment de torsion en fonction de l'angle de torsion à l'extrémité. Comparés à la solution analytique basée sur la théorie de poutre de Vlasov [113] et au modèle numérique du modèle de Battini, les résultats obtenus par le modèle proposé, en tenant compte de la contribution du terme de Wagner, montrent une très bonne corrélation. On peut constater que, bien que simulé dans le domaine des matériaux élastiques, la relation entre le moment de torsion et l'angle de torsion n'était plus linéaire, en raison de la non-linéarité géométrique provoquée par l'introduction du terme de Wagner. Il est évident que, sans prendre en compte le terme de Wagner, le modèle est considéré comme un modèle de géométrie linéaire qui donne une réponse purement linéaire.

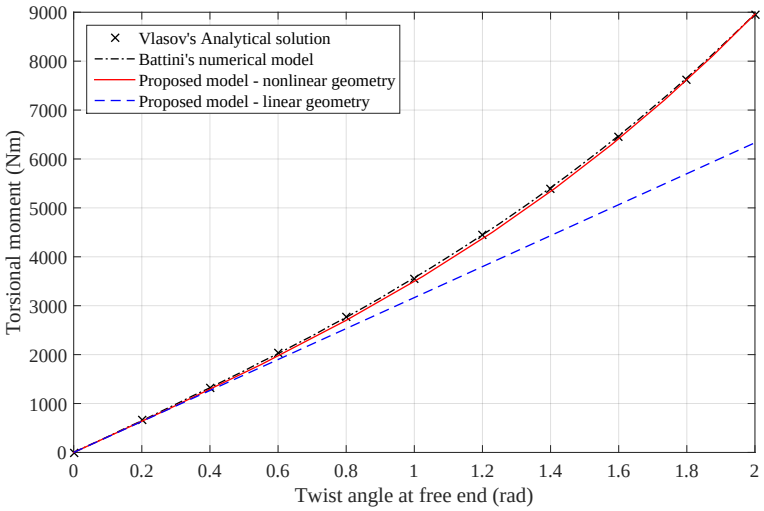

Figure 7-22 – La réponse de torsion dans la condition géométrique non linéaire.

Dans le cas d'une poutre d'appui simple en BA, le spécimen G5 est simulé avec la nouvelle formulation en grand déplacement. Aucune différence significative entre le modèle géométrique linéaire et non linéaire n'a pu être observée dans le diagramme de moment de torsion - angle de torsion linéaire sur la Figure 7-23. En utilisant une approche de simulation par déplacement imposé, le moment de torsion à la fissuration est atteint à 2,5 mrad/m, ce qui correspond à la même valeur de 29,26 kN dans les deux modèles. Aucune différence n'a donc été constatée entre les deux modèles dans la phase précédant de la fissuration du béton. Dans la phase après la fissuration, le moment de torsion ultime a été atteint à 55 mm pour les deux modèles et a donné une valeur de 73,51 kN pour le modèle linéaire et de 73,55 kN pour le modèle non linéaire. Seulement une différence relative très mineure de 0,05 % a été enregistrée.

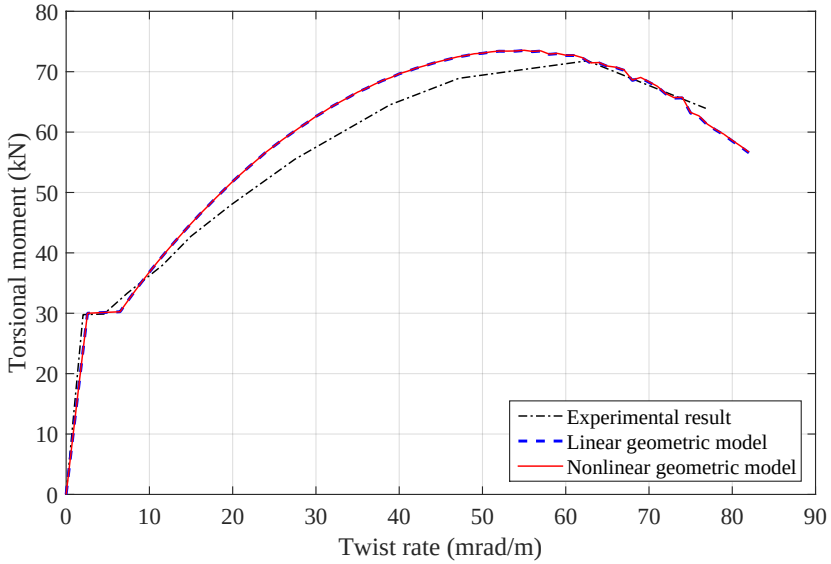

Figure 7-23 – Courbe de moment de torsion - angle de torsion linéaire du spécimen G5 sous l'effet de torsion simulée par le modèle de conditions géométriques linéaire et non linéaire.

Conclusions

Dans cette thèse de doctorat, en utilisant une approche multifibre et d'analyse de section, un élément fini 3D est développé pour les éléments en BA soumis à des sollicitations combinées M-N-V-T. Ce modèle est capable de prendre en compte les non linéarités géométriques et matérielles, le phénomène de gauchissement de la section droite, et la contribution des armatures transversales.

De plus, l'approche enrichie de polynôme de Lagrange a été complètement mise en œuvre dans le modèle proposé utilisant la formulation en déplacement, ainsi qu'une comparaison avec l'approche enrichie de la théorie de Saint-Venant pour la prise en compte de l'effet de torsion. Les exemples numériques ont donné de bons résultats et ont montré des corrélations raisonnables entre les deux approches. Grâce à sa généralité, la mise en œuvre réussie des polynômes de Lagrange dans le modèle proposé offre également davantage de possibilités pour des recherches plus approfondies sur différentes formes de sections, telles que T ou L.

Les résultats satisfaisants obtenus dans le domaine des matériaux non linéaire ont permis l'adaptation de la théorie de MCFT au modèle de comportement du béton dans la formulation proposée. Dans cette thèse de doctorat, basée sur la MCFT, un modèle constitutif cohérent, adapté à une utilisation dans la formulation de poutre multifibres 2D, a été développé pour l'élément BA en cas de torsion pure. La discrétisation de la

section droite en différentes régions selon l'état de contrainte (c'est-à-dire zone 1D, zone 2D et zone 3D), proposée par d'autres chercheurs, a été utilisée et améliorée dans ce travail. Une nouvelle formulation permettant de déterminer l'épaisseur effective de la zone 2D a été également proposée. Le processus de calibration effectué par l'auteur dans ce travail, qui utilisait les paramètres d'*ingénierie* pour augmenter la capacité à appliquer le modèle proposé dans des simulations pratiques, peut également offrir des idées et des recommandations à d'autres chercheurs dans des études similaires.

Le cas d'éléments BA soumis à des sollicitations combinées cisaillement-flexion-torsion dans des conditions géométriques non linéaires a également été traité dans le présent travail. Une approche co-rotationel a été utilisée pour développer des éléments de poutre. Les résultats satisfaisants obtenus à travers plusieurs exemples dans la littérature ont montré que le concept de co-rotationel avait été mis en œuvre avec succès dans le modèle proposé.

Bibliography

[1] ACI Committee 318. *Building code requirements for reinforced concrete (ACI 318-95) and commentary (ACI318 R-95)*. Detroit, Mich. : American Concrete Institute, 1995. Index.

[2] D. Addessi and P. Di Re. A 3d mixed frame element with multi-axial coupling for thin-walled structures with damage. *Frattura ed Integrita Strutturale*, 8:178–195, 07 2014.

[3] J. M. Bairan. *A Non-linear Coupled Model for the Analysis of Reinforced Concrete Sections under Bending, Shear, Torsion and Axial Forces*. PhD thesis, Departament d'Enginyeria de la Construcciniversitat Politica de Catalunya, Espa005.

[4] J. Bairnd A. Mari. Multiaxial-coupled analysis of rc cross-sections subjected to combined forces. *Engineering Structures*, 29:1722–1738, 08 2007.

[5] J-M. Battini. *Co-rotational beam elements in instability problems*. PhD thesis, Royal Institute of Technology, Stockholm, Sewden, 2002.

[6] J-M. Battini and C. Pacoste. Co-rotational beam elements with warping effects in stability problems. *Computer Methods in Applied Mechanics and Engineering*, 191:1755–1789, 02 2002.

[7] T. Baumann. Zur frage der netzbewehrung von flachentragwerken. *Der Bauingenieur*, 46(6):367–377, 1972.

[8] A. Belarbi and T. T. C. Hsu. Constitutive laws of concrete in tension and reinforcing bars stiffened by concrete. *ACI Structural Journal*, 91(4):465–474, 1995.

[9] A. Belarbi and T. T. C. Hsu. Constitutive laws of softened concrete in biaxial tension-compression. *ACI Structural Journal*, 92(5):562–573, 1995.

[10] T. Belytschko, J. Fish, and B. E. Engelman. A finite element with embedded localization zones. *Computer Methods in Applied Mechanics and Engineering*, 70:59–89, 1988.

[11] S.U. Benscoter. Theory of torsion bending for multicell beams. *American Society of Mechanical Engineers - Transactions - Journal of Applied Mechanics*, 21(1):25–34, 1954.

[12] E. C. Bentz. *Sectional Analysis of Reinforced Concrete Members*. PhD thesis, University of Toronto, Toronto, Canada., 2000.

[13] E.C. Bentz. Explaining the riddle of tension stiffening models for shear panel experiments. *ASCE Journal of Structural Engineering*, 131(9):1422–1425, 2005.

[14] B. Bresler and A. C. Scordelis. Shear strength of reinforced concrete beams. *J. Am. Concr. Inst.*,, 60(1):51–72, 1963.

[15] S. Capdevielle. *Introduction du gauchissement dans les ments finis multifibres pour la modsation non linre des structures en bn arm* . PhD thesis, Universit Grenoble Alpes, 2016.

[16] S. Capdevielle, S. Grange, F. Dufour, and C. Desprez. A multifiber beam model coupling torsional warping and damage for reinforced concrete structures. *European Journal of Environmental and Civil Engineering*, pages 1–22, 09 2015.

[17] CEB-FIP. *Model Code for Concrete Structures*. CEB-FIP International Recommendations, third edition, Comite Euro-International du Beton, 1973.

[18] P. Ceresa, L. Petrini, R. Pinho, and R. Sousa. A fibre flexureshear model for seismic analysis of rc-framed structures. *Earthquake Engineering and Structural Dynamics*, 38:565 – 586, 04 2009.

[19] V. Cervenka. Constitutive model for cracked reinforced concrete. *ACI Structural Journal*, 82(6):877–882, 1985.

[20] E.C. Chan. *Nonlinear Geometric, Material and Time-dependent Analysis of Reinforced Concrete Shells with Edge Beams*. PhD thesis, University of California, Berkeley, 1982.

[21] R. W. Clough. *Effect of Stiffness Degradation on Earthquake Ductility Requirements*. Report (University of California, Berkeley. Dept. of Civil Engineering). Structural Engineering Laboratory, University of California, 1966.

[22] M. P. Collins. Torque-twist characteristics of reinforced concrete beams. In *Inelasticity and non-linearity in structural concrete*, pages 211–232. Study No. 8, University of Waterloo Press, Waterloo, Ontario, Canada, 1973.

[23] M. P. Collins, Walsh P. F., Archer F. E., and Hall A. S. Reinforced concrete beams subjected to combined torsion, bending and shear. Technical report, UNICIV Report, No. R-14, University of New South Wales, 1965.

[24] M. P. Collins, Walsh P. F., Archer F. E., and Hall A. S. Ultimate strength of reinforced concrete beams subjected to combined torsion and bending. In *Torsion of Structural Concrete*, pages 279–402. American Concrete Institute, Detroit, 1968.

[25] M. P. Collins and D. Mitchell. Shear and torsion design of prestressed and non-prestressed concrete beam. *PCI Journal*, 25(5):32–100, 1980.

[26] M. P. Collins and D. Mitchell. *Prestressed Concrete Basics*. Canadian Prestressed Concrete Institute; Ottawa, ON, Canada, 1987.

[27] C. A. Coulomb. Recherches thiques et expmentales sur la force de torsion et sur l'sticite des fils de metal. *Histoire de l'Acade royale des sciences*, 1784.

[28] H. J. Cowan. An elastic theory for the torsional strength of rectangular reinforced concrete beams. *Magazine of Concrete Research*, 2:3–8, 07 1950.

[29] A. Csikos and I. Hegedus. Torsion of reinforced concrete beams. *2nd International PhD Symposium in Civil Engineering, Budapest*, 1998.

[30] P. Di Re. *3D beam-column finite elements under tri-axial stress-strain states: non-uniform shear stress distribution and warping*. PhD thesis, Sapienza Universit Roma, Italy, 2017.

[31] P. Di Re and D. Addessi. A mixed 3d corotational beam with cross-section warping for the analysis of damaging structures under large displacements. *Meccanica*, 53, 09 2017.

[32] A. Duleau. Essai thique et expmentale sur la rstance du fer forg*journal*, 1820.

[33] E. N. Dvorkin, A. M. Cuitino, and G. Gioia. Finite elements with dispacement interpolated embedded localization lines insensitive to mesh size and distortions. *International Journal for Numerical Methods in Engineering*, 30:541–564, 1990.

[34] L. Elfgren. *Reinforced concrete beams loaded in combined torsion, bending and shear : a study of the ultimate load-carrying capacity*. PhD thesis, Chalmers University of Technology, Goteborg, Sweden, 1971.

[35] L. Elfgren, I. Karlsson, and Losberg A. Torsion-bending-shear interaction for concrete beams. *Journal of the Structural Division*, 100(ST 8):1657–1676, 1974.

[36] Auricchio F. Nonlinear finite element analysis. Class notes, ROSE School, Pavia, Italy, 2003.

[37] R. Faria, J. Oliver, and M. Cervera. Modeling material failure in concrete structures under cyclic actions. *Journal of Structural Engineering*, 130:1997–2005, 2005.

[38] Z. Friedman and J. Kosmatka. An improved two-node timoshenko beam finite element. *Computeurs and Structures*, 47:473–481, 05 1993.

[39] D. Gay and R. Boudet. A technical theory of dynamical torsion for beams of any cross-section shapes. *Journal of Mechanical Design - J MECH DESIGN*, 102, 07 1980.

[40] M. F. Giberson. *The response of nonlinear multi-story structures subjected to earthquake excitation*. PhD thesis, California Institute of Technology, 1967.

[41] F. Gruttmann, R. Sauer, and W. Wagner. Theory and numerics of three-dimensional beams with elastoplastic material behavior. *International Journal for Numerical Methods in Engineering*, 48:1675–1702, 08 2000.

[42] J. Guedes, P. Pegon, and A. V. Pinto. A fibre/timoshenko beam element in castem 2000. Technical report, Special Publication Nr. I.94.31 Applied Mechanics Unit, Safety Technology Institute, Commission of the European Communities, Joint Research Centre, Ispra Establishment, Italy, 1994.

[43] J. Guedes and A. V. Pinto. A numerical model for shear dominated bridge piers. In *Proceedings of the Second Italy-Japan Workshop on Seismic Design and Retrofit of Bridges, Rome, Italy.*, 1997.

[44] A. Hillerborg, M. Modeer, and P. E. Petersson. Analysis of crack formation and crack growth in concrete by means of fracture mechanics and finite elements. *Cement and Concrete Research*, 6:773–782, 1921.

[45] T. T. C. Hsu. Torsion of structural concrete-plain cocnrete rectangular sections. *Special Publication*, 18:203–238, 1968.

[46] T. T. C. Hsu. *Torsion of reinforced concrete*. Van Nostrand Reinhold, New York, 1984.

[47] T. T. C. Hsu. Shear flow zone in torsion of reinforced concrete. *Journal of Structural Engineering-asce - J STRUCT ENG-ASCE*, 116, 11 1990.

[48] T. T. C. Hsu and Y. L. Mo. *Unified Theory of Concrete Structure*. John Wiley and Sons Ltd, 2010.

[49] T. T. C. Hsu, L. X. Zhang, and T. Gomez. A servo-control system for universal panel tester. *Journal of Testing and Evaluations*, 23(6):424–430, 1995.

[50] T. T. C. Hsu and R. R. H. Zhu. Softened membrane model for reinforced concrete elements in shear. *ACI Structural Journal*, 99(4):460–469, 2002.

[51] T.T.C. Hsu. Stresses and crack angles in concrete membrane elements. *Journal of Structural Engineering*, 124(12):1476–1484, 1998.

[52] T.T.C Hsu and Y.L. Mo. Softening of concrete in torsional members-theory and tests (part i). *Journal of the American Concrete Institute*, 82:290–303, 05 1985.

[53] C-H. Jeng. Softened membrane model for torsion in reinforced concrete members. *Advances in Engineering Research*, 2:251–338, 01 2012.

[54] M. Jirasek and Z. P. Bazan. *Inelastic Analysis of Structures*. Wiley, 2001.

[55] Kondoh K. and Atluri N. Large-deformation, elasto-plastic analysis of frames under nonconservative loading, using explicitly derived tangent stiffness based on assumed stresses. *Comp. Mech.*, 2:1–25, 1987.

[56] N. Khoder. *Enrichissement des poutres multifibres pour le calcul des contraintes transversales et la prise en compte du confinement dans les sections en bn arm* . PhD thesis, Universit Grenoble Alpes, France, 2018.

[57] N. Khoder, S. Grange, and Y. Sieffert. Enhancement of a 2d multifiber beam element in the case of reinforced concrete structures for taking into account the lateral confinement of concrete due to stirrups. *European Journal of Environmental and Civil Engineering*, Special Issue:2323–2329, 01 2017.

[58] P. Kotronis. *Cisaillement dynamique de murs en bn armods simplifiD et 3D*. PhD thesis, Ecole Normale Supeure de Cachan, 2000.

[59] P. Kotronis and Mazars J. Simplified modelling strategies to simulate the dynamic behaviour of r/c walls. *Journal of Earthquake Engineering*, 9(2):285–306, 2005.

[60] C. La Borderie. *Phms unilatux dans un matau endommageable: modsation et application analyse de structures en bn*. PhD thesis, Universit Paris VI, France, 1991.

[61] P. Lampert and B. Thrlimann. Ultimate strength and design of reinforced concrete beams in torsion and bending. *IABSE publications*, 31(3):645–655, 1971.

[62] V. Le Corvec. *Nonlinear 3d frame element with multi-axial coupling under consideration of local effects*. PhD thesis, University of California, Berkeley, 2012.

[63] J-Y. Lee, S-W. Kim, and J-H. Kim. Torsional strength and failure modes of reinforced concrete beams subjected to pure torsion. *Journal of the Korea Concrete Institute*, 20, 01 2008.

[64] S. H. Lee, S-K. Yoon, S. H. Yoon, Y. K. Hong, and J-Y. Lee. Torsional behavior of reinforced concrete beams predicted by a compatibility-aided truss model. *International Journal of Structural and Civil Engineering Research*, 01 2016.

[65] J. Lemaitre and J.L. Chaboche. *Mechanics of Solids Material*. Cambridge University Press, 1990.

[66] N. N. Lessig. Determination of load-carrying capacity of rectangular reinforced concrete elements subjected to flexure and torsion, study no. 5. Technical report, Institut Betona i Zhelezobetona [Institute of Concrete and Reinforced Concrete], Moscow, 1959.

[67] A. Marini and Spacone E. Analysis of reinforced concrete elements including shear effects. *ACI Structural Journal*, 103(3):645–655, 2006.

[68] L. Martinelli. *Modellazione di Pile di Ponti in C. A. a Travata Soggetti ad Eccitazione Sismica*. PhD thesis, Dipartimento di Ingegneria Strutturale, Politecnico di Milano, Milano, Italy, 1998.

[69] J. Mazars. A description of micro- and macroscale damage of concrete structures. *Engineering Fracture Mechanics*, 25(5-6):729–737, 1986.

[70] J. Mazars, F. Hamon, and S. Grange. A new 3d damage model for concrete under monotonic, cyclic and dynamic loadings. *Materials and Structures*, 6(2):1–15, 2014.

[71] J. Mazars, P. Kotronis, F. Ragueneau, and G. Casaux. Using multifiber beams to account for shear and torsion: Applications to concrete structural elements. *Computer Methods in Applied Mechanics and Engineering*, pages 7264–7281, 11 2006.

[72] A. E. McMullen and J. Warwaruk. The torsional strength of rectangular reinforced beams subjected to combined loading. Technical report, Report No. 2, Civil Engineering Department, University of Alberta, Alberta, Canada, 1967.

[73] M. Menegotto and P. E. Pinto. Slender rc compressed members in biaxial bending. *Journal of Structural Division*, 103(3):587–605, 1977.

[74] D. Mitchell and M.P. Collins. Diagonal compression field theory - a rational model for structural concrete in pure torsion. *ACI Journal*, 71:396–408, 01 1974.

[75] E. Morsch. *Der Eisenbetonbau, seine Anwendung und Theorie*. Wayss and Feytag, A. G., Im Selbstverlag der Firma, Neustadt a. d. Haardt, 1902.

[76] J. Navarro-Gregori, P. Miguel Sosa, M. Fernandez, and F. Filippou. A 3d numerical model for reinforced and prestressed concrete elements subjected to combined axial, bending, shear and torsion loading. *Engineering Structures*, 29:3404–3419, 12 2007.

[77] C. L. Navier. *Rms lecons donn le des ponts et chauss sur l'application mnique establissement des constructions et des machines*. Firmin Didet, Paris, 1826.

[78] M. P. Nielsen. Om forskydningsarmering i jernbetonjaelker (on shear reinforcement in reinforced concrete beams). *Bygningsstatiske Meddelelser*, 38(3), 1968.

[79] H. Nylander. *Vridning och vridningsinspanning vid betongkonstruktioner (Torsion and torsional restraint by concrete structures).* Distribueras av Ab Tidsskriften Byggmastaren, Stockholm, 1945.

[80] Standards Association of Australia. *SAA Concrete Structures Code.* A.S. CA2-1973, 1973.

[81] State Committee on Construction of the USSR Council of Ministers. *Structural Standards and Regulations.* State Publishing Offices for Literature on Structural Engineering, Architecture and Structural Materials, Moscow, 1962. (in Russian).

[82] W. M. Onsongo. *The diagonal compression field theory for reinforced concrete beams subjected to combined torsion, flexure and axial load.* PhD thesis, University of Toronto, Toronto, 1978.

[83] X.B. Pang and T.T.C. Hsu. Behavior of reinforced concrete membrane elements in shear. *Structural Journal of the American Concrete Institute*, 92(6):665–679, 1995.

[84] X.B. Pang and T.T.C. Hsu. Fixed-angle softened-truss model for reinforced concrete. *Structural Journal of the American Concrete Institute*, 93(2):197–207, 1996.

[85] S. Popovics. A numerical approach to the complete stress-strain curve of concrete. *Cement and Concrete Research*, 3(5):583–599, 1973.

[86] L. Prandtl. *Zur Torsion von prismatischen Stn.* Ludwig Prandtl Gesammelte Abhandlungen. Springer, Berlin, Heidelberg, 1903. (in German).

[87] B. G. Rabbat and M. P. Collins. A variable angle space truss model for structural concrete members subjected to complex loading. In *Douglas McHenry International Symposium on Concrete and Concrete Structures*, pages 547–587. SP-55, American Concrete Institute, Detroit, 1978.

[88] K. Rahal and M. P. Collins. Effect of thickness of concrete cover on shear-torsion interaction - an experimental investigation. *ACI Structural Journal*, 92:334–342, 05 1995.

[89] K. N. Rahal and M. P. Collins. Analysis of sections subjected to combined shear and torsion - a theoretical model. *ACI Structural Journal*, 92(4):1–13, 1995.

[90] K. N. Rahal and M. P. Collins. Combined torsion and bending in reinforced and prestressed concrete beams. *ACI Structural Journal*, 100(2):443–473, 2003.

[91] G. Ranzo. *A Non-linear Coupled Model for the Analysis of Reinforced Concrete Sections under Bending, Shear, Torsion and Axial Forces.* PhD thesis, Universit Roma La Sapienza, Roma, Italy, 2000.

[92] G. Ranzo and M. Petrangeli. A fibre finite beam element with section shear modelling for seismic analysis of rc structures. *Journal of Earthquake Engineering*, 2(3):443–473, 1998.

[93] E. Raush. *Design of reinforced concrete in torsion.* PhD thesis, Technische Hochschule, Berlin, Germany, 1929.

[94] M. Remino. *Shear Modeling of Reinforced Concrete Structures.* PhD thesis, Dipartimento di Ingegneria Civile, Universitgli Studi di Brescia, Brescia, Italy, 2004.

[95] W. Ritter. *Die Bauweise Hennebique*. Schweizerishe Bauzeitung, Zurich, 1899.

[96] G. Roniolo and M. di Prisco. *Reinforced Concrete Design to Eurocode 2*. Springer, 2017. Index.

[97] J. B. de Saint-Venant. Mire sur la torsion des prismes. *Mires des savants angers*, 1853.

[98] A. Saritas. *Mixed Formulation Frame Element for Shear Critical Steel and Reinforced Concrete Members*. PhD thesis, University of California, Berkeley, 2006.

[99] A. Saritas and F. Filippou. A beam finite element for shear critical rc beams. *ACI Special Publication*, SP-237-19:295–310, 2006.

[100] A. Saritas and F. Filippou. Analysis of rc walls with a mixed formulation frame finite element. *Computers and Concrete*, 12(4):519–536, 2013.

[101] A. C. Scordelis. Computer models for nonlinear analysis of reinforced and prestressed concrete structures. *PCI Journal*, 29:116–135, 11 1984.

[102] E. Spacone, F.C. Filippou, and F.F. Taucer. Fiber beam-column model for nonlinear analysis of r/c frames: Part 1. formulation. *Earthquake Engineering and Structural Dynamics*, 25(7):711–725, 1996.

[103] N. J. Stevens, S. M. Uzumeri, M. P. Collins, and G. T. Will. Constitutive model for reinforced concrete finite element analysis. *ACI Structural Journal*, 88:49–59, 01 1991.

[104] F. F. Taucer, E. Spacone, and F. C. Filippou. A fiber beam-column element for seismic response analysis of reinforced concrete structures. Technical report, Earthquake Engineering Research Center, University of California, Berkeley, 1991.

[105] S. Timoshenko. *Theory of Elasticity*. McGraw-Hill Book Co., N.Y.„ 1934.

[106] H. Valipour and S. Foster. Nonlinear reinforced concrete frame element with torsion. *Engineering Structures - ENG STRUCT*, 32:988–1002, 04 2010.

[107] F. J. Vecchio. Towards cyclic load modelling of reinforced concrete. *ACI Structural Journal*, 96(2):193–202, 1999.

[108] F. J. Vecchio. Disturbed stress field model for reinforced concrete: Formulation. *ASCE Journal of Structural Engineering*, 126(9):1070–1077, 2000.

[109] F. J. Vecchio and M. P. Collins. Response of reinforced concrete to in-plane shear and normal stresses. Publication no. 82-03, Department of Civil Engineering, University of Toronto, 1982.

[110] F. J Vecchio and M. P. Collins. The modified compression-field theory for reinforced concrete elements subjected to shear. *Journal of the American Concrete Institute*, 83:219–231, 03 1986.

[111] F. J. Vecchio and M. P. Collins. Predicting the response of reinforced concrete beams subjected to shear using modified compression field theory. *ACI Structural Journal*, 85:258–268, 05 1988.

[112] F. J. Vecchio and R. G. Selby. Toward compression-field analysis of reinforced concrete solids. *Journal of Structural Engineering-asce - J STRUCT ENG-ASCE*, 117, 06 1991.

[113] V.Z. Vlasov. *Thin Walled Elastic Beams*. Fizmatgiz, Moscow, 1959.

[114] W. Weaver and J.M. Gere. *Matrix Analysis of Framed Structures.*, chapter Fundamentals of the Stiffness Method. Springer, Boston, MA, 1990.

[115] R. Xu, H. Jiansheng, and W. Chen. Saint-venant torsion of orthotropic bars with inhomogeneous rectangular cross section. *Composite Structures - COMPOS STRUCT*, 92:1449–1457, 05 2010.

[116] V. K. Yudin. Determination of the load-carryig capacity of rectangular reinforced concrete elements subjected to combined torsion and bending. *Beton i Zelezobeton (Concrete and Reinforced Concrete), Moscow*, 6:265–269, 1962.

[117] R. R. H. Zhu and T. T. C. Hsu. Poisson effect in reinforced concrete membrane elements. *ACI Structural Journal*, 99(5):631–640, 2002.

Appendix

7.1 - Shape functions in two-node Timoshenko beam element

Shape functions for displacement vector:

$$
\begin{aligned}
N_1 &= 1 - \frac{x}{L}; \qquad N_2 = \frac{x}{L} \\
N_{3y/z} &= \frac{1}{1+\phi_{y/z}} \left[2\left(\frac{x}{L}\right)^3 - 3\left(\frac{x}{L}\right)^2 - \phi_{y/z}\frac{x}{L} + 1 + \phi_{y/z} \right] \\
N_{4y/z} &= \frac{L}{1+\phi_{y/z}} \left[\left(\frac{x}{L}\right)^3 - \left(2 + \frac{\phi_{y/z}}{2}\right)\left(\frac{x}{L}\right)^2 + \left(1 + \frac{\phi_{y/z}}{2}\right)\frac{x}{L} \right] \\
N_{5y/z} &= -\frac{1}{1+\phi_{y/z}} \left[2\left(\frac{x}{L}\right)^3 - 3\left(\frac{x}{L}\right)^2 - \phi_{y/z}\frac{x}{L} \right] \\
N_{6y/z} &= \frac{L}{1+\phi_{y/z}} \left[\left(\frac{x}{L}\right)^3 - \left(1 - \frac{\phi_{y/z}}{2}\right)\left(\frac{x}{L}\right)^2 - \frac{\phi_{y/z}}{2}\frac{x}{L} \right] \\
N_{7y/z} &= \frac{6}{\left(1+\phi_{y/z}\right)L} \left[\left(\frac{x}{L}\right)^2 - \frac{x}{L} \right] \\
N_{8y/z} &= \frac{1}{1+\phi_{y/z}} \left[3\left(\frac{x}{L}\right)^2 - \left(4 + \phi_{y/z}\right)\frac{x}{L} + 1 + \phi_{y/z} \right] \\
N_{9y/z} &= -\frac{6}{\left(1+\phi_{y/z}\right)L} \left[\left(\frac{x}{L}\right)^2 - \frac{x}{L} \right] \\
N_{10y/z} &= \frac{1}{1+\phi_{y/z}} \left[3\left(\frac{x}{L}\right)^2 - \left(2 - \phi_{y/z}\right)\frac{x}{L} \right]
\end{aligned}
$$

with $\phi_{y/z}$ le ratio de rigidity between bending and shear with respect to y and z axis, respectively.

$$
\phi_y = \frac{12}{L^2}\frac{\int_S Ey^2 dA}{\kappa_y \int_S GdS}; \qquad \phi_z = \frac{12}{L^2}\frac{\int_S Ez^2 dA}{\kappa_z \int_S GdS}
$$

κ_y and κ_z the shear correction factor in y and z direction, respectively.

Shape functions for strain vector:

$$
\begin{aligned}
B_1 &= \frac{\partial N_1}{\partial x} = -\frac{1}{L}; \qquad B_2 = \frac{\partial N_2}{\partial x} = \frac{1}{L} \\
B_{3y/z} &= \frac{\partial N_{3y/z}}{\partial x} - N_{7y/z} = -\frac{\phi_{y/z}}{L\left(1+\phi_{y/z}\right)} \\
B_{4y/z} &= \frac{\partial N_{4y/z}}{\partial x} - N_{8y/z} = -\frac{\phi_{y/z}}{2\left(1+\phi_{y/z}\right)} \\
B_{5y/z} &= \frac{\partial N_{5y/z}}{\partial x} - N_{9y/z} = \frac{\phi_{y/z}}{L\left(1+\phi_{y/z}\right)} \\
B_{6y/z} &= \frac{\partial N_{6y/z}}{\partial x} - N_{10y/z} = -\frac{\phi_{y/z}}{2\left(1+\phi_{y/z}\right)} \\
B_{7y/z} &= -\frac{\partial N_{7y/z}}{\partial x} = -\frac{6}{L\left(1+\phi_{y/z}\right)}\left(\frac{2x}{L^2} - \frac{1}{L}\right) \\
B_{8y/z} &= -\frac{\partial N_{8y/z}}{\partial x} = \frac{1}{\left(1+\phi_{y/z}\right)}\left(\frac{6x}{L^2} - \frac{4+\phi_{y/z}}{L}\right) \\
B_{9y/z} &= -\frac{\partial N_{9y/z}}{\partial x} = -\frac{6}{L\left(1+\phi_{y/z}\right)}\left(\frac{2x}{L^2} - \frac{1}{L}\right) \\
B_{10y/z} &= -\frac{\partial N_{10y/z}}{\partial x} = \frac{1}{\left(1+\phi_{y/z}\right)}\left(\frac{6x}{L^2} - \frac{2-\phi_{y/z}}{L}\right)
\end{aligned}
$$

7.2 - Lagrange Interpolation polynomial and Enhanced Compatibility matrix

Longitudinal interpolation matrix $\mathbf{L}(x)$ of $(3 \times 3.3.n_w)$:

$$
\mathbf{L}(x) = \begin{bmatrix} \mathbf{L}_1(x) & \dots & \mathbf{L}_i(x) & \dots \mathbf{L}_{nw}(x) \end{bmatrix} \tag{7.13}
$$

$\mathbf{L}_i(x)$ is a matrix of 3×3.3, containing the 1D Lagrange polynomial at section i:

$$
\mathbf{L}_i(x) = \begin{bmatrix}
L_i(x) & 0 & 0 & L_i(x) & 0 & 0 & L_i(x) & 0 & 0 \\
0 & L_i(x) & 0 & 0 & L_i(x) & 0 & 0 & L_i(x) & 0 \\
0 & 0 & L_i(x) & 0 & 0 & L_i(x) & 0 & 0 & L_i(x)
\end{bmatrix} \tag{7.14}
$$

Sectional interpolation matrices $\mathbf{S}_x(y,z)$ of $(3.3.n_w \times 3.s_w.n_w)$:

$$
\mathbf{S}_x(y,z) = \begin{bmatrix}
\hat{\mathbf{S}}_x(y,z) & \mathbf{0}_w & \mathbf{0}_w \\
\mathbf{0}_w & \hat{\mathbf{S}}_x(y,z) & \mathbf{0}_w \\
\mathbf{0}_w & \mathbf{0}_w & \hat{\mathbf{S}}_x(y,z)
\end{bmatrix}; \quad
\hat{\mathbf{S}}_x(y,z) = \begin{bmatrix}
\mathbf{S}_x^u(y,z) & \mathbf{0}_{3sw} & \mathbf{0}_{3sw} \\
\mathbf{0}_{3sw} & \mathbf{S}_x^v(y,z) & \mathbf{0}_{3sw} \\
\mathbf{0}_{3sw} & \mathbf{0}_{3sw} & \mathbf{S}_x^w(y,z)
\end{bmatrix} \tag{7.15}
$$

where $\mathbf{0}_w$ is a zero matrix of $(9 \times 3.s_w)$ columns; $\mathbf{0}_{3sw}$ is a zero matrix of $(3 \times s_w)$; $\mathbf{S}_x^u(y,z)$, $\mathbf{S}_x^v(y,z)$ and $\mathbf{S}_x^w(y,z)$ are three matrices of $(3 \times s_w)$ containing the row vector $\bar{\mathbf{S}}(y,z)$ in equation (3.20) and the zero row vector of s_w columns:

$$\mathbf{S}_x^u(y,z) = \begin{bmatrix} \bar{\mathbf{S}}(y,z) \\ \mathbf{0}_{sw} \\ \mathbf{0}_{sw} \end{bmatrix}; \quad \mathbf{S}_x^v(y,z) = \begin{bmatrix} \mathbf{0}_{sw} \\ \bar{\mathbf{S}}(y,z) \\ \mathbf{0}_{sw} \end{bmatrix}; \quad \mathbf{S}_x^w(y,z) = \begin{bmatrix} \mathbf{0}_{sw} \\ \mathbf{0}_{sw} \\ \bar{\mathbf{S}}(y,z) \end{bmatrix}; \tag{7.16}$$

Sectional interpolation matrices $\mathbf{S}_{yz}(y,z)$:

$$\mathbf{S}_{yz}(y,z) = \begin{bmatrix} \hat{\mathbf{S}}_{yz}(y,z) & \mathbf{0}_w & \mathbf{0}_w \\ \mathbf{0}_w & \hat{\mathbf{S}}_{yz}(y,z) & \mathbf{0}_w \\ \mathbf{0}_w & \mathbf{0}_w & \hat{\mathbf{S}}_{yz}(y,z) \end{bmatrix}; \quad \hat{\mathbf{S}}_{yz}(y,z) = \begin{bmatrix} \mathbf{S}_{yz}^u(y,z) & \mathbf{0}_{3sw} & \mathbf{0}_{3sw} \\ \mathbf{0}_{3sw} & \mathbf{S}_{yz}^v(y,z) & \mathbf{0}_{3sw} \\ \mathbf{0}_{3sw} & \mathbf{0}_{3sw} & \mathbf{S}_{yz}^w(y,z) \end{bmatrix} \tag{7.17}$$

$\mathbf{S}_{yz}^u(y,z)$, $\mathbf{S}_{yz}^v(y,z)$ and $\mathbf{S}_{yz}^w(y,z)$ are three matrices of $(3 \times s_w)$ containing the derivation with respect to y and z of the row vector $\bar{\mathbf{S}}(y,z)$ in equation (3.20) and the zero row vector of s_w columns:

$$\mathbf{S}_{yz}^u(y,z) = \begin{bmatrix} \mathbf{0}_{sw} \\ \dfrac{\partial \bar{\mathbf{S}}(y,z)}{\partial y} \\ \dfrac{\partial \bar{\mathbf{S}}(y,z)}{\partial z} \end{bmatrix}; \quad \mathbf{S}_{yz}^v(y,z) = \begin{bmatrix} \mathbf{0}_{sw} \\ \mathbf{0}_{sw} \\ \mathbf{0}_{sw} \end{bmatrix}; \quad \mathbf{S}_{yz}^w(y,z) = \begin{bmatrix} \mathbf{0}_{sw} \\ \mathbf{0}_{sw} \\ \mathbf{0}_{sw} \end{bmatrix} \tag{7.18}$$

7.3 - Cross section details and materials properties of experimental torsion tests

In Hsu test, the concrete cover thickness is 19 mm for all specimens, while the materials properties and reinforcement's dimensions are varied and cited as follows (Table 7.3):

Table 7.3 – Details of specimen of torsion tests carried by Hsu [45].

Beam	f_c (MPa)	Longitudinal rebar (mm)	f_{sl} (MPa)	Stirrup (mm) and (mm)	f_{st} (MPa)
B1	27.58	12.7	314	9.5 at 152	341
B2	28.61	15.9	316	12.7 at 181	320
B3	28.06	19.1	328	12.7 at 127	320
B4	30.54	22.2	320	12.7 at 92	323
B5	29.03	25.4	332	12.7 at 70	321
B6	28.82	28.7	332	12.7 at 57	323
B7	25.99	12.7	320	12.7 at 127	319
B8	26.75	12.7	322	12.7 at 57	320
B9	28.82	19.1	319	9.5 at 152	343
B10	26.48	28.7	3334	9.5 at 152	342
C1	26.34	9.5	341	9.5 at 216	341
C2	26.54	12.7	334	9.5 at 117	345
C3	26.89	15.9	331	12.7 at 140	330
C4	26.48	19	336	12.7 at 98	328
C5	27.23	22.2	328	12.7 at 73	329
C6	27.58	25.4	316	12.7 at 54	328
G1	26.34	9.5	341	9.5 at 216	341
G2	26.54	12.7	334	9.5 at 117	345
G3	26.89	15.9	331	12.7 at 140	330
G4	26.48	19	336	12.7 at 98	328
G5	27.23	22.2	328	12.7 at 73	329
G6	27.58	25.4	316	12.7 at 54	328
G7	27.23	22.2	328	12.7 at 73	329
G8	27.58	25.4	316	12.7 at 54	328
N1	26.34	9.5	341	9.5 at 216	341
N1a	26.54	12.7	334	9.5 at 117	345
N2	26.89	15.9	331	12.7 at 140	330
N2a	26.48	19	336	12.7 at 98	328
N3	27.23	22.2	328	12.7 at 73	329
N4	27.58	25.4	316	12.7 at 54	328
M1	26.34	9.5	341	9.5 at 216	341
M2	26.54	12.7	334	9.5 at 117	345
M3	26.89	15.9	331	12.7 at 140	330
M4	26.48	19	336	12.7 at 98	328
M5	27.23	22.2	328	12.7 at 73	329
M6	27.58	25.4	316	12.7 at 54	328
I1	26.34	9.5	341	9.5 at 216	341
I2	26.54	12.7	334	9.5 at 117	345
I3	26.89	15.9	331	12.7 at 140	330
I4	26.48	19	336	12.7 at 98	328
I5	27.23	22.2	328	12.7 at 73	329
I6	27.58	25.4	316	12.7 at 54	328
J1	26.34	9.5	341	9.5 at 216	341
J2	26.54	12.7	334	9.5 at 117	345
J3	26.89	15.9	331	12.7 at 140	330
J4	26.48	19	336	12.7 at 98	328

In the test of Lee et al. [63], the concrete cover thickness is 20 mm for all specimens, while the compressive strength of concrete $f_c = 42.6$ (MPa), the material properties and steel's dimension are cited as in Table 7.4).

Table 7.4 – Details of specimen of torsion tests carried by Lee et al. [63].

Beam	Longitudinal rebar (mm)	f_{sl} (MPa)	Stirrup (mm) and (mm)	f_{st} (MPa)
T1-1	4×12.7	410	9.5 at 130	370
T1-2	6×12.7	410	9.5 at 85	370
T1-3	8×12.7	410	9.5 at 65	370
T1-4	6×15.9	510	12.7 at 75	355
T2-1	4×12.7	410	9.5 at 225	370
T2-2	4×15.9	510	9.5 at 130	370
T2-3	6×15.9	510	9.5 at 88	370
T2-4	2×12.7 4×19	512.4	9.5 at 75	370

In the test of Csikos & Hegedus [29], the concrete cover thickness is 15 mm for all specimens, while the concrete used was C20 and the yielding strength of steel is 240 MPa in all cases (Table 7.5).

Table 7.5 – Details of specimen of torsion tests carried by Csikos & Hegedus. [29].

Series	Longitudinal rebar (mm)	Stirrup (mm) and (mm)
B	4×6	6 at 130
C	4×6	6 at 65
D	8×6	6 at 130
E	8×6	6 at 65

INSA de RENNES
Service des Formations

AVIS DU JURY SUR LA REPRODUCTION DE LA THESE SOUTENUE

Titre de la thèse:
Développement d'un modèle d'élément fini 3D pour des poutres en béton armé soumis à des sollicitations M-N-V-T

Nom Prénom de l'auteur : NGUYEN TUAN ANH

Membres du jury :
- Monsieur RAGUENEAU Frédéric
- Monsieur LE GROGNEC Philippe
- Madame COMBESCURE Christelle
- Monsieur MARTINELLI Enzo
- Monsieur KOTRONIS Panagiotis
- Monsieur NGUYEN Quang Huy

Président du jury : Panagiotis Kotronis

Date de la soutenance : 28 Novembre 2019

Reproduction de la these soutenue

☒ Thèse pouvant être reproduite en l'état
☐ Thèse pouvant être reproduite après corrections suggérées

Fait à Rennes, le 28 Novembre 2019

Signature du président de jury

Le Directeur,

M'hamed DRISSI

UNIVERSITE BRETAGNE SCIENCES LOIRE POUR L'INGENIEUR

INSA RENNES

Titre : Développement d'un modèle d'élément fini 3D pour des poutres en béton arme soumis à des sollicitations complexes M-N-V-T.

Mots clés : béton armé, élément fini, multifibre, gauchissement, torsion, sollicitation complexe, grand déplacement

Résumé : Le travail présenté dans ce mémoire porte sur le développement d'un modèle EF non linéaire pour des poutres BA soumis à des sollicitations combinées M-N-V-T. Afin de prendre en compte du couplage entre la torsion et la flexion, un élément poutre multifibre 3D enrichi est développé en utilisant l'approche de la plasticité distribuée et la formulation en déplacement. La première partie concerne le développement modèle EF qui se base sur l'enrichissement des hypothèses cinématique de poutre de Timoshenko, avec l'introduction des dégrée de liberté supplémentaires, afin de prendre en compte l'effet de gauchissement et de distorsion. L'un des objectifs de cette thèse est de proposer une méthode simple pour inclure la contribution des armatures transversales sur la raideur et la résistance de la section droite. Pour cela, une procédure itérative basée sur l'équilibre des contraintes entre les armatures et le béton est proposée. Le comportement 2D du béton armé est modélisé à l'aide de la théorie de Modified of Compression Field Theory (MCFT). La deuxième partie est consacrée à l'analyse numérique des éléments en béton et en BA soumis à torsion pure. Une nouvelle relation contrainte-déformation du béton fissuré est proposée dans le cadre de la MCFT en calibrant avec des résultats expérimentaux. La troisième partie est dédiée à l'analyse numérique des poutres BA soumis à des sollicitations combinées. Le modèle EF développé est validé par plusieurs numérique-analytique-expérimentale comparaisons. L'interaction entre le cisaillement, la flexion et la torsion est étudiée. Enfin, la dernière partie est dédiée à l'étude du comportement des éléments BA en grand déplacement.

Title : Development of an enhanced finite element model for reinforced concrete members subjected to combined shear-bending-torsion actions.

Keywords : reinforced concrete, finite element analysis, multi-fiber, warping, torsion, combined loading, large displacement

Abstract : This PhD thesis deals with the development of a non-linear finite element (FE) model for reinforced concrete (RC) members under coupling of multi-axial actions and in particular under torsion. Using the sectional-fiber approach and the displacement-based formulation, an enhanced multi-fiber 3D beam element is developed for predicting the behavior of RC elements subjected to arbitrary loading conditions (shear, bending and/or torsion). The first part concerns the FE formulation based on the enhancement of Timoshenko's beam kinematic assumptions with introducing of some additional degrees of freedom at each monitoring section, in order to take into account the phenomena of warping and eventually, distortion. Focusing on RC structures, one of the objectives is to find the simple way to include the transversal reinforcement into the cross-section analysis of the multi-fiber FE model, using behavior models based on the Modified of Compression Field Theory (MCFT) and its extension. The second part deals with the numerical analysis of concrete and RC members subjected to pure torsion. A constitutive law for concrete in tension is proposed within the framework of the MCFT in which the material parameters are determined by the calibration process of several experimental tests. In the third part, the interactions between shear, bending and torsion are investigated by comparing with the analytical solutions of skew-bending theory and several experimental tests in literature. Finally, the last part is dedicated to the investigation of the enhanced FE multi-fiber beam model under large displacement conditions, using a corotational framework.